



HAL
open science

Towards a combined statistical shape and musculoskeletal modeling framework for pediatric shoulder joint

Asma Salhi

► **To cite this version:**

Asma Salhi. Towards a combined statistical shape and musculoskeletal modeling framework for pediatric shoulder joint. Medical Imaging. Ecole nationale supérieure Mines-Télécom Atlantique, 2019. English. NNT: 2019IMTA0137 . tel-02414431

HAL Id: tel-02414431

<https://theses.hal.science/tel-02414431>

Submitted on 16 Dec 2019

HAL is a multi-disciplinary open access archive for the deposit and dissemination of scientific research documents, whether they are published or not. The documents may come from teaching and research institutions in France or abroad, or from public or private research centers.

L'archive ouverte pluridisciplinaire **HAL**, est destinée au dépôt et à la diffusion de documents scientifiques de niveau recherche, publiés ou non, émanant des établissements d'enseignement et de recherche français ou étrangers, des laboratoires publics ou privés.

THESE DE DOCTORAT DE

L'ÉCOLE NATIONALE SUPERIEURE MINES-TELECOM
ATLANTIQUE BRETAGNE PAYS DE LA LOIRE - IMT ATLANTIQUE

ECOLE DOCTORALE N° 601
*Mathématiques et Sciences et Technologies
de l'Information et de la Communication*
Spécialité : *Signal, Image Vision*

Par

Asma SALHI

Towards a Combined Statistical Shape and Musculoskeletal Modeling Framework for Pediatric Shoulder Joint

Thèse présentée et soutenue à Brest, le 21/06/2019
Unité de recherche : LaTIM (Laboratoire de traitement de l'Information Médicale)
Thèse N° : 2019IMTA0137

Rapporteurs avant soutenance :

Laurence CHEZE	Professeure, Université Claude
Bernard Lyon 1	
Faten CHAIEB	MCU, HDR, INSAT, Tunis

Composition du Jury :

Dominique LE NEN	PU-PH, CHU, Université de Brest
Président	
Laurence CHEZE	Professeure, Université Claude Bernard
Lyon 1	
Rapporteuse	
Faten CHAIEB	MCU, HDR, INSAT, Tunis
Rapporteuse	
Marcel LUTHI	MCU, Université de Bâle, Suisse
Examineur	
Bhushan BOROTIKAR	Ingénieur de Recherche, CHU, Brest
Encadrant	
Valérie BURDIN	Professeure, IMT Atlantique, Brest
Directrice de thèse	
Sylvain BROCHARD	PU-PH, CHU, Université de Brest
Co-directeur de thèse	

Acknowledgments

I would like to sincerely thank Pr. Valerie Burdin for being supportive and helpful throughout my PhD research and academics. Her guidance in my thesis was truly exceptional. I would also like to express my deepest gratitude to my supervisor Dr. Bhushan Borotikar, whose knowledge and patience have been phenomenal in the completion of this work. His timely inputs and expertise were essential to all the aspects of this thesis project. A particular thanks to Pr. Sylvain Brochard for his constructive recommendations on this project and guidance with the clinical aspects of my work. I appreciate all the discussions with him, which were very valuable in helping me better understand the interest of this project from a clinical perspective.

Many thanks to my colleagues from ITI department and LaTIM. I am very fortunate to have worked with many great researchers, clinicians, and surgeons. Their professional and personal support are gratefully acknowledged.

I would also like to thank my friends for their support and encouragement.

Last but not the least, I would like to thank my family for being the pillar of strength in my success and accomplishments.

Vers un framework combinant la modélisation statistique de forme et la modélisation musculo-squelettique pour l'articulation de l'épaule pédiatrique : Résumé étendu

1. Contexte et Motivations

L'appareil locomoteur humain est une structure complexe composée d'os, d'articulations, de cartilages articulaires, de muscles et de ligaments [1]. Les mouvements sains du système musculo-squelettique exigent une synchronisation et un équilibre des forces produites par de multiples muscles qui sont contrôlés par le système neuro-musculaire [1, 3]. En cas de maladie ou de trouble, une ou plusieurs composantes de l'appareil locomoteur sont perturbées, ce qui entraîne des mouvements anormaux ou douloureux. Le nombre de maladies et blessures, qu'elles soient musculaires ou osseuses, est en augmentation dans le monde entier selon le rapport du CDC de 2017 [4] ou de Barroso et Thiele [5] qui rapportent une tendance similaire. Alors que les maladies musculo-squelettiques résultent d'une réponse physiopathologique à des facteurs internes ou externes, les troubles représentent une perturbation du fonctionnement normal due à ces maladies [2, 3, 6-8]. De nombreux types de maladies, transmissibles et non transmissibles, affectent négativement le système musculo-squelettique. Non seulement cela menace le mode de vie normal des individus, mais cela a aussi un impact négatif sur les dépenses de santé. De plus, les maladies non transmissibles et les blessures sportives perturbent l'appareil locomoteur humain et peuvent rendre la personne vulnérable aux troubles musculo-squelettiques (TMS) (ex. arthrose précoce), ce qui affecte sa qualité de vie [6, 9]. Inévitablement, ces conditions limitent les activités de plein air des populations concernées, réduisent ainsi la croissance normale des enfants et restreignent également l'intégration sociale des séniors.

Les progrès importants de ces dernières années en matière d'imagerie médicale et des dispositifs médicaux d'une part et des avancées technologiques (Machine Learning, Modélisation computationnelle, impression 3D, etc, ...) d'autre part, permettent de mieux diagnostiquer et traiter les TMS. C'est particulièrement le cas pour les TMS chez la population pédiatrique où le résultat de ces traitements a un impact à long terme sur le système musculo-squelettique, et par conséquent sur leur qualité de vie [7]. Dans le traitement des TMS pédiatriques, l'imagerie médicale est généralement utilisée à des fins diagnostiques, tandis que les dispositifs médicaux sont davantage utilisés pour le traitement et la

réadaptation. Les outils technologiques tels que la modélisation statistique des formes peuvent aider les chirurgiens et les cliniciens pour l'évaluation morphologique de la structure musculo-squelettique [10]. Cependant, ces outils peuvent fournir des informations (tant qualitatives que quantitatives), et une aide précieuse à chaque étape de la gestion des TMS pour évaluer les mécanismes articulaires sous-jacents et les déséquilibres de force [11]. Ces informations comprennent un diagnostic précis (du déséquilibre des forces), des stratégies de traitement optimisées (pour la chirurgie ou la réadaptation), une évaluation précise de la récupération et des visites de suivi (en rétablissant des mécanismes articulaires sains) [12-16]. Les domaines de modélisation computationnelle comprennent généralement (mais sans s'y limiter) la modélisation par éléments finis, la modélisation par éléments physiques discrets et la modélisation musculo-squelettique multi-corps. La modélisation multi-corps est un moyen efficace et non invasif pour évaluer le fonctionnement du système musculo-squelettique en utilisant des principes de dynamique et en dérivant des paramètres musculaires et articulaires tels que les moments articulaires, les forces musculaires et les bras de levier [17, 18]. Ainsi, la modélisation musculo-squelettique multi-corps permet d'obtenir des cinématiques prédictives, d'effectuer des études de simulation, d'identifier les relations « cause-effet ». Toutefois, le problème de disponibilité des données associées de la structure musculo-squelettique représente un obstacle à la réalisation et l'utilisation de ces modèles [1]. En effet, le système musculo-squelettique humain dispose d'un grand nombre de variables qui sont difficilement mesurables.

L'articulation de l'épaule, l'une des articulations les plus complexes de l'appareil locomoteur, est souvent soumise à de multiples TMS [7, 19-22]. Les troubles les plus courants de l'articulation de l'épaule sont les déchirures de la coiffe des rotateurs, l'arthrose, l'épaule gelée, les fractures et les malformations de l'épaule [8, 9, 20-22]. Pour la plupart de ces TMS, une chirurgie est nécessaire pour la récupération maximale de la motricité de l'épaule. Durant la phase préopératoire, il est primordial de connaître la forme pré-morbide de l'os pour optimiser les guides de coupe et mettre en place l'implant, ce qui, à son tour, permet de restaurer la fonction normale de l'épaule. Chez les enfants, d'autres TMS existent comme la paralysie obstétricale de plexus brachiale (POPB). La POPB est une lésion nerveuse qui entraîne une déformation et une paralysie partielle ou totale de membre supérieur [7, 19, 23]. Des interventions thérapeutiques rééducatives et souvent chirurgicales sont souvent proposées pour favoriser la récupération maximale de la motricité. Toutefois, le manque de compréhension du comportement musculaire anormal réduit considérablement le succès du traitement. La modélisation musculo-squelettique peut être utilisée efficacement pour élucider les mécanismes patho-mécaniques de la POPB afin de développer les stratégies d'évaluation clinique, de rééducation fonctionnelle ou de traitement. Cependant, les modèles musculo-squelettiques de l'articulation de l'épaule sont limités dans la littérature et, à ce jour, il n'existe aucun modèle pédiatrique de l'épaule développé pour représenter et étudier le fonctionnement anormal de l'épaule chez les enfants avec POPB [16].

La modélisation musculo-squelettique a été largement utilisée dans la littérature pour évaluer le fonctionnement de l'épaule [22, 24, 25]. Des modèles biomécaniques de l'épaule adulte ont été développés et utilisés pour comprendre les problèmes cliniques [26, 27]. Toutefois, les hypothèses multiples et les cadres de modélisation génériques utilisés dans ces études réduisent l'utilité clinique de ces modèles. Une façon d'éliminer les hypothèses est de mener des expériences, mais ce n'est pas toujours faisable, car la plupart des expériences visant à obtenir de tels paramètres ont tendance à être soit invasives, soit coûteuses. L'imagerie médicale peut également être utilisée pour obtenir certains paramètres. Cependant, les individus doivent passer par un processus d'imagerie qui peut ne pas toujours être faisable ou souhaitable. Par exemple, dans la population pédiatrique, il n'est pas souhaitable

d'exposer l'enfant à plusieurs doses de radiation. Une troisième approche novatrice consisterait à combiner la modélisation musculo-squelettique avec des outils de modélisation statistique des formes (MSF) pour profiter des avancées technologiques de chaque domaine. De multiples paramètres nécessaires pour personnaliser les modèles musculo-squelettiques générique pourraient être obtenus en utilisant la modélisation statistique de forme. Ces paramètres incluent la forme morphologique de l'os, les régions d'insertion musculaire, les formes manquantes (dus au protocole d'imagerie médicale ou à la morbidité) et l'épaisseur corticale de l'os. Bien qu'une telle tentative de combiner ces deux domaines existe dans la littérature, celle-ci se limite à dériver l'épaisseur de l'os cortical utilisant les MSF et incorporer cette information dans des modèles par éléments finis.

Il ressort clairement des descriptions ci-dessus que 1) les troubles musculaires et osseux sont à la hausse à l'échelle mondiale, ce qui a des répercussions sur la qualité de vie et impacte le système de santé avec une hausse des coûts; 2) les troubles de l'épaule chez les adultes et les enfants constituent une préoccupation en ce qui concerne les outils d'évaluation nécessaires en chirurgie et en évaluation clinique; 3) les progrès technologiques en imagerie médicale, modélisation statistique et modélisation de la forme musculo-squelettique ont démontré individuellement leur capacité à évaluer les TMS; 4) la modélisation musculo-squelettique joue un rôle clé dans l'évaluation clinique des TMS de l'épaule; toutefois, il existe peu de modèles adultes et aucun modèle pédiatrique ; 5) l'élaboration de modèles musculo-squelettiques propres à un sujet peut permettre de mieux comprendre la mécanique des troubles de l'épaule; cependant, le manque de moyens pour en tirer des paramètres de base propres au patient constitue un obstacle dans cette recherche; 6) un nouveau cadre formant la convergence des technologies avancées pour éliminer des hypothèses dans la construction des modèles musculosquelettiques de l'épaule doit être conçu.

2. Objectifs

L'objectif général de ma thèse consistait à construire un cadre de travail combinant deux domaines de recherche - la modélisation statistique de la forme (MSF) et la modélisation musculo-squelettique pour évaluer les TMS de l'articulation de l'épaule pédiatrique. Pour établir un tel cadre, il était d'abord nécessaire d'adresser les questions liées aux différents domaines de recherche. Ainsi, en fonction de la disponibilité des données, des ressources et du temps, les objectifs spécifiques suivants ont été poursuivis dans ce travail de thèse.

- 1) Construire une MSF d'os d'épaule adultes et rapporter l'utilité clinique d'une telle MSF pour prédire de nouvelles formes osseuses.
- 2) Illustrer et valider la capacité des MSF de l'épaule à prédire avec précision les régions d'insertion musculaire pour de nouvelles formes osseuses dans la population adulte.
- 3) Illustrer et vérifier de façon critique la capacité des MSF de la scapula adulte à prédire la forme scapulaire complète à partir d'une omoplate présentant des parties manquantes.
- 4) Intégrer l'algorithme de prédiction de l'insertion musculaire dans un modèle musculo-squelettique existant de l'articulation de l'épaule adulte et comparer les changements dans les résultats de la mécanique articulaire.

5) Développer un modèle pédiatrique d'articulation musculo-squelettique de l'épaule dans OpenSim (un logiciel libre) à partir des données d'un enfant sain.

6) Illustrer l'utilisation d'un modèle pédiatrique d'articulation musculo-squelettique de l'épaule chez un enfant avec POPB pour déterminer la cinématique de l'articulation scapulo-thoracique et gléno-humérale ainsi que les paramètres mécaniques articulaires (moments articulaires, forces articulaires, forces musculaires) pendant une activité de flexion scapulaire, du côté sain et du côté pathologique.

Ce modèle sera utilisé ultérieurement pour évaluer la POPB en effectuant des simulations spécifiques à un sujet pour les activités de la vie quotidienne.

3. Contenu du manuscrit

Le manuscrit de ma thèse est structuré en trois parties. Outre le chapitre d'introduction (chapitre 1) et de conclusion et perspectives (chapitre 11), les trois parties, telles qu'elles sont présentées dans le manuscrit, sont décrites ci-dessous.

Partie I : « Anatomie et biomécanique de l'épaule chez l'adulte »

La première partie (chapitres 2 et 3) décrit l'anatomie et la biomécanique de l'épaule adulte.

Chapitre 2 : Ce chapitre explique l'anatomie squelettique et fonctionnelle de l'épaule adulte. De brèves explications avec illustrations sont fournies pour les terminologies anatomiques utilisées dans l'articulation de l'épaule. De plus, la structure squelettique, les articulations, les muscles et les mouvements de l'articulation de l'épaule sont également expliqués en détail. De telles informations sont cruciales pour la compréhension et le développement de la modélisation de l'articulation de l'épaule (MSF et musculo-squelettique).

Chapitre 3 : Le complexe de l'épaule est composé principalement de 4 articulations, à savoir l'articulation scapulo-thoracique, l'articulation sterno-claviculaire, l'articulation acromio-claviculaire et l'articulation gléno-humérale. Ce chapitre est donc divisé en quatre parties. Chaque partie décrit la biomécanique de chaque articulation en termes de cinématique (mouvement articulaire), de cinétique (force articulaire) et de contraintes (stabilité articulaire).

Partie II : « Modélisation statistique de la forme pour prédire les données d'entrée du modèle musculo-squelettique patient-spécifique »

La seconde partie (chapitres 4, 5 et 6) comprend une description des méthodologies de la modélisation statistique de forme et ses applications pour créer un modèle géométrique statistique de la scapula (chapitre 4), pour prédire des zones d'attachement musculaire spécifiques au sujet sur la scapula et l'humérus (chapitre 5) utilisant les MSF, et pour prédire la forme complète de la scapula adulte à partir de données partielles (chapitre 6).

Chapitre 4 : Ce chapitre comporte deux sous-parties. Dans la première partie, l'état de l'art de la modélisation statistique de forme (et ses applications) a été présenté. Ensuite, les méthodes utilisées dans les étapes intermédiaires de la construction de MSF (mise en correspondance, recalage rigide et non rigide) ont été brièvement décrites pour sensibiliser le lecteur à ces notions, qui seront utilisées et mieux illustrées dans les chapitres suivants. Enfin, une étude a été conduite pour analyser la validité clinique du MFS de la scapula.

La figure 1 montre le pipeline mis en place pour créer un MFS scapulaire adulte et évaluer la validité clinique du MFS scapulaire augmenté en suivant les étapes suivantes :

- 1- Construction du MSF scapulaire : Une base de données d'imagerie d'échantillons d'os secs et de scanners cadavériques ($n = 27$) a été utilisée pour cette étude. Des images tomodensitométriques ont été acquises, segmentées manuellement (Amira, FEI, Hillsboro, V5.4) et un maillage de surface isotrope et de même nombre de points (15000) pour chaque échantillon a été créé. Nous avons utilisé un pipeline proposé et évalué antérieurement au sein de notre équipe, Iterative Median Closest Point - Gaussian Mixture Model (IMCP-GMM) [28]. Il peut être résumé en trois étapes principales : alignement mutuel médian rigide, alignement non rigide pour établir la correspondance bijective des maillages au travers de la base d'apprentissage, puis analyse en composantes principales.
- 2- Augmentation du MFS avec les points anatomiques : le MFS scapulaire construit a été ensuite augmenté par la définition de 16 points anatomiques issus de zones cliniquement pertinentes. Trois cas ont été testés et comparés. Ceux-ci ont été repartis sur toute la scapula avec une distinction importante du nombre de point anatomiques situés dans la zone glénoïde.
- 3- Evaluation de la validité clinique : une évaluation des différents modèles statistiques augmentés a été réalisée en comparant la forme de la région de glénoïde prédite et la forme originale de 6 spécimens n'ayant pas été utilisés lors de l'élaboration du MSF scapulaire (extérieurs à la base d'apprentissage).

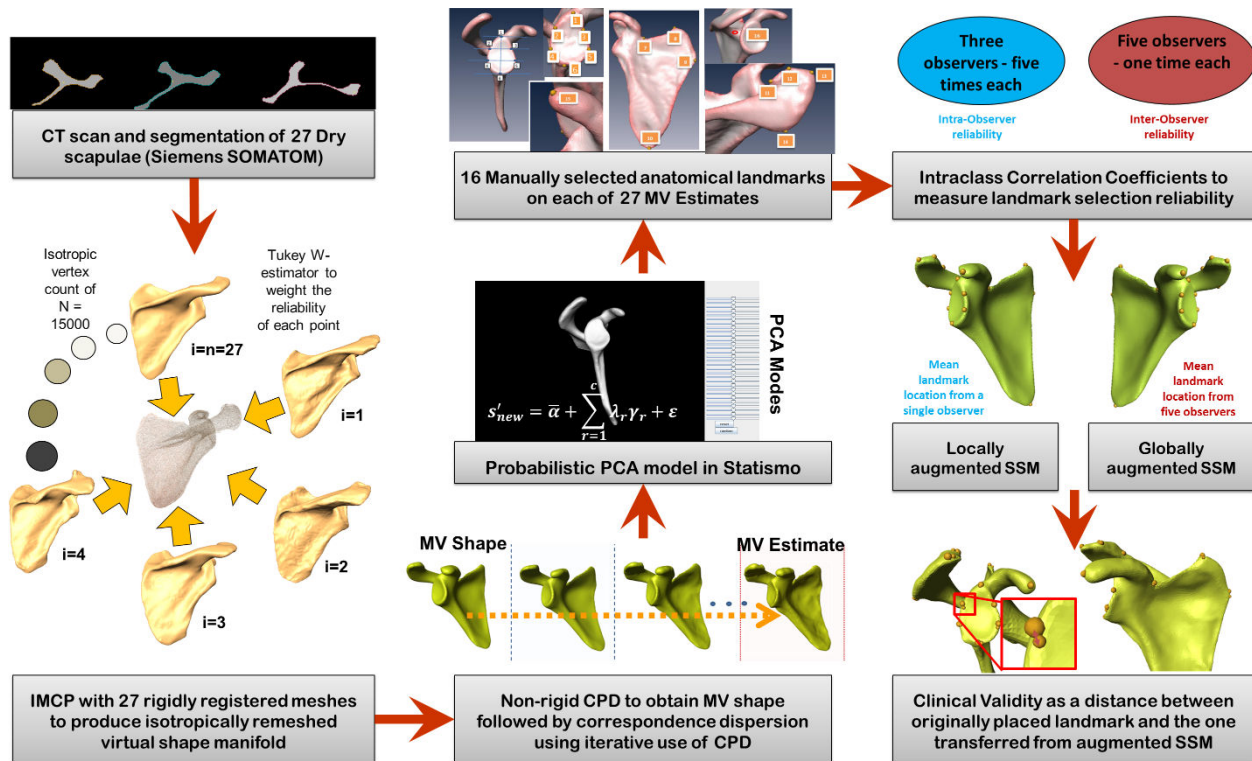


Figure 1 : Pipeline schématique montrant la méthodologie utilisée pour évaluer la validité clinique d'un MFS scapulaire augmenté.

Chapitre 5 : Ce chapitre comporte à nouveau deux parties. La première partie présente la méthode utilisée pour prédire automatiquement les régions d'insertion musculaire en construisant un MFS avec les informations d'insertion musculaire. Deux MSF, de la scapula et l'humérus, sont créés à partir d'une base de données de 27 scapula et 28 humérus suivant la méthode présentée dans le chapitre 4. Pour chacun des os de la base de données, les régions d'insertions musculaires (origine/insertion) de six muscles (Supraspinatus, Infraspinatus, subscapularis, teres major, teres minor et deltoïde) ont été identifiés sur le maillage par deux observateurs. Les sommets représentatifs des insertions musculaires ont été labélisés sur chaque os et transférés sur la forme moyenne du MSF des deux os. La validité des régions de ces insertions musculaires sur la forme moyenne a d'abord été confirmée visuellement par un clinicien expert. Ensuite, pour valider cette approche, ces régions ont été transférées, via le modèle statistique augmenté, sur les os d'une base de données externes constituée d'os sud-africains segmentés manuellement (10 scapula et 8 humérus). Cette méthode a été validée en comparant les régions d'insertion musculaire prédites avec celles manuellement labélisées sur les os externes. La validité de la prédiction a été jugée excellente sur la base de mesures de distances (distance moyenne, RMS et Hausdorff) et du coefficient de similarité de Dice. Dans la deuxième partie, une stratégie visant à combiner la MSF et la modélisation musculo-squelettique a été illustrée. L'effet de la personnalisation des insertions musculaire a été analysé sur les résultats issus d'un modèle musculo-squelettique de l'épaule. Des images scanners des épaules de dix nouveaux sujets ont été utilisées. Les os de la scapula et de l'humérus ont été manuellement segmentés. Puis, les insertions musculaires ont été prédites via les MSF augmentés. Le modèle musculo-squelettique de l'épaule de Newcastle (NSM), constitué de 6 segments rigides, 11 degrés de liberté, 31 muscles et 3

ligaments a été mis en œuvre, à partir du modèle générique classiquement mis à l'échelle d'une part, et avec les 12 insertions musculaires personnalisées et la géométrie osseuse d'autre part. Pour chaque sujet deux modèles musculo-squelettiques ont été construits : un modèle générique et un modèle personnalisé. Deux mouvements de l'épaule sont alors simulés pour chaque sujet : abduction et élévation dans le plan de la scapula au cours desquels le modèle calcule les efforts musculaires et les actions de contact articulaire en minimisant un coût fonctionnel. Ces mesures sont ensuite comparées entre modèle générique et modèle personnalisé. Les comparaisons des forces de contact articulaires ne révèlent pas de différences significatives lors des deux mouvements, à l'exception de la composante antéro-postérieure dans les angles d'élévation extrêmes. Les bras de levier des six muscles étaient significativement différents tout au long des deux mouvements. Les forces musculaires étaient significativement différentes pour le deltoïde postérieur, le teres major et le teres minor lors du mouvement d'abduction ; et pour le deltoïde moyen, le deltoïde postérieur, le supraspinatus, l'infraspinatus, le subscapularis et le teres major pour le mouvement d'élévation dans le plan de la scapula.

Chapitre 6 : Ce chapitre a été présenté sous forme d'un article pour une publication dans un journal. Le but de cette étude était de créer et d'évaluer un pipeline basé sur la modélisation statistique de formes qui peut prédire avec précision la partie manquante dans différentes régions de l'os de la scapula. Cette étude comprend quatre étapes. Lors de la première étape, les formes scapulaires 3D ont été obtenues par segmentation manuelle à partir d'images CT de 82 échantillons secs. Dix échantillons de cette base de données ont été extraits de la base d'apprentissage pour représenter différentes catégories morphologiques particulières à des fins d'évaluation. Les échantillons restants ont été examinés par l'expert médical pour vérifier leur normalité anatomique, puis utilisés pour construire le MSF scapulaire.

Dans la deuxième étape, quatre défauts ont été créés virtuellement sur dix scapula externes à l'aide d'un logiciel d'imagerie 3D (Amira, FEI, Hillsboro, V5.4). Ces 10 scapula ont été sélectionnées pour représenter chaque type de classification anatomique de l'os scapulaire par au moins une instance. Ainsi, la forme de la glène a été classée comme étant de type 0, I, II et III en fonction de la morphologie glénoïdale et en particulier de l'incisure. L'acromion a été classé comme type I, II et III sur la base d'une morphologie plate, courbe et crochue. Deux échantillons ont été sélectionnés pour représenter un Angle d'Épaule Critique (AEC) élevé ou faible et une inclinaison de glène ante et rétroversée. Les défauts d'imagerie virtuels étaient classés en 4 groupes (Figure 2) :

- Groupe 1 : représente une perte légère de l'os glénoïdien
- Groupe 2 : représente une perte sévère de l'os glénoïdien
- Groupe 3 : partie supérieure manquante de l'omoplate (une partie de l'acromion et du processus coracoïde).
- Groupe 4 : partie inférieure manquante de l'omoplate (fosses scapulaires inférieures),

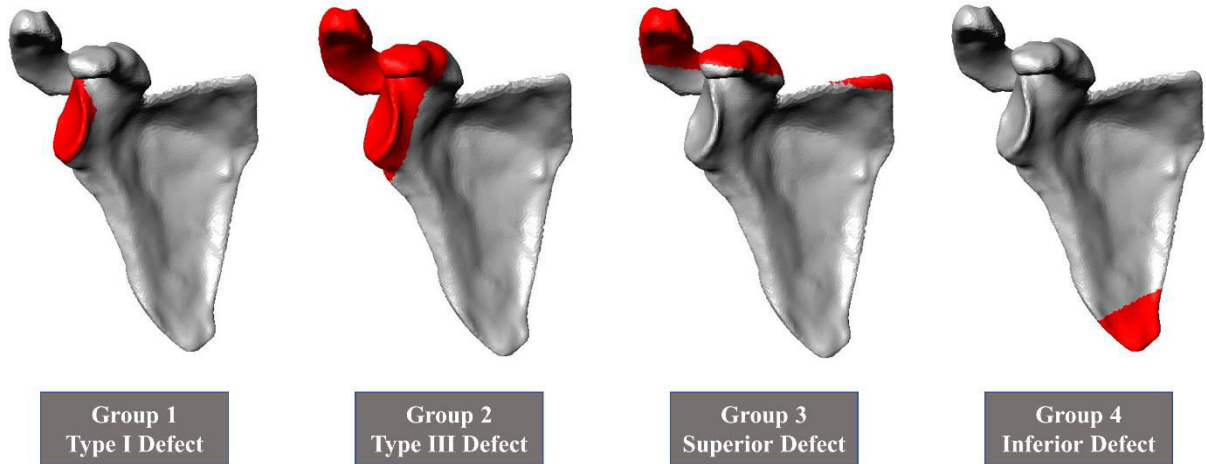


Figure 2 : Création virtuelle de quatre groupes de défauts scapulaires. Les parties en rouge sont supprimées de la scapula.

Dans la troisième étape, un algorithme de reconstruction, basé sur le modèle MSF, a été développé pour prédire la forme scapulaire complète des 40 scapulae avec des défauts scapulaires créés précédemment.

Lors de la dernière étape, des évaluations ont été faites en comparant la forme de l'os prédite avec sa contrepartie originale en utilisant :

- Des mesures anatomiques classiques (inclinaison de la glène, version de la glène, centre glène et CSA),
- Des mesures de distance (moyenne géométrique, Hausdorff, moyenne quadratique) et des mesures de similarité (coefficient Dice).

Un tel algorithme représente un outil très puissant, durant la phase de planification pré-opératoire, pour dériver l'anatomie pré-morbide de l'omoplate à partir des formes scapulaires avec des parties manquantes.

Partie III : « Modélisation musculo-squelettique de l'épaule pédiatrique »

La troisième partie inclut une description de la paralysie obstétricale du plexus brachial pédiatrique (chapitre 7) et de la dynamique multi-corps rigides (chapitre 8), le développement d'un modèle musculo-squelettique de l'épaule de l'enfant (chapitre 9) et l'utilisation de ce modèle pour déterminer la cinématique et les moments nets articulaires dans une étude de cas (chapitre 10).

Chapitre 7 : Ce chapitre fournit une description de la pathologie de la POBP avec une revue de littérature de ses répercussions structurelles et fonctionnelles. L'impact morpho-fonctionnel de cette pathologie a été ensuite présenté. Les modèles musculo-squelettiques existants qui ont été utilisés pour l'évaluation de la pathologie en question ont été identifiés et discutés. Enfin, les défis et les limitations de la pratique actuelle, en terme d'utilisation des modèles musculo-squelettiques d'épaule adulte pour simuler les pathologies de l'épaule pédiatrique, ont été discutés.

Chapitre 8 : Ce chapitre résume la théorie de la dynamique multi-corps rigides puis présente les modèles musculaires et enfin les modèles musculo-squelettiques existants, notamment pour le complexe de l'épaule. La dynamique des systèmes multi-corps a été présentée en termes de cinétique et cinématique des articulations et les équations de Newton-Euler du mouvement, sont dérivées. Une description de la théorie de la contraction musculaire et un aperçu de la modélisation musculaire pour les systèmes dynamiques sont ensuite discutés. Puis, les concepts de dynamique inverse et directe et les informations d'introduction sur les logiciels open source OpenSim sont fournis dans ce chapitre. On trouvera à la fin de ce chapitre une synthèse des différents modèles musculo-squelettiques de l'épaule développés dans la littérature.

Chapitre 9 : Ce chapitre décrit en détail le processus de développement d'un modèle d'articulation de l'épaule pédiatrique, en utilisant la plateforme OpenSim. Le modèle inclut quatre segments osseux rigides (thorax, clavicule, omoplate, humérus). Les coordonnées des segments osseux sont dérivées à partir d'une IRM d'une jeune fille âgée de 10 ans en bonne santé et les recommandations de la Société Internationale de Biomécanique (ISB) ont été suivies pour définir les repères de chaque segment. Ces segments ont été reliés entre eux via les articulations sterno-claviculaire, acromio-claviculaire, gléno-humérale et scapulo-thoracique avec 13 degrés de liberté au total. Le modèle inclut 52 lignes d'action pour représenter 14 muscles. Les trajets musculaires sont décrits à l'aide de points de passage fixes et mobiles, ainsi qu'en définissant des surfaces de contour lorsque cela s'avère nécessaire en utilisant l'algorithme disponible dans la plateforme OpenSim. Le modèle développé constitue le premier modèle musculo-squelettique d'épaule pédiatrique.

Chapitre 10 : Il illustre la capacité du modèle développé au chapitre précédent à évaluer la paralysie obstétricale du plexus brachial pédiatrique à partir de données expérimentales de mouvement. Un protocole expérimental rigoureux est mis en œuvre pour mesurer le mouvement de flexion de l'épaule, pour les côtés sain et pathologique, d'un enfant atteint de la POPB. Le modèle de l'épaule pédiatrique développé, décrit dans le chapitre 9, est mis à l'échelle du sujet en utilisant les marqueurs cutanés dans une position statique de référence. La cinématique des articulations gléno-humérale et scapulo-thoracique est calculée dans OpenSim par optimisation globale, en attribuant un même poids à tous les marqueurs. Ces mouvements ont été comparés entre le côté sain et le côté pathologique. Ensuite, la cinématique dérivée du modèle a été utilisée pour déterminer les moments et les forces articulaires et les forces musculaires en utilisant respectivement des outils d'optimisation dynamique inverse et statique dans la plateforme OpenSIM.

Chapitre 11 : Ce chapitre fournit un bref résumé de l'étude et un aperçu des résultats de cette thèse en considérant les objectifs décrits précédemment. Enfin, des perspectives et des orientations futures de ce travail de recherche ont été proposées.

4. Résultats issus de mes travaux de thèse

Il est rappelé que l'objectif global de cette thèse est de construire un cadre combinant deux domaines de recherche - la modélisation statistique de forme (MSF) et la modélisation musculo-squelettique pour évaluer les troubles musculo-squelettiques de l'épaule pédiatrique.

Comme proposé dans le premier objectif, des MSF des os d'épaule adulte ont été construits et une étude sur l'analyse de la validité clinique de ces MSF pour prédire de nouvelles formes osseuses a été conduite. Nous avons appris que lorsqu'un MSF est augmenté d'un ensemble de point anatomiques, l'utilité clinique d'un tel MSF augmenté est plus élevée que celle d'un MSF non augmenté.

Dans le cadre du deuxième objectif, nous avons illustré et validé la méthodologie pour prédire avec précision les régions d'insertion musculaire des os de l'omoplate et de l'humérus. Au cours de ce processus, nous avons appris que la méthodologie proposée est générique et peut s'appliquer à tous les os et à toutes les régions d'insertion musculaire respectives.

Dans le cadre du troisième objectif, j'ai développé un algorithme pour prédire avec précision la partie manquante dans différentes régions de l'os de la scapula. Cet algorithme peut être utilisé efficacement dans la planification pré-chirurgicale pour prédire la forme pré-morbide de l'os, ce qui constitue une information importante pour la planification d'une intervention chirurgicale réussie. Cet algorithme peut également être utilisé pour prédire la forme scapulaire complète à partir de données d'imagerie incomplètes et donc des informations géométriques de l'omoplate spécifiques au sujet pourraient être incorporées dans les aspects de modélisation musculo-squelettique.

Le quatrième objectif était axé sur l'élaboration d'un cadre intégrant des domaines MSF et musculo-squelettique pour parvenir à un modèle avec des paramètres spécifiques à chaque sujet. Nous avons utilisé un modèle musculo-squelettique de l'épaule (le modèle NSM) déjà développé et l'algorithme de prédiction d'insertion musculaire pour générer un modèle musculo-squelettique spécifique patient. La comparaison entre les modèles génériques et les modèles spécifiques au sujet a montré une modification des efforts musculaires, des forces de contact articulaire et des bras de levier. Les résultats obtenus ont bien été corroborés avec la littérature. Ainsi, il a été illustré à la fin de la partie II qu'un cadre combinant la MSF et la modélisation musculo-squelettique peut être établi pour les évaluations biomécaniques de l'épaule des adultes.

La partie III de la thèse portait sur le développement de la modélisation musculo-squelettique de l'épaule pédiatrique. Après avoir présenté un bref résumé de la théorie de la dynamique des systèmes multi-corps, un modèle d'articulation de l'épaule pédiatrique a été construit. Ce modèle inclut 13 degrés de liberté et 52 lignes d'action pour représenter 14 muscles. Les muscles ont été modélisés comme des muscles de type Hill-Type et aucun ligament n'était présent dans le modèle. Le modèle a été développé sur la plateforme open-source, OpenSim, spécialement conçue pour la modélisation musculo-squelettique. Bien qu'il n'ait pas été validé, ce modèle constitue le premier modèle musculo-squelettique d'épaule pédiatrique.

Dans le chapitre 10, ce modèle générique a été mis à l'échelle et utilisé pour illustrer la différence entre le côté sain et le côté pathologique d'une épaule pédiatrique, en termes de cinématique des articulations gléno-humérale et scapulo-thoracique pour le mouvement de flexion.

Bien que de multiples solutions inédites aient été proposées dans le cadre de cette thèse, chacune des solutions présentait des limites. Ces limitations existent dans la partie explorant les MSF ainsi que dans la partie associée à la modélisation musculo-squelettique. Pour la partie MSF, la première limite est le nombre d'échantillons utilisé pour construire les MSF des os de l'épaule adulte et la deuxième limite était l'indisponibilité des données pédiatriques pour construire des MSF des os de l'épaule pédiatrique incluant une bonne variabilité anatomique. Toutefois, cette thèse a permis de créer un cadre générique pour dériver les formes osseuses et les insertions musculaires spécifiques au sujet utilisant les MSF. Dans le domaine de la modélisation musculo-squelettique, la première limite est la validation du modèle développé et des simulations. Pour valider le modèle, nous aurions besoin d'un protocole expérimental

pour acquérir des données sur les enfants atteints de POPB. L'établissement d'un tel protocole dans la population pédiatrique nécessite une approbation du comité d'éthique de la recherche, ce qui est un processus difficile et long puisqu'il implique aussi les parents. Comme ce n'était pas possible dans le cadre de ma thèse, je n'ai pas pu construire une telle base de données. Ainsi, le modèle développé n'est pas validé. Toutefois, les prédictions du modèle pouvaient être comparées qualitativement à celles d'autres études. Pour les mêmes raisons l'indisponibilité des données pédiatriques, un cadre combinant la MSF et la modélisation musculo-squelettique n'a pas pu être établie. Toutefois, les méthodes proposées pourront être facilement réutilisées avec des données pédiatriques, lorsqu'un tel ensemble de données sera disponible.

5. Publications issues de la thèse

Salhi A, Burdin V, Boutillon A, Brochard S, Mutsvangwa T, and Borotikar B. "*Statistical Shape Modeling Approach to Predict Missing Scapular Bone*" Ann. Biomed. Eng., sous presse, Sept. 2019

Salhi A, Burdin V, Mutsvangwa T, Sivarasu S, Brochard S, Borotikar B. "*Subject specific Shoulder Muscle Attachment Region Prediction Using Statistical Shape Models: A Feasibility Study.*" 39th Annual International Conference of the IEEE Engineering in Medicine and Biology Society (EMBC'17), Jeju Island, Korea, 2017

Salhi A, Glenday J, Burdin V, Sivarasu S, Brochard S, Borotikar B. "*Illustrating the effect of subject-specific muscle insertions on joint and muscle mechanics in a shoulder joint model.*" XXVII Congress of the International Society of Biomechanics, Calgary, Canada, August 2019

Salhi A, Burdin V, Brochard S, Borotikar B. "*Development of a pediatric shoulder model to evaluate obstetric brachial plexus palsy.*" 31st Conference of European Academy of Childhood Disability, Paris, May 2019

Salhi A, Burdin V, Brochard S, Gupta A, Borotikar B. "*Statistical Shape Modeling Approach To Predict Missing Scapular Bone: Applications In Pre-Surgery Planning And Modeling.*" 42nd Annual Meeting of the American Society of Biomechanics, Rochester, MN, USA, August 8th – 11th, 2018

Salhi A, Burdin V, Brochard S, Borotikar B. "*Development Of Pediatric Shoulder Model To Evaluate Obstetric Brachial Plexus Palsy.*" 12th Meeting of the International Shoulder Group, Mayo Clinic, Rochester, MN, USA, August 12-13, 2018

Salhi A, Borotikar B, Mutsvangwa T, Brochard S, Burdin V. "*Comparing statistical shape model based mesh fitting methods using open source scalismo toolbox: towards patient-specific biomechanics modeling.*" XXVI Congress of the International Society of Biomechanics, Brisbane, Australia, 2017

Salhi A, Burdin V, Mutsvangwa M, Sivarasu S, Brochard S, Borotikar B. "*Muscle attachment region prediction using statistical shape models: a feasibility study for subject-specific shoulder biomechanics modeling.*" XXVI Congress of the International Society of Biomechanics, Brisbane, Australia, 2017

Salhi A, Burdin V, Mutsvangwa T, Sivarasu S, Brochard S, Borotikar B. "*Muscle attachment region prediction using statistical shape models: a feasibility study for subject-specific shoulder biomechanics modeling.*" 7th International Conference on Computational Bioengineering, Compiègne, France, 2017

Salhi A, Mutsvangwa, T, Chimhundu C, Borotikar B, Burdin V. "A comparison of two model fitting methods for transferring mesh correspondences: Implications to scapular bone using statistical shape modelling" 54th National Congress of the South African Association of Physicists in Medicine and Biology (SAAPMB), 2016

6. Références

- [1] D. A. Winter, *The biomechanics and motor control of human gait : normal, elderly and pathological*, 2nd ed. Waterloo, Ont. : University of Waterloo Press, 1991.
- [2] W. Herzog, *Skeletal Muscle Mechanics: From Mechanisms to Function*. John Wiley & Sons, 2000.
- [3] A. Steindler, *Kinesiology of the Human Body Under Normal & Pathological Conditions*. Charles C Thomas Pub Ltd, 1977.
- [4] "Fact Sheet - Injury Data | WISQARS | Injury Center | CDC," 24-Jul-2018. [Online]. Available: <https://www.cdc.gov/injury/wisqars/facts.html>. [Accessed: 27-Apr-2019].
- [5] G. C. Barroso and E. S. Thiele, "MUSCLE INJURIES IN ATHLETES.," *Rev. Bras. Ortop.*, vol. 46, no. 4, pp. 354–358, Aug. 2011.
- [6] "Arthritis-Related Statistics | Data and Statistics | Arthritis | CDC," 10-Oct-2018. [Online]. Available: https://www.cdc.gov/arthritis/data_statistics/arthritis-related-stats.htm. [Accessed: 28-Mar-2019].
- [7] J. R. Crandall, B. S. Myers, D. F. Meaney, and S. Z. Schmidtke, Eds., *Pediatric Injury Biomechanics: Archive & Textbook*. New York: Springer-Verlag, 2013.
- [8] M. N. Doral and J. Karlsson, Eds., *Sports Injuries: Prevention, Diagnosis, Treatment and Rehabilitation*, 2nd ed. Berlin Heidelberg: Springer-Verlag, 2015.
- [9] "Sports injuries to the shoulder and elbow." [Online]. Available: <https://www.livres-medicaux.com/sports-injuries-to-the-shoulder-and-elbow.html>. [Accessed: 23-Feb-2019].
- [10] M. Lüthi, C. Jud, T. Gerig, and T. Vetter, "Gaussian Process Morphable Models," *ArXiv160307254 Cs*, Mar. 2016.
- [11] R. Begg and M. Palaniswami, *Computational Intelligence for Movement Sciences: Neural Networks and Other Emerging Techniques*. Idea Group Inc (IGI), 2006.
- [12] V. Carbone, M. M. van der Krogt, H. F. J. M. Koopman, and N. Verdonshot, "Sensitivity of subject-specific models to errors in musculo-skeletal geometry," *J. Biomech.*, vol. 45, no. 14, pp. 2476–2480, Sep. 2012.
- [13] T. Kleiber, N. Popovic, J. Bahm, and C. Disselhorst-Klug, "A modeling approach to compute modification of net joint forces caused by coping movements in obstetric brachial plexus palsy," *J. Brachial Plex. Peripher. Nerve Inj.*, vol. 8, no. 1, p. 10, Oct. 2013.
- [14] H. G. Kwatny and G. L. Blankenship, "Symbolic construction of models for multibody dynamics," *IEEE Trans. Robot. Autom.*, vol. 11, no. 2, pp. 271–281, Apr. 1995.
- [15] F. E. Zajac, "Muscle and tendon: properties, models, scaling, and application to biomechanics and motor control," *Crit. Rev. Biomed. Eng.*, vol. 17, no. 4, pp. 359–411, 1989.
- [16] W. Cheng, R. Cornwall, D. L. Crouch, Z. Li, and K. R. Saul, "Contributions of muscle imbalance and impaired growth to postural and osseous shoulder deformity following brachial plexus birth palsy: a computational simulation analysis," *J. Hand Surg.*, vol. 40, no. 6, pp. 1170–1176, Jun. 2015.

- [17] S. L. Delp *et al.*, "OpenSim: open-source software to create and analyze dynamic simulations of movement," *IEEE Trans. Biomed. Eng.*, vol. 54, no. 11, pp. 1940–1950, Nov. 2007.
- [18] A. Seth *et al.*, "OpenSim: Simulating musculoskeletal dynamics and neuromuscular control to study human and animal movement," *PLoS Comput. Biol.*, vol. 14, no. 7, p. e1006223, Jul. 2018.
- [19] Charles A. Rockwood Jr MD, Michael A. Wirth MD, and Steven B. Lippitt MD, *Rockwood and Matsen's The Shoulder, 2 Volume Set: Expert Consult - Online and Print*, 4 edition. Philadelphia, PA: Saunders, 2009.
- [20] R. Lugo, P. Kung, and C. B. Ma, "Shoulder biomechanics," *Eur. J. Radiol.*, vol. 68, no. 1, pp. 16–24, Oct. 2008.
- [21] A. G. Cutti and H. E. J. (DirkJan) Veeger, "Shoulder biomechanics: today's consensus and tomorrow's perspectives," *Med. Biol. Eng. Comput.*, vol. 47, no. 5, pp. 463–466, May 2009.
- [22] H. E. J. Veeger and F. C. T. van der Helm, "Shoulder function: the perfect compromise between mobility and stability," *J. Biomech.*, vol. 40, no. 10, pp. 2119–2129, 2007.
- [23] C. Pons, F. T. Sheehan, H. S. Im, S. Brochard, and K. E. Alter, "Shoulder muscle atrophy and its relation to strength loss in obstetrical brachial plexus palsy," *Clin. Biomech. Bristol Avon*, vol. 48, pp. 80–87, Oct. 2017.
- [24] F. C. van der Helm, "Analysis of the kinematic and dynamic behavior of the shoulder mechanism," *J. Biomech.*, vol. 27, no. 5, pp. 527–550, May 1994.
- [25] F. C. van der Helm and G. M. Pronk, "Three-dimensional recording and description of motions of the shoulder mechanism," *J. Biomech. Eng.*, vol. 117, no. 1, pp. 27–40, Feb. 1995.
- [26] D. C. Ackland, C. J. Goodwin, M. G. Pandy, D. C. Ackland, C. J. Goodwin, and M. G. Pandy, "Computational Modelling in Shoulder Biometrics," <http://services.igi-global.com/resolvedoi/resolve.aspx?doi=10.4018/978-1-59140-836-9.ch013>, 01-Jan-2001. [Online]. Available: <https://www.igi-global.com/gateway/chapter/6818>. [Accessed: 09-Nov-2018].
- [27] A. A. Nikooyan, H. E. J. Veeger, E. K. J. Chadwick, M. Praagman, and F. C. T. van der Helm, "Development of a comprehensive musculoskeletal model of the shoulder and elbow," *Med. Biol. Eng. Comput.*, vol. 49, no. 12, pp. 1425–1435, Dec. 2011.
- [28] T. Mutsvangwa, V. Burdin, C. Schwartz, and C. Roux, "An automated statistical shape model developmental pipeline: application to the human scapula and humerus," *IEEE Trans Biomed Eng*, vol. 62, pp. 1098–107, Apr. 2015.

Table of Contents

List of figures.....	vii
List of Tables	xi
Abbreviations.....	xiii
Chapter 1.....	1
Introduction	1
1.1 Motivation.....	1
1.2 Aims.....	3
1.3 Thesis Outline.....	3
1.4 Chapter 1 References.....	6
Part I: Adult shoulder anatomy and biomechanics.....	
Chapter 2.....	9
Skeletal and functional anatomy of the adult shoulder	9
2.1 Introduction	9
2.2 Anatomical terminology.....	10
2.3 The skeletal Structure	11
2.3.1 The shoulder girdle	11
2.3.2 The sternum	11
2.3.3 The clavicle.....	12
2.3.4 The scapula	12
2.3.5 The humerus	13
2.4 The Joints	14
2.4.1 The sternoclavicular (SC) joint	14
2.4.2 The acromioclavicular (AC) joint	15
2.4.3 The glenohumeral (GH) joint	15
2.4.4 The scapulothoracic (ST) joint.....	16
2.5 The Muscles	17
2.5.1 Scapulohumeral group.....	17
2.5.2 Axioscapular group	19

2.5.3 Axiohumeral group	21
2.5.4 Other muscle group	22
2.6 - The Motions	22
2.7 Chapter 2 References.....	25
Chapter 3.....	27
Shoulder Biomechanics.....	27
3.1 Introduction	27
3.2 GH: Glenohumeral Joint.....	30
3.2.1 GH Joint Kinematics (motions).....	30
3.2.2 GH Joint Constraints (stability)	31
3.2.3 GH Joint Kinetics (strength)	33
3.3 ST: Scapulothoracic Joint	33
3.3.1 ST Joint Kinematics (motions).....	34
3.3.2 ST Joint Constraints (stability).....	34
3.3.3 ST Joint kinetics (strength)	34
3.4 AC: Acromioclavicular Joint.....	35
3.4.1 AC Joint Kinematics (motions)	35
3.4.2 AC Joint Constraints (stability)	35
3.4.3 AC Joint Forces (strength)	36
3.5 SC: Sternoclavicular Joint	36
3.5.1 SC Joint Kinematics (motions).....	36
3.5.2 SC Joint Constraints (stability).....	36
3.5.3 SC Joint Forces (strength)	37
3.6 Chapter 3 References.....	38
Part II: Statistical Shape Modeling to predict subject-specific musculoskeletal model inputs.....	
Chapter 4.....	41
Augmented Statistical Shape Model of scapular bone for clinical use.....	41
4.1 Introduction	41
4.2 State-of-the-art in SSM and related research.....	42
4.2.1 Statistical shape models.....	42
4.2.2 Registration.....	44

4.2.3 Gaussian Process Morphable Models.....	45
4.3 Rationale for understanding Clinical Utility of scapula SSM.....	46
4.4 Materials and Methods.....	47
4.4.1 SSM Development.....	47
4.4.2 Augmented SSM creation for comparisons	49
4.4.3 Intra- and inter-observer reliability	53
4.4.4 Clinical Utility	53
4.5 Results.....	54
4.5.1 Intra- and inter-observer reliability	54
4.5.2 Clinical Validity	59
4.6 Discussion.....	61
4.7 Chapter 4 References.....	67
Chapter 5.....	73
Subject-specific musculoskeletal models using a novel muscle attachment region prediction algorithm based on Statistical Shape Models	73
5.1 Introduction	73
5.2 Materials and Methods.....	74
5.2.1 Bone SSM Development	75
5.2.2 Muscle region selection	75
5.2.3 Selection of Muscle attachment region on the SSM.....	75
5.2.4 Augmented SSM deformation to external bone shapes.....	76
5.2.5 Validation of muscle insertion region prediction	76
5.2.6 Imaging database acquisition for building musculoskeletal model.....	76
5.2.7 Newcastle shoulder model (NSM) adaptation.....	76
5.3 Results.....	77
5.3.1 Intra- and inter-observer reliability	77
5.3.2 Augmented SSM building.....	77
5.3.3. Validity of muscle insertion predictions	82
5.3.4 Comparison of joint and muscle mechanics	85
5.4 Discussion.....	91
5.5 Chapter 5 References.....	94
Chapter 6.....	97

Statistical shape modeling approach to predict missing scapular bone: applications in pre-surgery planning and musculoskeletal modeling	97
6.1 Introduction	97
6.1.1 Structure of this chapter	97
6.1.2 Rationale to target missing part in scapular bone	97
6.2 Materials and Methods.....	99
6.2.1 Scapula SSM Building	99
6.2.2 Virtual scapular defect creation.....	100
6.2.3 Missing part prediction algorithm	101
6.2.4 Prediction error quantification	102
6.3 Results.....	102
6.3.1 SSM building and robustness.....	102
6.3.2 Virtual scapular defect	104
6.3.2 Gaussian regression and prediction error assessment.....	104
6.4 Discussion.....	107
6.5 Conclusion.....	110
4.6 Chapter 6 References.....	111
Part III: Musculoskeletal modeling of pediatric shoulder joint model.....	
Chapter 7.....	117
Obstetrical Brachial Plexus Palsy and its evaluation using musculoskeletal modeling: state of the art and challenges	117
7.1 Introduction	117
7.2 Obstetrical Brachial Plexus Palsy OBPP.....	118
7.2.1 Description of the pathology	118
7.2.2 Musculoskeletal impact of OBPP	118
7.2.3 Biomechanical description of OBPP (the impact on kinematics).....	120
7.3 Pediatric MSK modeling for clinical applications	122
7.3.1 Crutch-assisted gait model [35]	123
7.3.2 Wheelchair mobility model [36]	123
7.4 Pediatric MSK modeling for OBPP	123
7.4.1 Kleiber model	124
7.4.2 Crouch model.....	124

7.4.3 Cheng model	125
7.5 Challenges and limitation of the current MSK model simulations for OBPP	125
7.5.1 Limitations.....	125
7.5.2 Challenges.....	126
7.6 Chapter 7 References.....	127
Chapter 8.....	131
Multibody system dynamics: theory and Applications in Shoulder	131
8.1 Introduction	131
8.2 Multibody dynamics.....	132
8.2.1 Joint Kinetics and kinematics	132
8.2.2 Multibody musculoskeletal dynamics.....	134
8.2.3 Inverse Dynamics	135
8.2.4 Forward Dynamics	135
8.2.5 Combined inverse-forward dynamics	136
8.2.6 Open source and commercial software.....	136
8.3 Muscle modeling.....	137
8.3.1 Muscle contraction theory.....	138
8.3.2 Muscle computational model	140
8.3.3 Muscle Paths	145
8.4 Musculoskeletal models of the Shoulder.....	146
8.5 Chapter 8 References.....	151
Chapter 9.....	155
Development of a pediatric shoulder joint model.....	155
9.1 Introduction	155
9.2 Kinematics.....	156
9.2.1 Bone: Geometry and embedded coordinate system.....	156
9.2.2 Muscles geometry: insertions, paths and wrapping surfaces.....	162
9.2.3 Joint geometry	170
9.3 Dynamics.....	178
9.3.1 Body segment parameters.....	178
9.3.2 Muscle (actuator) dynamics.....	181

9.4 Summary and conclusion	187
9.5 Chapter 9 References.....	189
Chapter 10.....	193
Simulating OBPP pathology using the pediatric shoulder model: A Feasibility Study.....	193
10.1 Introduction	193
10.2 Kinematics Simulations	193
10.2.1 Experimental data collection	193
10.2.2 Scaling	195
10.2.3 Inverse kinematics	198
10.3 Inverse Dynamics	202
10.4 Discussion.....	207
10.5 Chapter 10 References.....	208
Chapter 11.....	209
Summary and Future Perspectives	209
11.1 Summary	209
11.2 Perspectives	210
11.3 Future directions.....	213

List of figures

Figure 2. 1: Anatomical planes and axes of the human body [5]	10
Figure 2. 2: <i>The shoulder girdle</i> [5].	11
Figure 2. 3: Anterior and posterior views of the left scapula [5].	12
Figure 2. 4: Anterior and posterior views of the left scapula [5].	13
Figure 2. 5: Sternoclavicular joint and its ligaments [5].	14
Figure 2. 6: Acromioclavicular joint and its ligaments [5].	15
Figure 2. 7: <i>Glenohumeral joint and its ligaments</i> [5].	16
Figure 2. 8: <i>Scapulohumeral muscles</i> [5].	17
Figure 2. 9: <i>Axioscapular muscles</i> [5].	19
Figure 2. 10: Motions description of the upper limb (Adapted from Charlton, 2004 [15]).	23
Figure 3. 1: Leonardo da Vinci's earlier depiction of shoulder musculature (Courtesy: LeonardoDaVinci.net)	27
Figure 4. 1: A schematic diagram showing the methodology used to determine clinical validity of an augmented statistical shape model of the adult scapula bone.	48
Figure 4. 2: Anatomical landmark locations on the scapular bone for proposed augmented SSM (aSSMproposed).	50
Figure 4. 3: Augmented SSM set1 (aSSMset1): Landmark set without considering clinical significance of landmark locations.	51
Figure 4. 4: Augmented SSM set2 (aSSMset2): Landmark set without considering clinical significance of landmark locations in the glenoid region. No landmarks were selected in the glenoid region and rest of the landmarks were equally distributed over the scapular shape to map the entire shape.	52
Figure 4. 5: Sample goodness of fit in the glenoid region for three augmented SSMs.	60
Figure 4. 6: Comparing the four SSMs (non-augmented SSM, augmented SSM proposed, augmented SSM set1, and augmented SSM set2) for their fitting quality to predict the glenoid region.	61
Figure 5. 1: Frequency level representations of muscle insertion VIDs on humerus for all six muscles. Frequency levels ranged from 50% to 100%.	78

Figure 5. 2: Frequency level representations of muscle insertion VIDs on humerus for all six muscles. Frequency levels ranged from 50% to 100%.	79
Figure 5. 3: Visualization of first seven principal modes of variation of an augmented scapula bone SSM on its posterior muscle insertions.....	80
Figure 5. 4: Visualization of first seven principal modes of variation of an augmented humerus bone SSM on its anterior muscle insertions.	81
Figure 5. 5: Visual check of attachment region of scapula bone..	82
Figure 5. 6: Visual check of attachment region of humerus bone.....	83
Figure 5. 7: Example of muscle regions prediction on one of the external scapulae and humeri.	84
Figure 5. 8: Joint contact forces during GH abduction for generic and subject-specific insertion constructs.	86
Figure 5. 9: Joint contact forces during scapular plane elevation for generic and subject-specific insertion constructs.....	87
Figure 5. 10: Muscle moment arms during GH abduction movement for generic and subject-specific insertion constructs..	88
Figure 5. 11: Muscle moment arms during scapular plane elevation movement for generic and subject-specific insertion constructs..	89
Figure 5. 12: Muscle forces arms during GH abduction movement for generic and subject-specific insertion constructs.....	90
Figure 5. 13: Muscle forces arms during scapular plane elevation movement for generic and subject-specific insertion constructs.	91
Figure 6. 1: Virtual defect creation: Four types of virtual defects created from each external scapular shape.....	101
Figure 6. 2: Robustness and cross-validation measures of the scapula statistical shape model. Top left: Compactness, Top right: Generality in RMS, and Bottom right: Specificity in mm.	103
Figure 6. 3: Statistical shape model (SSM) of the scapula and the first five principal modes of variations.	104
Figure 6. 4: Ten external scapular shapes categorically selected for evaluation.	105
Figure 6. 5: Box plots indicating the prediction errors in Critical shoulder angle (top left), Glenoid inclination (top right), Glenoid version (bottom left), and Glenoid center (bottom right) for each type of defect (type I, type III, Superior, and Inferior). Each box corresponds to inter-quartile range of 50%....	107
Figure 6. 6: Comparison of prediction errors of the current study with those reported by Plessers et al. [21].	108
Figure 8. 1: Skeletal Muscle structure (adapted from https://www.forcefulaction.wordpress.com)	138

Figure 8. 2: Skeletal muscle shapes and fiber orientations. (Adapted from https://www.studyblue.com)	139
Figure 8. 3: <i>Hill-type muscle model</i> [20].....	141
Figure 8. 4: Muscle Force-Length and force-velocity curve [7].	142
Figure 8. 5: Relationship among sarcomere length, contractile force, and contraction velocity under isotonic conditions [23].....	143
Figure 9. 1: <i>Model building: From MRI data to 3D reconstruction</i>	157
Figure 9. 2: <i>Thorax coordinate system according to ISB.</i>	158
Figure 9. 3: <i>Clavicle coordinate system according to ISB.</i>	159
Figure 9. 4: <i>Scapula coordinate system according to ISB.</i>	160
Figure 9. 5: <i>Humerus coordinate system according to ISB.</i>	161
Figure 9. 6: (A) Back, top and side views of ellipsoid covering posterior ribs (B) front and side views of the ellipsoid covering the anterior ribs.	165
Figure 9. 7: latissimus dorsi and trapezius with scapular insertion wrapping around the posterior ribs.	166
Figure 9. 8: Pectoralis Major with clavicular insertion and Pectoralis major with sternum insertion wrapping around the anterior ribs.	166
Figure 9. 9: Humeral column wrapping surface (cylinder) with posterior deltoid wrapping.	167
Figure 9. 10: Muscles wrapping around the humeral head wrapping surface, including supraspinatus, subscapularis, deltoid anterior, middle deltoid, infraspinatus and teres Minor.	167
Figure 9. 11: Concept of a mobilizer to define a joint between two bodies (adapted from [3]).....	171
Figure 9. 12: Model structure topology.	171
Figure 9. 13: Sternoclavicular joint coordinate system.	172
Figure 9. 14: Landmark selected to fit an ellipsoid (front and back views) and fitted ellipsoid.	174
Figure 9. 15: Ellipsoid passing through the posterior rib surface and equatorial plane (shown in red) passing through the centroid of the scapula.	175
Figure 9. 16: Scapulothoracic joint coordinate system.....	176
Figure 9. 17: Glenohumeral joint coordinate system.	177
Figure 10. 1: An adolescent with OBPP was enrolled at CHRU and motion analysis data was collected on both impaired and non-impaired shoulders. Marker set-up on the impaired arm is shown here.	195
Figure 10. 2: Schematic diagram explaining the scaling process adapted.....	196
Figure 10. 3: Model after scaling (static pose).....	198

Figure 10. 4: Healthy and impaired kinematic model movement in one forward flexion cycle movement.	199
Figure 10. 5: Thorax-ground kinematics for all six degrees of freedom.....	200
Figure 10. 6: Sternoclavicular kinematics for three rotational degrees of freedom..	200
Figure 10. 7: Glenohumeral kinematics for three rotational degrees of freedom.....	201
Figure 10. 8: Scapulothoracic kinematics for scapular upward rotation, scapular abduction, scapular elevation and scapula winging.....	202
Figure 10. 9: Schematic diagram of inverse dynamics tool input and output parameters	202
Figure 10. 10: Net joint torque for forward flexion movement between healthy and impaired side in the glenohumeral plane of elevation.....	203
Figure 10. 11: Net joint torque for forward flexion movement between healthy and impaired side in the glenohumeral plane of horizontal abduction.	204
Figure 10. 12: Net joint torque for forward flexion movement between healthy and impaired side in the axial rotation.	204
Figure 10. 13: Net joint torque for forward flexion movement between healthy and impaired side for scapula abduction.....	205
Figure 10. 14: Net joint torque for forward flexion movement between healthy and impaired side for scapula elevation.	205
Figure 10. 15: Net joint torque for forward flexion movement between healthy and impaired side for scapula upward rotation.....	206
Figure 10. 16: Net joint torque for forward flexion movement between healthy and impaired side for scapula winging.....	206

List of Tables

Table 2. 1: Scapulohumeral muscle group origin, insertion, and function	19
Table 2. 2: <i>Axioscapular muscle group origin, insertion, and function.</i>	21
Table 4. 1: Inter-observer reliability interclass correlation coefficients (ICCs) in X, Y, and Z coordinates of anatomical landmarks selection for $\alpha\text{SSM}_{\text{set1}}$ and $\alpha\text{SSM}_{\text{set2}}$	54
Table 4. 2: Inter-observer Standard Error of Measurement (SEM) in mm in X, Y, and Z coordinates of anatomical landmarks selection for $\alpha\text{SSM}_{\text{set1}}$ and $\alpha\text{SSM}_{\text{set2}}$	55
Table 4. 3: Intra-observer reproducibility interclass correlation coefficients (ICCs) values in X, Y, and Z coordinates of anatomical landmarks for both the observers on $\alpha\text{SSM}_{\text{set1}}$	56
Table 4. 4: Intra-observer Standard Error of Measurement (SEM) in mm in X, Y, and Z coordinates of anatomical landmarks for both the observers on $\alpha\text{SSM}_{\text{set1}}$	57
Table 4. 5: Intra-observer reproducibility interclass correlation coefficients (ICCs) values in X, Y, and Z coordinates of anatomical landmarks for both the observers on $\alpha\text{SSM}_{\text{set2}}$	58
Annexure Table 4. 6: Intra-observer Standard Error of Measurement (SEM) in mm in X, Y, and Z coordinates of anatomical landmarks for both the observers on $\alpha\text{SSM}_{\text{set2}}$	59
Table 4. 7: Prediction error in the critical shoulder angle in terms of individual angle differences between angle obtained from the original shape and the angle predicted by each SSM type.....	62
Table 4. 8: Prediction error in the glenoid inclination angle in terms of individual angle differences between angle obtained from the original shape and the angle predicted by each SSM type.....	63
Table 4. 9: Prediction error in the lateral acromion angle in terms of individual angle differences between angle obtained from the original shape and the angle predicted by each SSM type.....	64
Table 4. 10: Prediction error in the glenopolar angle in terms of individual angle differences between angle obtained from the original shape and the angle predicted by each SSM type.	65
Table 5. 1: Selected frequency levels by experts for scapula and humerus muscle insertions.....	79
Table 5. 2: Average validity error of muscle origin region predictions on ten external scapulae for six muscles.	85
Table 5. 3: Average validity error of muscle origin region predictions on ten external humeri for six muscles:	85

Table 6. 1: Mean prediction errors when comparing the results of missing part prediction with original shapes of external scapulae for anatomical measures of glenoid inclination, glenoid version, critical shoulder angle (CSA), and glenoid center.....	105
Table 6. 2: Mean prediction errors when comparing the results of missing part prediction with original surface meshes of external scapulae for distance and similarity measures.	106
Table 7. 1: RoM of shoulder affected by OBPP and its association with muscular deficiency ..	121
Table 7. 2: ST and GH ROM for the Abduction motion in the three groups (Unaffected, Erb’s palsy and Extended Erb’s palsy) (as reported by Russo et al. [33])	122
Table 8. 1: Model type, degrees of freedom, first use and validation method used.	147
Table 8. 2: Definitions of joint rotation centers used, number of muscles used, methods used to determine segment inertias and musculotendon parameters.....	148
Table 8. 3: Body segment parameters used in the models.	148
Table 9. 1: <i>MRI acquisition parameters</i>	156
Table 9. 2: <i>Demographic patient information</i>	156
Table 9. 3: <i>Position of bony landmarks (in cm) used to define the segments’ locale frames determined using a Matlab algorithm (Mathworks, Natick, MA, USA).</i>	161
Table 9. 4: <i>Transformation matrices of the segment’s local frames, computed using a Matlab algorithm (Mathworks, Natick, MA, USA). (frame origin coordinates are in meters)</i>	162
Table 9. 5: <i>Muscle presented in the models, number of fascicules presenting each muscle and coordinates of origins and insertions.</i>	163
Table 9. 6: <i>Muscle wrapping surfaces used in the model. All the coordinates are in meters</i>	169
Table 9. 7: <i>The muscles affected by the wrapping and the associated wrapping surfaces</i>	169
Table 9. 8: <i>Summary of Joint definitions</i>	177
Table 9. 9: <i>studies on pediatric mass distribution CG: center of gravity</i>	178
Table 9. 10: <i>Inertial parameters for the model segments</i>	181
Table 9. 11: <i>origin and insertion coordinates</i>	183
Table 9. 12: <i>Muscle volumes, muscle lengths, and tendon lengths derived from MRI data and by adapting length and volume ratios from the literature</i>	185
Table 9. 13: <i>Muscle dynamics model input parameters</i>	187

Abbreviations

AC	Acromioclavicular
CT	Computed Tomography
DC	Dice coefficient
DoF	Degree of Freedom
EMG	Electromyography
GH	Glenohumeral
ISB	International Society of Biomechanics
MRI	Magnetic Resonance Imaging
MSK	Musculoskeletal
OBPP	Obstetrical Brachial Plexus Palsy
PCSA	Physiological Cross-Sectional Area
RoM	Range of Motion
RMS	Root Mean Square
SC	Sternoclavicular
SSM	Statistical Shape Modeling
ST	Scapulothoracic

Chapter 1

Introduction

1.1 Motivation

Human musculoskeletal system is a complex structure composed of bones, joints, articulating cartilages, muscles, and ligaments [1]. This structure is primarily moved by musculotendon actuators for a desired function relating to a daily or sports activity [2]. **The healthy musculoskeletal system requires a fine synchronization and balance of forces produced by multiple muscles crossing the joints used in the motion and controlled by neuromuscular system** [1], [3]. While the muscles provide mobility, the bones provide structural stability to the musculoskeletal system. In the event of a disease or disorder, one or multiple components of the musculoskeletal system are perturbed, leading to abnormal or painful motion. **Muscle and bone diseases and injuries** are on the rise worldwide as per CDC Report from 2017 [4] and also reported by Barroso and Thiele [5]. While musculoskeletal diseases result from a pathophysiological response to internal or external factors, disorders are a disruption of normal function due to such diseases [2], [3], [6]–[8]. Many types of diseases, **communicable and non-communicable**, adversely affect the musculoskeletal system. This not only threatens the healthy lifestyle of a group or an individual but also **has a debilitating impact on the health-related costs**. Furthermore, the non-communicable diseases and sports injuries perturb the human musculoskeletal system and may make the **person vulnerable to musculoskeletal disorders (MSDs)** (e.g. early onset osteoarthritis), affecting their quality of life [6], [9]. These conditions also limit outdoor activities of the concerned populations and hence reduce children’s growth and senior’s ability to integrate with the society.

Advancements in **medical imaging, machine learning, medical devices and computational modeling** are critical in the diagnosis and treatment of MSDs. This is especially true for MSDs in pediatric population where the outcome of these treatments has a long-term impact on the quality of life and the health of the musculoskeletal system [7]. In the treatment of pediatric MSDs, medical imaging is typically used for diagnostic purposes whereas medical devices are more applied in the treatment and rehabilitation. Machine learning tools such as statistical shape modeling can assist surgeons and clinicians for the morphological assessment of the musculoskeletal structure [10]. Computational modeling tools, however, can provide valuable insights and assistance (both qualitative and quantitative) at every single stage of the MSD management in evaluating the underlying joint mechanics and force imbalances [11]. These insights include accurate diagnosis (of force imbalance), optimized treatment strategies (for surgery or rehabilitation), accurate evaluation of recovery and follow-up visits (by restoring healthy joint mechanics) etc [12]–[16]. Computational modeling domains typically include (but not limited to) finite element modeling, discrete element physics-based modeling, and multi-body musculoskeletal modeling. Multi-

body modeling has a unique advantage in evaluating the function of the musculoskeletal system using dynamics principles and deriving muscle and joint related parameters such as joint moments, muscle forces and moment arms etc [17], [18]. Thus multi-body musculoskeletal modeling can derive predictive kinematics, perform “what-if” studies, and identify “cause-effect” relationships etc. However, individually, these technologies may lack accuracy, efficiency, reliability, and cost-effectiveness. For example, musculoskeletal modeling of a single joint needs a derivation of multiple parameters from the musculoskeletal structure which may or may not be readily available, limiting the efficacy of the model [1]. Furthermore, computational tools are typically not validated for their clinical utility.

Shoulder joint, being one of the most complex joints in the musculoskeletal system, is often subjected to multiple disorders [7], [19]–[22]. The most common disorders in shoulder joint are **rotator cuff tears, shoulder arthritis, frozen shoulder, shoulder bone fractures and bone deformities** [8], [9], [20]–[22]. Shoulder joint disorders affect scapular bone and lead to damaged bone, rapid bone loss, restricted shoulder function, and chronic pain and ultimately need surgical intervention. In all these disorders, the impaired shoulder function leads to reduced quality of life. During the surgical treatment, surgeons should know a pre-morbid bone shape to optimize cutting guides and implant placement which in turn restore healthy shoulder function. Furthermore, pediatric population has certain disorders like obstetrical brachial plexus palsy (OBPP), a nerve injury that leads to shoulder deformity and dysfunction [7], [19], [23]. Surgical treatment and rehabilitation are typical remedies, however, the lack of understanding in abnormal muscular behavior drastically reduces the success of treatment. **Musculoskeletal modeling can be effectively used to elucidate the patho-mechanics of OBPP** to expand on the clinical assessment, rehabilitation or treatment strategies. **However, musculoskeletal models of the shoulder joint are limited in the literature** and to date, there is no pediatric shoulder model developed to target OBPP [16].

Musculoskeletal modeling to evaluate shoulder function has been used by multiple researchers [22], [24], [25]. **Shoulder musculoskeletal models for adult population have been developed and used to understand clinical problems** [26], [27]. However, multiple assumptions and generic modeling frameworks, used in these studies, reduce the clinical utility of these models. One way to eliminate the assumptions made is to conduct experiments but that is not always feasible as most of the experiments for deriving such parameters tend to be either invasive or costly. Medical imaging can also be used for devising certain parameters. However, individuals must go through imaging process which may not be feasible or desirable at all times. For e.g., in pediatric population, we can expose the children to multiple radiations for follow-up visits after. **A third and novel approach would be to combine musculoskeletal modeling with statistical shape modeling tools to benefit from the ubiquity of each domain.** Multiple parameters such as morphological shape of the bone, muscle insertion regions, missing shapes during medical imaging or due to morbidity, cortical bone thickness, and generating new shapes that are still valid within population, could be obtained using statistical shape modeling approach. While such an attempt of combining two domains is made in the literature, it is limited to deriving cortical bone thickness and finite element modeling domain.

Rationale: It is clear from the descriptions above that 1) muscle and bone disorders are globally on the rise impacting quality of life and leading to higher healthcare costs, 2) shoulder disorders in adult and pediatric populations are a concern with assessment tools needed in surgery and clinical assessment, 3) technological advances in medical imaging, statistical shape modeling, and musculoskeletal modeling domains have been individually proven to be able to assess MSDs, 4) musculoskeletal modeling assumes

a key role in clinical assessment of shoulder disorders, however, limited adult models exist and no pediatric models exist, 5) subject-specific musculoskeletal model development has a potential to closely understand the patho-mechanics of shoulder disorders, however lack of means to derive subject-specific model input parameters is a stumbling block in this research, 6) a novel framework forming the confluence of advanced technologies to eliminate assumptions in building shoulder musculoskeletal models must be devised.

1.2 Aims

The global aim of my thesis is to build a combined framework of two research domains – Statistical Shape Modeling (SSM) and musculoskeletal modeling to evaluate musculoskeletal disorders in pediatric shoulder joint. To build such framework, concerns and questions related to individual research domains must be addressed first. Thus, depending on the availability of data, resources, and time, following specific aims were targeted in this thesis.

- 1) To build an SSM of adult shoulder bones and report a clinical utility of such SSM in predicting new bone shapes.
- 2) To illustrate and validate the capability of shoulder bone SSMs to accurately predict muscle insertion regions for new bone shapes in adult population.
- 3) To illustrate and critically examine the efficacy of scapula bone SSMs in predicting complete scapular shape from partial shape in adult population.
- 4) To integrate muscle insertion prediction algorithm into an existing musculoskeletal model of adult shoulder joint and compare the changes in joint mechanics outcomes.
- 5) To develop a pediatric musculoskeletal shoulder joint model in OpenSim (an open source software) from a healthy child data.
- 6) To illustrate the use of pediatric musculoskeletal shoulder joint model in one OBPP child for determining scapulothoracic and glenohumeral joint kinematics as well as joint mechanics parameters (joint moments, joint forces, muscle forces etc.) during a scapular flexion activity and on both healthy and impaired sides.

This model will be used in future (not in the scope of the thesis) for evaluating OBPP by making subject-specific simulations for daily living activities.

1.3 Thesis Outline

Considering multiple research domains included in this thesis, I have divided the manuscript into three parts.

Part I: The first part describes adult shoulder anatomy and biomechanics in brief and is covered by chapters 2 and 3.

Chapter 2: This chapter explains the skeletal and functional anatomy of the adult shoulder. Brief explanations with illustrations are provided for anatomical terminologies used in shoulder joint.

Furthermore, the skeletal structure, the joints, the muscles, and the motions involved in the shoulder joint are also explained in detail. Such information is crucial in the understanding and development of shoulder joint modeling (SSM and musculoskeletal).

Chapter 3: This chapter explains adult shoulder biomechanics in detail. I have divided this chapter on the basis of four joints that form the shoulder joint complex viz. Scapulothoracic joint, sternoclavicular joint, acromioclavicular joint, and glenohumeral joint. The biomechanics of each joint is then described in terms of kinematics (joint motion), kinetics (joint strength), and constraints (joint stability).

Part II: The second part deals with a brief description of SSM methodology, studies conducted in SSM (aims 1, 2, 3) and lays a foundation work of proposed combined framework by illustrating it for adult shoulder joint (aim 4).

Chapter 4: This chapter has two sub-parts. In the first part, I provide a brief introduction to the SSM theory and state-of-the-art practices to build (Gaussian Process Morphable Models) and use (Registration) SSM. In the second part, I explain how a scapular SSM was built and illustrate a) whether an SSM augmented with anatomical landmarks performs better fitting and provides improved clinical utility over non-augmented SSM and b) which anatomical landmark sets provide best augmentation strategy. The results of this research are then used in further studies where a model fitting process needs scapula augmentation using anatomical landmarks.

Chapter 5: This chapter again has two sub-parts. In the first part, I describe the method used to automatically predict the muscle insertion regions by building an SSM with muscle insertion information embedded in it and then this embedded information during an SSM fitting process to new bone shape. This algorithm is then illustrated on scapula and humerus bones for six shoulder muscle insertion predictions (Supraspinatus, Infraspinatus, subscapularis, teres major, teres minor, and deltoid) and subsequently validated against manually quantified muscle regions on 3D bone shapes. In the second part, a strategy to combine SSM and musculoskeletal modeling is illustrated. To do this, first the algorithm is used to predict muscle insertions on 10 cadaveric specimens which are in turn used to build 10 shoulder joint models using a Newcastle Shoulder Model (NSM). Each model is then simulated for an abduction movement and corresponding muscle moment arms and muscle forces are compared between NSM embedded insertions and my algorithm predicted insertions.

Chapter 6: This chapter reports an SSM algorithm development to predict a pre-morbid shape of scapular bone given a bone shape with partial bone missing as a starting point. The algorithm is then evaluated on ten new scapular shapes. Each new scapular shape is used to create four defective bone shapes with defects that are synthetically created to mimic glenoid bone loss or missing bone due to incomplete imaging. Evaluations are made by comparing algorithm predicted bone shape with its original counterpart using anatomical, distance, and similarity measures. Such an algorithm is a powerful tool in pre-surgery planning software to derive pre-morbid anatomy of the scapula.

Part III: The third part includes a brief description of pediatric musculoskeletal disorder (OBPP), theory of multi-body dynamics, pediatric shoulder musculoskeletal model development (aim 5) and an illustration of the capability of this model for its use in determining inverse kinematics and inverse dynamics in one case study (aim 6).

Chapter 7: This chapter provides a brief description of OBPP pathology and literature concerning its evaluation using musculoskeletal modeling. The chapter provides brief detail on the musculoskeletal impact of the OBPP pathology on each of the shoulder bones and muscles. It also provides how the shoulder biomechanics is affected due to the pathology. In the end, this chapter discusses the existing musculoskeletal models that are used for the evaluation of OBPP. It is interesting to note that all the models used in the literature are scaled down from a generic adult shoulder model.

Chapter 8: This chapter provides a description of multibody system dynamics and its applications in shoulder joint. Multibody system dynamics is explained for understanding joint kinetics and kinematics and deriving Newton-Euler equations of motion for the dynamics of a holonomic system. A detailed description of muscle contraction theory and an overview of muscle modeling for dynamic systems is discussed. The concepts of inverse and forward dynamics and introductory information on OpenSim open source software is provided in this chapter. The chapter concludes with the list and brief descriptions of existing shoulder musculoskeletal models in the literature that are extensively used for research on adult shoulder joints.

Chapter 9: This chapter describes in detail the development process for building a pediatric shoulder joint model using OpenSim. The model represents four rigid bone segments (thorax, clavicle, scapula, humerus). The coordinates of bone segments are derived from an MRI scan of a 10-year-old healthy child. These segments were connected at the sternoclavicular, acromioclavicular, glenohumeral, and scapulothoracic joint with total 13 degrees of freedom. Our model consists of 53 musculotendon actuators representing 13 shoulder muscles. The body segment parameters and musculotendon model parameters are derived from the literature. This is the first pediatric shoulder musculoskeletal model dedicated for research in pediatric shoulder joint.

Chapter 10: This chapter used a motion capture data from one adolescent with OBPP to simulate the musculoskeletal model for inverse kinematics and inverse dynamics problems. First, the model developed in Chapter 9 above was scaled to anthropometric data of the OBPP child. Next, using the inverse kinematics tool from OpenSim, the glenohumeral and scapulothoracic kinematics was determined successfully. This model incorporates scapulothoracic joint with four degrees of freedom to represent scapular upward rotation, internal rotation, winging and abduction. These motions were compared between healthy and pathological side. Next, the model derived kinematics was used for determining the joint moments and forces and muscle forces using inverse dynamic and static optimization tools respectively.

Chapter 11: This chapter provides a brief summary of the study and an overview of the findings of this thesis considering the aims previously described. Finally, perspectives and future directions to extend this research work were proposed.

1.4 Chapter 1 References

- [1] D. A. Winter, *The biomechanics and motor control of human gait : normal, elderly and pathological*, 2nd ed. Waterloo, Ont. : University of Waterloo Press, 1991.
- [2] W. Herzog, *Skeletal Muscle Mechanics: From Mechanisms to Function*. John Wiley & Sons, 2000.
- [3] A. Steindler, *Kinesiology of the Human Body Under Normal & Pathological Conditions*. Charles C Thomas Pub Ltd, 1977.
- [4] “Fact Sheet - Injury Data | WISQARS | Injury Center | CDC,” 24-Jul-2018. [Online]. Available: <https://www.cdc.gov/injury/wisqars/facts.html>. [Accessed: 27-Apr-2019].
- [5] G. C. Barroso and E. S. Thiele, “MUSCLE INJURIES IN ATHLETES.,” *Rev. Bras. Ortop.*, vol. 46, no. 4, pp. 354–358, Aug. 2011.
- [6] “Arthritis-Related Statistics | Data and Statistics | Arthritis | CDC,” 10-Oct-2018. [Online]. Available: https://www.cdc.gov/arthritis/data_statistics/arthritis-related-stats.htm. [Accessed: 28-Mar-2019].
- [7] J. R. Crandall, B. S. Myers, D. F. Meaney, and S. Z. Schmidtke, Eds., *Pediatric Injury Biomechanics: Archive & Textbook*. New York: Springer-Verlag, 2013.
- [8] M. N. Doral and J. Karlsson, Eds., *Sports Injuries: Prevention, Diagnosis, Treatment and Rehabilitation*, 2nd ed. Berlin Heidelberg: Springer-Verlag, 2015.
- [9] “Sports injuries to the shoulder and elbow.” [Online]. Available: <https://www.livres-medicaux.com/sports-injuries-to-the-shoulder-and-elbow.html>. [Accessed: 23-Feb-2019].
- [10] M. Lüthi, C. Jud, T. Gerig, and T. Vetter, “Gaussian Process Morphable Models,” *ArXiv160307254 Cs*, Mar. 2016.
- [11] R. Begg and M. Palaniswami, *Computational Intelligence for Movement Sciences: Neural Networks and Other Emerging Techniques*. Idea Group Inc (IGI), 2006.
- [12] V. Carbone, M. M. van der Krogt, H. F. J. M. Koopman, and N. Verdonschot, “Sensitivity of subject-specific models to errors in musculo-skeletal geometry,” *J. Biomech.*, vol. 45, no. 14, pp. 2476–2480, Sep. 2012.
- [13] T. Kleiber, N. Popovic, J. Bahm, and C. Disselhorst-Klug, “A modeling approach to compute modification of net joint forces caused by coping movements in obstetric brachial plexus palsy,” *J. Brachial Plex. Peripher. Nerve Inj.*, vol. 8, no. 1, p. 10, Oct. 2013.
- [14] H. G. Kwatny and G. L. Blankenship, “Symbolic construction of models for multibody dynamics,” *IEEE Trans. Robot. Autom.*, vol. 11, no. 2, pp. 271–281, Apr. 1995.
- [15] F. E. Zajac, “Muscle and tendon: properties, models, scaling, and application to biomechanics and motor control,” *Crit. Rev. Biomed. Eng.*, vol. 17, no. 4, pp. 359–411, 1989.
- [16] W. Cheng, R. Cornwall, D. L. Crouch, Z. Li, and K. R. Saul, “Contributions of muscle imbalance and impaired growth to postural and osseous shoulder deformity following brachial plexus birth palsy: a computational simulation analysis,” *J. Hand Surg.*, vol. 40, no. 6, pp. 1170–1176, Jun. 2015.
- [17] S. L. Delp *et al.*, “OpenSim: open-source software to create and analyze dynamic simulations of movement,” *IEEE Trans. Biomed. Eng.*, vol. 54, no. 11, pp. 1940–1950, Nov. 2007.
- [18] A. Seth *et al.*, “OpenSim: Simulating musculoskeletal dynamics and neuromuscular control to study human and animal movement,” *PLoS Comput. Biol.*, vol. 14, no. 7, p. e1006223, Jul. 2018.

- [19] Charles A. Rockwood Jr MD, Michael A. Wirth MD, and Steven B. Lippitt MD, *Rockwood and Matsen's The Shoulder, 2 Volume Set: Expert Consult - Online and Print*, 4 edition. Philadelphia, PA: Saunders, 2009.
- [20] R. Lugo, P. Kung, and C. B. Ma, "Shoulder biomechanics," *Eur. J. Radiol.*, vol. 68, no. 1, pp. 16–24, Oct. 2008.
- [21] A. G. Cutti and H. E. J. (DirkJan) Veeger, "Shoulder biomechanics: today's consensus and tomorrow's perspectives," *Med. Biol. Eng. Comput.*, vol. 47, no. 5, pp. 463–466, May 2009.
- [22] H. E. J. Veeger and F. C. T. van der Helm, "Shoulder function: the perfect compromise between mobility and stability," *J. Biomech.*, vol. 40, no. 10, pp. 2119–2129, 2007.
- [23] C. Pons, F. T. Sheehan, H. S. Im, S. Brochard, and K. E. Alter, "Shoulder muscle atrophy and its relation to strength loss in obstetrical brachial plexus palsy," *Clin. Biomech. Bristol Avon*, vol. 48, pp. 80–87, Oct. 2017.
- [24] F. C. van der Helm, "Analysis of the kinematic and dynamic behavior of the shoulder mechanism," *J. Biomech.*, vol. 27, no. 5, pp. 527–550, May 1994.
- [25] F. C. van der Helm and G. M. Pronk, "Three-dimensional recording and description of motions of the shoulder mechanism," *J. Biomech. Eng.*, vol. 117, no. 1, pp. 27–40, Feb. 1995.
- [26] D. C. Ackland, C. J. Goodwin, M. G. Pandy, D. C. Ackland, C. J. Goodwin, and M. G. Pandy, "Computational Modelling in Shoulder Biometrics," <http://services.igi-global.com/resolvedoi/resolve.aspx?doi=10.4018/978-1-59140-836-9.ch013>, 01-Jan-2001. [Online]. Available: <https://www.igi-global.com/gateway/chapter/6818>. [Accessed: 09-Nov-2018].
- [27] A. A. Nikooyan, H. E. J. Veeger, E. K. J. Chadwick, M. Praagman, and F. C. T. van der Helm, "Development of a comprehensive musculoskeletal model of the shoulder and elbow," *Med. Biol. Eng. Comput.*, vol. 49, no. 12, pp. 1425–1435, Dec. 2011.

Part I: Adult shoulder anatomy and biomechanics

Chapter 2

Skeletal and functional anatomy of the adult shoulder

2.1 Introduction

Shoulder is one of the most complex and functionally active joint in the human musculoskeletal system. Shoulder complex has a very interesting structure and it relates to evolution of human beings from quadrupedal to bipedal locomotion. Due to this evolution, humans have acquired a vast range of motion to their shoulder complex to be able to do multiple hand tasks and gestures. First important functional requirement is that shoulder complex is not a weightbearing joint, but it must be able to withstand weightbearing capacity if needed. This requirement makes the shoulder complex a unique joint in terms of its structure and function. Further, shoulder complex is responsible for all our daily mundane activities starting from brushing our teeth, eating, putting clothes, working, hand sports (e.g. badminton), driving, cleaning, gesturing etc.

In lower limb structure, weight of the body is passed through ankle and knee joint to hip joint and pelvic bone is able to withstand it. Pelvic bone also holds the torso (upper body) together. Thus, pelvic bone is a rigid body that is connected to upper and lower structures and thus has a higher load bearing capacity. But that means whenever there is a load on pelvic bone, it will be passed on to spinal column as well – as they are connected to pelvic bone [1]. In contrast to this, for shoulder complex, the load-bearing joint is gleno-humeral joint which is made from scapula and humerus bones. Interestingly, all the load coming onto this joint will ultimately be passed to scapular bone, but scapular bone is literally a floating bone in the musculoskeletal structure and it absorbs most of the load coming onto gleno-humeral joint while passing a very small amount to torso through clavicular articulation [1]–[3]. Thus, scapula plays a dampener role when it comes to load-sharing and transmission [4]. This brings a whole new meaning to shoulder complex and any abnormality in its structural composition directly hamper the quality of life.

In this chapter, I will briefly explain the structure of shoulder joint with respect to anatomy and function. I will provide a brief overview of the three components of shoulder structure, the bones, the joints, and muscles and then review shoulder motions and how each component plays role in each motion. All the illustrations in this chapter are adapted from an educational software on anatomy (Complete Anatomy, 3D4Medical Inc., USA) with which I have a personal subscription [5].

2.2 Anatomical terminology

The definition of anatomical planes and axes provide a standardized ground of communication between doctors, clinicians and engineers. This anatomical terminology allows description of location of different regions in the human body. Equally, it allows us to describe in a unified way the movement of a body segment with respect to its reference body segment for a given motion.

Three principal anatomical planes are defined (figure 2.1):

- ▶ The coronal plane (Frontal plane) is the vertical plane that divides the human body into front (ventral) and back (dorsal) portions. It sweeps the space from right to left and from head to foot through the body.
- ▶ The sagittal plane (Median plane) is the vertical plane that divides the human body into right and left. It passes from front to back and from head to foot through the body.
- ▶ The transverse plane (Axial plane) is the horizontal plane that divides the human body into upper part and lower part. This plane is perpendicular to sagittal and coronal planes.

These planes have cardinal property which makes them different than geometric planes. That means there is only one plane for each type which divide the body into two equal parts.

Three associated axes to these planes are mainly defined as (figure 2.1):

- ▶ The antero-posterior axis (Sagittal axis): The horizontal axis defined by the intersection of the transverse and the sagittal planes, passing from posterior to anterior.
- ▶ The medio-lateral axis (Frontal axis): The horizontal axis formed by the intersection of transverse and frontal planes (passing from left to right).
- ▶ The superior-inferior axis (Vertical axis): The vertical axis defined by the intersection of sagittal and frontal planes (from head to foot).

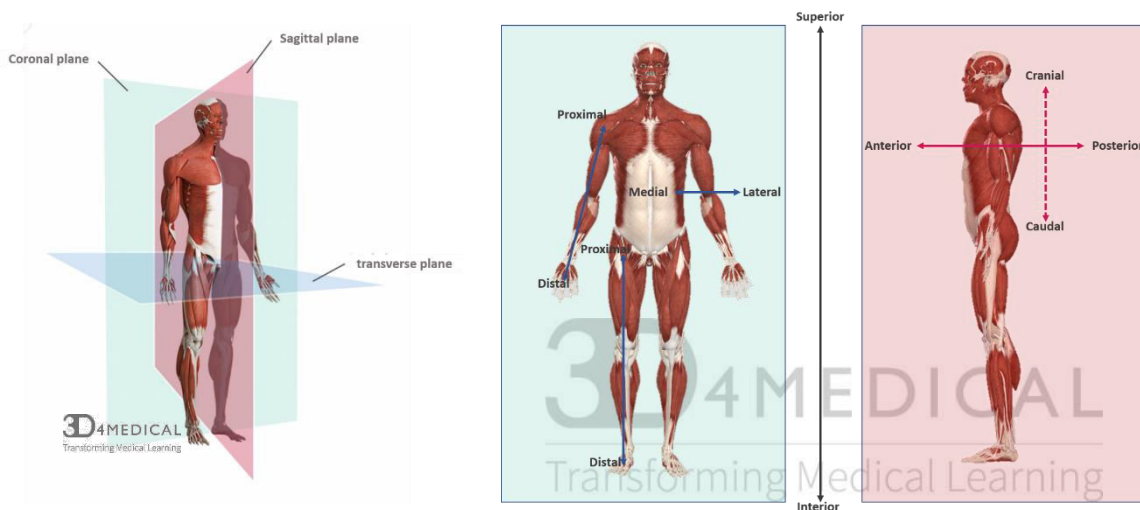


Figure 2. 1: Anatomical planes and axes of the human body [5]

2.3 The skeletal Structure

2.3.1 The shoulder girdle

The shoulder girdle, also called the pectoral girdle, is bony structure that supports the upper limb by attaching the arm to the axial skeleton (manubrium) (figure 2.2). It is composed by two anterior clavicles and two posterior scapulae. These bones form an incomplete ring around the upper part of the thoracic cage. Each clavicle articulates with the scapula and the manubrium region of the sternum. The scapula is attached to the thoracic cage by skeletal muscle only and has no bony ligaments connected with it. This makes the shoulder complex one of the most unstable structure of the human body.

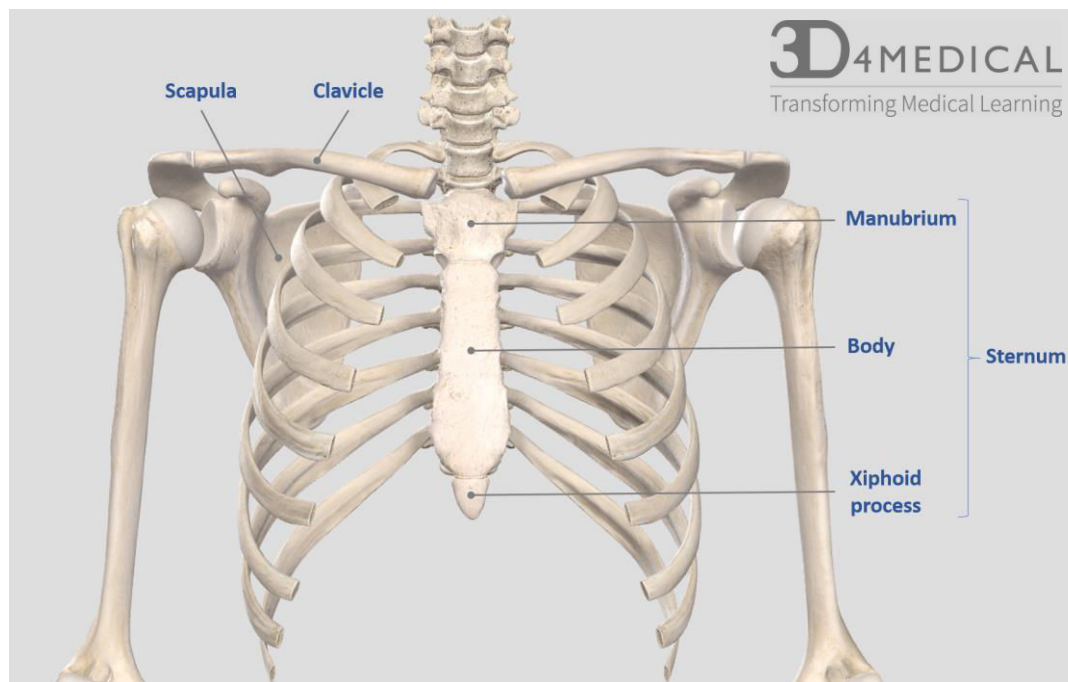


Figure 2. 2: *The shoulder girdle* [5].

2.3.2 The sternum

The sternum is a T-shaped bone located at the middle of the front of the ribs. It is composed of three parts: the manubrium, the body (a.k.a. gladiolus) and the xiphoid process (figure 2.2). The manubrium is the widest and the most superior part of the sternum. It joins with the clavicle at the sternoclavicular joint and the first and second pairs of ribs through their costal cartilage [6]. The gladiolus is the middle and largest part of the sternum [6]. It articulates superiorly with the manubrium (manubriosternal joint) and inferiorly with the xiphoid process (xiphisternal joint). It articulates with the costal cartilages of the third, fourth, fifth and sixth ribs. In addition, the pectoralis major muscle attaches the humerus to the anterior surface of the body and the manubrium of the sternum [6]. The xiphoid process is the smallest and the most inferior part of the sternum. It has a highly variable shape and size. In some individuals, it articulates with the costal cartilage of the seventh rib.

2.3.3 The clavicle

The clavicle is S-shaped bone located at the superior region of the thoracic cage (figure 2.2). The medial end of the clavicle is known as sternal extremity which articulates with the manubrium of the sternum to form the sternoclavicular joint [6]. The lateral end of clavicle is known as acromial extremity which articulates with acromion process of the scapula to form the acromioclavicular joint. Mechanically, the clavicle acts as a strut to anchor the upper limb to the trunk. Several important muscles for the shoulder movement have their attachment regions on the clavicle, including the deltoid, trapezius, sternocleidomastoid, and pectoralis major [6].

2.3.4 The scapula

The scapula is a flat triangular bone located over the upper part of the posterior thoracic cage (figure 2.3). It is thicker at the site of formation of its four bony processes: acromion, coracoid, spine, and glenoid. Anterior concavity of the scapula in sagittal plane creates an articulating surface against the first ribs of the thoracic cage. At the posterior surface of the scapula, the scapular spine creates the infraspinatus and the supraspinatus fossae. Glenoid cavity of the scapula is shallow and articulates with the proximal head of the humerus forming the glenohumeral joint.

The scapular bone serves as ground of attachment sites for 18 shoulder muscles [3]. These muscles are categorized as scapulohumeral, axioscapular and muscles of the upper limb (triceps brachii, biceps brachii, coracobrachialis)[3].

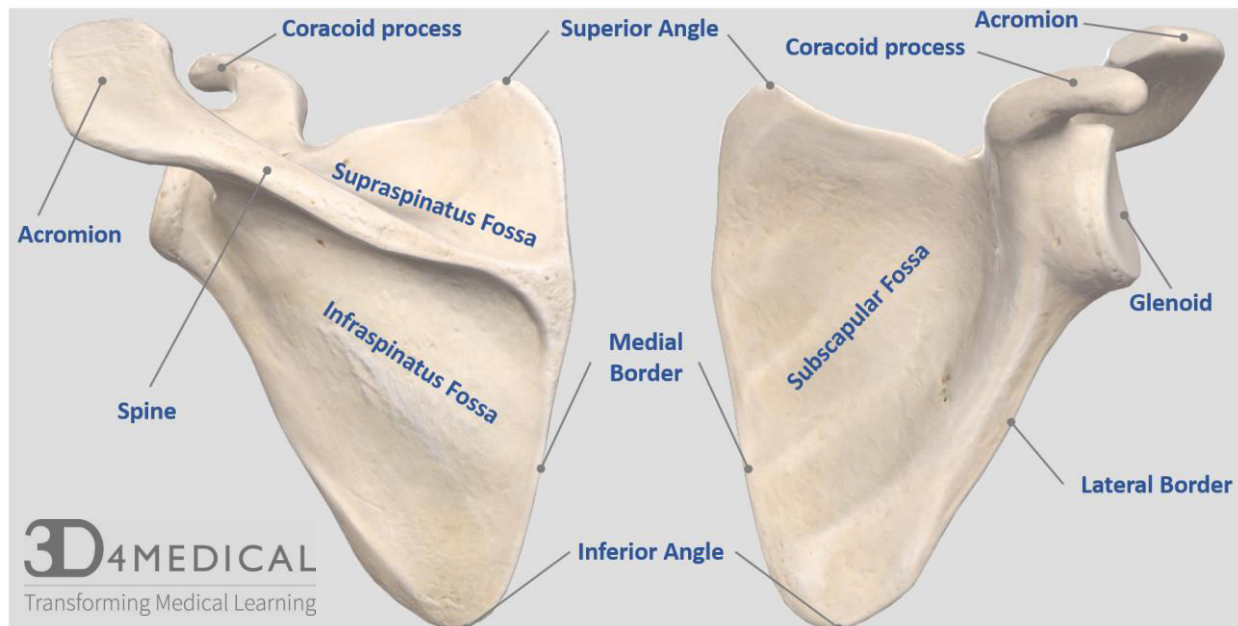


Figure 2. 3: Anterior and posterior views of the left scapula [5].

The scapulohumeral muscle group includes the deltoid, infraspinatus, supraspinatus, subscapularis, teres

major and teres minor muscles. These muscles are mainly responsible for the glenohumeral motion in multiples planes. The axioscapular muscle group includes the levator scapulae, pectoralis minor, serratus anterior, rhomboids, and trapezius muscles. These muscles participate significantly in the all the scapular motions.

2.3.5 The humerus

The humerus is the longest bone in the arm (figure 2.4). The proximal part of the humerus consists of the humeral head and the anatomical neck and two bony processes called greater and lesser tuberosities. The humeral head is its articular surface at the proximal end. Spherical shape of the humeral head allows the motion of the humerus in a complete circle and the rotation around its long axis. The anatomical neck lies between the tuberosities and the head. The greater and lesser tuberosities serve as attachment sites for rotator cuff muscles (more information in section 2.5). Bellow the tuberosities, the humerus narrows into the surgical neck. As its name indicates, it is the focus of surgeons due to its tendency to fracture. The shaft has a cylindric shape in its upper part and more triangular at its distal part. The lower proximity of the humerus consists of two epicondyles (lateral and medial epicondyles), two processes (capitulum and trochlea), and three fossae (coronoid fossa, radial fossa, and olecranon fossa).

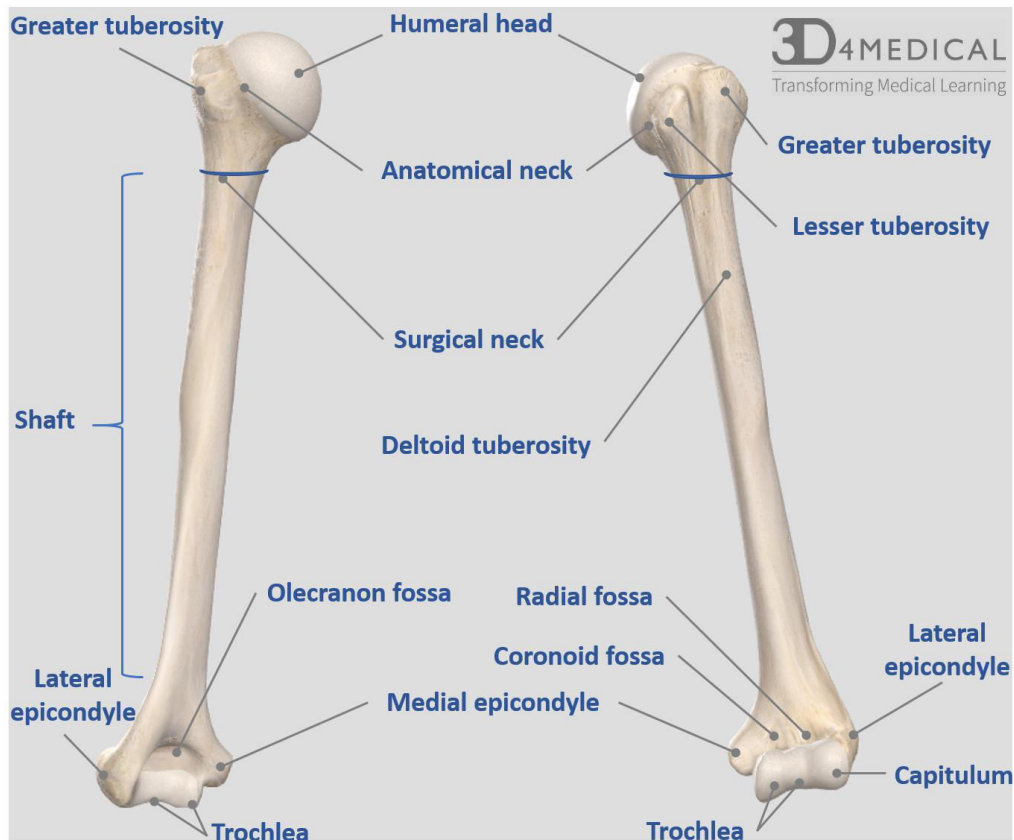


Figure 2. 4: Anterior and posterior views of the left scapula [5].

The humerus articulates proximally with the glenoid fossa of scapula through the humeral head forming the glenohumeral joint. More distally, the capitulum and the trochlea articulate with radius and ulna forearm bones respectively forming the elbow joint.

2.4 The Joints

The shoulder complex consists of four joints, three anatomical and one functional. The anatomical joints of shoulder are: sternoclavicular joint, acromioclavicular joint, and glenohumeral joint, whereas the scapulothoracic joint is regarded as the functional joint.

2.4.1 The sternoclavicular (SC) joint

The sternoclavicular (SC) joint is a synovial joint between the manubrium of the sternum, the first costal cartilage and the proximal end of the clavicle (figure 2.5). The SC joint is the only articulation between the axial skeleton and the upper limb [7]. The articular surfaces of the medial end of the clavicle and the manubrium have unequal dimensions and surface shapes, thereby making the joint not very stable. The joint stability is more provided by its ligamentous structure (anterior and posterior sternoclavicular or capsular ligaments, anterior and posterior costoclavicular ligaments and interclavicular ligaments) and its articular disc. The articular disc is a fibrocartilage layer between the two cavities or the articular surfaces of the clavicle and the sternum.

The sternoclavicular ligaments together help stabilizing the joint during depression of the clavicle by providing the minimal rotation occurred. Nevertheless, the posterior sternoclavicular ligament plays more stabilizing role of the lateral end of the clavicle during inferior depression [2]. The interclavicular ligament attaches both left and right medial ends of the clavicle with some fibers attached to the manubrium of the sternum [2]. The Costoclavicular ligaments connect the inferior part of the medial end of the clavicle with the superior part of first rib. These ligaments participate significantly on the stability of the sternoclavicular joint.

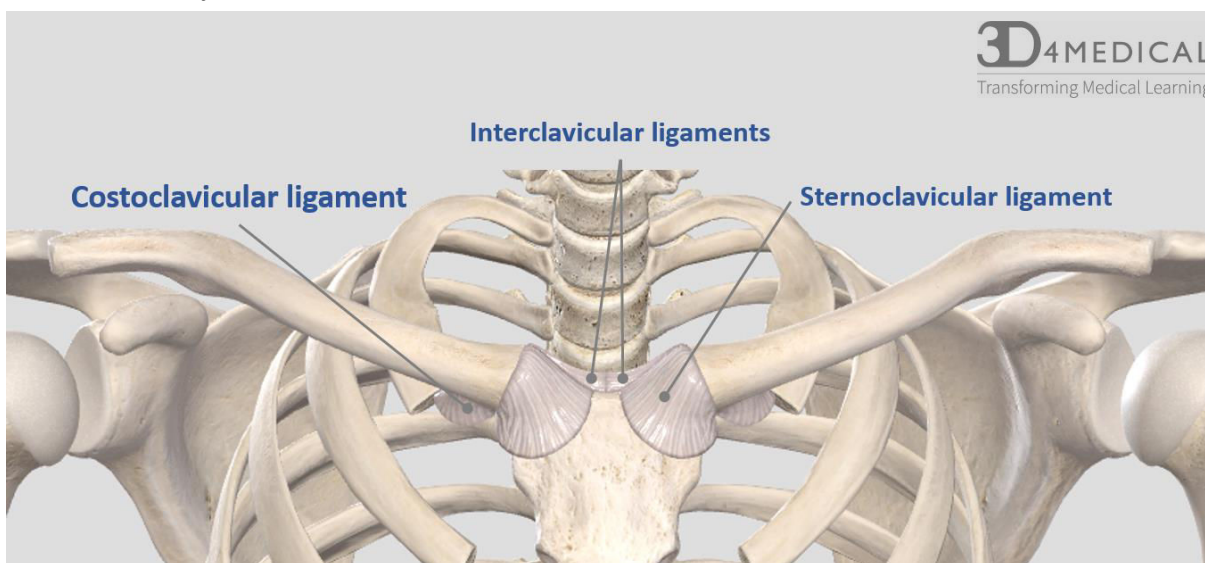


Figure 2. 5: Sternoclavicular joint and its ligaments [5].

2.4.2 The acromioclavicular (AC) joint

The acromioclavicular (AC) joint is a synovial joint linking the lateral end of the clavicle and the acromion of the scapula (figure 2.6) The joint capsule and the ligaments around the AC joint contribute together to maintain the joint stability.

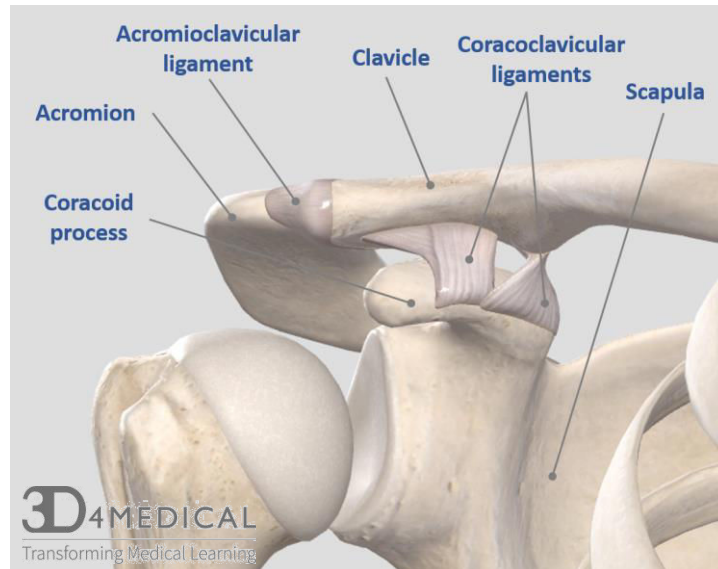


Figure 2. 6: Acromioclavicular joint and its ligaments [5].

The AC joint capsule cannot maintain the joint integrity without the reinforcement of the ligaments both superiorly and inferiorly. Many studies consider the acromioclavicular ligament as main stabilizer of this joint compared to other joint ligaments, preventing joint anteroposterior displacement [2]. Further stability of the AC joint in vertical direction is provided by the coracoclavicular ligament, which is composed of conoid and trapezoid ligaments. Both these ligaments attach from the clavicle to the coracoid process of the scapula.

2.4.3 The glenohumeral (GH) joint

The glenohumeral (GH) joint is a ball and socket type synovial joint formed between the glenoid cavity of the scapula and the head of the humerus (figure 2.7). The articular surface disproportion of the glenoid fossa and the humeral head permits a greater mobility in the joint. Indeed, the glenoid fossa of the scapula is shallow, whereas the humeral head has a large spheroid shape. A fibrocartilaginous glenoid labrum covers the glenoid fossa and deepens the socket by up to 50%. However, given the highly deformable nature of the labrum [8], its effect on the joint stability is not very clear.

The GH joint capsule surrounds the structures of the joint, extending from the border of the glenoid fossa to the anatomical neck of the humerus. The presence of synovial membrane and many synovial bursae (subscapular bursa, subcoracoid bursa, and subacromial bursa) between the articular surfaces and around the joint help reduce the joint friction by holding the synovial fluid. The ligaments play an important role

in maintaining the stability of the bony structures.

For the GH joint, the main ligaments are: glenohumeral ligaments (superior, middle and inferior), coracohumeral ligament, transverse humeral ligament, coracoacromial ligament (figure 2.7). The glenohumeral ligaments connect the glenoid cavity to the humerus anteriorly. They mainly help prevent the anterior joint dislocation. The coracohumeral ligament attaches the posterior tip of the coracoid process to the greater and lesser tubercles of the humerus, thus, reinforcing the superior part of the GH joint capsule. The transverse humeral ligament spans the surface between the lesser and greater tubercle of the humerus. Its main function is to hold the tendon of the long head biceps brachii muscle in the intertubercular sulcus. The coracoacromial ligament runs from the lateral part of the coracoid process to the acromion, forming the coraci-acromial arch. These ligaments together have a potential stabilizing role, but the skeletal muscles surrounding the GH joint remain the major stabilizer of the joint. Each muscle has different contribution on stability but the rotator cuff muscles (infraspinatus, supraspinatus, subscapularis and teres minor muscles) have the highest. These muscles will be discussed more in details bellow in this chapter.

In the shoulder complex, the GH joint is considered as the most critical joint for its extensive range of movement, thereby its exposure to injuries and joint dislocations.

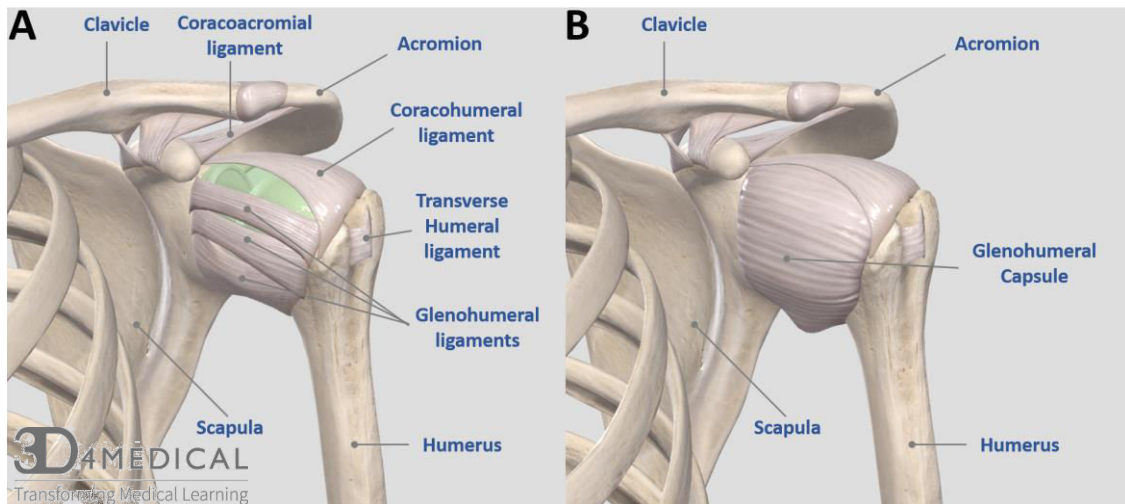


Figure 2. 7: *Glenohumeral joint and its ligaments* [5].

2.4.4 The scapulothoracic (ST) joint

Anatomically, the scapulothoracic (ST) joint is not considered as a true joint for its lack of joint characteristic such as cartilaginous or synovial tissues. It is regarded as a functional joint.

Functionally, it is defined by the articulation of the scapula against the posterosuperior part of the thorax, depending on the AC and SC joints. It is a sliding "Joint" of the scapula on approximately the 2-7th ribs anteriorly [2]. This contact area between scapula and thorax is often known as the scapulothoracic gliding plane (STGP). The scapula is held against the thorax only by skeletal muscles that originate or insert on

the scapula either deeply or superficially [2]. The interdependency of the ST joint on the AC and SC joints leads to a closed-chain linkage, going from the sternum to clavicle via SC joint, then from clavicle to scapula through AC joint and back to thorax via ST joint [2].

2.5 The Muscles

The shoulder musculature is responsible for maintaining the stability while providing a high range of mobility [9]. The stability of shoulder complex is mainly ensured by muscles. It is a complex structure, ranging from massive muscles, also called prime-movers, to fine muscles called stabilizers and muscles fixators. The prime shoulder muscles are mainly grouped into three muscle groups ([10], [11],[12]): 1) Scapulohumeral group, 2) Axioscapular group, and 3) Axiohumeral group, without ignoring the role of other muscles that impact the shoulder movement.

2.5.1 Scapulohumeral group

This is a group of muscles connecting the scapular bone to the humerus bone (table 2.1). This group is comprised of seven muscles: a) deltoid, b) infraspinatus, c) subscapularis, d) supraspinatus, e) teres minor, f) teres major, and g) coracobrachialis. They are the main contributors of the upper limb movement (Figure 2.8).

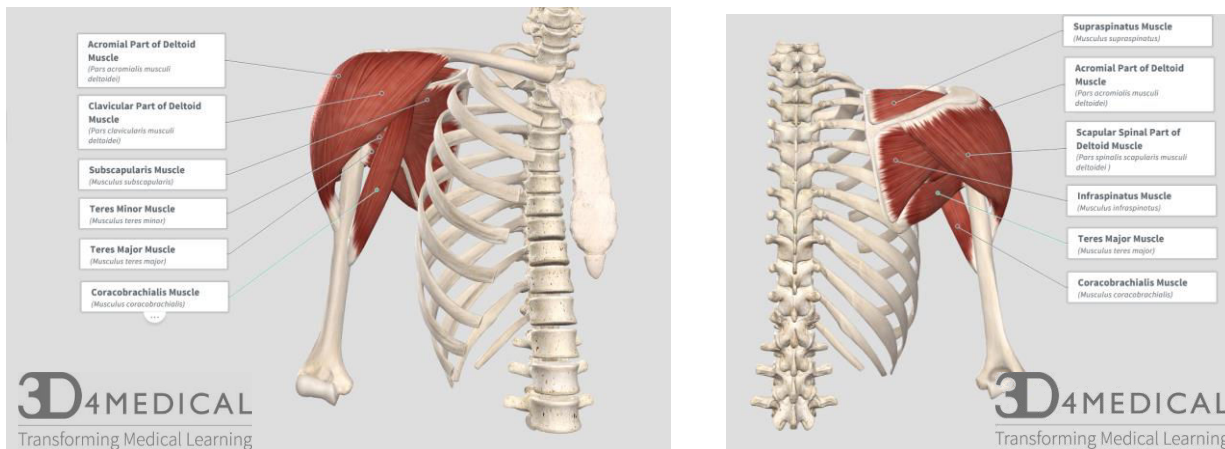


Figure 2. 8: *Scapulohumeral muscles* [5].

a) The deltoid is the prime abductor of the arm. Anatomically, it is formed by three sub-sets of fibers: Anterior deltoid, Middle deltoid and Posterior deltoid, whereas, electromyography (EMG) studies showed that it is functionally made up from at least seven different groups independently activated by the nervous system [13]. Anterior, middle and posterior deltoid groups originate from the third lateral portion of the clavicle, the acromion and the spine of the scapula respectively. Then, they are all attached at the same location on the humerus - the deltoid tuberosity of the humerus. Deltoid muscle is mainly responsible for arm rotation, flexion and abduction. The most frequent injury of deltoid is called deltoid strain which is characterized by intense pain when lifting up the arm in different planes.

b) - e) The infraspinatus muscle originates on the infraspinatus fossa on the scapular bone and extends

upward diagonally and inserts superiorly on the greater tuberosity of the humerus. The **subscapularis muscle** originates from the subscapularis fossa on the scapula and attaches on the lesser tuberosity of the humerus and it is considered as main internal rotator of the arm. The **supraspinatus muscle** originates from the supraspinatus fossa and inserts on the superior portion of the greater tuberosity. It helps mainly to initiate the abduction of the humerus and maintaining the glenohumeral stability during arm elevation by pulling the humeral head medially toward the glenoid fossa. The **teres minor** muscle extends from the lateral border of posterior scapular bone the greater tuberosity of the humerus and it helps adduction and external rotation of the arm. The infraspinatus, subscapularis, supraspinatus and teres minor muscles together form the rotator cuff muscle group. The rotator cuff muscles have an important role maintaining the glenohumeral joint stability by holding the humeral head against the small glenoid fossa of the scapula while the arm moves throughout the glenohumeral joint. During abduction, this muscle group act as compressor of the glenohumeral joint, allowing the deltoid to elevate the arm while avoiding the humeral dislocation. The injury of one or more of this group of muscle is called rotator cuff tear (full or partial). Most of the time, it is the supraspinatus, which is affected, leading to severe shoulder pain.

f) The teres major muscle originates from the lower lateral border and inferior angle of the scapula and attaches on the intertubercular sulcus of the humerus. It serves as medial rotator and adductor of the humerus and it also helps maintaining the glenohumeral stability.

g) The coracobrachialis muscle has the smallest attachment origin of the three muscles with attachment on the coracoid process of the scapula (the two others are pectoralis minor and biceps brachii). It goes down the arm and attaches on the mid-shaft of the humerus. Its main function is to flex and adduct the arm by moving it in the front of the body and pulling it toward the sagittal plane.

Table 2. 1: Scapulohumeral muscle group origin, insertion, and function

Muscle		Origin	Insertion	Main Function
Deltoid	Anterior deltoid	The lateral portion of the clavicle	The Deltoid tuberosity of the humerus	Flexion and medial rotation of the arm
	Middle deltoid	The acromion of the scapula	The Deltoid tuberosity of the humerus	Abduction of the arm
	Posterior deltoid	The spine of the scapula	The Deltoid tuberosity of the humerus	Extension and lateral rotation of the arm
Infraspinatus		The infraspinatus fossa of the scapula	The greater tuberosity of the humerus	External rotation
Subscapularis		The subscapularis fossa	The lesser tuberosity of the humerus	Internal rotation
Supraspinatus		The supraspinatus fossa	The greater tuberosity of the humerus	Abduction
Teres minor		The lateral border of the scapula	The greater tuberosity of the humerus	External rotation
Teres major		The lower lateral border and inferior angle of the scapula	The intertubercular sulcus of the humerus	Medial rotation and adduction of the arm
Coracobrachialis		The coracoid process	The mid-shaft of the humerus	Flexion and adduction of the arm

2.5.2 Axioscapular group

This is a group of muscle originating from the thorax to the scapular bone (Table 2.2 and Figure 2.9). This group is comprised of four muscles: trapezius, rhomboids, levator scapulae and serratus anterior. Topologically, these muscles span the scapulothoracic gliding surface.

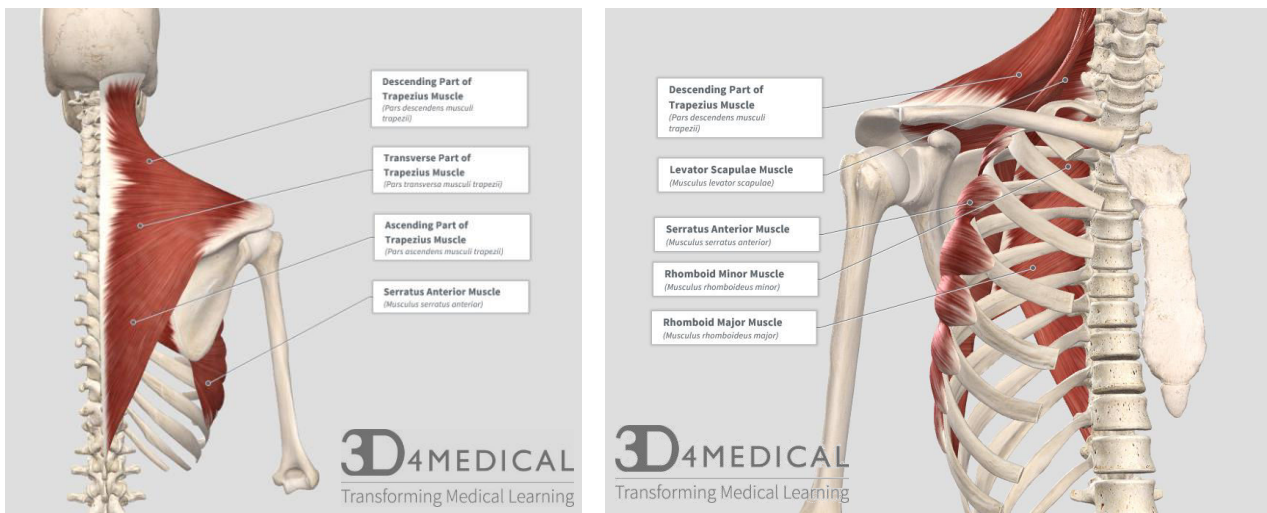


Figure 2. 9: Axioscapular muscles [5].

The trapezius muscle is one of the largest superficial muscles on the back. Functionally, it is divided into three sub-regions: superior trapezius, middle trapezius and inferior trapezius. The fibers of the superior trapezius originate from the occipital protuberance of the occipital bone, the spinous processes of C1-C7 vertebrae and the ligamentum nuchae and insert on the dorsal border of the lateral third of the clavicle. It mainly serves as scapular elevator and contribute in scapular upward rotation. The middle trapezius arises from the spinous process of C7-T5 vertebrae and ligamentum nuchae and inserts on the surface going from the medial margin of the acromion to the spine of the scapula. It produces retraction of the scapula. As continuation of other insertions of trapezius parts, the inferior trapezius originates from spinous processes of T5-T12 of vertebrae and inserts on the medial part of the spine of the scapular bone. This trapezius sub-region produces depression of the scapula. Fibers of different trapezius sub-regions are known to be contracting independently of each other [11], allowing multiple tasks for the same muscle.

Topologically, the two rhomboid muscles (Rhomboid minor and rhomboid major) are located under the trapezius muscle. The rhomboid minor muscle arises from the spinous processes of the C7 and T1 vertebrae and inserts on medial border of the scapula at the level of scapular spine. Whereas, the rhomboid major muscle originates inferiorly to the rhomboid minor muscle on the spinous processes of the T2-T7 vertebrae and inserts on the medial border of the scapula directly from the end of the rhomboid major muscle insertion inferiorly until the inferior angle. Both the rhomboid muscles together produce the scapular retraction and elevation.

The levator scapulae muscle attaches at the transverse processes of the first four cervical vertebrae and spans the neck to insert on the superior angle of the scapula. One of its main functions is to elevate the scapula during shoulder elevation.

The serratus anterior muscle spans the anterolateral part of the thorax cage under the scapula. Its fibers originate from the first eight ribs and insert on the anterior surface of the scapular medial border. The contraction of the serratus anterior allows the scapula to protract, holding the scapula against the rib cage.

The pectoralis minor originates at front surface of the third, fourth and fifth ribs and inserts on the coracoid process of the scapula.

Table 2. 2: Axioscapular muscle group origin, insertion, and function.

Muscle	Origin	Insertion	Main Function
Superior trapezius	The occipital protuberance of the occipital bone, the spinous processes of C1-C7 vertebrae and the ligamentum nuchea.	The dorsal border of the lateral third of the clavicle	Elevation of the scapula
Middle trapezius	The spinous process of C7-T5 vertebrae, ligamentum nuchea	The medial margin of the acromion and the spine of the scapula	Retraction of the scapula
Inferior trapezius	The spinous processes of T5-T12 of vertebrae	The medial part of the spine of the scapular bone	Depression of the scapula
Rhomboid Minor	The spinous processes of the C7 and T1 vertebrae	The medial border of the scapula at the level of scapular spine	Scapular retraction and elevation
Rhomboid Major	The spinous processes of the T2-T7 vertebrae	The medial border of the scapula from the scapular spine to the inferior angle	Scapular retraction and elevation
Levator scapulae	The transverse processes of the C1-C4 vertebrae	The superior angle of the scapula	Scapular elevation, neck flexion
Serratus anterior	The first eight ribs anterolaterally	The medial Border of the scapula anteriorly	Scapular protraction
Pectoralis minor	The third, fourth and fifth ribs	The coracoid process of the scapula	Draw the scapula forward and downward

2.5.3 Axiohumeral group

This is a group of muscle originating from the thorax to the humerus bone (Table 2.3). This group is comprised two large muscles: latissimus dorsi, pectoralis major and pectoralis minor.

They are considered as prime movers of the shoulder, assisting further the scapula and the humerus motions. The latissimus dorsi muscle is a large flat muscle on the back originating from the spinous processes of T6-T12 vertebrae, iliac crest of sacrum, thoracolumbar fascia and lower three ribs and inserting on the floor of the intertubercular sulcus of the humerus. The pectoralis major is a thicker flat muscle having origin attachment on the medial third of the clavicle, the sternum and first six ribs with one insertion attachment on the lateral lip of the intertubercular sulcus of the humerus. These two muscle contribute together to adduct and medially rotate the humerus [9].

Table 2. 3: Axiohumeral muscle group.

Muscle	Origin	Insertion	Main function
Latissimus dorsi	The spinous processes of T6-T12 vertebrae, iliac crest of sacrum, thoracolumbar fascia and lower three ribs	The floor of the intertubercular sulcus of the humerus	Extension, adduction, medial rotation of the humerus; depression of the scapula
Pectoralis major	The medial third of the clavicle, the sternum and first six ribs	The lateral lip of the intertubercular sulcus of the humerus	Flexion, medial rotation and adduction of the humerus

2.5.4 Other muscle group

The shoulder muscles listed above in different groups are responsible for the shoulder girdle function, but we should not ignore the role of other shoulder muscles that act on the glenohumeral joint. Among these muscle we found the long and short heads of biceps brachii arising from the scapula and inserting on the radius and contribute on arm flexion/extension, the triceps brachii muscle with its three heads (long, lateral and medial) originating from both scapula and humerus and inserting on the ulna , and subclavius muscle which originates at the superior portion of the first rib cage and inserts on the middle third of the clavicle inferiorly and plays an important role on stabilizing the SC joint.

2.6 - The Motions

Shoulder complex provides an extreme range of motion to the upper arm. The upper arm motion with the anatomical terminology is typically described by following:

- 1) Abduction and adduction of the arm
- 2) Flexion/extension of the arm
- 3) internal and external rotation of the arm
- 4) circumduction
- 5) Scapular protraction/retraction, elevation/depression, and upward/downward rotation
- 6) forearm motions

All the daily activities performed using upper arm can be described by above motion terminologies. Each of this motion is a combination of multiple bone articulations and muscle activations. In this section we will explain these combinations for each motion described above but without describing the details of joint axes and muscle forces and moment arms. Such details will form the part of shoulder biomechanics and will be described in chapter 3.

Most of the above terminologies are related to GH joint motion in different planes. It is important to understand the range of motion for each of these motions for an adult healthy shoulder (Table 2.4).

Restrictions or constraints in these range of motions restricts the ability of arm to perform many daily activities.

Table 2. 4: Normal range of motions for adult shoulder complex [14].

Action	Range of Motion
Abduction of the arm	170° – 180°
Adduction of the arm	50° – 75°
Internal rotation of the arm	60° – 100°
External rotation of the arm	80° – 90°
Horizontal abduction and adduction	130°
Scapular elevation	170° – 180°
Circumduction	200° in horizontal and 360° in sagittal plane

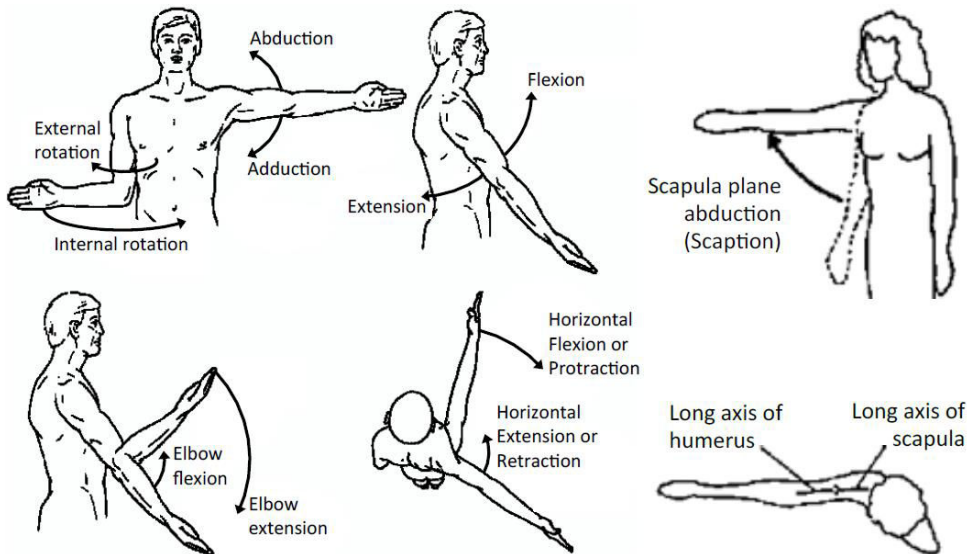


Figure 2. 10: Motions description of the upper limb (Adapted from Charlton, 2004 [15]).

Following table (Table 2.5) explains the bones and muscles involved in each of the motions above:

Table 2. 5: Motions and their functional relationship with bones and muscles.

Motion	Bones involved	Joints involved	muscles involved
Abduction of the arm	Humerus, scapula, clavicle	GH, SC, AC, ST	Middle deltoid, supraspinatus
Adduction of the arm	Humerus, scapula, clavicle	GH, SC, AC, ST	Pectoralis major, Teres major, latissimus dorsi
Internal rotation of the arm	Humerus, scapula, clavicle	GH, SC, AC, ST	Subscapularis
External rotation of the arm	Humerus, scapula, clavicle	GH, SC, AC, ST	Teres minor, infraspinatus
Horizontal abduction	Humerus, scapula, clavicle	GH, SC, AC, ST	Posterior deltoid, infraspinatus, teres minor
Horizontal adduction	Humerus, scapula, clavicle	GH, SC, AC, ST	Pectoralis major, anterior deltoid
Flexion of the arm	Humerus, scapula, clavicle	GH, SC, AC, ST	Anterior deltoid, pectoralis major (Clavicular)
Extension of the arm	Humerus, scapula, clavicle	GH, SC, AC, ST	Posterior deltoid, latissimus dorsi, teres major, pectoralis major (sternal)
Circumduction	Humerus, scapula, clavicle	GH, SC, AC, ST	All muscles

2.7 Chapter 2 References

- [1] D. A. Winter, *The biomechanics and motor control of human gait: normal, elderly and pathological*, 2nd ed. Waterloo, Ont. : University of Waterloo Press, 1991.
- [2] Charles A. Rockwood Jr MD, Michael A. Wirth MD, and Steven B. Lippitt MD, *Rockwood and Matsen's The Shoulder, 2 Volume Set: Expert Consult - Online and Print*, 4 edition. Philadelphia, PA: Saunders, 2009.
- [3] W. B. Kibler and A. D. Sciascia, Eds., *Disorders of the Scapula and Their Role in Shoulder Injury: A Clinical Guide to Evaluation and Management*. Springer International Publishing, 2017.
- [4] H. E. J. Veeger and F. C. T. van der Helm, "Shoulder function: the perfect compromise between mobility and stability," *J. Biomech.*, vol. 40, no. 10, pp. 2119–2129, 2007.
- [5] "3D4Medical – Award-winning 3D Anatomy and Medical Apps." [Online]. Available: <https://3d4medical.com/>. [Accessed: 14-Apr-2019].
- [6] H. Gray and H. V. Carter, *Anatomy of the human body*, 20th ed. / thoroughly rev. and re-edited by Warren H. Lewis. Philadelphia: Lea & Febiger, 1918.
- [7] E. D. Hauser, "Avulsion of the tendon of the subscapularis muscle," *J. Bone Joint Surg. Am.*, vol. 36-A, no. 1, pp. 139–141, Jan. 1954.
- [8] J. Carey, C. F. Small, and D. R. Pichora, "In situ compressive properties of the glenoid labrum," *J. Biomed. Mater. Res.*, vol. 51, no. 4, pp. 711–716, Sep. 2000.
- [9] H. E. J. Veeger and F. C. T. van der Helm, "Shoulder function: the perfect compromise between mobility and stability," *J. Biomech.*, vol. 40, no. 10, pp. 2119–2129, 2007.
- [10] D. C. Ackland, C. J. Goodwin, M. G. Pandy, D. C. Ackland, C. J. Goodwin, and M. G. Pandy, "Computational Modelling in Shoulder Biometrics," <http://services.igi-global.com/resolvedoi/resolve.aspx?doi=10.4018/978-1-59140-836-9.ch013>, 01-Jan-2001. [Online]. Available: <https://www.igi-global.com/gateway/chapter/6818>. [Accessed: 09-Nov-2018].
- [11] Martini, *Fundamentals of Anatomy & Physiology, 5th edition, hc, 2001*. AI 0130172928, 2001.
- [12] L. S. Lippert and J. Hurrell, *Clinical Kinesiology and Anatomy*. F. A. Davis Company, 2017.
- [13] J. M. M. Brown, J. B. Wickham, D. J. McAndrew, and X.-F. Huang, "Muscles within muscles: Coordination of 19 muscle segments within three shoulder muscles during isometric motor tasks," *J. Electromyogr. Kinesiol. Off. J. Int. Soc. Electrophysiol. Kinesiol.*, vol. 17, no. 1, pp. 57–73, Feb. 2007.
- [14] D. J. Magee, *Orthopedic Physical Assessment*. W.B. Saunders, 1997.
- [15] Iain William. Charlton, "A model for the prediction of the forces at the glenohumeral joint," University of Newcastle upon Tyne, Newcastle upon Tyne, 2004.

Chapter 3

Shoulder Biomechanics

3.1 Introduction

Shoulder complex has been studied for more than 500 years and the first ever mention was made by the famous artist and renaissance Leonardo da Vinci. To improve his artwork, Da Vinci turned to body structures and was the first artist to study the physical proportions of men, women and children as well. He focused on bones and muscles and analyzed their structure and function in mechanical terms. Da Vinci's historical work has been described in detail by a famous upper limb surgeon from Brest, Prof. Dominique Le Nen, in his book: LÉONARD DE VINCI: Un anatomiste visionnaire [1]. Incidentally, this year marks the 500th death anniversary of Da Vinci.

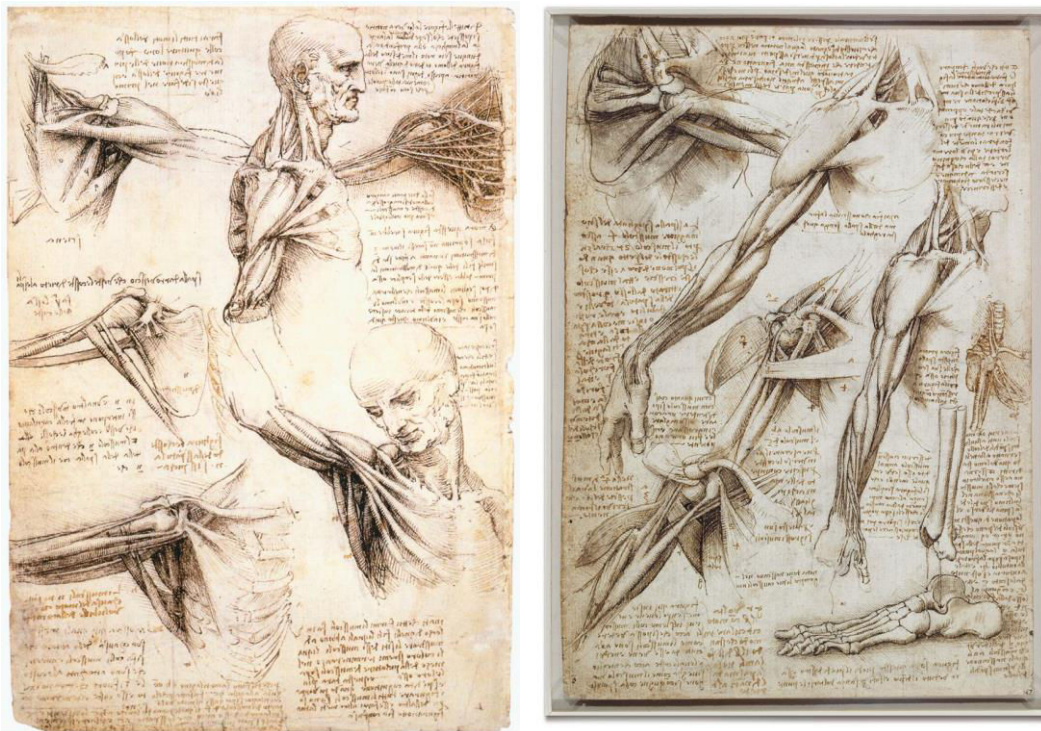


Figure 3. 1: Leonardo da Vinci's earlier depiction of shoulder musculature (Courtesy: LeonardoDaVinci.net)

A brief review of the anatomical complexity of the shoulder is already presented in Chapter 2. Functionally, the shoulder is the most active joint in the human musculoskeletal system. Let us first summarize the joint structure of the shoulder. Shoulder complex is made up from four principle joints:

- 1) Glenohumeral (GH) joint,
- 2) Scapulothoracic (ST) joint,
- 3) Acromioclavicular (AC) joint, and
- 4) Sternoclavicular (SC) joint.

Of these, GH joint has more mobility than stability and is responsible for all the arm motions. On the other hand, SC joint is the only joint that connects the components of the shoulder to the axial skeleton. This requires shoulder muscles to stabilize and secure shoulder girdle (clavicle and scapula) on thorax during static and dynamic conditions. The mobility of shoulder joint is the result of motion in both GH joint and ST joint. However, in the literature, the arm motion is typically reported as the rotation of a fictional thoracohumeral joint [2]. The motion of thoracohumeral joint is intuitive to understand and clinically preferred as it can be visualized clearly, but it is a combination of humerus motion with respect to the scapula and scapular motion with respect to the thorax. Further, abduction or flexion of the arm is simply regarded as arm elevation [3]. Most of the thoracohumeral motion takes place in the GH joint (glenohumeral elevation of up to 120°) ([4], [5]) and in addition to this, the humerus is able to rotate axially about 135° relative to the scapula (Chapter 2) [4]. Rest of the thoracohumeral motion is the result of scapula gliding on the thorax. The contribution of scapular motion to arm elevation follows a general pattern in which scapular motion is responsible for approximately 1/3rd of the total arm elevation. This process is called scapulohumeral rhythm (SHR) [6], [7].

The complex biomechanics of shoulder is typically categorized and studied according to the four joints listed above (GH, ST, AC, and SC), which makes it easier to understand and follow. In this chapter, I will explain shoulder biomechanics following a similar methodology. Within each joint, the biomechanics will be explained in three parts: motion, stability and forces.

1) Joint kinematics: motion

In general, joint kinematics may be divided into two-dimensional (2D) planar motion and three-dimensional (3D) spatial motion. With planar motion, moving bony segment both translates and rotates around the fixed segment. This motion is easy to understand as the user can easily isolate the motion in each plane and can intuitively relate to the joint motion. Spatial 3D motion is more challenging to understand and evaluate. However, using 3D motion is an accurate technique to specify joint motion as cross-talk between two axes can hamper the meaningful evaluation of planar motion, especially in cases of abnormal joint motions.

For general planar or gliding motion of the articular surface, the terms sliding, spinning, and rolling are commonly used. Let us give the definitions: Sliding motion is a pure translation of moving surface with respect to a fixed segment. Spinning is the exact opposite of sliding and the contact point on the fixed surface does not change, Rolling is a combination of sliding and spinning where the contact points are constantly changing. A more characteristic description of planar motion, however, can be based on rotation around a point or axis, which is defined as an instantaneous axis of rotation (IAR). Theoretically, the IAR could be determined accurately if the velocities of the points on the rigid body are measurable. In practice, an alternative technique based on the method of Rouleaux [8] is commonly adopted.

Each joint motion can be accurately specified using total six degrees of freedom (DoF) – three rotations and three translations. It is important to understand the distinction between a joint motion and motion

of each body forming the joint. The analysis of rigid body requires three linear and three angular coordinates to specify the location and orientation of a rigid body in space. Similarly, the analysis and evaluation of a joint require three linear and three angular coordinates. The two most commonly used methods for the description of joint kinematics are Eulerian angle and screw displacement axis. For example, if the joint is stable and the motion can be assumed to be that of a ball and socket joint, it is sufficient to consider only the rotations of the joint and the translations can be neglected. In this case, Eulerian angles are the most suited way to describe motion. In situations that require the analysis or evaluation of joint displacement, the screw displacement axis description is most appropriate. The rotation and translation components of displacement of the humerus relative to the glenoid or scapula are defined by rotation around and translation along a unique screw axis. The advantage of using a screw axis is that the orientation of the screw axis remains invariant regardless of the reference coordinate axis used. However, in my thesis, I used Eulerian angles as they relate the best to intuitive clinical outcomes.

2) Joint constraints: stability

Joint constraints are the means and mechanisms by which joint achieves stability in its static as well as dynamic states. Thus, joint constraints are typically divided into static and dynamic constraints. The constraints are provided by the anatomical structures such as ligaments, muscles, tendons, cartilage, and shape of the joint. Static constraints hold the joint together and limit the passive joint motion in order to prevent the joint from dislocations. Dynamic constraints stabilize the joint during motion and prevent the joint from subluxations. In typical joints, ligaments act as static stabilizers whereas muscles around the joint act as dynamic stabilizers and joint shape defines the translational or rotational limitations (or lack thereof).

3) Joint kinetics: forces or strength

Joint kinetics provide the means to understand and evaluate healthy articulation of the joint during any underlying joint motion and also to identify joint abnormality. Multiple techniques exist to directly measure the joint kinetics, however, these are invasive techniques. As explained in chapter 2, shoulder muscles are responsible for creating shoulder joint motion and generating forces between the articulating surfaces. Joint kinetics is typically evaluated using following measures:

- 1) Muscle moment arms – Defined as a perpendicular 2D or 3D distance joining the joint center and the muscle line of action [9].
- 2) Joint reaction forces – Defined as a resultant force or forces in each joint coordinate axes and are mostly determined using computational models of the shoulder joint [9].
- 3) Joint moments – Defined as a product of muscle moment arms and muscle forces around the joint axis [9].
- 4) Joint contact mechanics – Defined as a measure of force distribution (stress) and its location (trajectory) over the articular surfaces of the joint [9].
- 5) Joint power- Defined as the rate of work done by the joint during motion [9].

With regards to shoulder joint kinetics, we will revisit some of these measures in Chapter 10.

3.2 GH: Glenohumeral Joint

Glenohumeral joint is the most versatile joint of the shoulder complex. Typically, arm motions are a combination of all four shoulder joints with the GH joint being the primary joint, the ST joint being secondary and SC and AC joint motions occurring only at the extreme positions. This makes the GH joint a recipient of multiple injuries and disorders. Based on the structure (Chapter 2), GH joint is mechanically the most unstable joint and thus needs support from all the groups of muscles. GH joint motion has been studied over 100 years with different means of measurements and having multiple contradictory reports due to use of imperfect devices or confusion with respect to the terminologies. The main reason of this confusion or debate is the existence of sequence dependent nature of rotation which is termed as Codman's paradox [10], [11]. Codman's paradox can be explained as follows: in the resting anatomical position with medial epicondyle of the humerus pointing towards the midline of body, if the arm is brought forward to 90° flexion and abducted 90° in horizontal plane and then brought back to resting position, the medial epicondyle is no more pointing towards the midline but anteriorly away from the body [10], [11]. Interestingly, the humerus is never axially rotated. The simple understanding of this phenomenon is that serial angular rotations are not additive but are sequence dependent. Multiple rotations about orthogonal axes must therefore be defined by the sequence of rotation. These sequential rotations are called Eulerian angles. This confusion is significantly resolved by using two reference frames. First, scapular motion is best defined in reference to the classic anatomic reference system of the trunk. Second, humeral motion is described in reference to the scapula [10], [12].

3.2.1 GH Joint Kinematics (motions)

Before understanding the dynamic motions of the GH joint, it is important to understand the resting pose of normal adult GH joint. Resting pose of the GH joint is more described through the resting position of the humerus. It is also important from the standpoint of model building process as the relative GH rotations and translations are reported from resting pose as zero or reference pose. Such resting pose is due to combination of static constraints (stabilizers) and resting state of muscles around the GH joint. Identifying normal resting state or pose has clinical relevance and can identify multiple problems associated with muscle imbalances present in the pathological shoulder joint. This is especially true for pediatric shoulder and childhood disabilities associated with shoulder complex.

Resting position of the humerus: The humeral head rests in the center of glenoid cavity when viewed in the plane of glenoid surface, which is commonly regarded as dead meridian plane [3]. The humeral head and shaft are thought to lie in the plane of scapula. The 30° retroversion of the articular orientation is compensated by the 30° anterior rotation of the scapula on the trunk.

GH motion is occasionally reported as a planar joint articulating motion. Many techniques have been used to describe and quantify the 3D motion of the GH joint. Early research studies used more cadaveric observations to describe the kinematics of the joint [12], [13]. Nowadays, with technological advances, many other techniques are used to measure joint motions in vivo. Among these techniques, we find the imaging modalities such as magnetic resonance images (MRI) used to determine 3D kinematics of the GH motion [14]. The natural kinematic of the GH joint is described by three rotational DOF and three transitional DOF. Despite the huge interest in the literature on GH joint kinematics, translations of this joint still pose a controversy. In absence of any instability, GH joint can be described by three rotations only since the humeral head translations could be neglected. In this case, the joint can be modelled as

ball-and-socket joint. Humeral rotations with respect to scapula can occur in the frontal (coronal), sagittal, and scapular planes. These rotations include abduction-adduction, flexion-extension, internal-external rotations of the humerus. Abduction-Adduction represents the arm elevation in the coronal (frontal) plane away from-toward the rib cage. Flexion-Extension describes the forward-upward motion of the arm in the sagittal plane. Internal-external rotation is of the humerus in the medial-lateral direction.

The plane of the maximal arm elevation was demonstrated to be 23° anterior to the scapular plane and in this positions the humerus was typically found to be 30-35° externally rotated [15]. During arm elevation, the humeral head translates inferiorly-superiorly between 0.3 and 0.35 mm, whereas, anterior translation is 3.8mm during flexion and posterior translation is 4.9mm during extension [16]. This difference of translations amount in the two directions could be explained by the shape of the glenoid cavity. The glenoid articular surface of the GH joint has a concave shape with a slight retroversion of 6.2° in healthy adults [17]. An abnormality in glenoid shape, such as change in cavity dimensions or higher retroversion decrease in the degree of conformity between glenoid concavity and humeral head, leading to a posterior shoulder instability [18]. In fact, the glenoid concavity is slightly less in the anterior-posterior direction (radius of curvature=40.6 ± 14mm) as compared to superior-inferior direction (radius of curvature=32.2 ± 7.6mm) [19]. GH joint kinematics can be affected by many pathologies of the shoulder [19].

3.2.2 GH Joint Constraints (stability)

The glenohumeral joint has both static and dynamic stabilizers. The static stabilizers can be further divided into articular and capsuloligamentous components. Knowledge of GH constraints has a major clinical relevance concerning anterior dislocation of humeral head, posterior and multidirectional instability of the shoulder. GH dislocation occurs at an incidence of 11 - 17 per 100, 000 population. Of all glenohumeral dislocations approximately 70% occur in males.

Static stabilizers:

Humeral head: The physiological retroversion of the humeral head confers some stability, with significantly less than 30° of retroversion being associated with anterior instability. The version of the glenoid is important too, with excessive retroversion leading to posterior instability.

Glenoid: Although the radius of the glenoid is 2 mm greater than that of the humeral head [3], the congruity of the glenohumeral joint confers anatomical stability. Further stability arises from the peripheral thickening of the glenoid cartilage and deformation of the cartilage during loading. The force acting across the joint is increased by the relatively small surface area of the glenoid (one-third of the humeral head). There is also a negative pressure within the joint, leading to a vacuum effect 'sucking' the humeral head into the joint. Both factors add to the stability of the GH joint [13].

Glenoid labrum: This structure provides approximately 20% of the total stabilizing force across the GH joint. Glenoid labrum is composed of fibrocartilaginous tissue, and is triangular in cross-section, though it is more rounded inferiorly. The labrum is about 9 mm in cross-section superoinferiorly, but only 5 mm in an anteroposterior direction. The weakest part of the labrum-capsule complex is at approximately at the 4 o'clock position, and it is here that tears of the labrum (Bankart lesions) occur [14].

Glenohumeral ligament complex: This consists of the superior, middle and inferior glenohumeral ligaments. The superior glenohumeral ligament (SGHL) originates from the supraglenoid tubercle, anterior to the long head of biceps. It inserts near the lesser tuberosity of the humerus. The SGHL is contained within a triangular space called the rotator interval, along with the middle glenohumeral ligament, coracohumeral ligament and anterior capsule. It is thought that the rotator interval may act as a restraint against extreme flexion, extension, adduction and external rotation. The SGHL is the primary restraint to inferior translation of the humeral head in the adducted shoulder [15].

The middle glenohumeral ligament arises from the supraglenoid tubercle and anterosuperior labrum. It inserts into the lesser tuberosity, providing stability anteriorly between 0° and 90° of abduction. The most restraint to anterior translation occurs between 45° and 60° of abduction [16].

The inferior glenohumeral ligament (IGHL) is composed of anterior and posterior bands, with the axillary pouch between them, supporting the humeral head in a sling. Of the inferior glenohumeral ligament 85% originates from the labrum, and the insertion of the ligament is inferior to the greater and lesser humeral tuberosities. The anterior band of the IGHL tightens in 90° of abduction and external rotation, preventing anterior and inferior translation of the humeral head. This position is found in the late cocking phase in throwing sports. This part of the ligament forms a weak link that predisposes to Bankart lesions. The posterior band is tight in 90° of flexion and internal rotation, conferring further stability [16].

The IGHL is the primary stabilizing structure in the abducted shoulder and is the most frequently injured part of the capsule, leading to instability. Tightness of the IGHL causes impingement and increased shear forces on the superior labrum, which are linked to superior labral tears from anterior to posterior (SLAP lesions) [16].

Coracohumeral ligament: A key component of the rotator interval is the coracohumeral ligament. It is composed of anterior and posterior bands, inserting into the lesser and greater tuberosities respectively. The anterior band is tightest with the shoulder externally rotated, and the posterior band tightest in internal rotation. This results in the restriction of anterior inferior translation during these movements. An injury to the rotator interval may therefore lead to increased translation of the humeral head and instability [17].

Dynamic stabilizers: The dynamic stabilizers increase the stability of the shoulder joint during active movement. Their effect is to compress the humeral head against the glenoid and to reduce humeral head translation. When the dynamic stabilizers are inactive (as in the anaesthetized patient), the shoulder is less stable during movement.

The rotator cuff: The muscles of the cuff are key dynamic stabilizers of the shoulder. Their contraction compresses the humeral head into the glenoid fossa, mainly during the midrange of shoulder motion, with the glenohumeral and coracohumeral ligaments being more important at the extremes of movement. This is called the concavity-compression effect. It is most pronounced when the compressive load and glenoid depth are maximized. The posterior and anterior rotators of the humeral head have approximately the same cross-sectional depth, allowing an equal force couple to act across the glenohumeral joint. This prevents anterior or posterior translation. In addition to its dynamic effects the rotator cuff has been demonstrated to confer stability even in cadaveric studies. A greater than 50% tear in the cuff leads to significantly increased translation of the humeral head center after application of a

controlled force, with this being more pronounced if the anterior and posterior components are both affected [18].

The biceps: The biceps tendon has a Y-shaped origin from the superior labrum. During contraction, it depresses the humeral head and adds to glenohumeral stability. It is believed to reduce translation in the anteroposterior and superoinferior planes. It probably plays more of a role in cuff or labral deficient shoulders.

The position of the scapula: This dictates the version and angulation of the glenoid. A rotatory force couple is responsible for normal scapulothoracic dynamics, with the upper component consisting of the levator scapulae, upper trapezius, and the upper fibers of the serratus anterior. The lower component is composed of the lower trapezius and the lower fibers of serratus anterior. If the function of any of these muscle groups is impaired, it leads to alteration of scapulothoracic movement and can cause secondary instability of the shoulder.

The deltoid muscle: This provides a superior shear force to the humeral head. The inferior force of the rotator cuff normally counters this. In the cuff deficient patient, the unopposed pull of the deltoid can elevate the humeral head from the glenoid and cause cuff arthropathy.

Proprioception: Dynamic proprioceptors help to moderate shoulder movement during its range. If this system does not function, then subluxation and subsequent injury can occur or worsen [16].

3.2.3 GH Joint Kinetics (strength)

In most of the literature, GH joint forces are studied either for certain activities (for e.g. wheelchair propulsion) or for three basic arm motions viz. abduction-adduction, scapular plane elevation (flexion), and internal-external rotation of the humerus with or without elbow flexion. Most of the studies are based on cadaveric experiments and can only best approximate the complex relationship between the muscle forces, their lines of actions, and resultant GH joint forces. For example, during abduction, the maximal compression force on GH joint is up to half the body weight at 90° abduction [20]. The orientation and location of the glenoid forces is another important parameter with centrally located joint reaction forces associated with supraspinatus activity [21].

3.3 ST: Scapulothoracic Joint

The ST joint is considered as “virtual” joint for its lack of the anatomical joint characteristics. It is functional articulation, characterized by the scapular motion on the thorax. During arm elevation, the scapula moves over thorax (rib cage) boundary to contribute achieving a full range of motion (ROM). The scapular gliding on the thorax participates significantly on arm elevation. This kinematic interaction between the scapula and the humerus during movement is called scapulohumeral rhythm.

3.3.1 ST Joint Kinematics (motions)

Resting position of the scapula: The resting position of the scapula relative to trunk is anteriorly rotated about 30° with respect to the frontal plane as viewed from top. In normal shoulders, scapula is also rotated upward about 3° with respect to the sagittal plane as viewed from back [22]. Finally, scapula is tilted forward about 20° with respect to frontal plane when viewed from side [23]. This resting posture of scapula remain unchanged even after applying the load of up to 20Kg to the extremity [23]. Then, the 3D motion of the scapula with respect to the thorax was measured using a stereophotogrammetry at 2 different ROM during arm elevation. During the first half of elevation, 60° of scapular abduction, 20° of posterior tilt and 6° of internal rotation were occurred.

The 3D motion of the scapula with respect to the thorax is described by three rotations and two coupled translations. The three rotations are defined as internal rotation, abduction, tilt of scapula whereas the two translations are defined as superior-inferior & forward-backward displacements. Further, clinically meaningful motions of scapula are defined as protraction and retraction. Protraction is defined as a combination of backward movement of the scapula and anterior tilt (rotation of the scapula around AC joint). Retraction is defined as a combination of upward movement of the scapula and posterior tilt. ST lateral rotation involves more passive mechanical elements such as glenohumeral ligament, whereas ST tilt and ST protraction is more produced by muscles actions [24].

A restricted motion of the ST joint affects GH extension and external rotation, whereas it doesn't affect GH internal rotation [19], which indicates the point that GH internal rotation occur mainly in the GH joint. On another hand, the fusion of the GH joint increase significantly the ST internal rotation. In healthy adult subjects, to perform a personal care activity, a 15° of ST internal rotation occurs, whereas, the fusion of the GH joint results on 51° of ST internal rotation to perform the same activity [19]. For younger population, with Brachial plexus birth palsy, a clinical study reports that a decrease in the GH joint motion results in an increase in the ST joint motion [25].

3.3.2 ST Joint Constraints (stability)

ST joint stability is provided by fasciae attached to scapula and muscles. The deep fascia of the neck that covers the sternocleidomastoid and trapezius muscles joints the spine of the scapula, the clavicle, and the head, producing passive suspension. The deep fascia of the back provides also static stability. The vertical muscles, such as the upper trapezius, levator scapulae, and serratus anterior are considered as main static and dynamic stabilizers of the ST joint [19]. It is reported that during arm elevation, these vertical muscles are actively contracted. The dynamic contraction of the middle and inferior trapezius, rhomboids, and serratus anterior work on maintaining scapular stability while providing different arm mobilities. A functional deficiency of these muscle results in scapular winging [19].

3.3.3 ST Joint kinetics (strength)

The trapezius and the serratus anterior are the prime mover of the scapular abduction. The protraction is mainly initiated and controlled by the serratus anterior and the pectoralis minor muscle dynamic contraction, whereas, retraction motion is a mainly a result of the middle trapezius and rhomboid movers' function. In an electromyographic (EMG) study by Moseley et al. [26], the pectoralis major is thought to be the main scapular depressor rather than protractor, since it appeared to be less active then the serratus

anterior muscle during scapular protraction whereas it was more active than the other scapular muscles during scapular depression.

3.4 AC: Acromioclavicular Joint

Most of the time the AC and the SC joints have a coupled motion, that means, the motion of one joint depends on the motion of the other joint. This dependency is mainly limited by the coracoclavicular and acromioclavicular ligaments. The AC joint's main function is to transmit the forces from the upper extremity to the clavicle. The AC joint is more exposed to injuries as compared to SC joint.

3.4.1 AC Joint Kinematics (motions)

The AC joint motion that occurs during arm elevation is a complex motion [3] comprising of all three joint axes. Considering the rotation of the clavicle with respect to the scapula, these rotations can be described as: anteroposterior rotation, superoinferior rotation, and anterior and posterior axial rotation. The anteroposterior rotation of the clavicle with respect to the scapula is three times more important than superoinferior rotation. The anterior axial rotation of the clavicle follows the arm abduction linearly and may attain 35° for a full ROM of arm abduction.

3.4.2 AC Joint Constraints (stability)

The AC joint capsule and the ligamentous structure of the joint work together to maintain the joint stability, avoiding clavicular and/or scapular displacements in any plane.

AC joint capsule is a thin fibrous capsule. Its functionality is strengthened by capsular ligaments superiorly and inferiorly to ensure joint integrity. In a study by Debski et al., the release of the capsule provoked important anterior-to-posterior instability [27].

Acromioclavicular ligament: The main function of this ligament is to resist posterior translation and axial rotation of the AC joint. This ligament has two classifications – anterior and posterior – based on their positions. For the anterior acromioclavicular ligament, the tightness of this ligament occurs with the posterior rotation of the clavicle with respect to the scapula. For the posterior acromioclavicular ligament, the tightness of this ligament occurs with the anterior rotation of the clavicle with respect to the scapula. The insertion of the trapezius muscle and the origin of the deltoid muscle reinforces the acromioclavicular ligament

Coracoclavicular ligament: This ligament connects the posterior part of the coracoid process of the scapula to the inferior lateral part of the clavicle. It is formed by two parts: the trapezoid ligament (lateral part) and the conoid ligament (medial part). Its structure is described as a fibrocartilaginous structure [28]. The medial conoid ligament has a vertical orientation allowing resistance against scapular depression relative to clavicle and downward rotation of the scapula [19]. The tightening of the conoid ligament results on a posterior rotation of the clavicle around its axis because of the posterior attachment position of this ligament. The conoid ligament constraint the axial rotation anteriorly and posteriorly. The lateral trapezoid ligament has a horizontal orientation. This ligament resists mainly the scapular displacement with respect to the clavicle. This ligament also constraints posterior axial rotation of the clavicle with respect to scapula. The primary function of the coracoclavicular ligament is to produce clavicular motion needed for a full ROM during arm elevation.

The coracoclavicular ligament is thought to be the main stabilizer of the AC joint [19]. Other researchers consider the acromioclavicular ligament as the main AC joint ligament, resisting anteroposterior displacement [3].

3.4.3 AC Joint Forces (strength)

The main kinetic role of this joint is to transmit the forces from the upper extremity to the clavicle [29]. Studies have shown that conoid and trapezoid ligaments resisted 50 and 65% of the forces applied, respectively [30]. They also found that the AC ligaments acted as a primary restraint to posterior displacement of the clavicle and posterior axial rotation, regardless of the degree of displacement. In general, studies found that joint stability in horizontal plane is mediated by the Acromioclavicular ligament and stability in vertical plane is provided by coracoclavicular ligament [27], [29], [31], [32].

3.5 SC: Sternoclavicular Joint

SC joint is the only articulation between the axial skeleton and the upper extremity. Stability of this joint is thought to be maintained by soft tissue structures such as, anterior and posterior capsules, costoclavicular ligament, interclavicular ligament, and anterior and posterior sternoclavicular ligaments. The SC is a sturdy joint and is very uncommonly a subject of instability [33]. This may explain the relative limited number of studies focusing on this joint as compared with studies on other joints with higher instability. Both SC and AC joint rotations are mostly required in a wide range of arm motion.

3.5.1 SC Joint Kinematics (motions)

Most of the time the SC joint is considered as a ball-and-socket joint [34], [35], with three rotations of the clavicle segment with respect to the sternum. These three rotations are 1) Elevation-depression, 2) Protrusion-retraction, and 3) Upward-downward rotation. SC elevation is more occurred by anatomical mechanics including passive elements like coracoclavicular ligament. SC backward rotation (protrusion) and SC retraction occur more as a result of muscle actions [24].

Axial rotation of the clavicle is demonstrated to be a main key element of shoulder motion, particularly for arm elevation. The SC joint can have an upward rotation of up to 35°, an anterior-posterior of up to 35°, and up to 45°-50° of axial rotation [3]. During the entire cycle of arm elevation, clavicle elevates and rotates, whereas posterior rotation of the clavicle occurs only after 90° of arm elevation [3]. Delgado and associates reported that for a typical abduction and flexion motion of the arm, the clavicle moves between 27° and 33° for retraction, 25° and 28° for elevation and 14° to 15° for posterior rotation [36]. A constrained rotation of the clavicular results in a limited elevation of the arm (up to 110° of elevation only)

3.5.2 SC Joint Constraints (stability)

The stability of SC joint in this section is explained considering each structure that contributes to the joint integrity at the time. The stability of SC joint is maintained by two capsules and four ligaments. The tension produced by ligaments is the main stabilizer of the joint on both sides. The anterior sternoclavicular ligament maintains the clavicle resting position. It is important to mention that bony stability at this joint is reduced due to the small articular surface of both clavicle (medial end) and manubrium. Thereby, these stabilizers have an important role maintaining the shoulder stability.

Articular disc is a fibrocartilaginous plate between the clavicle and the manubrium. Its location as a separator between the articular surfaces, allows the clavicle to move more freely with respect to the manubrium. It acts like a shock absorber [37]. It helps the interclavicular ligament and capsular ligament to avoid inferior displacement of the clavicle.

Anterior capsule plays important role resisting anterior displacement of the clavicle [38].

Posterior capsule has the most important role of resisting anterior and posterior translations of the clavicle [38].

Anterior sternoclavicular ligament has a very important functional role. This ligament is the main resister to upward displacement of the clavicle and plays an important role in avoiding lateral displacement of the clavicle [19].

Posterior sternoclavicular ligament: it strengthens the anterior capsule to resist anterior displacement of the clavicle.

Interclavicular ligament is the main resistor against inferior displacement of the clavicle [3]. The posterior portion of this ligament strengthen the joint capsule to resist anterior displacement (Protrusion).

Costoclavicular ligament prevents elevation of the clavicle laterally and superiorly [3]. The anterior part of this ligament resists posterior displacement. This ligament is thought to be the most strong and the most important ligament of the SC joint, constraining elevation of the pectoral girdle [38].

3.5.3 SC Joint Forces (strength)

There are no muscles that have attachments on only the bones forming the SC joint directly. The SC joint is reported to follow the motion of the scapula [39]. The muscles having their attachments on the clavicle such as, deltoid, pectoralis major, trapezius and sternocleidomastoid, affect clavicular movement, thereby affect the dynamics of the SC joint.

3.6 Chapter 3 References

- [1] D. Le Nen, "LÉONARD DE VINCI - Un anatomiste visionnaire, Dominique Le Nen - livre, ebook, epub." [Online]. Available: <http://www.editions-harmattan.fr/index.asp?navig=catalogue&obj=livre&no=31307&razSqlClone=1>. [Accessed: 01-Feb-2019].
- [2] F. C. van der Helm and G. M. Pronk, "Three-dimensional recording and description of motions of the shoulder mechanism," *J. Biomech. Eng.*, vol. 117, no. 1, pp. 27–40, Feb. 1995.
- [3] Charles A. Rockwood Jr MD, Michael A. Wirth MD, and Steven B. Lippitt MD, *Rockwood and Matsen's The Shoulder, 2 Volume Set: Expert Consult - Online and Print*, 4 edition. Philadelphia, PA: Saunders, 2009.
- [4] D. J. Magermans, E. K. J. Chadwick, H. E. J. Veeger, and F. C. T. van der Helm, "Requirements for upper extremity motions during activities of daily living," *Clin. Biomech. Bristol Avon*, vol. 20, no. 6, pp. 591–599, Jul. 2005.
- [5] F. C. van der Helm and G. M. Pronk, "Three-dimensional recording and description of motions of the shoulder mechanism," *J. Biomech. Eng.*, vol. 117, no. 1, pp. 27–40, Feb. 1995.
- [6] J. G. Bonnin, "The Shoulder. By E. A. Codman.," *J. Bone Joint Surg. Br.*, vol. 49-B, no. 1, pp. 206–206, Feb. 1967.
- [7] E. A. Codman, *The shoulder; rupture of the supraspinatus tendon and other lesions in or about the subacromial bursa*. Boston, Mass: T. Todd Company, printers, 1934.
- [8] P. S. Walker, *Human joints and their artificial replacements*, 1st Edition edition. Springfield, Ill: Thomas, 1977.
- [9] B. M. Nigg and W. Herzog, *Biomechanics of the Musculo-skeletal System*, 3rd Edition. Wiley, 2007.
- [10] M. L. Pearl, J. A. Sidles, S. B. Lippitt, D. T. Harryman, and F. A. Matsen, "Codman's paradox: Sixty years later," *J. Shoulder Elbow Surg.*, vol. 1, no. 4, pp. 219–225, Jul. 1992.
- [11] A. K. Saha, "The classic. Mechanism of shoulder movements and a plea for the recognition of 'zero position' of glenohumeral joint," *Clin. Orthop.*, no. 173, pp. 3–10, Mar. 1983.
- [12] T. B. Johnston, "The movements of the shoulder-joint a plea for the use of the 'plane of the scapula' as the plane of reference for movements occurring at the humero-scapular joint," *BJS*, vol. 25, no. 98, pp. 252–260, 1937.
- [13] S. G. Doody, J. C. Waterland, and L. Freedman, "Scapulo-humeral goniometer," *Arch. Phys. Med. Rehabil.*, vol. 51, no. 12, pp. 711–713, Dec. 1970.
- [14] W. Sahara, K. Sugamoto, M. Murai, H. Tanaka, and H. Yoshikawa, "The three-dimensional motions of glenohumeral joint under semi-loaded condition during arm abduction using vertically open MRI," *Clin. Biomech. Bristol Avon*, vol. 22, no. 3, pp. 304–312, Mar. 2007.

- [15] A. O. Browne, P. Hoffmeyer, S. Tanaka, K. N. An, and B. F. Morrey, "Glenohumeral elevation studied in three dimensions," *J. Bone Joint Surg. Br.*, vol. 72, no. 5, pp. 843–845, Sep. 1990.
- [16] D. T. Harryman, J. A. Sidles, J. M. Clark, K. J. McQuade, T. D. Gibb, and F. A. Matsen, "Translation of the humeral head on the glenoid with passive glenohumeral motion," *J. Bone Joint Surg. Am.*, vol. 72, no. 9, pp. 1334–1343, Oct. 1990.
- [17] B. Fuchs, B. Jost, and C. Gerber, "Posterior-inferior capsular shift for the treatment of recurrent, voluntary posterior subluxation of the shoulder," *J. Bone Joint Surg. Am.*, vol. 82, no. 1, pp. 16–25, Jan. 2000.
- [18] H. Inui *et al.*, "Glenoid shape in atraumatic posterior instability of the shoulder," *Clin. Orthop.*, no. 403, pp. 87–92, Oct. 2002.
- [19] N. E. Pratt, "Anatomy and Biomechanics of the Shoulder," *J. Hand Ther.*, vol. 7, no. 2, pp. 65–76, Apr. 1994.
- [20] V. T. Inman, J. B. Saunders, and L. C. Abbott, "Observations of the function of the shoulder joint. 1944.," *Clin. Orthop.*, no. 330, pp. 3–12, Sep. 1996.
- [21] R. W. Bassett, A. O. Browne, B. F. Morrey, and K. N. An, "Glenohumeral muscle force and moment mechanics in a position of shoulder instability.," *J. Biomech.*, vol. 23, no. 5, pp. 405–415, 1990.
- [22] M. D. Lazarus, J. A. Sidles, D. T. Harryman, and F. A. Matsen, "Effect of a chondral-labral defect on glenoid concavity and glenohumeral stability. A cadaveric model," *J. Bone Joint Surg. Am.*, vol. 78, no. 1, pp. 94–102, Jan. 1996.
- [23] U. Laumann, "Kinesiology of the Shoulder Joint," in *Shoulder Replacement*, 1987, pp. 23–31.
- [24] X. Robert-Lachaine, P. Allard, V. Godbout, and M. Begon, "3D shoulder kinematics for static vs dynamic and passive vs active testing conditions," *J. Biomech.*, vol. 48, no. 12, pp. 2976–2983, Sep. 2015.
- [25] S. A. Russo *et al.*, "Scapulothoracic and glenohumeral contributions to motion in children with brachial plexus birth palsy," *J. Shoulder Elbow Surg.*, vol. 23, no. 3, pp. 327–338, Mar. 2014.
- [26] J. B. Moseley, F. W. Jobe, M. Pink, J. Perry, and J. Tibone, "EMG analysis of the scapular muscles during a shoulder rehabilitation program," *Am. J. Sports Med.*, vol. 20, no. 2, pp. 128–134, Apr. 1992.
- [27] R. E. Debski, I. M. Parsons, S. L. Woo, and F. H. Fu, "Effect of capsular injury on acromioclavicular joint mechanics," *J. Bone Joint Surg. Am.*, vol. 83-A, no. 9, pp. 1344–1351, Sep. 2001.
- [28] B. Ockert, V. A. Braunstein, C. J. Sprecher, Y. Shinohara, C. Kirchhoff, and S. Milz, "Attachment sites of the coracoclavicular ligaments are characterized by fibrocartilage differentiation: a study on human cadaveric tissue.," *Scand. J. Med. Sci. Sports*, vol. 22, no. 1, pp. 12–17, 2012.
- [29] M. F. Saccomanno, C. DE Ieso, and G. Milano, "Acromioclavicular joint instability: anatomy, biomechanics and evaluation.," *Joints*, vol. 2, no. 2, pp. 87–92, Jun. 2014.
- [30] K. Fukuda, E. V. Craig, K. N. An, R. H. Cofield, and E. Y. Chao, "Biomechanical study of the ligamentous system of the acromioclavicular joint.," *J. Bone Joint Surg. Am.*, vol. 68, no. 3, pp. 434–440, Mar. 1986.

- [31] A. R. Motamedi, F. T. Blevins, M. C. Willis, T. P. McNally, and M. Shahinpoor, "Biomechanics of the coracoclavicular ligament complex and augmentations used in its repair and reconstruction.," *Am. J. Sports Med.*, vol. 28, no. 3, pp. 380–384, Jun. 2000.
- [32] P. A. Dawson *et al.*, "Relative contribution of acromioclavicular joint capsule and coracoclavicular ligaments to acromioclavicular stability.," *J. Shoulder Elbow Surg.*, vol. 18, no. 2, pp. 237–244, Apr. 2009.
- [33] F. Martetschläger, R. J. Warth, and P. J. Millett, "Instability and degenerative arthritis of the sternoclavicular joint: a current concepts review," *Am. J. Sports Med.*, vol. 42, no. 4, pp. 999–1007, Apr. 2014.
- [34] P. M. Ludewig, V. Phadke, J. P. Braman, D. R. Hassett, C. J. Cieminski, and R. F. LaPrade, "Motion of the Shoulder Complex During Multiplanar Humeral Elevation," *J. Bone Jt. Surg.*, vol. 91, no. 2, pp. 378–389, Feb. 2009.
- [35] R. L. Lawrence, J. P. Braman, R. F. LaPrade, and P. M. Ludewig, "Comparison of 3-Dimensional Shoulder Complex Kinematics in Individuals With and Without Shoulder Pain, Part 1: Sternoclavicular, Acromioclavicular, and Scapulothoracic Joints," *J. Orthop. Sports Phys. Ther.*, vol. 44, no. 9, pp. 636–645, Aug. 2014.
- [36] G. Gutierrez Delgado *et al.*, "Procedure to describe clavicular motion," *J. Shoulder Elbow Surg.*, vol. 26, no. 3, pp. 490–496, Mar. 2017.
- [37] J. Kiel and K. Kaiser, "Sternoclavicular Joint Injury," in *StatPearls*, Treasure Island (FL): StatPearls Publishing, 2018.
- [38] E. E. Spencer, J. E. Kuhn, L. J. Huston, J. E. Carpenter, and R. E. Hughes, "Ligamentous restraints to anterior and posterior translation of the sternoclavicular joint," *J. Shoulder Elbow Surg.*, vol. 11, no. 1, pp. 43–47, Jan. 2002.
- [39] "Joint Structure and Function : A Comprehensive Analysis, 4th Edition - F.A. Davis Company," 31-Jan-2019. [Online]. Available: <https://www.fadavis.com/product/physical-therapy-joint-structure-function-levangie-norkin-4-old>. [Accessed: 31-Jan-2019].

**Part II: Statistical Shape Modeling to
predict subject-specific
musculoskeletal model inputs**

Chapter 4

Augmented Statistical Shape Model of scapular bone for clinical use

4.1 Introduction

The global aim of this thesis is to build a combined framework of two research domains – Statistical Shape Modeling (SSM) and musculoskeletal modeling. To build this framework, concerns and questions related to individual research domains must be addressed first. I propose that the use of SSM in this combined framework will be to derive subject-specific parameters of the musculoskeletal structure. These parameters will then be used as an input to musculoskeletal modeling, helping the model to predict realistic clinical outcomes and providing an accurate evaluation of underlying biomechanics. For SSM domain, these questions include:

- 1) whether the SSM of a bone has enough accuracy to be used to evaluate subject-specific morphology using model fitting process? If such capability can it be further enhanced by any means – for example, adding a set of landmarks to the SSM?
- 2) Musculoskeletal modeling is often developed on multiple assumptions about the musculoskeletal structure and its parameters. Can SSM play a complementary or augmentative role in musculoskeletal modeling by eliminating one or more of these assumptions and providing realistic parameters?
- 3) The strength of SSM lies in determining subject-specific morphology, muscle insertion regions, cortical bone thicknesses, bone mineral density values, and prediction of missing bone shape from the remaining shape. Can any or all of these strengths be explored in this framework?
- 4) SSMs can also provide valid shape instances within the population variation. These shape instances can very well be used to understand the effect of bone morphology on underlying joint mechanics. Can such a technique be employed in this combined framework?
- 5) Can an integrated framework provide tools to clinically diagnose musculoskeletal disorders in the pediatric population?
- 6) What are the tools and techniques to standardize and validate such integrated framework?

SSMs have been extensively used in computer vision pipelines and in medical image processing field [1]. SSMs describe an average shape distribution within a population [2, 3] from which one can analyze shape variations and construe shape characterization. When registered with new data sets, SSMs can facilitate evaluation, diagnosis, and treatment of musculoskeletal diseases [2, 4]. Such patient-specific models have

medical applications such as evaluating bone motion tracking or computer-aided orthopedic surgeries [1, 5, 6]. Despite its capability and wide usage in medical image segmentation, application of SSMs in surgical planning, biomechanics modeling, and clinical treatments has not been extensively explored. This could partially be due to the complexity involved in building the SSMs and due to our inability to validate these models with anatomical data. Thus, to use SSMs in biomechanical analysis as a clinical diagnostic tool, one would first require a necessary validation of their statistical integrity, computational stability, and prediction ability for clinically relevant areas.

In this chapter, I will introduce the state-of-the-art in the area of SSM and related research and report the research conducted to address the question no. 1 above. Since in my thesis, I work with shape analysis with geometric property variations (and not intensity-based statistical appearance models), the concepts related to shape models only are covered. These include the concepts and state-of-the-art in **point distributions models**, **point-to-point correspondences**, **rigid and non-rigid registration**, **Gaussian Process Morphable Models**, and **model fitting** techniques. All these concepts are explained in section 2. In the remaining part of this chapter, I report the research conducted to address the question no. 1. This part of the chapter is arranged as a journal manuscript format. In section 3, I will explain the rationale to build a scapula SSM and augment it with bony landmarks. This research addresses why such augmentation is necessary to improve the clinical utility of the scapular SSM and if one set of landmarks (or none) provide more utility than other sets. I explain the methods used for illustrating and comparing the clinical utility of three augmented SSMs in section 4. Section 5 covers the results obtained and section 6 is the discussion.

4.2 State-of-the-art in SSM and related research

4.2.1 Statistical shape models

“Shape” is defined as geometric information of an object that remains after removing differences in scale, location, and rotations [7]. Whereas “form” of an object is defined as geometric information containing “shape” and scale of an object. **Statistical shape modeling** is a branch of machine learning that deals with statistical understanding of the variability in a given shape family or population. Machine learning is the subfield of computer science that “gives computers the ability to learn without being explicitly programmed” (Arthur Samuel, 1959). Evolved from the study of pattern recognition and computational learning theory in artificial intelligence, machine learning explores the study and construction of algorithms that can learn from and make predictions on data. Such algorithms overcome strictly static program instructions by making data-driven predictions or decisions, through building a model from sample inputs. Pattern theory follows a five-point manifesto 1) Patterns have (hidden) structure, 2) Patterns should be modeled partly stochastically and partly deterministically, 3) Models should respect the structure of the patterns and should learn from data and should be validated by sampling, 4) Patterns always contain pure patterns, deformations and distortions, and 5) When modeled correctly, patterns show a large amount of conditional independence. SSM uses the principles of pattern theory to adhere to this manifesto and to learn geometric morphometrical characteristics of shapes under study.

Shape analysis in medical imaging encode geometric and intensity variation of objects and are more specifically known as statistical shape and statistical appearance models respectively. SSMs have been pioneered by Cootes and Taylor for modeling 2D shapes [8], and applied to 3D shapes by Blanz and Vetter [9] adding a reflectance and appearance model. SSMs have gained widespread use in computer vision and medical image analysis for modeling computed tomography (CT) and magnetic resonance imaging (MRI) data. A review of the field of medical image analysis lists more than 50 studies targeting a model-based segmentation for real-world medical applications [10]. These types of models are computed as the average of samples in a training set, with the model being representative of shape (SSM) and intensity (SAM) variation within the training set.

A variety of handcrafted shape features are reported in the literature [10]; however, the most commonly used descriptor is point distribution. Thus, we start with the concept of **point distribution models (PDMs)**. PDMs are the statistical models of shape and its variation derived from a given training or sample set of shapes. Considering that we have n shapes (after removing scale, location, and rotation) with N discrete geometric landmarks in each sample, then each shape is represented as a vector $S_i \in \mathbb{R}^{3N}$ and can be defined as:

$$S_i = (x_{i1}, x_{i2}, \dots, x_{iN}, y_{i1}, y_{i2}, \dots, y_{iN}, z_{i1}, z_{i2}, \dots, z_{iN})^T \quad \text{where } (i = 1 \dots n)$$

However, to build PDMs requires a basic assumption that the data points within shapes are in **one-to-one correspondence** with each other. That means that the k th landmark point in all the shapes represent the same anatomical point. Establishing accurate correspondence among similar features of training examples is of critical importance, especially in medical applications, and for that, image-based or mesh-based techniques are used [11]. For SSMs, the central challenge is bringing the dataset into anatomical correspondence and the choice of the most representative template of the collection of objects. Correspondence definition can range from the simpler case of identifying portions of the objects that are geometrically similar, to the more complex problem of relating elements that represent the same parts or serve the same function on the objects. These matching parts, however, may differ significantly in their geometry, structure within the context of the whole object, or even topology. Registration is the most viable methodology to obtain such dense correspondence in both computer vision and medical imaging field (see section 4.2.2).

Applying a standard multivariate statistic to model a probability distribution over these shapes with the assumption that shape variations can be modeled as **normal distributions** such that,

$$S \sim \mathcal{N}(\mu, \Sigma)$$

The mean μ and covariance Σ around the mean is given by:

$$\mu = \frac{1}{n} \sum_{i=1}^n S_i$$

$$\Sigma = \frac{1}{n-1} \sum_{i=1}^n (S_i - \mu) (S_i - \mu)^T$$

In geometric shapes, the number of points representing each shape (N) is very large and hence the covariance matrix above is unrealistically huge and difficult to tackle computationally. To resolve this, dimensionality reduction techniques are typically applied. One such technique is **Principal Component Analysis (PCA)**. PCA describes the data in a linearized space obtained through a global basis transformation and provides a parametric representation of the distribution. In other terms, PCA represents a shape distribution in terms of the mean shape and the deformation around this mean shape learned from the example dataset. This is represented as:

$$S = \bar{\mu} + \sum_{i=1}^n \alpha_i \sqrt{Evec_i Eval_i}$$

Where $(Evec_i, Eval_i)$ are the i th eigenvectors and eigenvalues of covariance matrix Σ and $\alpha_i \sim \mathcal{N}(0,1)$.

4.2.2 Registration

Registration tries find the optimal transformation that best aligns the structures of interest from reference shape to target shape or images and requires the selection of a feature space, a transformation type, similarity measure and search or optimization strategy [12]. The feature space can be raw voxels, intensity gradient, voxel intensity statistical information or features extracted from the image (points, edges, contours, graphs, surfaces and volumes). While the above constitute intrinsic features, extrinsic features can include fiducial markers placed surgically on the body prior to imaging. And while the trend is towards methods based on properties of individual voxels (largely due to a reduction in computational cost in recent times), surface-based methods that rely on segmentation of image objects, and subsequent alignment are also popular given their intuitiveness [13].

While rigid registration in geometric shapes is limited to orientation or principal axes matching, it forms the first and unavoidable step in performing non-rigid registration. Non-rigid registration is a technique of identifying portions of an image, a volume or a shape that are geometrically similar and relating elements that represent the same parts or serve the same function. Being a generalized mathematical it is largely used in robotics, computer vision and computer graphics for applications as diverse as optical hand-written character recognition [14], interpolation of intermediate frames in cartoon animation [15], human body or face motion tracking [16, 17]. It is also used in the medical imaging field for example to recover and analyze motion of the heart [18], to map the brain [19], in radiotherapy to allow tracking the progress of a tumour [20] or in surgical planning to be able to analyze a target structure and optimize the approach [21]. As mentioned above, non-rigid registration requires to compute the spatial transformation which maps each point of an image (or shape) onto its corresponding point on target image (or shape) and recovering the dense correspondence between both [22]. When it comes to technologies for shape registration, it is a process of determining the correspondence of features between shape samples. It facilitates viewing the structural variations of shapes in the same coordinate system and with same knowledge about the standard shape. This information is further used in either analyzing the pathology or disease in comparison with the standard or normal image or building statistical shape models of structural variations.

Non-rigid registration algorithms can be categorized as those targeting the image itself and its intensity, and those that target shapes and their properties. For image-intensity based registration, there are two common procedures: searching the optimization in the space of legal geometrical transformations with varying the transformation parameters or searching the optimization in the space of possible correspondences [23]. For feature-based methods, either silhouettes or a point-sets can be used. In the first case registration consists in representing the shape with a parametrized closed-curve or surface [24], in the second case correspondence is estimated relying on a distance criteria [25], or an underlying model used to represent the point-set [26] or following a decision tree [27]. In the second category, shapes are described by point-set or volume or surface or landmarks. The procedure for shape-based non-rigid registration is different because it requires to estimate a bijective point-to-point correspondence between the point-sets. This is famously known as point-set registration.

Studies and articles that focus on non-rigid registration of point-sets describe several methods that differ in terms of different aspects. The first aspect is the deformation model which defines the space of transformations allowed. Then when applying a transformation to the moving scene, one has to evaluate the similarity between the deformed shape and the original static model, and the resolution of the registration problem consists in optimizing the distance between these two shapes. The similarity measure depends on the objective function chosen to be minimized. But to evaluate the objective function between two shapes, a discrete point to point association has to be established, this is what is called correspondence. To determine this correspondence, one can consider the deterministic closest point or the probabilistic closest point, or normal or curvature information about the shapes. In terms of results, algorithms have to be compared according to their sensitivity to noise and outliers or missing parts, their sensitivity to local minima in the optimization process and the performance has to be evaluated on the outputs with figures of merit, Hausdorff distances and dice coefficient.

Non-linear transformations problems remain an unsolved problem [28] and remain at the forefront of registration research given the requirements of multi-modal fusion, multi-subject image registration and recently, imiomics [29]. In relation to statistical models, the choice of reference is important during the establishment of correspondence through registration. Selecting one specific instance from the sample leads to the obvious problem of bias induced by the choice of reference, making it difficult to reveal cross-class variability [54]. Only through a simultaneous examination of a whole set of objects from a particular class can one learn which features are important and the obvious route then becomes groupwise registration [30]. A second concern is that pairwise registration does not permit the simultaneous registration of all images in single optimization procedure, which prevents considering all image information simultaneously [29].

4.2.3 Gaussian Process Morphable Models

GPMMs in the current state of the art of statistical modelling, were pioneered by Dr Marcel Lüthi, and are a continuous generalization of SSM representations using PCA [31-33]. **Gaussian processes** generalize multivariate normal distributions to distributions over functions, and in GPMMs the functions modelled are deformations from a reference image/shape to another using a Gaussian process:

$$GP(\mu, K)$$

with mean function $\mu: \Omega \rightarrow \mathbb{R}^3$ and covariance (or kernel) function [31, 34] $K: \Omega \times \Omega \rightarrow \mathbb{R}^{3 \times 3}$.

Standard PCA based models represent just one special case of such a covariance function but any valid kernel function represents a probabilistic model of deformations. By exchanging the covariance function, a variety of different modelling techniques that have been developed independently such as free form deformations or various spline models, can be derived. From a conceptual point of view, this is very efficient since by a simple exchange of the kernel function, various shape models can be invoked. The combination of a statistical model and standard kernels from machine learning, can be used to reduce the bias of a statistical model; make models more local by breaking the global correlations; enable spatially varying kernel methods; and crucially for this project, model deformations on multiple scale levels [31]. This has allowed the formulation of classical non-rigid registration as the problem of fitting a Gaussian Process model, and thus to unify the concepts of shape model fitting and that of non-rigid image registration [31, 35]. The inherent probabilistic nature of Gaussian Processes appears to be ideal for many problems in medical image analysis. For example, Gaussian Process regression can be used to obtain full probabilistic models after constraining them, e.g. to interpolate given features. GPMMs have shown state of the art performance for shape modelling, and shape registration [31].

4.3 Rationale for understanding Clinical Utility of scapula SSM

For glenohumeral pathologies, clinicians typically use external palpation strategies along with range of motion tests to determine the extent of the injury/deformity [36, 37]. Surgeons on the other hand rely mostly on virtual palpations using 3D imaging for pre-surgical planning [38-40]. In the events such as recurrent posterior shoulder dislocation due to excessive glenoid retroversion, glenoid osteotomy is the choice of treatment/intervention. However, surgical processes for glenohumeral deformity corrections are becoming more and more computerized [41] and thus need patient-specific shoulder joint models created from radiographic imaging in order to analyze the morphology as well as to pre-determine the course of action during the actual surgical procedure. In all these processes, developing a quick, accurate, reliable, and patient specific shoulder model becomes a very important phenomenon [42, 43]. With the advent of statistical methods in medical image analysis, it is now possible to build and use statistical shape and appearance models for biological shapes [3, 4]. However, the ability to use these models in a clinical setting for patient-specific outcomes is not yet explored. SSMs can be effective only if they have improved clinical utility.

Previously, SSM has been used in a few biomechanical studies involving knee and hip joints [44-46], but has not been used in shoulder joints. Previous research on shoulder SSMs was focused on building methodological pipelines to build SSMs and did not evaluate these models in terms of their clinical validity [22, 47, 48]. **Computational robustness of an SSM can be checked through the measures of specificity, generality, and compactness [22, 49-52]. However, this does not automatically prove the clinical validity of the model as these measures do not specifically target clinically relevant areas.** Furthermore, shape fitting algorithms typically use a certain set of anatomical landmarks during the fitting process without considering the clinical relevance or efficacy of using such landmarks sets. Clinical validity on the other

hand can be determined by evaluating the SSM validation in the region of clinical relevance (for e.g., anatomical landmarks) [36]. **Thus, in order to prove their clinical validity, the tests of robustness and clinical validity must be mutually exhaustive.**

The objective of the study, reported here, was to illustrate a) whether an SSM augmented with anatomical landmarks performs better fitting and provides improved clinical utility over non-augmented SSM and b) which anatomical landmark sets provide best augmentation strategy. **For the scope of this study, the term ‘clinical utility’ was defined as the accuracy with which the scapular SSM can 1) achieve the goodness of fit in the glenoid region of scapular bone, and 2) predict the anatomical angles associated with this region.** We hypothesize that a categorical landmark selection process based on the glenoid region as a region of interest would improve the clinical utility of the scapular SSM in terms of goodness of fit and anatomical measurements. Objectives of the study are achieved by comparing the use of non-augmented SSM with three augmented SSMs for illustrating improvements in clinical utility. One of the three augmented SSMs was proposed earlier by Borotikar et al. [53] but whether it improves clinical utility in surgical planning of the glenoid region was not reported.

4.4 Materials and Methods

A total 33 dry scapulae bones were used in this study. The bone data consisted of two sets, one with 27 bones and another with six bones. A set of 27 dry bones were imaged using the SIEMENS SOMATOM Definition AS (Siemens Medical Solutions, Forchheim, Germany) scanner with a resolution of 0.96mm X 0.96mm X 0.6mm. Data for the remaining six bones were acquired from multiple resources that used various CT scanners with a maximum resolution of 0.4mm X 0.4mm X 1.5mm. A radiologist checked all the images for their anatomical integrity. For all the scapulae, signs of trauma were the only exclusion criteria and no demographical data were available.

4.4.1 SSM Development

Using a set of images for 27 bones, an SSM of scapula was developed. The methodology employed to develop the SSM is already been published [22], however is briefly explained here for clarity (Figure 1).

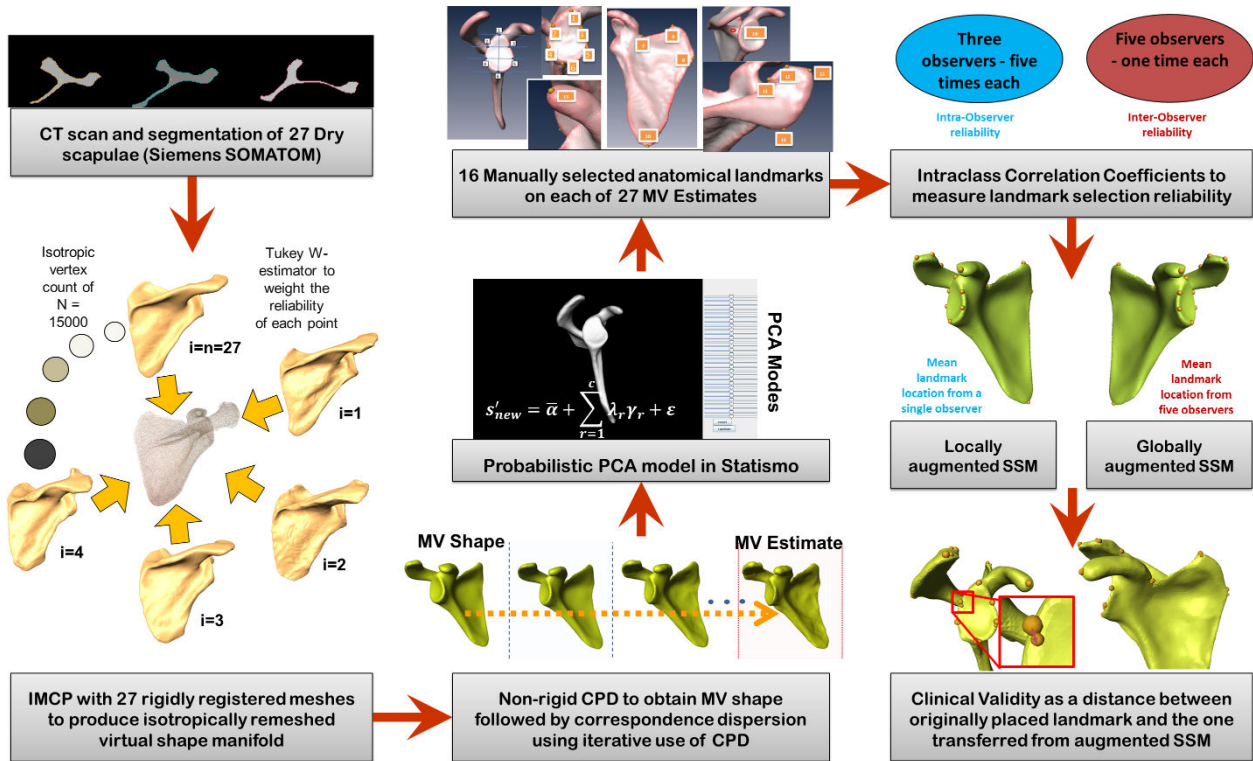


Figure 4. 1: A schematic diagram showing the methodology used to determine clinical validity of an augmented statistical shape model of the adult scapula bone. First, a statistical shape model of an adult scapula bone was built using 27 dry scapulae and following a previously published methodology [22]. Sixteen anatomical landmarks in clinically relevant regions of scapula were selected by multiple observers, tested for their reliability of selection, and used to augment the statistical shape model. Clinical validity was quantified as a distance between a manually selected anatomical landmark on original scapula instance and a landmark transferred from an augmented (locally or globally) statistical shape model.

All the preprocessing and segmentation was performed in Amira v5.4.3 (Visage Imaging: <http://www.vsg3d.com/>). For each segmented CT volume, a 3D surface mesh was extracted from the labeled images. The meshes were then smoothed and remeshed to have isotropic vertices with the vertex count set at $N = 15000$. Using the Iterative Median Closest Point (IMCP) algorithm, an intrinsic and unbiased consensus shape was established. In this groupwise rigid registration based algorithm [54], each sample was registered on a virtual form representing the consensus of the correspondence information in all the data (Figure 1). For each point in the data, robustly matching neighbor points were used to calculate a virtual corresponding point leading to the virtual shape building. By using a Tukey W-estimator to weigh the reliability of each point, a consensus emerged as a dense unorganized point cloud. This process eliminated the need for manual landmarking, region building and reference selection that induces bias. Making the intrinsic consensus shape as a reference, a non-rigid registration of the original data on the intrinsic consensus shape was performed using point set registration method called Coherence Point Drift (CPD) [55]. In this algorithm, the intrinsic consensus shape was refined and a principal component

analysis (PCA) was performed to obtain the mean from all the deformations. This 3D mean of the outcome of the CPD algorithm established the unbiased reference which was called as mean virtual (MV) shape (Figure 1). In the next step, CPD algorithm was iteratively used to transfer and optimize one-to-one correspondences of the MV shape on the original datasets to form MV estimates (Figure 1). Each of the MV estimates was a mesh of 15000 vertices in dense one-to-one correspondence with vertices of other instances and of the respective MV shape. Considering MV Estimates as the primary data, a probabilistic PCA was performed using a SCALISMO toolkit [56] and scapula SSM with size was developed (Figure 1).

This SSM will be referred to as $SSM_{\text{non-augmented}}$ throughout this study. Computational robustness of the $SSM_{\text{non-augmented}}$ has been reported earlier through the measures of generality, specificity, and compactness [22]. Briefly, compactness measures dimensionality reduction and reports model's ability to use as few shape parameters as possible to cover shape variability [50]. Generality measures a model's ability to represent unseen instances of the class of object [50]. This property highlights the capability of a model to fit to a new shape. Specificity measures the model's ability to generate instances of the species of objects similar to those in the training set [50].

4.4.2 Augmented SSM creation for comparisons

To fulfill the objectives of the study, three augmented SSMs were created: $\alpha SSM_{\text{proposed}}$, αSSM_{set1} , αSSM_{set2} . The $\alpha SSM_{\text{proposed}}$ was augmented with a proposed set of 16 clinically relevant anatomical landmarks (Figure 2) in the glenoid region [53] with previously evaluated inter- and intra-observer reliability for each landmark selection [53]. Specifically, 1) six landmarks were located on glenoid rim surrounding glenoid cavity (Figure 2a), 2) four landmarks were located on the medial and superior edges of Subscapular fossa (scapula blade) (Figure 2b), 3) four landmarks were located on the acromion (Figure 2c), 4) one landmark each was located on the coracoid process and the notch made by scapular spine with Supraspinous fossa (Figure 2d).

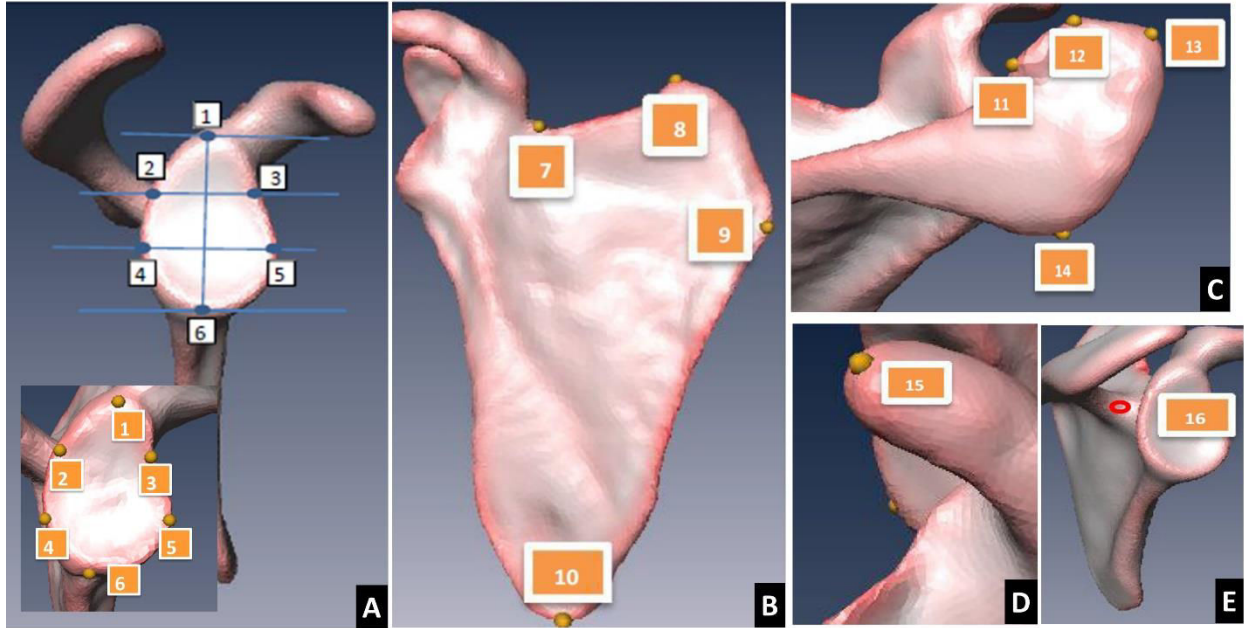


Figure 4. 2: Anatomical landmark locations on the scapular bone for proposed augmented SSM ($aSSM_{proposed}$). Sixteen landmarks were manually selected by three observers in clinically relevant regions of scapula. These include: A) six landmarks on the glenoid rim, B) four landmarks on the medial, superior and inferior edges of subscapular fossa, C) four landmarks on the acromion, D) one landmark on the coracoid process, and E) one on the notch made by scapular spine with Suprascapular fossa.

To illustrate the best augmentation strategy to improve fitting quality and clinical utility, two more sets of augmented SSMs ($aSSM_{set1}$ and $aSSM_{set2}$) having 16 anatomical landmarks each were created (Figure 3 and 4). Specifically, $aSSM_{set1}$ landmarks were selected without considering the clinical significance of their anatomical locations but covering the entire scapula shape. For $aSSM_{set2}$, no anatomical landmarks were selected in the glenoid cavity region (as against six landmarks in the $aSSM_{proposed}$ and three landmarks in $aSSM_{set1}$). In the hindsight, $aSSM_{set1}$ represented entire mapping of the scapular shape and $aSSM_{set2}$ represented scapular shape mapping when glenoid region is not accessible or damaged/morbid.

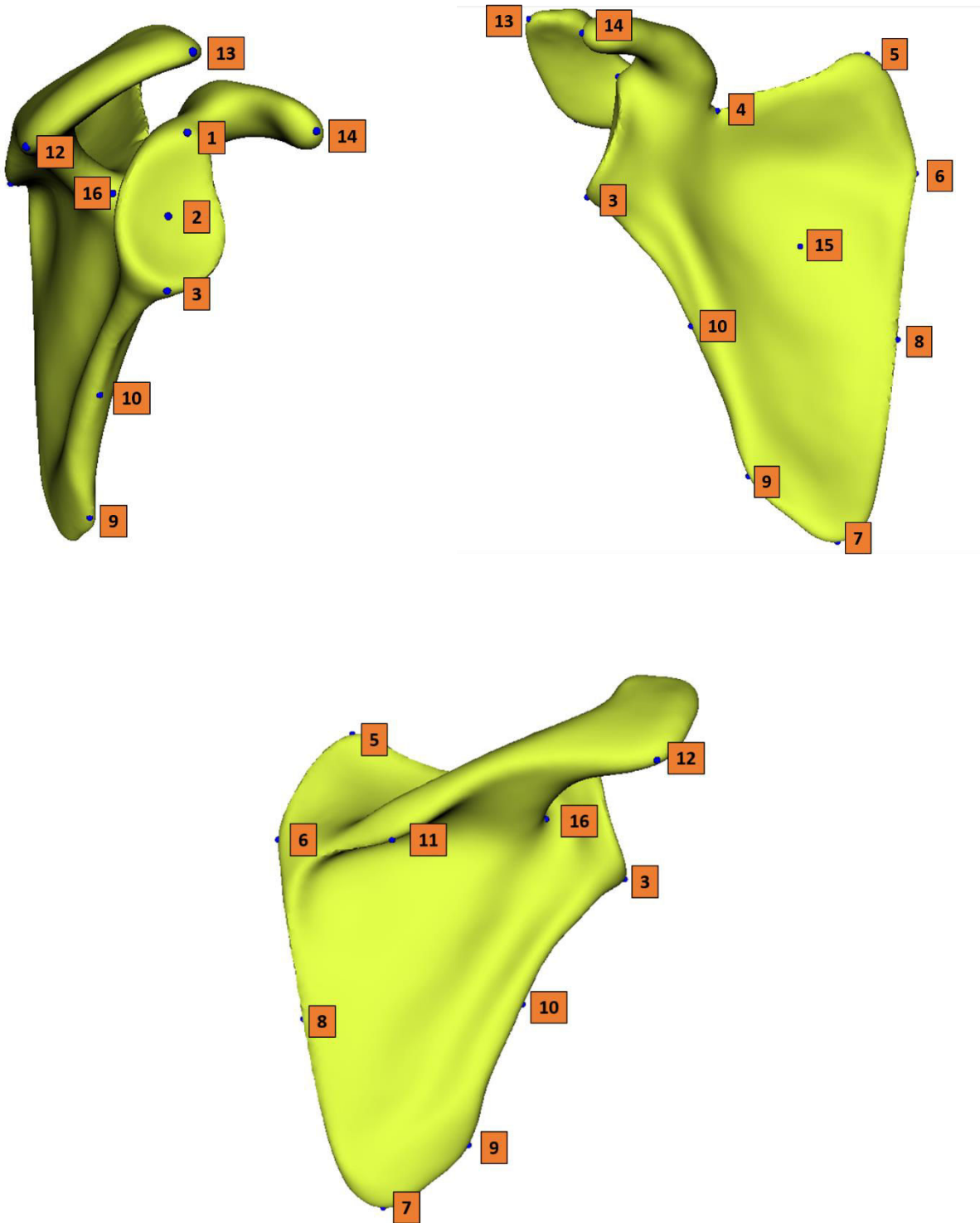


Figure 4. 3: Augmented SSM set1 (aSSMset1): Landmark set without considering clinical significance of landmark locations. Three landmarks were selected in the glenoid region and rest of the landmarks were equally distributed over the scapular shape to map the entire shape.

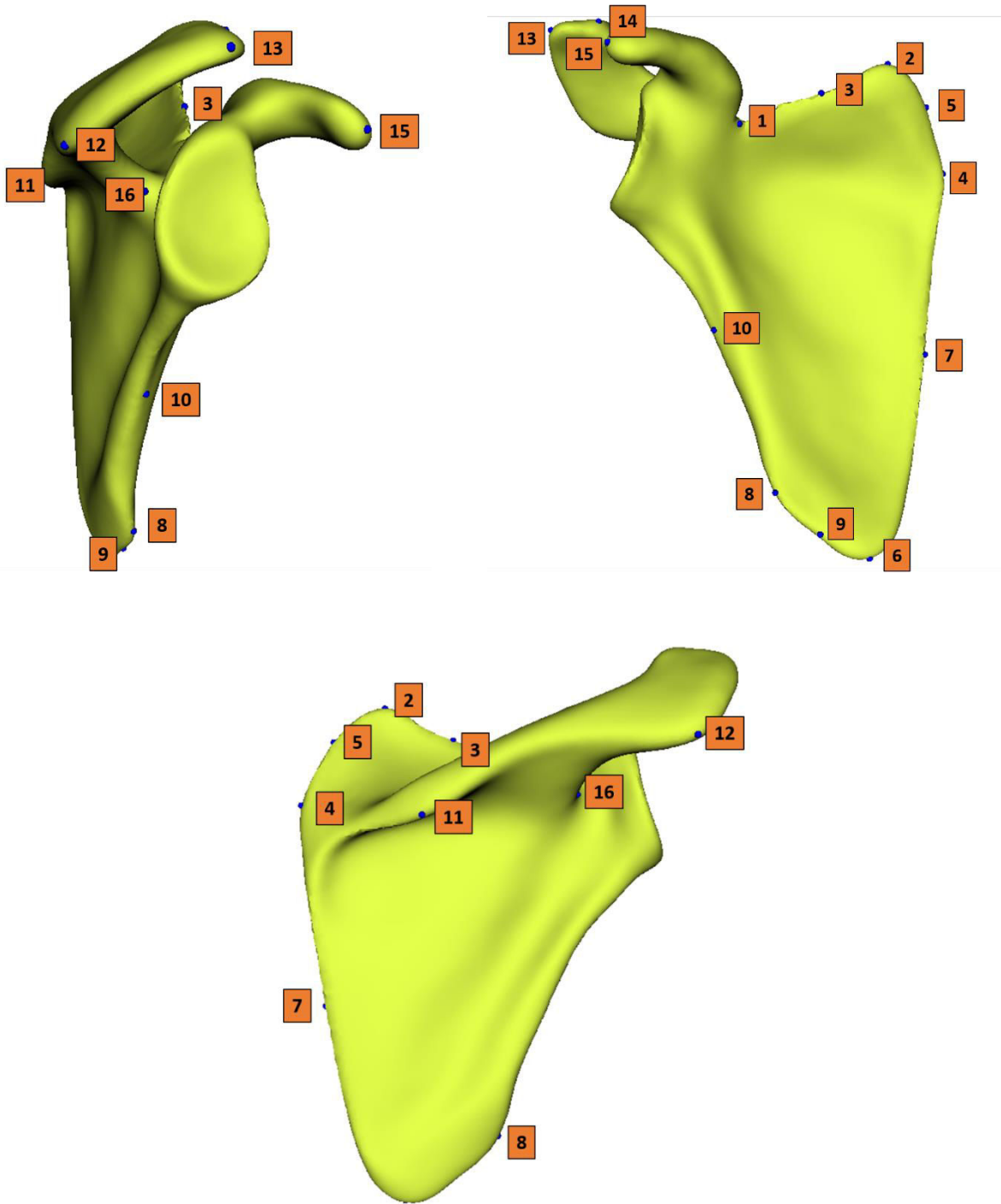


Figure 4. 4: Augmented SSM set2 (aSSMset2): Landmark set without considering clinical significance of landmark locations in the glenoid region. No landmarks were selected in the glenoid region and rest of the landmarks were equally distributed over the scapular shape to map the entire shape.

4.4.3 Intra- and inter-observer reliability

Inter- and intra-observer reliability analysis for anatomical landmark selection for proposed set is already performed and reported in a book chapter by Borotikar and colleagues [53]. For the purpose of completeness, similar analysis was performed on set1 and set2 on all 27 internal instances by two independent observers. For the intra-observer reproducibility evaluation, each observer repeated the landmark selection process two times per set. A time interval of 60 to 72 hours was allowed to expire between the trials while the order of instance selection was also randomized. Inter-observer reliability was defined by ICC, using a two-way mixed effects (choice of observers) analysis of variance (ANOVA) [57]. Intra-observer reproducibility was also defined by ICCs, using a two way ANOVA and considering the choice of the observer as fixed effects [57]. The Standard Error of Measurement ($SEM = SD * \sqrt{1-ICC}$, where SD is the standard deviation of the whole set of measures) was quantified for each set of landmark measurements. All the ICCs were obtained using Statistica (StatSoft, Inc., Paris, France).

4.4.4 Clinical Utility

Clinical utility was evaluated by fitting each of the augmented SSMs ($aSSM_{proposed}$, $aSSM_{set1}$, and $aSSM_{set2}$) and $SSM_{non-augmented}$ to six external scapulae (not used in SSM building) and comparing the predicted shape with the original shape (manually segmented from the CT scans) for fitting quality and anatomical measures in the glenoid region. The glenoid region of the scapula was identified by cutting the scapula through its surgical neck as previously described [58, 59]. The capability of $aSSM_{proposed}$ to fit to the glenoid region was compared with $aSSM_{set1}$ and $aSSM_{set2}$ and $SSM_{non-augmented}$. The fitting algorithm first performed rigid alignment of each SSM type (three augmented and $SSM_{non-augmented}$) to each of the external instances, followed by a one-time non-rigid (deformable) regression [60, 61]. A standard deformable model fitting algorithm (non-rigid iterative closest point) [62] was adopted in SCALISMO, an open source toolbox for creating and evaluating statistical shape algorithms [63].

Clinical utility was determined by quantifying the goodness of fit between the original glenoid region identified in the external scapulae and its predicted counterpart. The goodness of fit was quantified using three distance measures (mean distance, root mean square (RMS) distance, maximum (Hausdorff) distance [64]) and a similarity measure (Dice coefficient). Four anatomical measures associated with glenoid region were also selected. These include 1) Critical shoulder angle [65, 66], 2) Glenoid inclination [67], 3) Lateral acromion angle [68], and 4) glenopolar angle [69]. Differences between the original scapular shape and the predicted shape for each of the measures described above were first determined for each SSM type and termed as the prediction error. Prediction error for distance measures obtained from $SSM_{non-augmented}$, $aSSM_{set1}$, and $aSSM_{set2}$ was compared with $aSSM_{proposed}$ using paired student's T-tests. Prediction error for anatomical angle measures was qualitatively compared using absolute mean differences.

4.5 Results

4.5.1 Intra- and inter-observer reliability

Both the observers successfully completed the reliability tests for anatomical landmark selection for both the sets ($\alpha\text{SSM}_{\text{set1}}$, $\alpha\text{SSM}_{\text{set2}}$). Moderate to excellent ($\text{ICC} > 0.73$) intra- and inter-observer reliability was found for all X, Y and Z coordinates (Table 4.1, Table 4.3, and Table 4.5). The ICC for inter-observer reliability ranged from 0.74 to 0.98 for all the coordinates (Table 4.1). The ICC for intra-observer reproducibility for all the observers ranged from 0.79 to 0.96 for all the coordinates (Table 4.3 and Table 4.5). The SEM ranged from 0.05mm to 0.39mm for all intra- and inter-observer measurements (Table 4.2, Table 4.4, Table 4.6).

Table 4. 1: Inter-observer reliability interclass correlation coefficients (ICCs) in X, Y, and Z coordinates of anatomical landmarks selection for $\alpha\text{SSM}_{\text{set1}}$ and $\alpha\text{SSM}_{\text{set2}}$.

Landmark	X: Medial-Lateral		Y: Anterior-Posterior		Z: Superior-Inferior	
	$\alpha\text{SSM}_{\text{set1}}$	$\alpha\text{SSM}_{\text{set2}}$	$\alpha\text{SSM}_{\text{set1}}$	$\alpha\text{SSM}_{\text{set2}}$	$\alpha\text{SSM}_{\text{set1}}$	$\alpha\text{SSM}_{\text{set2}}$
1	0.96	0.91	0.92	0.94	0.93	0.91
2	0.74	0.90	0.82	0.89	0.91	0.93
3	0.96	0.80	0.92	0.74	0.98	0.80
4	0.76	0.77	0.83	0.87	0.84	0.82
5	0.97	0.82	0.85	0.81	0.89	0.76
6	0.74	0.92	0.86	0.85	0.86	0.88
7	0.92	0.79	0.96	0.80	0.91	0.74
8	0.74	0.82	0.76	0.84	0.77	0.87
9	0.85	0.85	0.87	0.75	0.90	0.84
10	0.76	0.79	0.74	0.74	0.77	0.77
11	0.85	0.81	0.78	0.75	0.82	0.75
12	0.85	0.82	0.91	0.90	0.88	0.89
13	0.91	0.88	0.93	0.87	0.92	0.91
14	0.95	0.89	0.93	0.92	0.95	0.81
15	0.73	0.91	0.74	0.90	0.76	0.87
16	0.85	0.83	0.87	0.84	0.92	0.88

Table 4. 2: Inter-observer Standard Error of Measurement (SEM) in mm in X, Y, and Z coordinates of anatomical landmarks selection for $\alpha\text{SSM}_{\text{set1}}$ and $\alpha\text{SSM}_{\text{set2}}$.

Landmark	X: Medial-Lateral		Y: Anterior-Posterior		Z: Superior-Inferior	
	$\alpha\text{SSM}_{\text{set1}}$	$\alpha\text{SSM}_{\text{set2}}$	$\alpha\text{SSM}_{\text{set1}}$	$\alpha\text{SSM}_{\text{set2}}$	$\alpha\text{SSM}_{\text{set1}}$	$\alpha\text{SSM}_{\text{set2}}$
1	0.26	0.19	0.25	0.32	0.16	0.27
2	0.37	0.09	0.18	0.19	0.25	0.30
3	0.13	0.14	0.35	0.14	0.11	0.27
4	0.27	0.10	0.05	0.19	0.29	0.21
5	0.15	0.12	0.20	0.09	0.13	0.24
6	0.27	0.14	0.19	0.10	0.35	0.16
7	0.28	0.20	0.20	0.37	0.14	0.31
8	0.07	0.08	0.30	0.38	0.30	0.12
9	0.13	0.36	0.16	0.25	0.11	0.29
10	0.12	0.37	0.31	0.08	0.14	0.12
11	0.27	0.22	0.21	0.14	0.08	0.18
12	0.33	0.22	0.06	0.18	0.24	0.27
13	0.16	0.17	0.11	0.33	0.28	0.32
14	0.31	0.36	0.29	0.07	0.23	0.09
15	0.27	0.18	0.21	0.07	0.19	0.37
16	0.05	0.10	0.10	0.12	0.26	0.32

Table 4. 3: Intra-observer reproducibility interclass correlation coefficients (ICCs) values in X, Y, and Z coordinates of anatomical landmarks for both the observers on $\alpha\text{SSM}_{\text{set1}}$.

Landmark	X: Medial-Lateral		Y: Anterior-Posterior		Z: Superior-Inferior	
	O - 1	O - 2	O - 1	O - 2	O - 1	O - 2
1	0.95	0.86	0.82	0.92	0.83	0.88
2	0.96	0.91	0.94	0.93	0.92	0.86
3	0.89	0.89	0.81	0.88	0.86	0.79
4	0.96	0.88	0.93	0.83	0.94	0.84
5	0.93	0.93	0.88	0.83	0.82	0.81
6	0.88	0.85	0.95	0.85	0.83	0.92
7	0.90	0.91	0.80	0.92	0.81	0.84
8	0.92	0.91	0.86	0.85	0.81	0.87
9	0.96	0.86	0.80	0.91	0.93	0.81
10	0.96	0.88	0.95	0.84	0.88	0.89
11	0.89	0.82	0.79	0.93	0.88	0.83
12	0.96	0.82	0.92	0.86	0.81	0.90
13	0.96	0.88	0.92	0.84	0.93	0.90
14	0.92	0.91	0.93	0.85	0.89	0.91
15	0.95	0.93	0.80	0.89	0.84	0.86
16	0.89	0.83	0.85	0.87	0.87	0.80

Table 4. 4: Intra-observer Standard Error of Measurement (SEM) in mm in X, Y, and Z coordinates of anatomical landmarks for both the observers on $\alpha\text{SSM}_{\text{set1}}$.

Landmark	X: Medial-Lateral		Y: Anterior-Posterior		Z: Superior-Inferior	
	O - 1	O - 2	O - 1	O - 2	O - 1	O - 2
1	0.25	0.13	0.31	0.09	0.22	0.29
2	0.26	0.11	0.30	0.27	0.27	0.19
3	0.25	0.25	0.14	0.14	0.22	0.30
4	0.33	0.10	0.24	0.19	0.35	0.18
5	0.13	0.21	0.23	0.25	0.13	0.27
6	0.27	0.21	0.22	0.17	0.10	0.18
7	0.14	0.30	0.31	0.26	0.10	0.28
8	0.10	0.20	0.14	0.18	0.09	0.27
9	0.24	0.18	0.16	0.25	0.18	0.17
10	0.20	0.25	0.10	0.26	0.20	0.13
11	0.20	0.27	0.33	0.19	0.17	0.28
12	0.26	0.21	0.25	0.08	0.28	0.32
13	0.29	0.17	0.20	0.16	0.25	0.16
14	0.17	0.12	0.25	0.19	0.29	0.25
15	0.26	0.23	0.22	0.15	0.33	0.19
16	0.19	0.15	0.25	0.13	0.34	0.29

Table 4. 5: Intra-observer reproducibility interclass correlation coefficients (ICCs) values in X, Y, and Z coordinates of anatomical landmarks for both the observers on $\alpha\text{SSM}_{\text{set2}}$.

Landmark	X: Medial-Lateral		Y: Anterior-Posterior		Z: Superior-Inferior	
	O - 1	O - 2	O - 1	O - 2	O - 1	O - 2
1	0.89	0.89	0.85	0.83	0.92	0.94
2	0.93	0.82	0.87	0.87	0.88	0.90
3	0.92	0.94	0.93	0.95	0.88	0.84
4	0.94	0.94	0.84	0.94	0.95	0.85
5	0.94	0.93	0.95	0.82	0.84	0.96
6	0.88	0.83	0.92	0.87	0.94	0.81
7	0.92	0.92	0.89	0.89	0.94	0.89
8	0.86	0.89	0.90	0.88	0.93	0.83
9	0.84	0.97	0.86	0.92	0.85	0.97
10	0.92	0.92	0.89	0.91	0.87	0.93
11	0.90	0.94	0.95	0.85	0.88	0.89
12	0.89	0.88	0.90	0.88	0.92	0.89
13	0.94	0.88	0.90	0.81	0.85	0.82
14	0.91	0.95	0.86	0.97	0.92	0.92
15	0.91	0.82	0.89	0.83	0.85	0.81
16	0.94	0.83	0.91	0.82	0.91	0.82

Table 4. 6: Intra-observer Standard Error of Measurement (SEM) in mm in X, Y, and Z coordinates of anatomical landmarks for both the observers on $\alpha\text{SSM}_{\text{set2}}$.

Landmark	X: Medial-Lateral		Y: Anterior-Posterior		Z: Superior-Inferior	
	O - 1	O - 2	O - 1	O - 2	O - 1	O - 2
1	0.25	0.17	0.08	0.26	0.05	0.10
2	0.09	0.11	0.09	0.22	0.28	0.32
3	0.27	0.21	0.23	0.27	0.21	0.26
4	0.31	0.16	0.18	0.26	0.31	0.17
5	0.18	0.35	0.10	0.11	0.19	0.11
6	0.28	0.34	0.18	0.09	0.17	0.19
7	0.20	0.07	0.09	0.37	0.26	0.20
8	0.09	0.29	0.06	0.10	0.11	0.09
9	0.10	0.14	0.27	0.06	0.18	0.24
10	0.16	0.19	0.20	0.23	0.28	0.12
11	0.24	0.23	0.29	0.33	0.20	0.17
12	0.26	0.35	0.23	0.26	0.27	0.24
13	0.26	0.18	0.20	0.11	0.24	0.13
14	0.13	0.36	0.26	0.17	0.20	0.14
15	0.19	0.15	0.28	0.20	0.11	0.25
16	0.07	0.83	0.31	0.82	0.22	0.82

4.5.2 Clinical Validity

The fitting algorithm was able to successfully deform each of the SSMs to the six external scapular shapes (Figure 4.5). Prediction error for all the distance measures (goodness of fit) was significantly lower for $\text{SSM}_{\text{non-augmented}}$ than the three augmented SSMs (Figure 4.6) except for maximum distance. Dice coefficient was significantly higher for $\alpha\text{SSM}_{\text{proposed}}$ compared to all other SSM types (Figure 4.6). Prediction error in terms of absolute mean difference for clinical angles was lowest using the $\alpha\text{SSM}_{\text{proposed}}$ for critical shoulder

angle, glenoid inclination, and lateral acromion angle (Table 4.7, Table 4.8, and Table 4.9). Whereas, for the glenopolar angle, the absolute mean difference was lowest using $SSM_{\text{non-augmented}}$ (Table 4.10).

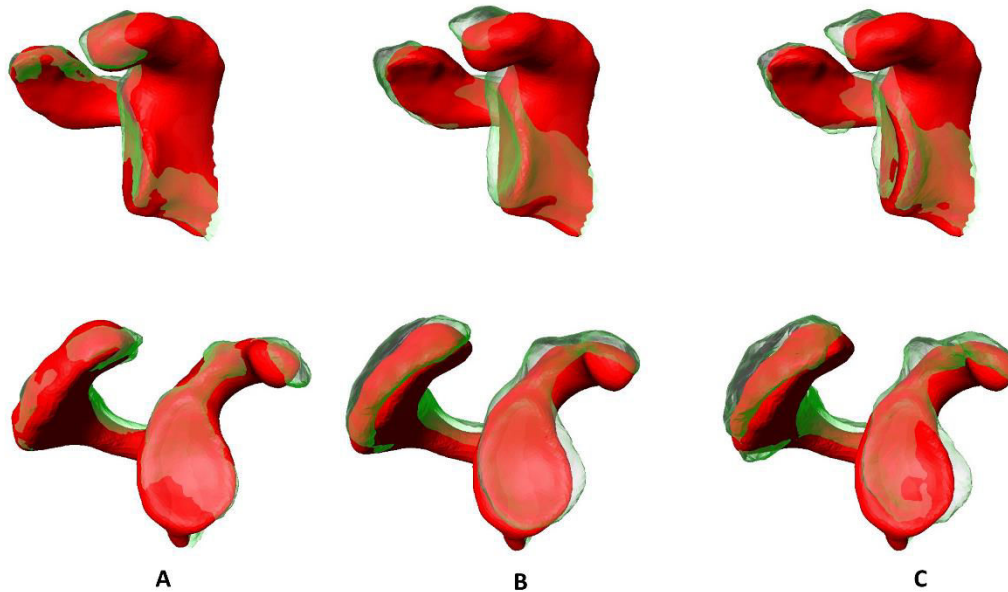


Figure 4. 5: Sample goodness of fit in the glenoid region for three augmented SSMs. Red color indicates original shape while the transparent green color indicates predicted shape after performing one-time non-rigid deformation for each augmented SSM. Two views for each fit are shown for each fitting where: A) Fitting result for $\alpha SSM_{\text{proposed}}$, B) Fitting results for αSSM_{set1} , and C) Fitting results for αSSM_{set2}

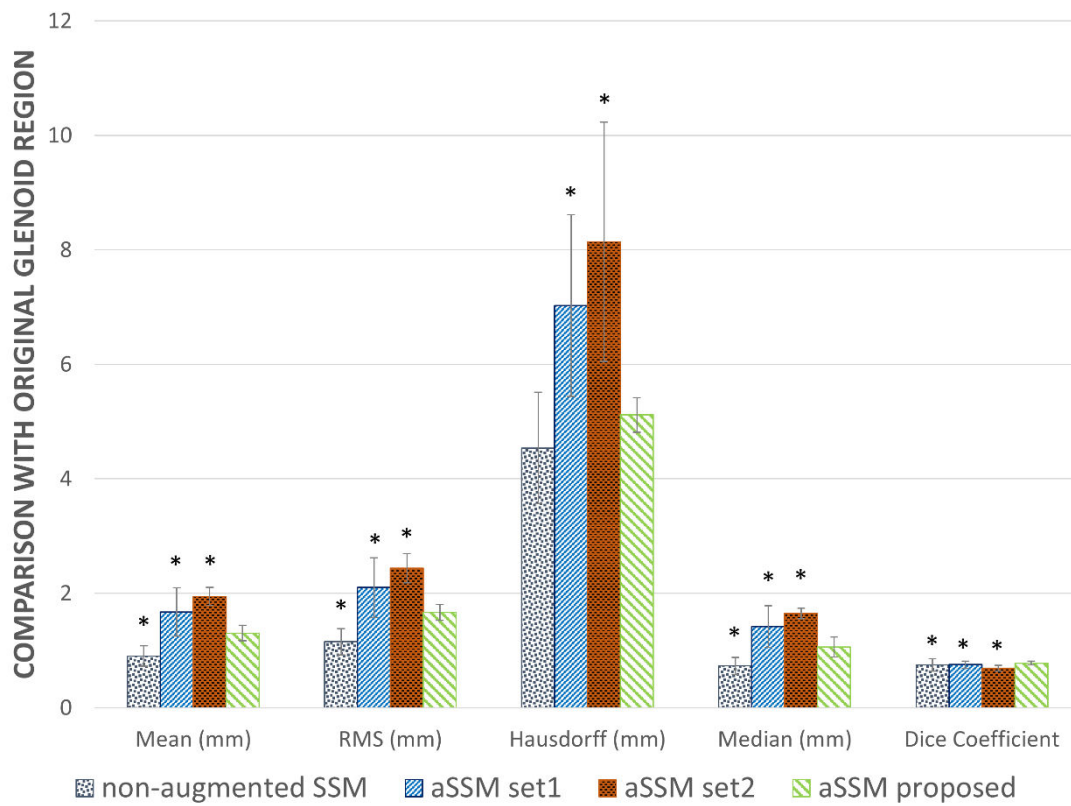


Figure 4. 6: Comparing the four SSMs (non-augmented SSM, augmented SSM proposed, augmented SSM set1, and augmented SSM set2) for their fitting quality to predict the glenoid region. The graph shows the performance of each SSM type quantified using the mean measures of distance and similarity from six external scapulae. Error bars on each column indicate ± 1 SD from the mean value. Significance was established when $p \leq 0.05$ and indicated using * above the bar graph. RMS: Root Mean Square distance, Hausdorff: Hausdorff distance metric used to report maximum distance between original and predicted shapes [64].

4.6 Discussion

This preliminary study highlighted the importance of using the scapula SSM augmented with categorically selected anatomical landmarks for the glenoid region, in pre-surgery planning tools. The results of this study reported that $SSM_{non-augmented}$ performed better in the goodness of fit measures whereas $aSSM_{proposed}$ performed better in determining anatomical angle measures that are clinically relevant. In doing so, this study also illustrated improvements in clinical utility when mapping of the glenoid region by anatomical landmarks was increased stepwise from landmark set 2 (no glenoid landmarks) to set 1 (three glenoid landmarks) and to proposed set (six glenoid landmarks).

Table 4. 7: Prediction error in the critical shoulder angle in terms of individual angle differences between angle obtained from the original shape and the angle predicted by each SSM type.

Anatomical Measure	Critical Shoulder Angle (°)									
	Original Scapula	SSM _{non-augmented}	Prediction error	α SSM _{proposed}	Prediction error	α SSM _{set1}	Prediction error	α SSM _{set2}	Prediction error	
Scap1	27.6	24.5	-3.1	26.0	-1.6	29.2	1.6	26.6	-1.0	
Scap2	47.2	34.9	-12.3	35.9	-11.3	32.7	-14.5	33.1	-14.1	
Scap3	27.7	32.7	5.0	28.4	0.7	29.0	1.3	28.3	0.6	
Scap4	34.0	31.7	-2.3	32.7	-1.3	33.4	-0.6	31.9	-2.1	
Scap5	36.6	33.5	-3.1	34.2	-2.4	33.1	-3.5	31.4	-5.2	
Scap6	27.0	31.4	4.4	30.3	3.3	31.0	4.0	30.7	3.7	
Mean Measure	33.35	31.45		31.25		31.40		30.33		
SD	7.17	3.32		3.39		1.80		2.22		
Absolute Mean Difference		5.03		3.43		4.25		4.45		
Min difference		2.30		0.70		0.60		0.60		
Max difference		12.30		11.30		14.50		14.10		

Table 4. 8: Prediction error in the glenoid inclination angle in terms of individual angle differences between angle obtained from the original shape and the angle predicted by each SSM type.

Anatomical Measure	Glenoid inclination (°)								
	Scapula Name	Original Scapula	SSM _{non-augmented}	Prediction error	α SSM _{proposed}	Prediction error	α SSM _{set1}	Prediction error	α SSM _{set2}
Scap1	68.0	73.7	5.7	71.0	3.0	69.0	1.0	71.3	3.3
Scap2	80.5	83.8	3.3	79.5	-1.0	83.6	3.1	83.3	2.8
Scap3	72.5	71.7	-0.8	73.0	0.5	74.4	1.9	78.9	6.4
Scap4	70.6	67.6	-3.0	74.6	4.0	79.8	9.2	80.3	9.7
Scap5	69.1	70.3	1.2	74.7	5.6	73.6	4.5	76.5	7.4
Scap6	73.6	71.8	-1.8	74.8	1.2	76.6	3.0	84.0	10.4
Mean Measure	72.38	73.15		74.60		76.17		79.05	
SD	4.09	5.11		2.57		4.65		4.30	
Absolute Mean Difference		2.63		2.55		3.78		6.67	
Min difference		0.80		0.50		1.00		2.80	
Max difference		5.70		5.60		9.20		10.40	

Table 4. 9: Prediction error in the lateral acromion angle in terms of individual angle differences between angle obtained from the original shape and the angle predicted by each SSM type.

Anatomical Measure	Lateral acromion angle (°)									
	Original Scapula	<i>SSM_{non-augmented}</i>	Prediction error	<i>αSSM_{proposed}</i>	Prediction error	<i>αSSM_{set1}</i>	Prediction error	<i>αSSM_{set2}</i>	Prediction error	
Scap1	93.8	99.9	6.1	87.0	-6.8	88.2	-5.6	100.0	6.2	
Scap2	82.2	86.7	4.5	84.6	2.4	87.1	4.9	88.8	6.6	
Scap3	76.6	81.3	4.7	80.2	3.6	86.5	9.9	86.9	10.3	
Scap4	76.1	81.8	5.7	78.6	2.5	81.5	5.4	85.1	9.0	
Scap5	85.5	82.2	-3.3	87.1	1.6	88.3	2.8	83.6	-1.9	
Scap6	89.1	83.7	-5.4	86.4	-2.7	83.3	-5.8	87.9	-1.2	
Mean Measure	83.88	85.93		83.98		85.82		88.72		
SD	6.39	6.50		3.37		2.55		5.33		
Absolute Mean Difference		4.95		3.27		5.73		5.87		
Min difference		3.30		1.60		2.80		1.20		
Max difference		6.10		6.80		9.90		10.30		

Table 4. 10: Prediction error in the glenopolar angle in terms of individual angle differences between angle obtained from the original shape and the angle predicted by each SSM type.

Anatomical Measure	Glenopolar angle (°)								
	Original Scapula	<i>SSM_{non-augmented}</i>	Prediction error	<i>αSSM_{proposed}</i>	Prediction error	<i>αSSM_{set1}</i>	Prediction error	<i>αSSM_{set2}</i>	Prediction error
Scap1	36.6	37.5	0.9	34.5	-2.1	38.2	1.6	34.9	-1.7
Scap2	47.4	42.4	-5.0	42.2	-5.2	37.7	-9.7	37.8	-9.6
Scap3	39.2	38.8	-0.4	36.9	-2.3	36.9	-2.3	32.8	-6.4
Scap4	44.2	44.1	-0.1	38.0	-6.2	34.4	-9.8	32.6	-11.6
Scap5	43.6	41.4	-2.2	36.1	-7.5	39.3	-4.3	35.7	-7.9
Scap6	39.5	39	-0.5	36.2	-3.3	34.8	-4.7	29.4	-10.1
Mean Measure	41.75	40.53		37.32		36.88		33.87	
SD	3.64	2.29		2.42		1.77		2.66	
Absolute Mean Difference		1.52		4.43		5.40		7.88	
Min difference		0.10		2.10		1.60		1.70	
Max difference		5.00		7.50		9.80		11.60	

Findings from the intra- and inter-observer reliability indicated that anatomical landmarks can be specified with excellent repeatability and reproducibility on image-based 3D bone models, however this may become a time-consuming task. A 3D patient specific scapular bone model derived from an augmented SSM could improve the accuracy and success ratio of shoulder surgeries to a great extent as it would present the surgeon with an opportunity to visually understand the subject specific morphology. Such a model, when clinically validated, may also be able to simulate the surgical procedure when used in a surgical planning tool such as BLUEPRINT (Tornier surgical solutions, www.tornierblueprint.com). This study also lays a foundation for an accurate and reliable pipeline development of augmented SSMs for automatic segmentation of bone structures from medical images. Results of ICCs for landmark selection achieved similar levels for all the three landmark sets, which provided another indirect reliability measure. Also, both the reliability measures were lower for landmarks that were not anatomically defined (landmarks 8, 10, and 15 in set1 or landmarks 3, 5, 7, 9, and 10 in set2). Thus, we do not recommend selecting these landmarks when creating an augmented SSM.

Results of prediction error in determining anatomical angle measures highlighted higher performance of the α SSM_{proposed} while revealing a pattern of fitting. For SSM_{non-augmented}, prediction errors were on both the negative and positive side of the original angle value for all the angles. But for augmented SSMs, the glenoid inclination was almost always overpredicted and the glenopolar angle was almost always underpredicted. This could be attributed to the position of landmarks in the augmented SSMs constraining the fitting in these regions and making it over or under predict.

State-of-the-art glenoid pre-surgery planning tools incorporate automatic 3D reconstruction of medical images using scapula SSMs. The fitting algorithm uses intensity information or landmark information derived from images. In these cases, anatomical landmarks play a crucial role either by providing an initial alignment or generating a posterior model for a recursive fitting algorithm. **The objectives and results of this preliminary study do not intend to prove that α SSM_{proposed} has sufficient accuracy for its use in a pre-surgical planning tool. However, it provides a clear distinction and a necessary rationale and validation for not relying only on the goodness of fit or SSM robustness (generality, specificity, compactness) measures when using the SSM for pre-surgical planning.**

Evaluating the efficacy of the fitting algorithm was not in the scope of this study. Since similar fitting algorithm and related parameters were used across the four SSM types in terms of initiation, level of fitting, and the number of vertices, the fitting errors were deemed equal and not affecting the analysis. Future efforts will be focused on enhancing the accuracy of fitting algorithms. Furthermore, checking the accuracy of partial or missing data was not in the scope of this paper, however, the augmented SSM would be used in this context in future studies. This study posed certain limitations: 1) the sample sufficiency in building the scapula SSM with 27 dry bones was not evaluated, which could reflect in errors while fitting the SSM to new data. 2) clinical utility was illustrated in only six external instances which may not cover all the variations of the glenoid region. Thus, further evaluations in the statistical stability of the SSM and completeness in terms of sample sufficiency are warranted.

In conclusion, the utility of SSM for its use in clinical applications is an under-evaluated problem. The goodness of fit and prediction errors in anatomical measures reported in this study presents the rationale of using augmented SSMs in the clinical setting and has a direct correlation with clinical accuracy. This study also lays a foundation for the development of an accurate and reliable methodology for the automatic segmentation of bone structures from medical images.

4.7 Chapter 4 References

- [1] G. P. Batchelor, Edwards, P.J., King, A.P., "3D Medical Imaging," in *3D Imaging, Analysis and Applications*, N. Pears, Liu, Y., Bunting, P., Ed., ed London: Springer-Verlag, 2012, pp. 445-495.
- [2] N. Sarkalkan, J. H. Waarsing, P. K. Bos, H. Weinans, and A. A. Zadpoor, "Statistical shape and appearance models for fast and automated estimation of proximal femur fracture load using 2D finite element models," *J Biomech*, vol. 47, pp. 3107-14, Sep 22 2014.
- [3] N. Sarkalkan, H. Weinans, and A. A. Zadpoor, "Statistical shape and appearance models of bones," *Bone*, vol. 60, pp. 129-40, Mar 2014.
- [4] T. Heimann and H. P. Meinzer, "Statistical shape models for 3D medical image segmentation: a review," *Med Image Anal*, vol. 13, pp. 543-63, Aug 2009.
- [5] P. Pratt, E. Mayer, J. Vale, D. Cohen, E. Edwards, A. Darzi, *et al.*, "An effective visualisation and registration system for image-guided robotic partial nephrectomy," *Journal of Robotic Surgery*, vol. 6, pp. 23-31, 2012/03/01 2012.
- [6] E. Stindel, J. L. Briard, P. Merloz, S. Plaweski, F. Dubrana, C. Lefevre, *et al.*, "Bone morphing: 3D morphological data for total knee arthroplasty," *Comput Aided Surg*, vol. 7, pp. 156-68, 2002.
- [7] A. M. Peter and A. Rangarajan, "Information geometry for landmark shape analysis: unifying shape representation and deformation," *IEEE Trans Pattern Anal Mach Intell*, vol. 31, pp. 337-50, Feb 2009.
- [8] T. F. Cootes, C. J. Taylor, D. H. Cooper, and J. Graham, "Active Shape Models-Their Training and Application," *Computer Vision and Image Understanding*, vol. 61, pp. 38-59, 1995/01/01 1995.
- [9] V. Blanz and T. Vetter, "A morphable model for the synthesis of 3D faces," in *Proceedings of the 26th annual conference on Computer graphics and interactive techniques*, 1999, pp. 187-194.
- [10] T. Heimann and H.-P. Meinzer, "Statistical shape models for 3D medical image segmentation: A review," *Medical image analysis*, vol. 13, pp. 543-563, 2009.
- [11] S. Bonaretti, C. Seiler, C. Boichon, M. Reyes, and P. Büchler, "Image-based vs. mesh-based statistical appearance models of the human femur: Implications for finite element simulations," *Medical Engineering and Physics*, vol. 36, pp. 1626-1635.
- [12] F. P. Oliveira and J. M. R. Tavares, "Medical image registration: a review," *Computer methods in biomechanics and biomedical engineering*, vol. 17, pp. 73-93, 2014.
- [13] J. P. Pluim, J. A. Maintz, and M. A. Viergever, "Mutual-information-based registration of medical images: a survey," *IEEE transactions on medical imaging*, vol. 22, pp. 986-1004, 2003.
- [14] J. Ma, J. Zhao, J. Tian, Z. Tu, and A. L. Yuille, "Robust Estimation of Nonrigid Transformation for Point Set Registration," in *2013 IEEE Conference on Computer Vision and Pattern Recognition*, 2013, pp. 2147-2154.
- [15] D. Sykora, J. Dingliana, and S. Collins, "As-rigid-as-possible image registration for hand-drawn cartoon animations," presented at the Proceedings of the 7th International Symposium on Non-Photorealistic Animation and Rendering, New Orleans, Louisiana, 2009.

- [16] Y. Wang, M. Gupta, S. Zhang, S. Wang, X. Gu, D. Samaras, *et al.*, "High Resolution Tracking of Non-Rigid Motion of Densely Sampled 3D Data Using Harmonic Maps," *International Journal of Computer Vision*, vol. 76, pp. 283-300, March 01 2008.
- [17] M. Zollhofer, M. Niessner, S. Izadi, C. Rehmann, C. Zach, M. Fisher, *et al.*, "Real-time non-rigid reconstruction using an RGB-D camera," *ACM Trans. Graph.*, vol. 33, pp. 1-12, 2014.
- [18] R. Bhagalia, J. D. Pack, J. V. Miller, and M. Iatrou, "Nonrigid registration-based coronary artery motion correction for cardiac computed tomography," *Med Phys*, vol. 39, pp. 4245-54, Jul 2012.
- [19] H. Chui, L. Win, R. Schultz, J. S. Duncan, and A. Rangarajan, "A unified non-rigid feature registration method for brain mapping," *Med Image Anal*, vol. 7, pp. 113-30, Jun 2003.
- [20] N. Chitphakdithai, V. L. Chiang, and J. S. Duncan, "Non-rigid registration of longitudinal brain tumor treatment MRI," *Conf Proc IEEE Eng Med Biol Soc*, vol. 2011, pp. 4893-6, 2011.
- [21] H. Elhawary, S. Oguro, K. Tuncali, P. R. Morrison, S. Tatli, P. B. Shyn, *et al.*, "Multimodality non-rigid image registration for planning, targeting and monitoring during CT-guided percutaneous liver tumor cryoablation," *Academic radiology*, vol. 17, pp. 1334-1344, 2010.
- [22] T. Mutsvangwa, V. Burdin, C. Schwartz, and C. Roux, "An automated statistical shape model developmental pipeline: application to the human scapula and humerus," *IEEE Trans Biomed Eng*, vol. 62, pp. 1098-107, Apr 2015.
- [23] A. Valsecchi, S. Damas, and J. Santamaria, "Evolutionary Intensity-based Medical Image Registration: A Review," *Current Medical Imaging Reviews*, vol. 9, pp. 283-297, // 2013.
- [24] L. J. Latecki, R. Lakamper, and T. Eckhardt, "Shape descriptors for non-rigid shapes with a single closed contour," in *Proceedings IEEE Conference on Computer Vision and Pattern Recognition. CVPR 2000 (Cat. No. PR00662)*, 2000, pp. 424-429 vol.1.
- [25] D. P. Huttenlocher, G. A. Klanderman, and W. J. Rucklidge, "Comparing images using the Hausdorff distance," *IEEE Transactions on Pattern Analysis and Machine Intelligence*, vol. 15, pp. 850-863, 1993.
- [26] H. Chui and A. Rangarajan, "A new point matching algorithm for non-rigid registration," *Computer Vision and Image Understanding*, vol. 89, pp. 114-141, 2003/02/01/ 2003.
- [27] T. K. Leung, M. C. Burl, and P. Perona, "Finding faces in cluttered scenes using random labeled graph matching," in *Proceedings of IEEE International Conference on Computer Vision*, 1995, pp. 637-644.
- [28] M. A. Viergever, J. A. Maintz, S. Klein, K. Murphy, M. Staring, and J. P. Pluim, "A survey of medical image registration—under review," ed: Elsevier, 2016.
- [29] R. Strand, F. Malmberg, L. Johansson, L. Lind, M. Sundbom, H. Ahlström, *et al.*, "A concept for holistic whole body MRI data analysis, Imiomics," *PLoS one*, vol. 12, p. e0169966, 2017.
- [30] T. Mutsvangwa, V. Burdin, C. Schwartz, and C. Roux, "An Automated Statistical Shape Model Developmental Pipeline: Application to the Human Scapula and Humerus," *Biomedical Engineering, IEEE Transactions on*, vol. 62, pp. 1098-1107, 2015.
- [31] M. Lüthi, T. Gerig, C. Jud, and T. Vetter, "Gaussian process morphable models," *IEEE transactions on pattern analysis and machine intelligence*, 2017.

- [32] M. Lüthi, C. Jud, T. Gerig, and T. Vetter, "Gaussian Process Morphable Models," *arXiv preprint arXiv:1603.07254*, 2016.
- [33] M. Lüthi, C. Jud, and T. Vetter, "A unified approach to shape model fitting and non-rigid registration," in *Machine learning in medical imaging*, ed: Springer, 2013, pp. 66-73.
- [34] J. Dölz, T. Gerig, M. Lüthi, H. Harbrecht, and T. Vetter, "Error-Controlled Model Approximation for Gaussian Process Morphable Models," *Journal of Mathematical Imaging and Vision*, October 24 2018.
- [35] J. Dölz, T. Gerig, M. Lüthi, H. Harbrecht, and T. Vetter, "Error-Controlled Model Approximation for Gaussian Process Morphable Models," *Journal of Mathematical Imaging and Vision*, pp. 1-15, 2018.
- [36] G. Gomes, Van Cauter, S., De. Beule, M., Vigneron, L., Pattyn, C., Audenaert, E., "Patient-specific modelling in orthopedics: from image to surgery.," in *Lecture Notes in Computational Vision and Biomechanics*, ed: Springer, 2013, pp. 109-129.
- [37] D. Paley, "Normal Lower Limb Alignment and Joint Orientation," in *Principles of Deformity Correction*, ed: Springer Berlin Heidelberg, 2002, pp. 1-18.
- [38] R. Nizard, "Computer assisted surgery for total knee arthroplasty," *Acta Orthop Belg*, vol. 68, pp. 215-30, Jun 2002.
- [39] R. A. Siston, N. J. Giori, S. B. Goodman, and S. L. Delp, "Surgical navigation for total knee arthroplasty: a perspective," *J Biomech*, vol. 40, pp. 728-35, 2007.
- [40] Y. S. Yoon, A. J. Hodgson, J. Tonetti, B. A. Masri, and C. P. Duncan, "Resolving inconsistencies in defining the target orientation for the acetabular cup angles in total hip arthroplasty," *Clin Biomech (Bristol, Avon)*, vol. 23, pp. 253-9, Mar 2008.
- [41] O. Verborgt, M. Vanhees, S. Heylen, P. Hardy, G. Declercq, and R. Bicknell, "Computer navigation and patient-specific instrumentation in shoulder arthroplasty," *Sports Med Arthrosc*, vol. 22, pp. e42-9, Dec 2014.
- [42] G. Zheng, M. G. Ballester, M. Styner, and L.-P. Nolte, "Reconstruction of Patient-Specific 3D Bone Surface from 2D Calibrated Fluoroscopic Images and Point Distribution Model," in *Medical Image Computing and Computer-Assisted Intervention – MICCAI 2006*. vol. 4190, R. Larsen, M. Nielsen, and J. Sporring, Eds., ed: Springer Berlin Heidelberg, 2006, pp. 25-32.
- [43] G. Zheng and S. Schumann, "3D reconstruction of a patient-specific surface model of the proximal femur from calibrated x-ray radiographs: A validation study," *Medical Physics*, vol. 36, pp. 1155-1166, 2009.
- [44] N. Baka, M. de Bruijne, T. van Walsum, B. L. Kaptein, J. E. Giphart, M. Schaap, *et al.*, "Statistical shape model-based femur kinematics from biplane fluoroscopy," *IEEE Trans Med Imaging*, vol. 31, pp. 1573-83, Aug 2012.
- [45] L. Modenese, A. T. Phillips, and A. M. Bull, "An open source lower limb model: Hip joint validation," *J Biomech*, vol. 44, pp. 2185-93, Aug 11 2011.
- [46] C. Rao, C. K. Fitzpatrick, P. J. Rullkoetter, L. P. Maletsky, R. H. Kim, and P. J. Laz, "A statistical finite element model of the knee accounting for shape and alignment variability," *Med Eng Phys*, vol. 35, pp. 1450-6, Oct 2013.

- [47] Y. M. Yang, D. Rueckert, and A. M. Bull, "Predicting the shapes of bones at a joint: application to the shoulder," *Comput Methods Biomech Biomed Engin*, vol. 11, pp. 19-30, Feb 2008.
- [48] M. Mayya, S. Poltaretskyi, C. Hamitouche, and J. Chaoui, "Mesh correspondence improvement using Regional Affine Registration: Application to Statistical Shape Model of the scapula," *IRBM*, Epub July 2015.
- [49] R. H. Davies, "Learning shapes: Optimal models for analyzing natural variability " Ph.D., University of Manchester, 2002.
- [50] M. A. Styner, K. T. Rajamani, L. P. Nolte, G. Zsemlye, G. Szekely, C. J. Taylor, *et al.*, "Evaluation of 3D correspondence methods for model building," *Inf Process Med Imaging*, vol. 18, pp. 63-75, Jul 2003.
- [51] H. Hufnagel, X. Pennec, J. Ehrhardt, N. Ayache, and H. Handels, "Computation of a probabilistic statistical shape model in a maximum-a-posteriori framework," *Methods Inf Med*, vol. 48, pp. 314-9, 2009.
- [52] A. Rasoulouian, R. Rohling, and P. Abolmaesumi, "Group-wise registration of point sets for statistical shape models," *IEEE Trans Med Imaging*, vol. 31, pp. 2025-34, Nov 2012.
- [53] B. Borotikar, T. Mutsvangwa, V. Burdin, E. Ghorbel, M. Lempereur, S. Brochard, *et al.*, "Augmented Statistical Shape Modeling for Orthopaedic Surgery and Rehabilitation," in *Medical Image Analysis and Informatics: Computer-Aided Diagnosis and Therapy*, P. M. d. Azevedo-Marques, A. Mencattini, M. Salmeri, and R. M. Rangayyan, Eds., ed Florida, USA: CRC Press, Taylor and Francis Group, 2017, pp. 369-426.
- [54] J. J. Jacq, T. Cresson, V. Burdin, and C. Roux, "Performing accurate joint kinematics from 3-D in vivo image sequences through consensus-driven simultaneous registration," *IEEE Trans Biomed Eng*, vol. 55, pp. 1620-33, May 2008.
- [55] A. Myronenko and X. Song, "Point set registration: coherent point drift," *IEEE Trans Pattern Anal Mach Intell*, vol. 32, pp. 2262-75, Dec 2010.
- [56] M. Lüthi, R. Blanc, T. Albrecht, T. Gass, O. Goksel, P. Buchler, *et al.*, "Statismo - A framework for PCA based statistical models.," *The Insight Journal*, vol. 1, pp. 1-18, 2012.
- [57] P. E. Shrout and J. L. Fleiss, "Intraclass correlations: uses in assessing rater reliability," *Psychol Bull*, vol. 86, pp. 420-8, Mar 1979.
- [58] T. P. Goss, "Fractures of Scapula: Diagnosis and treatment," in *Disorders of the shoulder: Diagnosis and Management*, J. P. Iannotti and G. R. Williams, Eds., ed Philadelphia: Lippincott Williams & Wilkins, 1999, pp. 597-637.
- [59] F. H. Hardegger, L. A. Simpson, and B. G. Weber, "The operative treatment of scapular fractures," *J Bone Joint Surg Br*, vol. 66, pp. 725-31, Nov 1984.
- [60] M. Lüthi, T. Gerig, C. Jud, and T. Vetter, "Gaussian Process Morphable Models," *IEEE Transactions on Pattern Analysis and Machine Intelligence*, vol. 40, pp. 1860-1873, 2018.
- [61] M. Lüthi, C. Jud, and T. Vetter, "A Unified Approach to Shape Model Fitting and Non-rigid Registration," Cham, 2013, pp. 66-73.
- [62] P. J. Besl and N. D. McKay, "A method for registration of 3-D shapes," *IEEE Transactions on Pattern Analysis and Machine Intelligence*, vol. 14, pp. 239-256, 1992.

- [63] M. Lüthi. (2014). *SCALable Image analysis and Shape MOdelling*. Available: <https://github.com/unibas-gravis/scalismo>
- [64] M. Dubuisson and A. K. Jain, "A modified Hausdorff distance for object matching," in *Proceedings of 12th International Conference on Pattern Recognition*, 1994, pp. 566-568 vol.1.
- [65] B. K. Moor, S. Bouaicha, D. A. Rothenfluh, A. Sukthankar, and C. Gerber, "Is there an association between the individual anatomy of the scapula and the development of rotator cuff tears or osteoarthritis of the glenohumeral joint?: A radiological study of the critical shoulder angle," *Bone Joint J*, vol. 95-B, pp. 935-41, Jul 2013.
- [66] T. Suter, A. Gerber Popp, Y. Zhang, C. Zhang, R. Z. Tashjian, and H. B. Henninger, "The influence of radiographic viewing perspective and demographics on the critical shoulder angle," *J Shoulder Elbow Surg*, vol. 24, pp. e149-58, Jun 2015.
- [67] U. Kandemir, R. B. Allaire, J. T. Jolly, R. E. Debski, and P. J. McMahon, "The relationship between the orientation of the glenoid and tears of the rotator cuff," *J Bone Joint Surg Br*, vol. 88, pp. 1105-9, Aug 2006.
- [68] M. P. Banas, R. J. Miller, and S. Totterman, "Relationship between the lateral acromion angle and rotator cuff disease," *J Shoulder Elbow Surg*, vol. 4, pp. 454-61, Nov-Dec 1995.
- [69] M. Tucek, O. Nanka, J. Malik, and J. Bartonicek, "The scapular glenopolar angle: standard values and side differences," *Skeletal Radiol*, vol. 43, pp. 1583-7, Nov 2014.

Chapter 5

Subject-specific musculoskeletal models using a novel muscle attachment region prediction algorithm based on Statistical Shape Models

5.1 Introduction

As explained in Chapter 4, statistical shape modeling (SSM) can be used for deriving multiple subject-specific geometrical parameters and material properties of a bone including cortical bone thickness, bone mineral density, bone morphology, pre-morbid bone geometry, etc. Many of these parameters can then be used as an input to musculoskeletal modeling to make generic models more subject-specific. The research focus of this chapter is illustrating the capability of statistical shape modeling (SSM) in **determining subject-specific muscle insertion regions for scapula and humerus bones**. Then **integrating the muscle insertion prediction algorithm in a musculoskeletal model of shoulder joint in adults** and showing how these subject-specific parameters produce significantly different results than when the model is built from generic muscle insertion information. Although the framework developed in this thesis is generic and can be applied to any other bones in the human musculoskeletal system, I have applied it on our bones of interest – scapula and humerus. This chapter is written in a manuscript format as we are in the process of writing a manuscript for this research work. Thus section 5.1.1 provides an introduction and objectives of this work. Section 5.2 provides methods employed, followed by results and discussions in sections 5.3 and 5.4 respectively. Parts of this research work have been submitted and published in conferences. **Subject-specific muscle insertion algorithm framework was published in an IEEE EMBS conference in 2017 [1] whereas the effect of implementing subject-specific muscle insertions in a generic shoulder model is recently accepted as a conference abstract at an International Society of Biomechanics conference to be held in Calgary, Canada in July 2019**. This chapter combines both these works and it is presented as a stand-alone manuscript.

Musculoskeletal (MS) modeling provides insights into the normal or abnormal biomechanical behavior of human musculoskeletal system [2]. However, assumptions made about the input parameters (e.g., bone and muscle inertia, bone segment center of mass, muscle insertions and activations) while developing such models make them generic and limit their clinical utility. Incorporating subject-specific parameters in the musculoskeletal model has been reported to produce accurate or altered results in the predicted joint mechanics using musculoskeletal models [3]–[10]. Indeed, subject-specific parameters improve the

accuracy and feasibility of outcomes of the musculoskeletal models thereby increasing the clinical utility of such models. However, most of the studies focus on the lower limb musculoskeletal models while studies based on upper limb and shoulder joint models are scarce. Shoulder MS modeling faces a huge challenge of subject specificity. While retrieving the muscle model parameters like tendon slack length and optimal fiber lengths pose a challenge, other derivable parameters such as muscle origins and insertion sites are also always almost approximated. This considerably affects the muscle force and moment arm predictions [6] and thus cannot be effectively used for pre-surgical or for rehabilitation assessments.

Muscle origin/insertion regions alone can play an important role in incorporating subject specificity for accurate predictions. In their study, Song and colleagues found that incorporating subject-specific hip muscle attachments reported significantly different joint reaction forces (Song, 2018). Similarly, Charles and Anderst (ASB2017 abstract) showed that including subject-specific muscle parameters results in altered muscle contributions in the knee joint. To date, several methods have been published to create subject-specific muscle insertion geometries of upper and lower limbs. These include linear scaling [11], [12], non-linear scaling [13] and manual digitization [12]. However, the accuracy of such prediction still remains low for shoulder muscle insertions. Thus, it is important to develop a tool to accurately predict muscle origin/insertion regions on shoulder bones without manual intervention.

SSM [14], [15], uses the statistical variability of the 3D structures for applications such as registration (automatic segmentation or model fitting) to the new imaging data, predicting missing shape, evaluating 3D bone morphological characteristics etc. The data driven point distribution models used in the SSM building framework generate point-to-point correspondences between the SSM and the original training shapes used in SSM building. Thus, being in correspondence, each point on the SSM has a unique ID which corresponds to the same location on all the original shapes. This characteristic of the SSM can be effectively used to embed the SSM with muscle insertion regions. Further, during registering the SSM to a new shape, such regions can be effectively tracked. We used these characteristics of the SSM to develop a muscle insertion prediction algorithm.

Thus, the aim of this study was twofold. First, to develop an SSM based pipeline to incorporate statistical variability for predicting subject-specific muscle regions in shoulder muscles. Second, to integrate the algorithm with a previously developed shoulder musculoskeletal models using an imaging data on older adults and to illustrate its application in the prediction of altered joint mechanics, muscle forces, and muscle moment arms during a simulated shoulder joint motion. An open source toolbox SCALISMO (<https://github.com/unibas-gravis/scalismo>) was used in this study to create and perform functions related to SSM. We also report the concurrent validity of the muscle insertion region prediction on a randomly selected population of shoulder bones (scapula and humerus).

5.2 Materials and Methods

This section describes the generation of two augmented SSMs - scapula and humerus - with six muscles each, muscle insertion region prediction and determining its concurrent validity in five systematic steps. The augmented scapula SSM includes the scapular bone and six muscle origins and the augmented

humerus SSM includes the humeral bone and the same six muscle insertions. Muscle origins/insertions are attachment regions modeled by a subset of vertices called vertex identifiers (VIDs) lying on the mean shape of the bone SSM.

5.2.1 Bone SSM Development

A French database of dry bone samples (27 scapulae and 28 humeri) was used for building the bone SSMs. Radiographic images of each sample were first acquired, manually segmented (Amira, FEI, Hillsboro, V5.4) and surface mesh models of each sample were created. The SSMs were built using previously published Iterative Median Closest Point – Gaussian Mixture Model (IMCP-GMM) pipeline [16]. Briefly, this method first rigidly aligns and simultaneously registers surfaces creating a Virtual manifold (15,000 vertices). Second, a non-rigid registration including GMM gives a point-to-point correspondence between all the database and the Virtual Mean Shape (VMS). Finally, a Probabilistic Principal Component Analysis embedded the shape variations in scapular and humeral bone populations. The SSM quality was tested using generality, specificity, and compactness criteria.

5.2.2 Muscle region selection

For the glenohumeral joint, six muscles that play an important role in the shoulder motion and function were selected for this study. These include four rotator cuff muscles viz. Infraspinatus (I-S), Subscapularis (Subscap), Supraspinatus (Suprasp), and Teres Minor (T-Min) and abductor muscles Teres Major (T-Maj) and Deltoid (figure 5B and 5D for scapula; figure 6B and 6D for humerus). For each bone, surface mesh of the database in correspondence, origin/insertion regions of these six muscular attachments were identified and masked by two observers using Meshlab (<http://meshlab.sourceforge.net/>). Inter-rater reliability for two randomly selected muscles was quantified by comparing the area of each muscle region obtained by each expert on each bone. Reliability was also confirmed by quantifying dice similarity coefficient for each muscle region. Thus, for reliability measures, 54 instances of muscle regions for each six muscles were in correspondence for the scapula, and similarly 56 instances for the humerus.

5.2.3 Selection of Muscle attachment region on the SSM

Using the correspondence within the database, a subset of VIDs representative of each muscle was extracted from each original shape of the database. For each muscle this subset represented all the VIDs from all the original instances. The muscle insertion region representative of this original instance population was selected by a two-step process. In the first step, the frequency of appearance of the VIDs was set ranging from 100% to 50% at every 10% level and for each level, a muscle insertion region visualization on the bone SSM was created for each muscle (Figure 5.1 and 5.2). In the second step, two experts – a junior and a senior anatomist – were provided with all the levels of muscle insertion visualizations for each muscle and the experts independently selected which frequency-level best represented the realistic muscle insertion regions. The best frequency that represented the best average shape of the muscle under consideration was then selected to create augmented SSM embedded with muscle insertion region VIDs. Careful consideration was given to the neighboring muscle insertions where an overlapping problem may exist. Such an overlapping may happen on the boundary regions of the neighboring muscles, as I-S, T-Maj and T-Min muscles which have origins in scapula bone or as I-S and T-

Min insertion regions on humerus. This process provided not only a statistical atlas describing the bone geometry variations of the training set through the mean virtual shape (MVS) and through different modes of variation but also the locations of the included attachment sites.

5.2.4 Augmented SSM deformation to external bone shapes

The respective augmented SSMs were used to transfer the muscle attachment sites on respective new bone shapes (scapula and humerus). A method of non-rigid iterative closest point fitting [17] was used to non-rigidly deform the augmented SSM including landmarking for the initialization. The muscular attachment regions were transferred on the original external bone shape by projection of the VIDs selected as a muscle site in its fitted surface (deformed MVS by fitting). The external database was South African bones segmented from CT scans of patients. Ten scapulae and eight humeri were randomly selected to evaluate the proposed method for predicting subject-specific muscle origin/insertion.

5.2.5 Validation of muscle insertion region prediction

On each of the external bone shapes, the validation of the muscle regions prediction was determined in two different ways. First, an expert (clinician) visually confirmed whether the predicted muscle attachments were “anatomically feasible”. Second, a gold standard was built by manually masking the six muscular regions on the same ten original instances for scapulae (eight for humerus). In order to compare with the result of the region prediction, four similarity measures were calculated between the same muscular region (transferred from the augmented SSM and manually masked): (Mean Distance (MD), Root Mean Square(RMS), Hausdorff Distance (HD)) and similarity index (Dice coefficient).

5.2.6 Imaging database acquisition for building musculoskeletal model

Computed tomography (CT) scans of ten right shoulders were acquired from five female and five male subjects who provided informed consent (age 62 ± 16 years). This acquisition was performed at the University of Cape Town, South Africa, in collaboration with their department of BME. After checking for the joint integrity and absence of pathology by the radiologists, 3D geometries of the humerus and scapula were reconstructed using the medical image software Mimics (Materialise, Leuven, Belgium).

5.2.7 Newcastle shoulder model (NSM) adaptation

Previously developed augmented SSMs (bone + muscle insertion/origin regions) for scapula and humerus bones (section 5.2.4) were non-rigidly registered [1] to the new shapes using a custom-made Gaussian regression algorithm in an open source toolbox called Scalismo [18]–[20]. During the regression process, the muscle insertion regions for six shoulder muscles viz. Deltoid, Supraspinatus, Infraspinatus, Subscapularis, Teres Major, Teres Minor, were automatically tracked and predicted on the new shapes [1]. A 3D biomechanical computer model, the NSM, was used for this study [21]. The NSM (Figure 3) represents a normal shoulder and includes six rigid bone segments (thorax, clavicle, scapula, humerus, radius and ulna). These segments are connected at the sternoclavicular (3 degrees of freedom, DoF), acromioclavicular (3 DoF), glenohumeral (3 DoF) and elbow (2 hinge) joints. Scapulothoracic and clavicle kinematics are simulated during the motions. This kinematic data were based on regression equations derived from the measurement of healthy subjects [22]. The model includes 31 muscles and 3 ligaments

of the upper extremity that are divided into 90 lines of action representing the anatomic muscle division into fascicles. An adapted Hill muscle model [23] is used to derive the limits of the force generating capacity of each muscle during a prescribed motion. These limits are then used by an inverse dynamic load-sharing algorithm, that minimizes physiological cost, to calculate muscle and joint contact forces.

Using a 3D biomechanical computational model, the NSM [21], shoulder movement simulations were performed for two model constructs for each subject. For the first construct, generic muscle insertions (those manually adjusted in the model) were used and for the second construct, algorithm predicted insertions were used. Abduction and scapular plane elevation motions were simulated. Changes in the joint contact forces, muscle moment arms, and muscle forces were compared between the two constructs for each subject using a student's t-test with statistical parametric mapping (SPM) [24].

5.3 Results

5.3.1 Intra- and inter-observer reliability

Excellent intra-class correlation coefficient (ICC) for inter-rater reliability was reported for the two muscle origin/insertion regions on scapula bone (I-S (ICC = 0.927) and T-Maj (ICC = 0.942)), as well as, on the humerus bone (I-S (ICC = 0.981) and T-Maj (ICC = 0.962)). Dice coefficient ranged from 0.821 to 0.987 indicating a high region similarity between observers.

5.3.2 Augmented SSM building

Muscle VIDs of all the original instances were extracted and successfully converted into frequency level representations from 100% to 50% for each muscle and for each bone (Figure 5.1 and 5.2). These were then transferred to the experts for the selection. Best frequency level selections are reported in table 1 for both the bones. The combination of the VIDs with the retained frequency and the Bone SSM forms the augmented SSM with muscle insertions. Validity of muscle deformations along with the deformations of augmented SSMs was visually confirmed for first seven principal components in both the bones and for all the muscles (Figure 5.3 and 5.4). This step also confirmed that there was no overlapping taking place between the neighboring muscle boundaries.

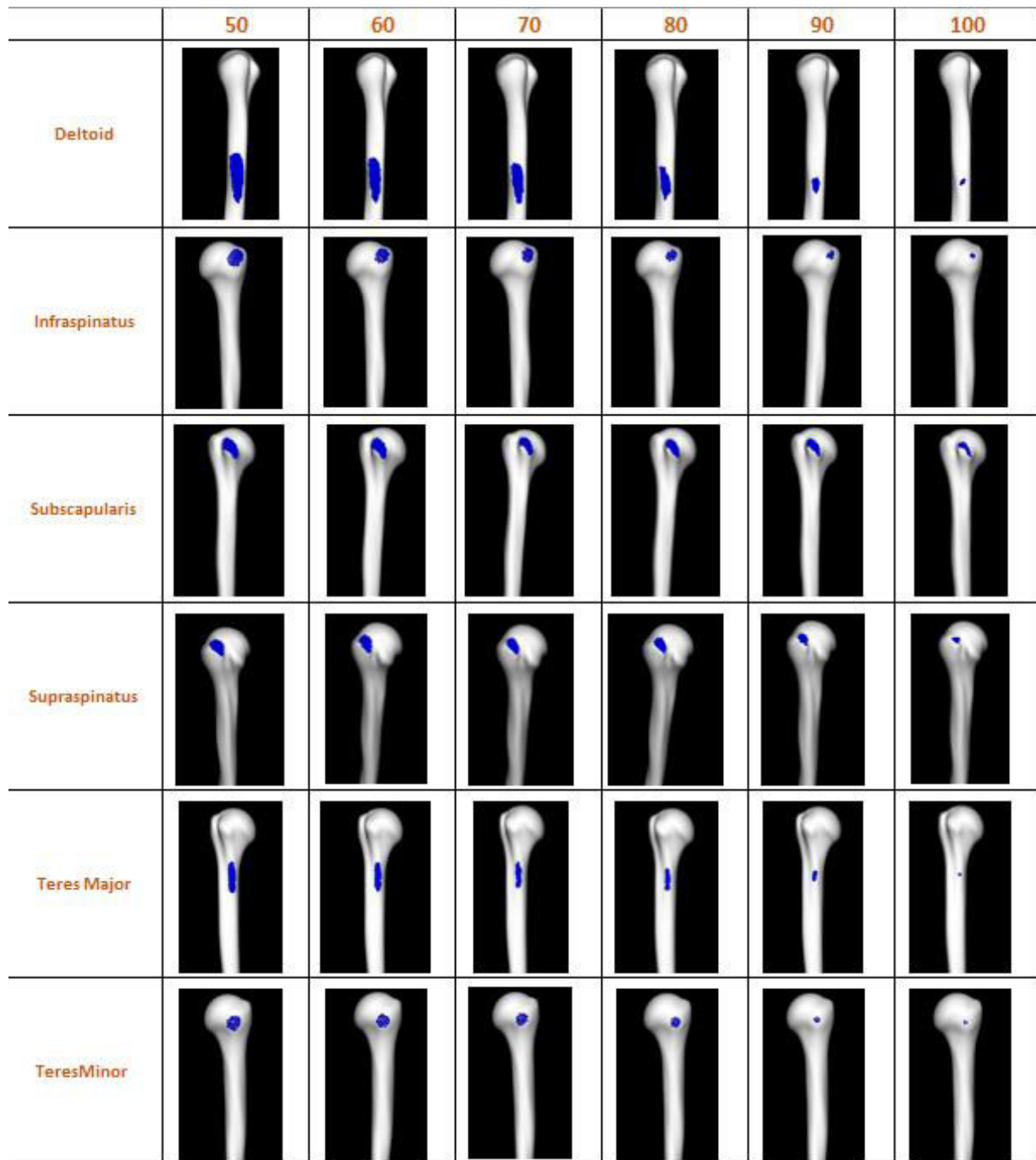


Figure 5. 1: Frequency level representations of muscle insertion VIDs on humerus for all six muscles. Frequency levels ranged from 50% to 100%.

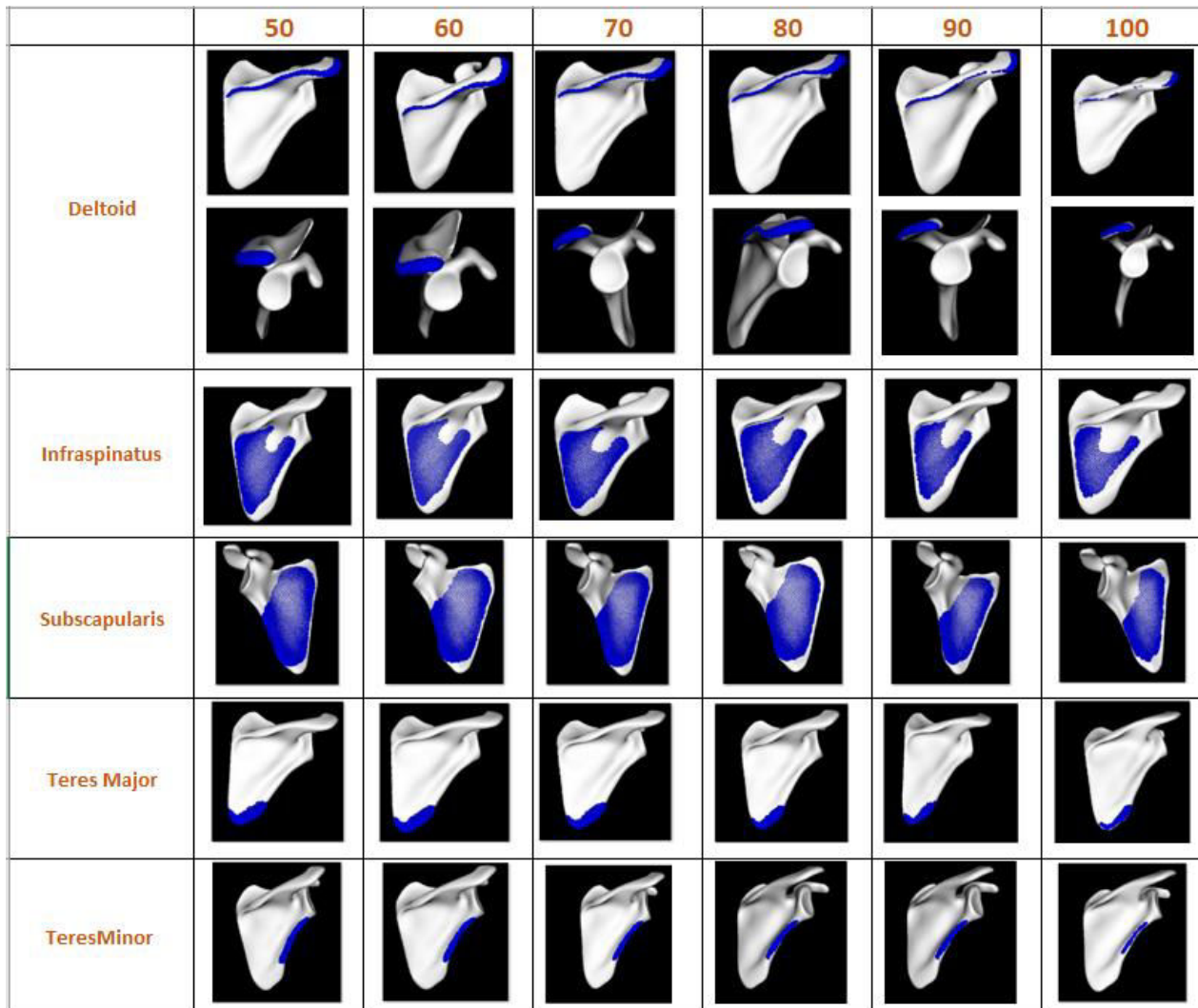


Figure 5. 2: Frequency level representations of muscle insertion VIDs on humerus for all six muscles. Frequency levels ranged from 50% to 100%.

Table 5. 1: Selected frequency levels by experts for scapula and humerus muscle insertions

Muscle Name	Humerus	Scapula
Deltoid	50	80
Infraspinatus	70	70
Subscapularis	80	80
Supraspinatus	90	60
Teres Major	80	100
Teres Minor	70	100

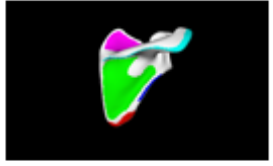
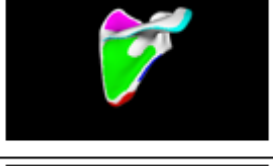
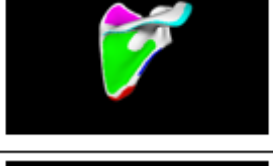
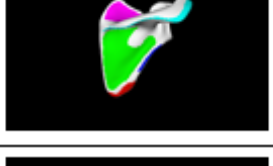
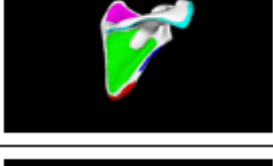
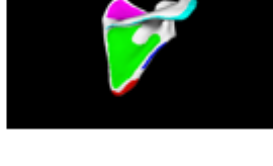
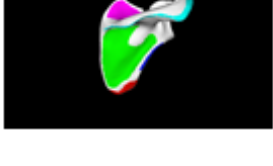
Mode	-3SD	Mean	+3SD
mode 1			
mode 2			
mode 3			
mode 4			
mode 5			
mode 6			
mode 7			

Figure 5. 3: Visualization of first seven principal modes of variation of an augmented scapula bone SSM on its posterior muscle insertions. As can be seen from the figure, the boundary conditions between adjacent muscles are obeyed in all the variations.

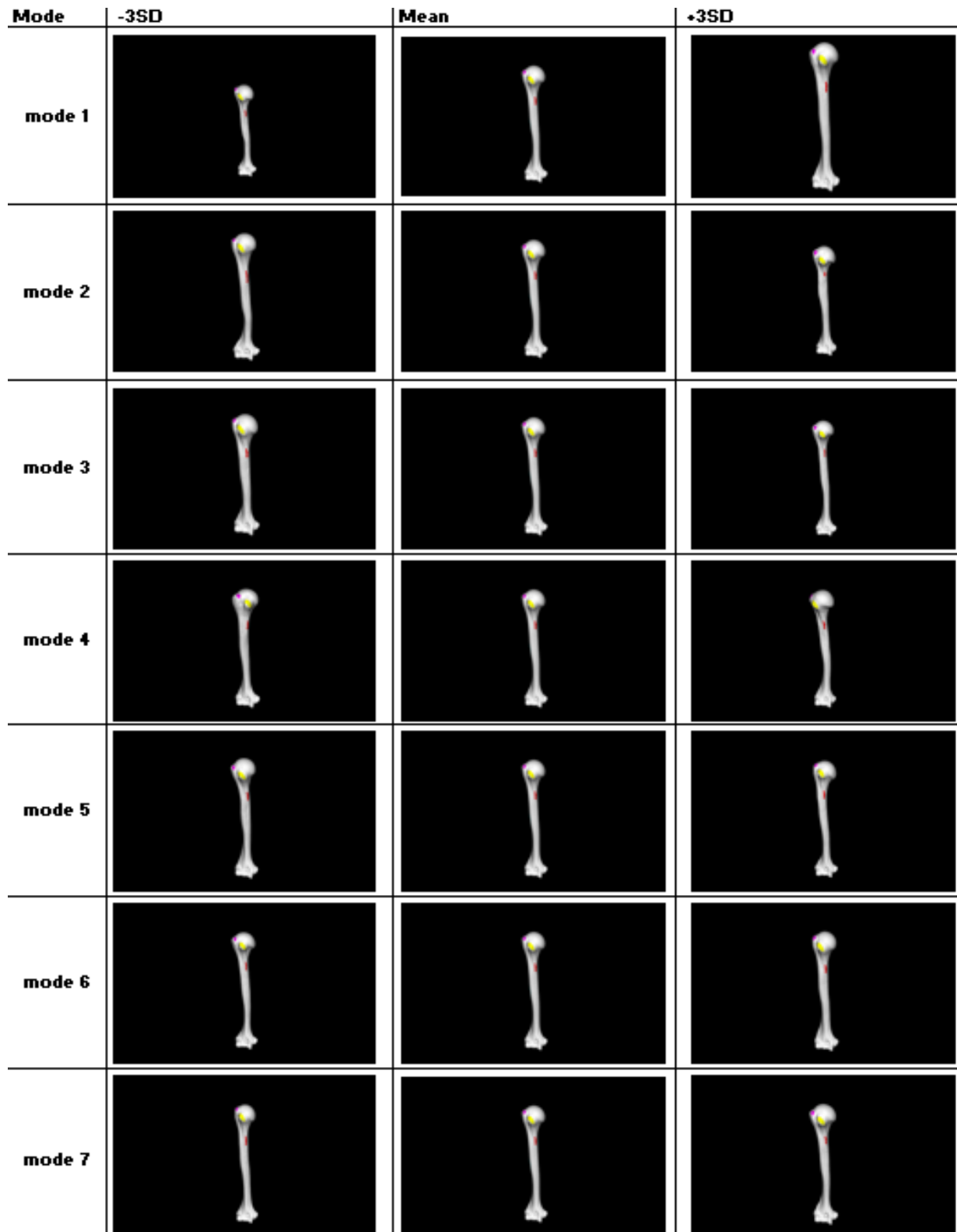


Figure 5. 4: Visualization of first seven principal modes of variation of an augmented humerus bone SSM on its anterior muscle insertions. As can be seen from the figure, the boundary conditions between adjacent muscles are obeyed in all the variations.

5.3.3. Validity of muscle insertion predictions

Validity of region prediction was visually confirmed by the expert in all ten external scapulae and eight external humeri (figures 5, 6 and 7). Tables 2 and 3 summarize the validation results for the same six muscles on scapula and humerus. Excellent concurrent validity of muscle region prediction was observed based on the mean and root mean square distance measures and also based on similarity coefficient (Tables 2 and 3). Validity measures indicated higher predictability for all six muscle regions on both the bones (Tables 2 and 3).

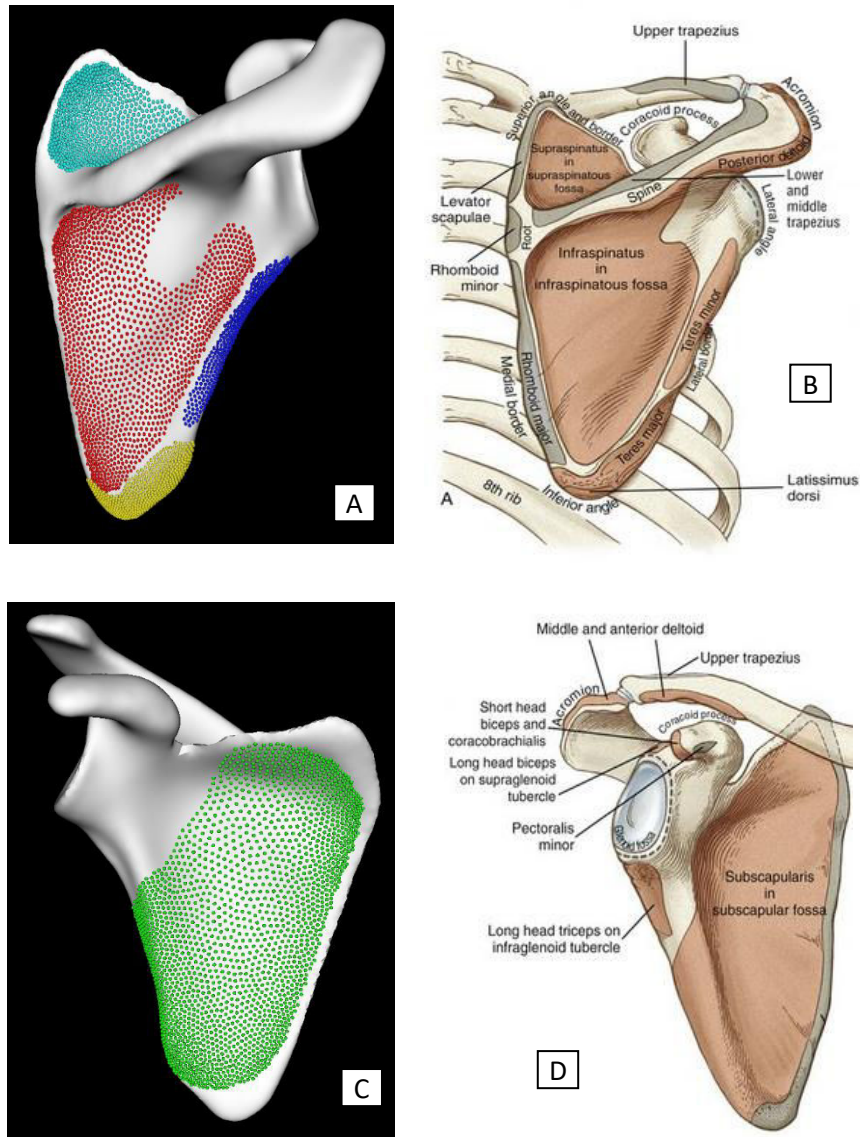


Figure 5. 5: Visual check of attachment region of scapula bone. A: posterior view of right scapula (MVS) with the final selection of VIDs of: I-S= Infraspinatus (Red), Suprasp= Supraspinatus(Light Bleu), T-Maj = Teres major (yellow), T-Min= teres minor(Dark bleu). B: posterior view of right scapula (from <http://clinicalgate.com/shoulder-complex/>). C: anterior view of right scapula (MVS) with the final selection of VIDs of: Subscapularis (Green). D: anterior view of right scapula (from <http://clinicalgate.com/shoulder-complex/>).

selection of VIDs of Subscap = subscapularis (Green). D: anterior view of right scapula (from <http://clinicalgate.com/shoulder-complex/>).

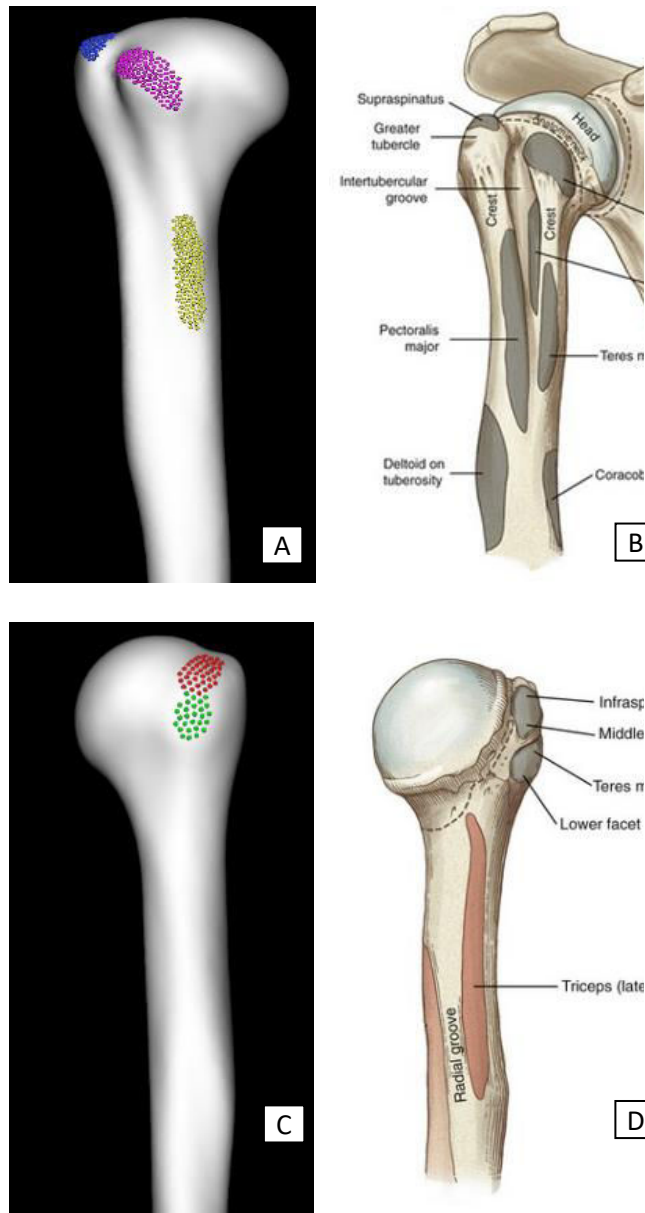


Figure 5. 6: Visual check of attachment region of humerus bone. A: anterior view of right humerus (MVS) with the final selection of VIDs of Subscap = subscapularis(Pink), Suprasp=Supraspinatus(Bleu) and T-Maj=Teres major(yellow). B: anterior view of right humerus (from <http://clinicalgate.com/shoulder-complex/>). C: posterior view of right humerus (MVS) with the final selection of VIDs of: I-S= Infraspinatus (Red) and T-Min= teres minor (Green). D: posterior view of right humerus (from <http://clinicalgate.com/shoulder-complex/>).

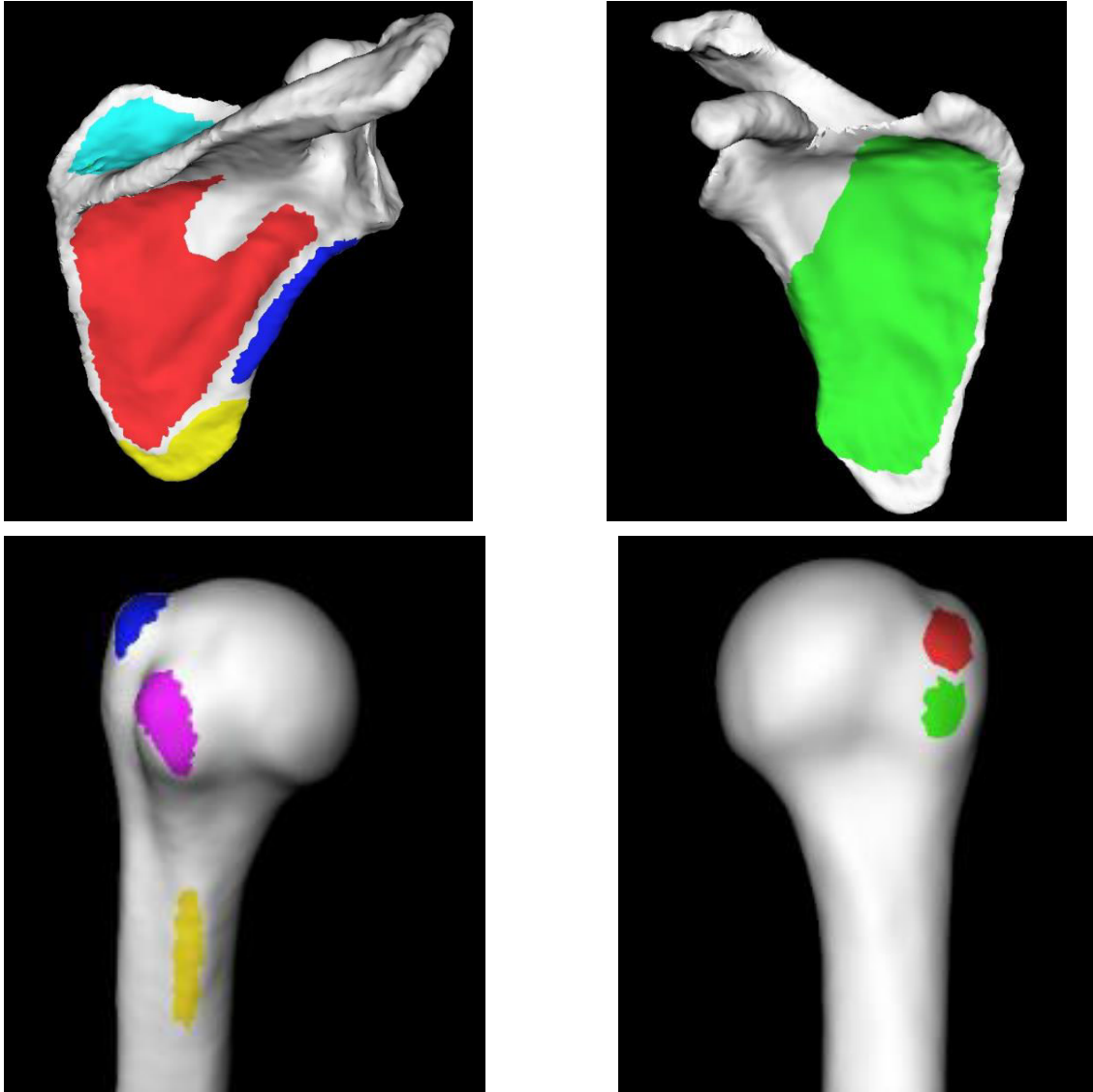


Figure 5. 7: Example of muscle regions prediction on one of the external scapulae and humeri. Subscapularis: pink on humerus and green on scapula, Supraspinatus: Blue on humerus and light blue on scapula, Teres major: yellow on humerus and scapula, teres minor: Green on humerus and dark blue on scapula and Infraspinatus: red on humerus and scapula.

Table 5. 2: Average validity error of muscle origin region predictions on ten external scapulae for six muscles: I-S = Infraspinatus, Subscap = Subscapularis, Suprasp = Supraspinatus, T-Maj = Teres Major, T-Min = Teres Minor, DEL = Deltoid, MD = Mean Distance, SD = Standard Deviation, RMS = Root Mean Square, HD = Hausdorff Distance, DC = Dice Coefficient

Muscle	MD (\pm SD) (mm)	RMS (mm)	HD (mm)	DC
I-S	0.20 (0.64)	0.68	4.82	0.98
Subscap	0.08(0.51)	0.57	4.51	0.98
Suprasp	0.05(0.25)	0.26	2.56	0.98
T-Maj	0.09 (0.38)	0.39	3.06	0.96
T-Min	0.11(0.46)	0.48	3.46	0.92
DEL	0.22(0.84)	0.79	4.27	0.94

Table 5. 3: Average validity error of muscle origin region predictions on ten external humeri for six muscles: I-S = Infraspinatus, Subscap = Subscapularis, Suprasp = Supraspinatus, T-Maj = Teres Major, T-Min = Teres Minor, DEL = Deltoid, MD = Mean Distance, SD = Standard Deviation, RMS = Root Mean Square, HD = Hausdorff Distance, DC = Dice Coefficient

Muscle	MD (\pm SD) (mm)	RMS (mm)	HD (mm)	DC
I-S	0.51 (1.03)	1.15	4.04	0.97
Subscap	0.37 (0.685)	0.79	2.76	0.97
Suprasp	0.33(0.72)	0.79	2.84	0.96
T-Maj	0.09 (0.38)	0.39	3.06	0.96
T-Min	1.01(1.32)	1.66	4.09	0.96
DEL	0.47	1.12	4.58	0.92

5.3.4 Comparison of joint and muscle mechanics

Ten NSM models for older adults were successfully adapted for each external imaging data. For each subject, muscle insertions for six muscles were successfully predicted using the augmented SSMs and

regression process. Each subject was successfully modeled with a generic muscle insertion construct and SSM predicted muscle insertion construct. Both constructs were successfully simulated for abduction and scapular plane elevation. SPM comparisons on joint contact forces revealed that there were no significant differences during abduction motion, and during scapular plane elevation, AP shear was significantly higher in higher elevation angles (figure 8 and 9). Muscle moment arms for all the six muscles were significantly different between the constructs for both abduction and scapular plane elevation movements (figure 10 and 11). Muscle forces were significantly different for posterior deltoid, teres major and teres minor during abduction movement (figure 12). Muscle forces were significantly different for middle deltoid, posterior deltoid, supraspinatus, infraspinatus, subscapularis, and teres major (figure 13).

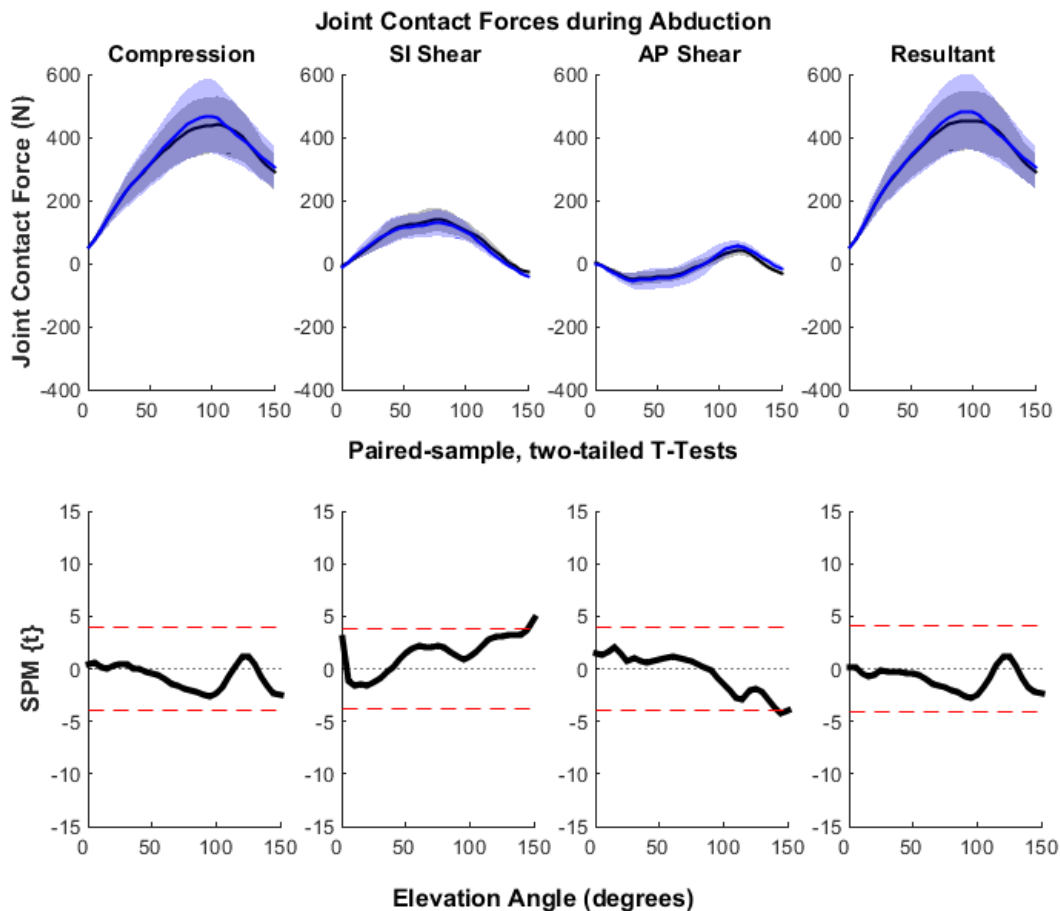


Figure 5. 8: Joint contact forces during GH abduction for generic and subject-specific insertion constructs. Each column corresponds to a joint contact force (from left to right: Compression, AP Shear, SI shear, resultant). Row 1: mean (bold line) and standard deviation (translucent area) plots. Blue represents the SSM predicted muscle insertion construct and black represents generic construct. Row 2: SPM T-Test output; the dashed red lines indicate the critical threshold value at $\alpha = 0.05$ and grey areas indicate clusters of significance.

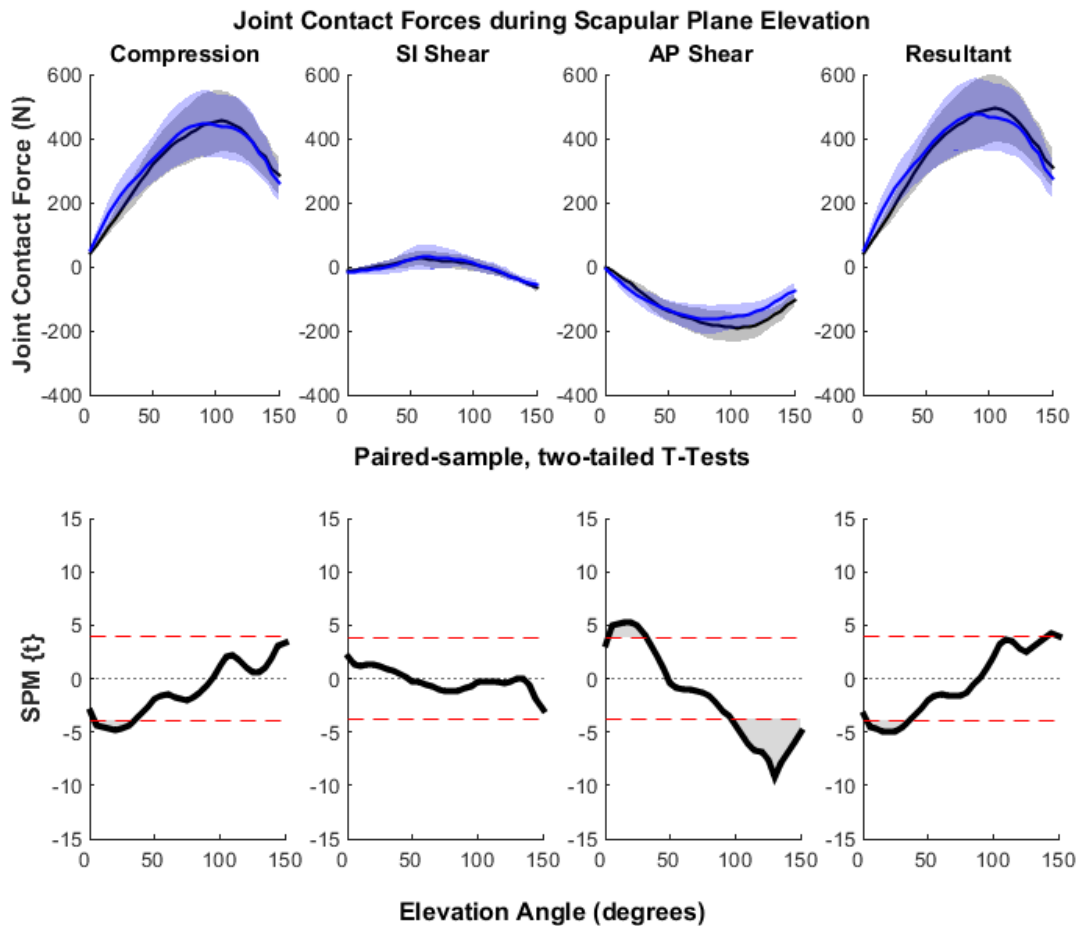


Figure 5. 9: Joint contact forces during scapular plane elevation for generic and subject-specific insertion constructs. Each column corresponds to a joint contact force (from left to right: Compression, AP Shear, SI shear, resultant). Row 1: mean (bold line) and standard deviation (translucent area) plots. Blue represents the SSM predicted muscle insertion construct and black represents generic construct. Row 2: SPM T-Test output; the dashed red lines indicate the critical threshold value at $\alpha = 0.05$ and grey areas indicate clusters of significance.

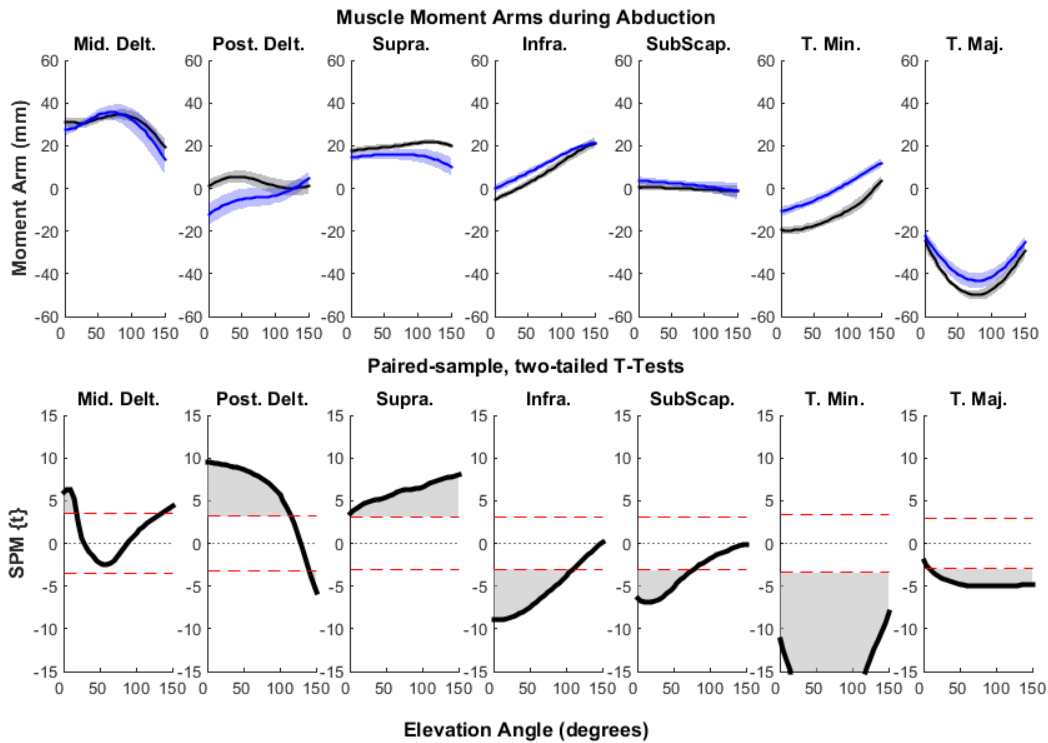


Figure 5. 10: Muscle moment arms during GH abduction movement for generic and subject-specific insertion constructs. Each column corresponds to a muscle (from left to right: Middle deltoid, posterior deltoid, supraspinatus, infraspinatus, subscapularis, teres minor, teres major). Row 1: mean (bold line) and standard deviation (translucent area) plots. Blue represents the SSM predicted muscle insertion construct and black represents generic construct. Row 2: SPM T-Test output; the dashed red lines indicate the critical threshold value at $\alpha = 0.05$ and grey areas indicate clusters of significance.

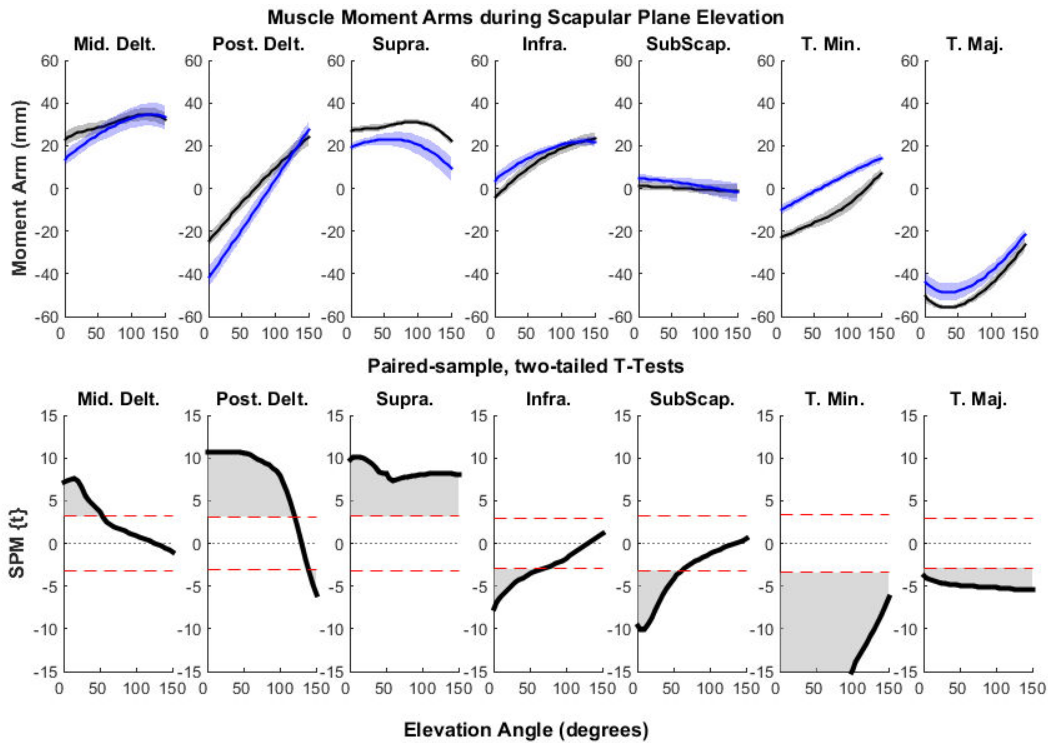


Figure 5. 11: Muscle moment arms during scapular plane elevation movement for generic and subject-specific insertion constructs. Each column corresponds to a muscle (from left to right: Middle deltoid, posterior deltoid, supraspinatus, infraspinatus, subscapularis, teres minor, teres major). Row 1: mean (bold line) and standard deviation (translucent area) plots. Blue represents the SSM predicted muscle insertion construct and black represents generic construct. Row 2: SPM T-Test output; the dashed red lines indicate the critical threshold value at $\alpha = 0.05$ and grey areas indicate clusters of significance.

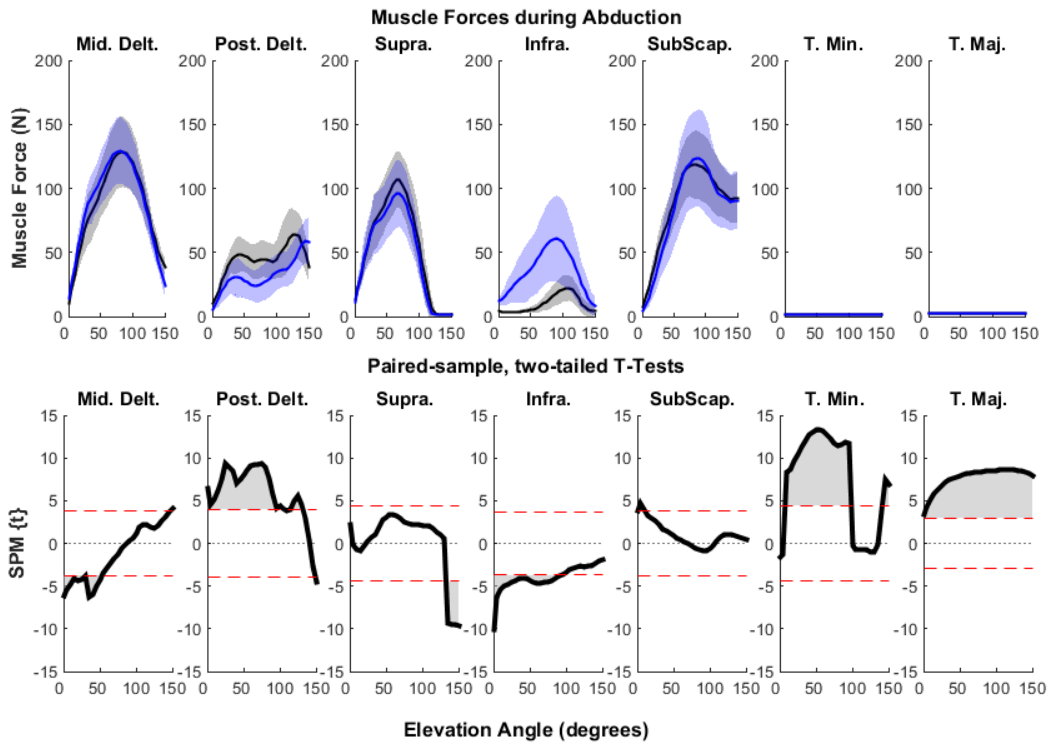


Figure 5. 12: Muscle forces arms during GH abduction movement for generic and subject-specific insertion constructs. Each column corresponds to a muscle (from left to right: Middle deltoid, posterior deltoid, supraspinatus, infraspinatus, subscapularis, teres minor, teres major). Row 1: mean (bold line) and standard deviation (translucent area) plots. Blue represents the SSM predicted muscle insertion construct and black represents generic construct. Row 2: SPM T-Test output; the dashed red lines indicate the critical threshold value at $\alpha = 0.05$ and grey areas indicate clusters of significance.

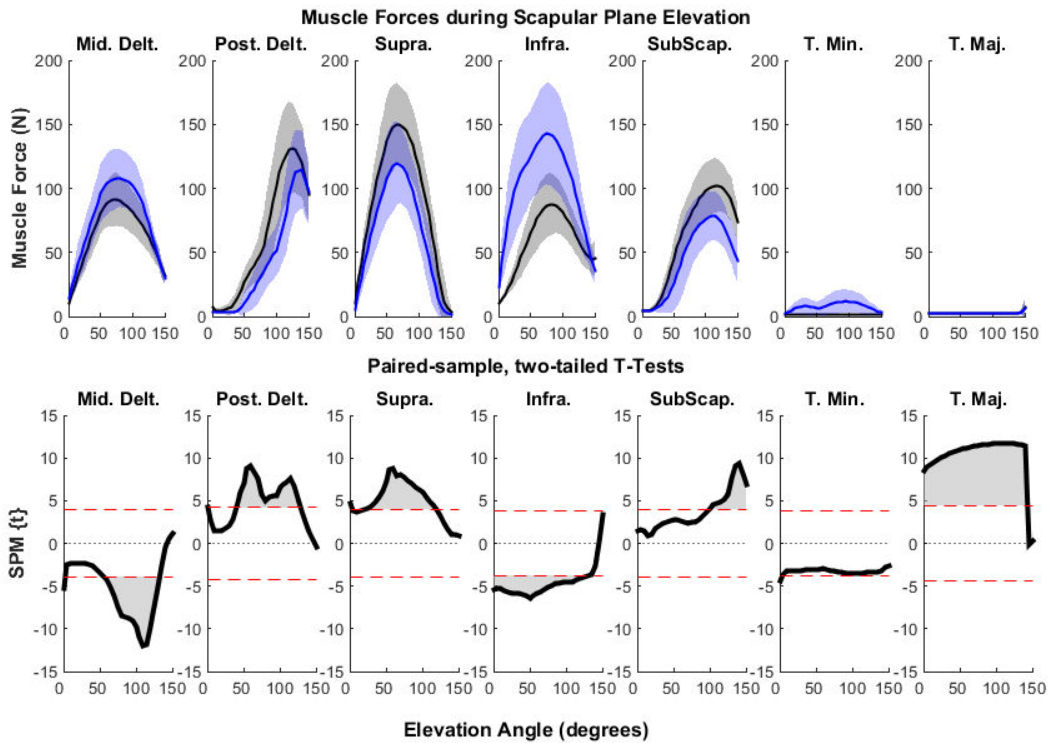


Figure 5. 13: Muscle forces arms during scapular plane elevation movement for generic and subject-specific insertion constructs. Each column corresponds to a muscle (from left to right: Middle deltoid, posterior deltoid, supraspinatus, infraspinatus, subscapularis, teres minor, teres major). Row 1: mean (bold line) and standard deviation (translucent area) plots. Blue represents the SSM predicted muscle insertion construct and black represents generic construct. Row 2: SPM T-Test output; the dashed red lines indicate the critical threshold value at $\alpha = 0.05$ and grey areas indicate clusters of significance.

5.4 Discussion

This study first illustrated the validity of subject-specific muscle origin/insertion region prediction using augmented bone SSMs. Then, it successfully integrated this subject-specific insertion prediction algorithm with a musculoskeletal modeling framework to make the musculoskeletal model one step closer to represent reality. This study was based on the idea that bone shapes can predict muscle origin/insertions regions and the excellent concurrent validity results confirm this for six major shoulder muscles. For all the muscle insertion prediction results, T-Min insertions on humerus had highest RMS error (1.66mm). This could be attributed to the difficulty of manually segmenting the T-Min attachment region on humerus. Furthermore, the smaller the origin/insertion region, the difficult it was to accurately segment.

Muscle insertion prediction algorithm: Findings of this study corroborates well with previous studies that predict muscle origin/insertion attachment sites. For example, Ding and colleagues used scaling method (linear or non-linear) [13], but the mean distance errors reported were up to 15mm using cadaveric shoulders as gold standard. Kaptein and Van der helm [25] concluded that up to 45% of muscle attachment regions can be predicted by means of geometrical models of the bones. But these results were influenced

by measurement errors and possible inter-individual differences. Pellikaan and colleagues [26] applied a morphing method to deform bone geometries including the muscle attachment sites between digitized scans of two cadavers and they found that for 69% of the muscle attachment sites the average error was smaller than 15mm. These errors are not accepted in the analysis of musculoskeletal mechanics as Carbone and colleagues [6] reported that 10mm perturbation in muscle insertion site can significantly change the muscle forces and moment arms. In the current study, validation errors were much improved and in the range of submillimeter accuracy. This could be attributed to the SSM based approach used which provides increased quality of fitting due to point-to-point correspondences, which in turn improves the accuracy of muscle origin/insertion regions prediction.

All the previous studies used cadaveric specimen as gold standard whereas the current study used expert segmentations as gold standard. This was considered as a limitation of the study and thus the absolute error in this study may not be known. In the hindsight, this method can be further incorporated into fitting the bone imaging data directly, thereby reducing the need to generate 3D mesh models. Such advancement would also help eliminate the tedious process of segmentation which is always time consuming and introduces segmentation errors. Although this study does not employ cadaveric shoulders, more validations are warranted for all the shoulder joint muscles.

Subject-specific musculoskeletal model: Whether subject-specific computational models can predict joint mechanics close to reality or not is a debated topic [8], [8], [9], [27], [28]. This study illustrated that subject-specific muscle insertions lead to altered muscle force balance strategies as well as altered muscle moment arms. Incorporating subject specific muscle insertion parameters in a musculoskeletal model is always a challenge. The scaling tool typically available in the modeling framework can scale down anthropometry values but the muscle insertion predictions get messed up in the process, leading to manual intervention. Further, even with manual process, it is very hard to detect muscle insertions for most of the shoulder muscles. On this background, the current study successfully developed a framework to integrate the SSM and musculoskeletal modeling domains.

Joint contact forces were almost unchanged between the two constructs except at the higher elevation angles for AP shear forces. This indicates that contact forces are not very sensitive to the changes in muscle insertion locations. While this may provide a valuable insight in the design of shoulder implants, it is also important to note that we reported the contact forces but not the peak contact locations. Depending on the changes in this peak location, one can derive a meaningful conclusion about the efficacy of subject-specific muscle insertions. Furthermore, increased AP shear in higher angles of elevation could be regarded as a concern in certain clinical evaluations as this may lead to glenohumeral dislocations. This also does not mean that contact forces will be different in other shoulder movements and a more comprehensive simulation study covering the set of daily movements is warranted.

Muscle moment arms are significantly increased for infraspinatus, subscapularis, teres major and teres minor and decreased for posterior deltoid and supraspinatus for both the simulated movements. This is an interesting finding as we expected the increase in all the muscle moment arms. The SSM based insertion algorithm provided muscle regions and not the attachment points for the musculotendon units used in the NSM model. We distributed the attachment points over the predicted insertion regions in isometric fashion. We believed that this also provided a mechanical stability to the model itself during the simulations. The attachment points in the insertion regions, when visually compared with the generic attachment points, were largely mismatched, explaining how we found the significant differences in all

the muscle moment arms. Furthermore, increased muscle moment arms may also indicate reduced forces to produce the same movement. However, this was not evident in the results of muscle forces. While supraspinatus and posterior deltoid muscles both reported increased muscle forces as expected and considering their reduced moment arms, this was not true for the other muscles that indicated higher moment arms. Thus, it can be hypothesized that the muscles with increased moment arms do not show similar load sharing mechanisms and certain muscles like infraspinatus are always preferred to carry more load. These results can provide more insights into how a rehabilitation strategy can be designed using such modeling framework.

5.5 Chapter 5 References

- [1] A. Salhi, V. Burdin, T. Mutsvangwa, S. Sivarasu, S. Brochard, and B. Borotikar, "Subject-specific shoulder muscle attachment region prediction using statistical shape models: A validity study.," *Conf. Proc. Annu. Int. Conf. IEEE Eng. Med. Biol. Soc. IEEE Eng. Med. Biol. Soc. Annu. Conf.*, vol. 2017, pp. 1640–1643, Jul. 2017.
- [2] S. L. Delp *et al.*, "OpenSim: open-source software to create and analyze dynamic simulations of movement," *IEEE Trans. Biomed. Eng.*, vol. 54, no. 11, pp. 1940–1950, Nov. 2007.
- [3] K. Song, A. E. Anderson, J. A. Weiss, and M. D. Harris, "Musculoskeletal models with generic and subject-specific geometry estimate different joint biomechanics in dysplastic hips.," *Comput. Methods Biomech. Biomed. Engin.*, vol. 22, no. 3, pp. 259–270, Feb. 2019.
- [4] L. Scheys, K. Desloovere, P. Suetens, and I. Jonkers, "Level of subject-specific detail in musculoskeletal models affects hip moment arm length calculation during gait in pediatric subjects with increased femoral anteversion.," *J. Biomech.*, vol. 44, no. 7, pp. 1346–1353, Apr. 2011.
- [5] M. Wesseling *et al.*, "Subject-specific geometrical detail rather than cost function formulation affects hip loading calculation.," *Comput. Methods Biomech. Biomed. Engin.*, vol. 19, no. 14, pp. 1475–1488, Nov. 2016.
- [6] V. Carbone, M. M. van der Krogt, H. F. J. M. Koopman, and N. Verdonchot, "Sensitivity of subject-specific models to errors in musculo-skeletal geometry," *J. Biomech.*, vol. 45, no. 14, pp. 2476–2480, Sep. 2012.
- [7] L. Bosmans *et al.*, "Sensitivity of predicted muscle forces during gait to anatomical variability in musculotendon geometry.," *J. Biomech.*, vol. 48, no. 10, pp. 2116–2123, Jul. 2015.
- [8] I. Jonkers, N. Sauwen, G. Lenaerts, M. Mulier, G. Van der Perre, and S. Jaecques, "Relation between subject-specific hip joint loading, stress distribution in the proximal femur and bone mineral density changes after total hip replacement.," *J. Biomech.*, vol. 41, no. 16, pp. 3405–3413, Dec. 2008.
- [9] G. Lenaerts *et al.*, "Subject-specific hip geometry and hip joint centre location affects calculated contact forces at the hip during gait.," *J. Biomech.*, vol. 42, no. 9, pp. 1246–1251, Jun. 2009.
- [10] M. Wesseling, L. Bosmans, C. Van Dijck, J. Vander Sloten, R. Wirix-Speetjens, and I. Jonkers, "Non-rigid deformation to include subject-specific detail in musculoskeletal models of CP children with proximal femoral deformity and its effect on muscle and contact forces during gait.," *Comput. Methods Biomech. Biomed. Engin.*, pp. 1–10, Jan. 2019.
- [11] T. A. Correa and M. G. Pandy, "A mass-length scaling law for modeling muscle strength in the lower limb," *J. Biomech.*, vol. 44, no. 16, pp. 2782–2789, Nov. 2011.
- [12] R. Matias, C. Andrade, and A. P. Veloso, "A transformation method to estimate muscle attachments based on three bony landmarks," *J. Biomech.*, vol. 42, no. 3, pp. 331–335, Feb. 2009.
- [13] Z. Ding, D. Nolte, C. Kit Tsang, D. J. Cleather, A. E. Kedgley, and A. M. J. Bull, "In Vivo Knee Contact Force Prediction Using Patient-Specific Musculoskeletal Geometry in a Segment-Based Computational Model," *J. Biomech. Eng.*, vol. 138, no. 2, p. 021018, Feb. 2016.
- [14] T. F. Cootes, C. J. Taylor, D. H. Cooper, and J. Graham, "Training Models of Shape from Sets of Examples," in *BMVC92*, D. H. Bs. DPhil MSc and R. B. BA, Eds. Springer London, 1992, pp. 9–18.

- [15] B. Borotikar, T. Mutsvangwa, V. Burdin, E. Ghorbel, M. Lempereur, S. Brochard, *et al.*, "Augmented Statistical Shape Modeling for Orthopaedic Surgery and Rehabilitation," in *Medical Image Analysis and Informatics: Computer-Aided Diagnosis and Therapy*, P. M. d. Azevedo-Marques, A. Mencattini, M. Salmeri, and R. M. Rangayyan, Eds., ed Florida, USA: CRC Press, Taylor and Francis Group, 2017, pp. 369–426.
- [16] T. Mutsvangwa, V. Burdin, C. Schwartz, and C. Roux, "An automated statistical shape model developmental pipeline: application to the human scapula and humerus," *IEEE Trans. Biomed. Eng.*, vol. 62, no. 4, pp. 1098–1107, Apr. 2015.
- [17] M. Lüthi, C. Jud, T. Gerig, and T. Vetter, "Gaussian Process Morphable Models," *ArXiv160307254 Cs*, Mar. 2016.
- [18] M. Luthi, T. Albrecht, and T. Vetter, *Probabilistic modeling and visualization of the flexibility in morphable models*. Springer-Verlag, Berlin, 2009.
- [19] M. Luthi, *Scalable Image Analysis and Shape Modelling. Contribute to unibas-gravis/scalismo development by creating an account on GitHub*. Graphics and Vision Research Group University of Basel, 2019.
- [20] M. Luthi *et al.*, "Statismo - A framework for PCA based statistical models.," *Insight J.*, vol. 1, pp. 1–18, 2012.
- [21] I. W. Charlton and G. R. Johnson, "A model for the prediction of the forces at the glenohumeral joint," *Proc. Inst. Mech. Eng. [H]*, vol. 220, no. 8, pp. 801–812, Nov. 2006.
- [22] N. D. Barnett, R. D. Duncan, and G. R. Johnson, "The measurement of three dimensional scapulohumeral kinematics--a study of reliability.," *Clin. Biomech. Bristol Avon*, vol. 14, no. 4, pp. 287–290, May 1999.
- [23] A. V. Hill, "The Heat of Shortening and the Dynamic Constants of Muscle," *Proc. R. Soc. Lond. B Biol. Sci.*, vol. 126, no. 843, pp. 136–195, 1938.
- [24] T. C. Pataky, "Generalized n-dimensional biomechanical field analysis using statistical parametric mapping.," *J. Biomech.*, vol. 43, no. 10, pp. 1976–1982, Jul. 2010.
- [25] B. L. Kaptein and F. C. T. van der Helm, "Estimating muscle attachment contours by transforming geometrical bone models," *J. Biomech.*, vol. 37, no. 3, pp. 263–273, Mar. 2004.
- [26] P. Pellikaan *et al.*, "Evaluation of a morphing based method to estimate muscle attachment sites of the lower extremity," *J. Biomech.*, vol. 47, no. 5, pp. 1144–1150, Mar. 2014.
- [27] G. Lenaerts *et al.*, "Subject-specific hip geometry affects predicted hip joint contact forces during gait.," *J. Biomech.*, vol. 41, no. 6, pp. 1243–1252, 2008.
- [28] G. Valente *et al.*, "Are Subject-Specific Musculoskeletal Models Robust to the Uncertainties in Parameter Identification?," *PLOS ONE*, vol. 9, no. 11, p. e112625, Nov. 2014.

Chapter 6

Statistical shape modeling approach to predict missing scapular bone: applications in pre-surgery planning and musculoskeletal modeling

6.1 Introduction

6.1.1 Structure of this chapter

While dealing with shoulder joint modeling, one important aspect is the morphological structure and analysis of the shoulder bones. This analysis is important from two perspectives – First to delineate the bone shape features (anatomical angles, pre-morbid shape, cutting guide planes, optimal cutting or drilling depths) that are important for surgery and surgery planning and second to identify bone characteristics (bone density, cortical bone thickness, muscle insertion and origin regions, bone mass and center of mass). In this chapter, we propose a SSM-based methodology to predict the pre-morbid scapular shape from an available incomplete (missing) information. The research conducted in this chapter is currently submitted as a manuscript for publication in the journal of Annals of Biomedical Engineering. I have presented the chapter in its manuscript format to have a logical flow.

6.1.2 Rationale to target missing part in scapular bone

As explained in chapter 2, scapula is an important bone that forms the shoulder complex and plays vital role in shoulder joint function [1]. It serves as bony ground for multiple shoulder muscle insertions which in turn help maintain the glenohumeral joint stability while providing a wide range of mobility [1]. Shoulder joint disorders including shoulder arthritis or cuff tear arthropathies affect scapular bone and lead to damaged bone, rapid bone loss, restricted shoulder function, and chronic pain [2-6] and ultimately need surgical intervention. Shoulder joint replacement is regarded as a safe and effective procedure to relieve pain and help resume daily activities [3, 7]. Thus, for shoulder disorders, pre-morbid as well as complete anatomy of the scapula remains an important reference for two scenarios: 1) surgical planning for shoulder joint-replacement procedures, and 2) biomechanics research to understand shoulder joint functionality in healthy, impaired, and post-surgical population.

Glenoid bone loss occurs in up to 90% of cases of traumatic anterior glenohumeral instability [8] thus pre-operative recognition of the glenoid bone loss for effective glenoid component placement is a key factor

for successful outcomes after surgical treatment [9]. Significant glenoid bone loss, if not effectively determined, can lead to improper base plate positioning and/or poor fixation and results in early baseplate failure in reverse shoulder arthroplasties [10]. On the other hand, to understand native and pathological shoulder biomechanics, researchers typically develop image-based shoulder biomechanics models. These models, when made subject-specific in terms of bone shape and muscle insertions, can be highly valuable to understand the underlying pathology from a functional perspective and to devise the treatment strategies [11-14]. In both these scenarios, the problem is the missing information about the scapular shape in terms of either pre-morbidity or completeness. For the first scenario, current pre-planning software tools lack the ability to estimate pre-morbid anatomy of the scapula from its current state and for the second scenario, to develop subject-specific shoulder models, researchers often deal with incomplete scapular images as many clinical imaging protocols do not cover the entire scapula.

To address the issue of estimating pre-morbid scapular geometry from patient's defective scapular bone shape, various techniques have been used previously. These include a use of contralateral bone as a template to predict the pre-morbid scapular morphology [15-17], glenoid vault model as a template to estimate glenoid version [18], measurement-based methods using anatomical correlations [19], and statistical shape modeling (SSM) based reconstruction methods [20, 21]. The template-based [18] and measurement-based [19] methods are limited to glenoid version estimation only. SSM-based reconstruction methods have been evaluated for scapula and humerus bones in the recent literature [21-23]. These studies typically create a missing bone structure artificially to reconstruct it from the SSM [21-23]. However, artificially created bone loss in the glenoid region and the results cannot be linearly extrapolated for their use in predicting pre-morbid morphology of diseased scapula. Another SSM based approach [20] make use of an SSM of glenoid region only – a region which is typically deformed in case of pathology and which needs a pre-morbid estimation. To address the issue of missing scapular image to develop subject-specific shoulder models, no attempts have been made in the literature to reconstruct the missing inferior or superior shape of scapular bone. These missing parts contain important information about muscle origins and bony landmarks for determining clinical measures such as critical shoulder angle or scapular length etc. As a result, thousands of routine clinical images cannot be used for building patient-specific models leading to waste of medical imaging resources in healthcare [24].

Thus, the aim of this study was to assess the feasibility and validity of predicting the pre-morbid and complete shape of the scapula bone by building an SSM based on Iterative Median Closest Point – Gaussian Processes Morphable Model (IMCP-GPMM) process [25, 26] and by using a Gaussian regression based reconstruction algorithm developed specifically for this SSM. We assumed that for healthy scapular bone, the rest of the scapula shape is moderate to excellent predictor of the missing part in its glenoid, inferior, or superior region. Healthy scapular shapes were used for artificially creating missing regions. These shapes were categorically selected to cover the anatomical classification of the glenoid region. Performance of the reconstructions was evaluated in terms of distance, similarity and anatomical measures.

6.2 Materials and Methods

This study was conducted in four steps. In the first step, three-dimensional (3D) triangular surface models of the scapular shapes were created from CT images. A small subset of these shapes was categorically selected for the evaluation purposes and the remaining shapes were used to build scapula SSM. In the second step, four virtual defects were created in each categorically selected shape. The virtual defects were created in the glenoid, inferior and superior regions of the scapula. In the third step, an SSM-based reconstruction algorithm was developed and used to predict the complete scapular shape using the defective shape as a target. In the last step, the accuracy of predicted complete shape was evaluated with the original complete shape in terms of distance, anatomical, and similarity measures.

6.2.1 Scapula SSM Building

An imaging database of dry bone samples ($n = 82$) was used for this study. CT scan images were acquired using the SIEMENS SOMATOM Definition AS scanner (Siemens Healthcare, Forchheim, Germany) with a resolution of 0.96mm X 0.96mm X 0.6mm. All the images were evaluated by two radiologists (years of experience: R1 = 19 years, R2 = 12 years) for bone integrity and one anatomist (years of experience: 15 years) for anatomical normality. Images were manually segmented (Amira, FEI, Hillsboro, V5.4), and 3D surface mesh models of each sample were created. For all the scapulae, no demographical data were available as the dry bones were acquired from the local anatomical department. Ten samples from this database were categorically selected for the evaluation purpose and the remaining samples were used to build the SSM of the scapula.

In this study, we used the IMCP-GPMM pipeline [25, 27, 28] to create the scapular SSM. The SSM building pipeline can be summarized in three main stages: rigid alignment with no reference bias, non-rigid alignment to establish point-to-point dense correspondence, and SSM creation using GPMM process. For rigid alignment, all the left scapular shapes were mirrored into right and processed with an in-house IMCP algorithm [26, 29] that removed any registration bias by mutual consensus and created a virtual manifold. This manifold was used in a coherence point drift (CPD) algorithm [30] to non-rigidly align and create a mean virtual shape as well as to establish point-to-point dense correspondence between the mean virtual shape and original shapes. In the third stage, we build an SSM as a GPMM using the mean virtual shape and all scapulae shapes in its correspondence. In this stage, a point distribution model (PDM) was built first using the mean virtual shape and its correspondence with original shapes. PDM models the shape variations s as normal distribution \mathcal{N} with mean μ and covariance matrix Σ as represented by:

$$s \sim \mathcal{N}(\mu, \Sigma)$$

A principal component analysis (PCA) was performed to compute normalized eigenvectors and eigenvalues of the covariance matrix Σ . A new shape s' is then defined as the linear combination of the eigenvectors to have a probabilistic representation of the PDM as

$$s' = \bar{s} + \sum_{i=1}^n \alpha_i \sqrt{d_i} \vec{\mu}_i$$

Where \bar{s} is the mean and μ_i and d_i are eigenvectors and eigenvalues of covariance matrix Σ and $\alpha_i \sim \mathcal{N}(0,1)$ making $s' \sim \mathcal{N}(\bar{s}, \Sigma)$ [25]. Thus, PDM is a model of deformations added to the mean shape and probability distribution is on the deformations. Using this known deformation field at each point of the PDM, we model the deformation field as gaussian process. Such formulation converts a PDM into its continuous form using GPMM process [25]. An open source toolbox for scalable image analysis and shape modeling (SCALISMO) [31] was used for building the SSM. Leave-on-out cross validation was performed [32] along with model specificity and compactness measures to evaluate the SSM robustness.

6.2.2 Virtual scapular defect creation

The ten samples external to the SSM building, were categorically selected from the scapulae database in such a way that they covered the anatomical classification of the scapular bone in its glenoid and acromion region. For this purpose, four anatomical classifications were used viz. shape of the glenoid (type 0, I, II, and III based on morphology of the glenoid notch) [33], acromion type (type I, II and III based on flat, curved, and hooked morphology) [34], critical shoulder angle (CSA) measure (high and low) [35], and glenoid version type (ante-version and retro-version) [36]. These measures were manually performed on all the 3D shapes and one sample each was selected to represent a shape in each anatomical classification.

Four scapular bone defects were virtually created on each of the ten external scapulae using an open source 3D visualization and mesh processing software (MeshLab) [37] which resulted in 40 defective scapular shapes. These virtual defects were divided into four groups as: 1) Group 1 (Figure 6.1): representing mild glenoid bone loss (using Wallace Classification type I defect) [38], 2) Group 2 (Figure 6.1): representing severe glenoid bone loss (using Wallace Classification type III defect) [38], 3) Group 3 (Figure 6.1): representing a missing superior region of the scapula (covering acromion and coracoid process), and 4) Group 4 (Figure 6.1): representing a missing inferior region of the scapula (covering the inferior angle of the scapula).

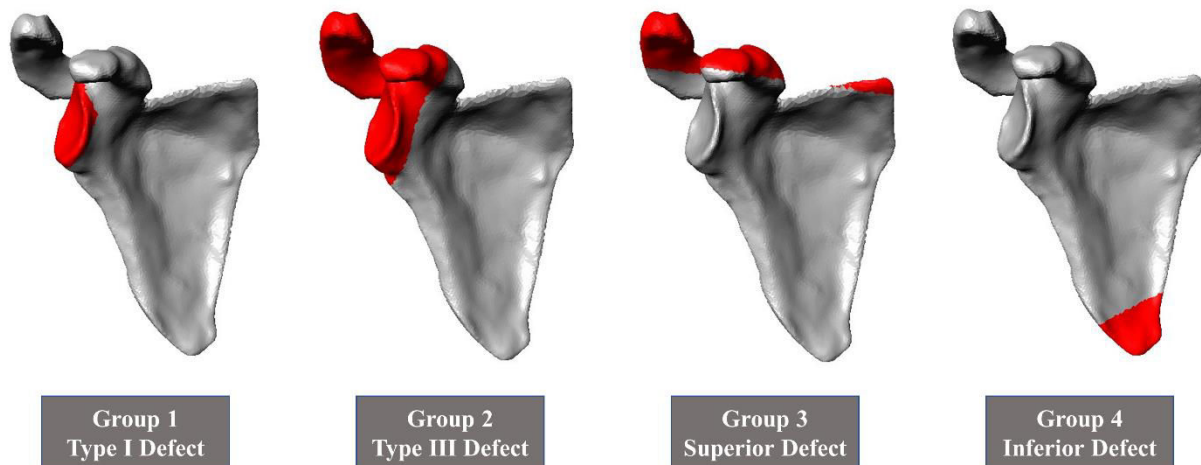


Figure 6. 1: Virtual defect creation: Four types of virtual defects created from each external scapular shape. These include Group 1: Simulating Wallace classification type I defect [38] representing mild glenoid bone loss, Group 2: Simulating Wallace classification type III defect [38] representing severe glenoid bone loss and affecting acromion and coracoid processes, Group 3: Simulating a missing superior part of the scapula, and Group 4: Simulating a missing inferior part of the scapula.

6.2.3 Missing part prediction algorithm

The scapular SSM with 95% of the population variability were retained with the help of principal modes of variations and subsequently used in the missing part prediction algorithm. The virtual bone defect shapes created before were used as a prior knowledge target shape (TS). A combination of principal components of the scapula SSM, which was the best approximation for the TS, was determined using Gaussian process regression method and used as a predictor of the missing shape. This algorithm was created using the open source software SCALISMO (University of Basel) [31] and was performed in three steps:

Step 1: Matching the centroids of the mean shape of the SSM (MS) and the TS.

Step 2: Rigid alignment: A set of 10 landmarks each were selected on the MS and TS. This landmark set was different for each of the target groups. Fifteen iterations of rigid Iterative Closest Point (ICP) algorithm [39, 40] were performed with a Procrustes analysis [41] that applied the best rigid transform on the MS after each iteration.

Step 3: Model fitting: This non-rigid deformation algorithm aimed at finding the closest shape variation of the SSM to TS using following steps –

- a) Find the identifiers (IDs) of the SSM that correspond to available partial TS: for each point in the TS, a closest point in the MS was found and corresponding IDs were recorded.
- b) Create a posterior model (PM): The landmarks used for the rigid alignment in step 2 were used to create the PM [42, 43], assuming a standard error for the landmark placement of

0.5mm. The landmark position of all the instances sampled from this posterior SSM were within the error parameter attributed to these landmarks.

- c) Perform non-rigid ICP: 20 iterations of non-rigid ICP were executed. In each iteration, the algorithm suggested a candidate correspondence between the points of the PM associated to IDs, then a Gaussian process regression was performed [25, 42] based on the prior knowledge and predicted shape was built.

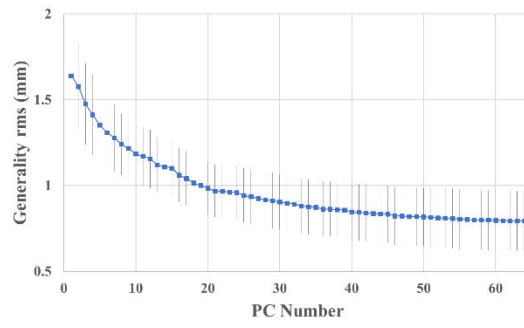
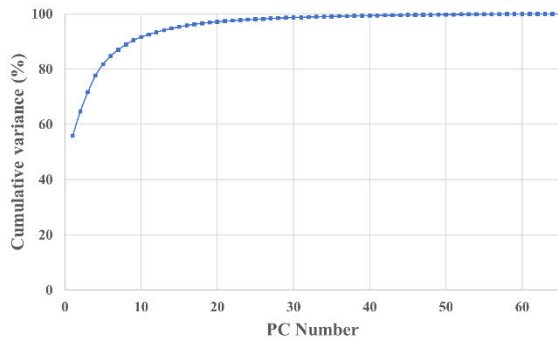
6.2.4 Prediction error quantification

The prediction error was defined as a difference of anatomical measures or distance metric between the original scapular shape and the one predicted by the algorithm. The prediction error was evaluated and reported using three different approaches. In the first approach, each 3D surface of the predicted shape and its original counterpart were discretized as point clouds [44] and distance errors for a given point on predicted surface to the closest point on the original surface were assessed. The distance errors were reported in the form of mean distance, maximum (Hausdorff) distance [45, 46], and root mean square (RMS) distance. In the second approach, error in predicting four anatomical measures that are considered as important angles for surgery pre-planning to restore shoulder functionality, was determined. These measures include glenoid version [36, 47], glenoid inclination [48], glenoid center location, and CSA [49, 50]. Each one of these angles was determined on the original and predicted shapes and the errors were reported. In the third approach, similarity index of the predicted shape with the original shape was determined and reported as the Dice Similarity Coefficient [51].

6.3 Results

6.3.1 SSM building and robustness

Five scapular shapes were discarded from the database for being anatomically abnormal and SSM was built using $n=67$ scapulae. Using the leave-one-out cross-validation, the generality of the SSM was found excellent with minimum and maximum RMS values being 0.79mm and 1.64mm (Figure 6.2). The specificity of the SSM ranged from 1.22mm to 1.74mm (Figure 6.2). For compactness measures, nine first principal components (PCs) accounted for 90% variability in the SSM whereas 15 first PCs accounted for 95% variability (Figure 6.2). Shape variations of the first five PCs are shown in Figure 6.3. As expected, the first principal component consisted of the size variation. The second principal component related closely to the height of the scapula. The third mode approximately accounted for variations in acromion orientation. The fourth SSM mode related closely to the width of the scapula. The fifth mode accounted for the thickness of the scapular bone in its glenoid and scapular plane regions.



Compactness: Accumulated variance of the model for principal components

Generality: Model's ability to accurately represent all valid instances

Specificity: Model's ability to only represent valid instances of the modeled bone

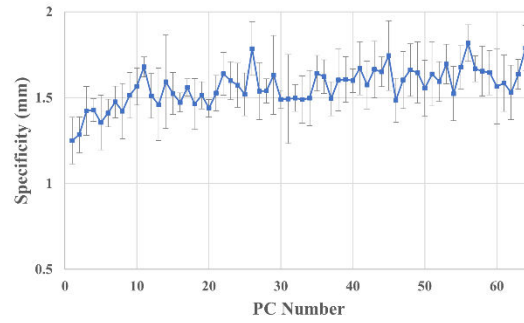


Figure 6. 2: Robustness and cross-validation measures of the scapula statistical shape model. Top left: Compactness, Top right: Generality in RMS, and Bottom right: Specificity in mm.

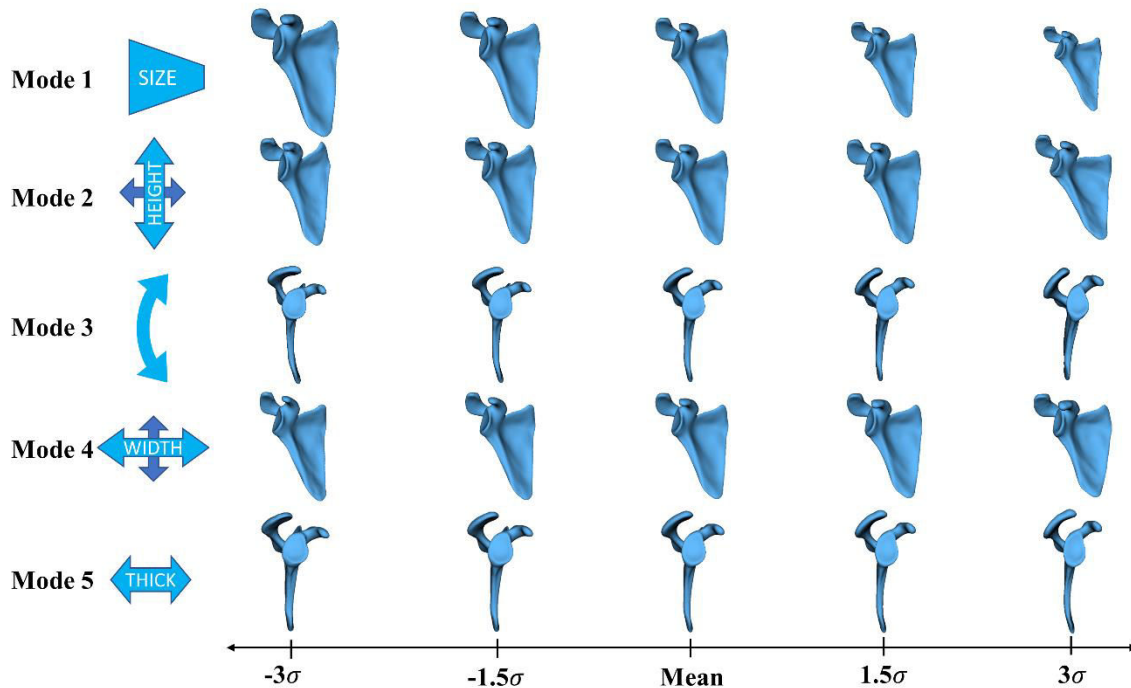


Figure 6. 3: Statistical shape model (SSM) of the scapula and the first five principal modes of variations. Variations in each principal component (mode) are shown by changing the standard deviation (σ) of the shape coefficient from -3σ to $+3\sigma$. First principal component (Mode 1) represents variation in size. Second principal component (Mode 2) reflects variation dominated in the height of the scapula. Third principal component (Mode 3) represents a variation in the concavity of the scapular blade. Fourth principal component (Mode 4) is accountable for variation in the scapular width. Fifth principal component (Mode 5) accounts for variation in the thickness of the scapular blade.

6.3.2 Virtual scapular defect

Ten scapular shapes mapped the anatomical classification system by having at least one representation in each of its class (Figure 6.4). The only class not found in the database was that of glenoid type III, which is considered as scarcely present in healthy population [33].

6.3.2 Gaussian regression and prediction error assessment

Fifteen principal modes representing 95% variability in the SSM were used in the Gaussian regression algorithm. Evaluation of predicted shapes revealed moderate to excellent outcomes (Table 6.1, Table 6.2). The prediction error in anatomical angle measures ranged from 1.0° to 2.2° (Table 6.1, Figure 6.5). For distance measures, the highest prediction error was 0.97mm (Group 4), 5.86mm (Group 1) and 1.30 (Group 2) for mean, Hausdorff, and RMS distances respectively (Table 6.2). Excellent similarity coefficient (Dice coefficient ≥ 0.81) with the original shapes was found (Table 6.2, Figure 6.1).

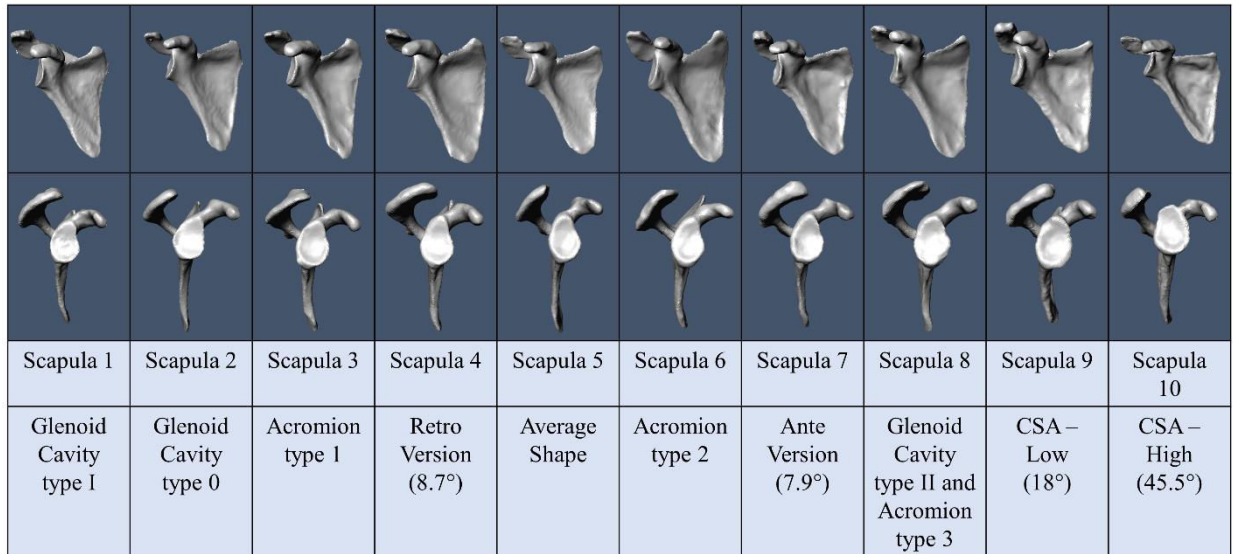


Figure 6. 4: Ten external scapular shapes categorically selected for evaluation. These shapes mapped the anatomical classification of scapula in its 1) Glenoid cavity (type 0, type I, and type II), 2) Acromion type (type 1, type 2, and type 3), 3) Version (ante-version and retro-version), and 4) Critical shoulder angle (CSA – High and low).

Table 6. 1: Mean prediction errors when comparing the results of missing part prediction with original shapes of external scapulae for anatomical measures of glenoid inclination, glenoid version, critical shoulder angle (CSA), and glenoid center. Min.: Minimum error value, Max.: Maximum error value, SD: Standard deviation.

Virtual Defect Group	Anatomical Measures											
	Glenoid Inclination (degree)			Glenoid Version (degree)			Glenoid Center (mm)			CSA (degree)		
	Mean (SD)	Min.	Max.	Mean (SD)	Min.	Max.	Mean (SD)	Min.	Max.	Mean (SD)	Min.	Max.
Group 1 (type I)	1.52 (0.76)	0.40	2.70	1.64 (0.56)	0.70	2.40	1.64 (0.59)	0.76	2.62	1.21 (0.55)	0.10	1.90
Group 2 (type III)	1.61 (0.76)	0.40	2.90	1.85 (0.41)	1.10	2.50	1.87 (0.26)	1.40	2.26	1.52 (0.64)	0.60	2.80
Group 3 (superior)	1.47 (1.27)	0.10	3.60	1.20 (0.87)	0.20	2.70	2.02 (0.93)	0.61	3.88	2.22 (0.79)	0.50	3.80
Group 4 (inferior)	1.98 (1.13)	0.50	4.00	1.01 (0.60)	0.10	2.00	1.39 (0.75)	0.29	2.62	1.11 (0.52)	0.20	1.80

Table 6. 2: Mean prediction errors when comparing the results of missing part prediction with original surface meshes of external scapulae for distance and similarity measures. Min.: Minimum error value, Max.: Maximum error value, SD: Standard deviation.

Virtual Defect Group	Distance Measures									Similarity Measure		
	Mean (mm)			Hausdorff (mm)			RMS			Dice Coefficient		
	Mean (SD)	Min.	Max.	Mean (SD)	Min.	Max.	Mean (SD)	Min.	Max.	Mean (SD)	Min.	Max.
Group 1 (type I)	0.91 (0.15)	0.69	1.14	5.61 (1.63)	3.81	8.41	1.21 (0.21)	0.88	1.54	0.82 (0.03)	0.75	0.86
Group 2 (type III)	0.97 (0.14)	0.77	1.21	5.84 (0.97)	4.11	7.04	1.30 (0.19)	1.02	1.59	0.81 (0.02)	0.76	0.86
Group 3 (superior)	0.94 (0.15)	0.74	1.22	5.03 (1.95)	1.21	8.50	1.29 (0.28)	0.96	1.96	0.82 (0.03)	0.77	0.87
Group 4 (inferior)	0.95 (0.21)	0.67	1.44	5.86 (2.21)	3.12	9.90	1.28 (0.33)	0.85	1.98	0.84 (0.01)	0.79	0.85

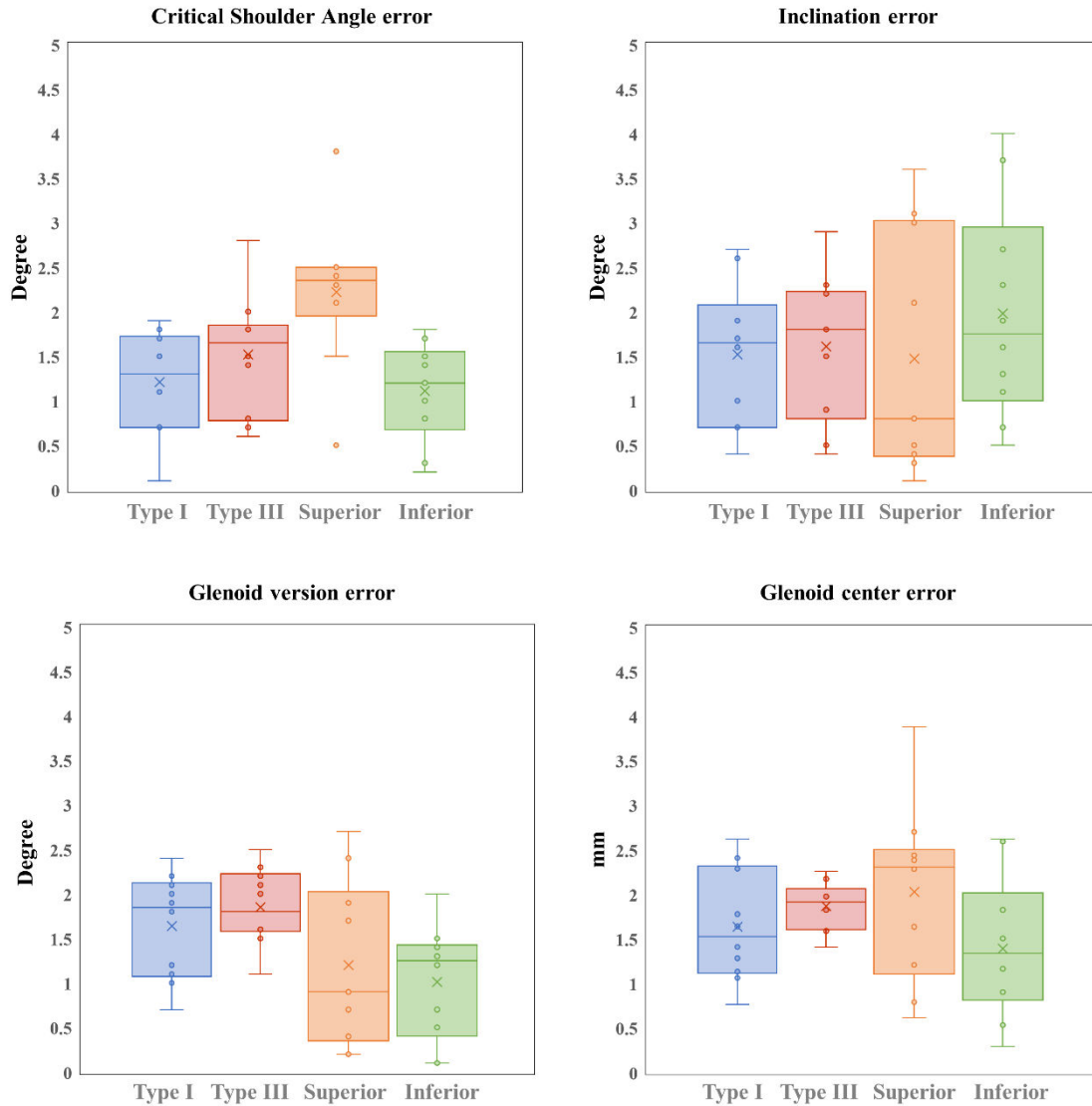


Figure 6. 5: Box plots indicating the prediction errors in Critical shoulder angle (top left), Glenoid inclination (top right), Glenoid version (bottom left), and Glenoid center (bottom right) for each type of defect (type I, type III, Superior, and Inferior). Each box corresponds to inter-quartile range of 50%. The median values are indicated by horizontal line whereas the mean values are indicated by x marker inside each box. The upper and lower whiskers indicate the values outside the middle 50%.

6.4 Discussion

Complete and accurate scapular shape reconstruction from partial data is an important aspect for multiple applications including surgical framework, computational modeling, and morphological assessment. This study illustrated the ability and accuracy of scapular bone SSM of French adult population in predicting missing scapular bone shape in its different regions. The combination of IMCP-GPMM and Gaussian

process regression algorithm employed in this study allowed us to reconstruct the shape of the scapula with higher accuracy in terms of anatomical, similarity, and distance measures, as compared with other studies. Such predictive capabilities can be employed in surgery pre-planning as well as developing patient-specific musculoskeletal models of the shoulder joint.

Anterior instability of the shoulder is a common and multifactorial problem, with osseous lesions existing on the glenoid, the humeral head or in combination [52]. In older patients, the risk of instability ranges from 10% to 20% [53]. Such glenoid instability invariably leads to glenoid bone loss and needs surgical correction. During the surgical treatment of glenoid instability (for e.g. shoulder arthroplasty), the information about pre-morbid glenoid anatomy is of prime importance as it can help identify the dimensions of bone plugs to lateralize the glenoid enough to match with its pre-morbid length. The virtual defects created in this study (glenoid defect of type I and type III) simulated this problem and prediction errors were much lower when compared to a recently published study [21]. In their study, Plessers and colleagues [21] used SSM based reconstruction method to reconstruct glenoid bone defects simulated in healthy scapular shapes. They reported prediction errors in glenoid inclination and version as 2.4° and 2.9° for type I defect and 3.4° and 2.9° for type III defect respectively. Compared to these, the prediction errors observed in our study were significantly lower in all the categories (Figure 6.6). Further, the standard deviation and maximum errors were also lower in our study in glenoid inclination as well as glenoid version as compared to the ones reported in Plessers [21](Figure 6). Plessers and colleagues did not report prediction errors in CSA or distance errors in terms of mean error or Hausdorff distance errors. Improvements in prediction accuracy could be attributed to the implementation of GPMM. The SSM developed by Plessers was based on PDM approach which may force an early discretization of the sample space. To make such models work efficiently and express all the possible target shapes, a very high number of training data is needed [25]. GPMM process, on the other hand, makes the sample space continuous by estimating the covariances from sample data and defining a probabilistic model directly on deformations, making them independent of discretization [25].

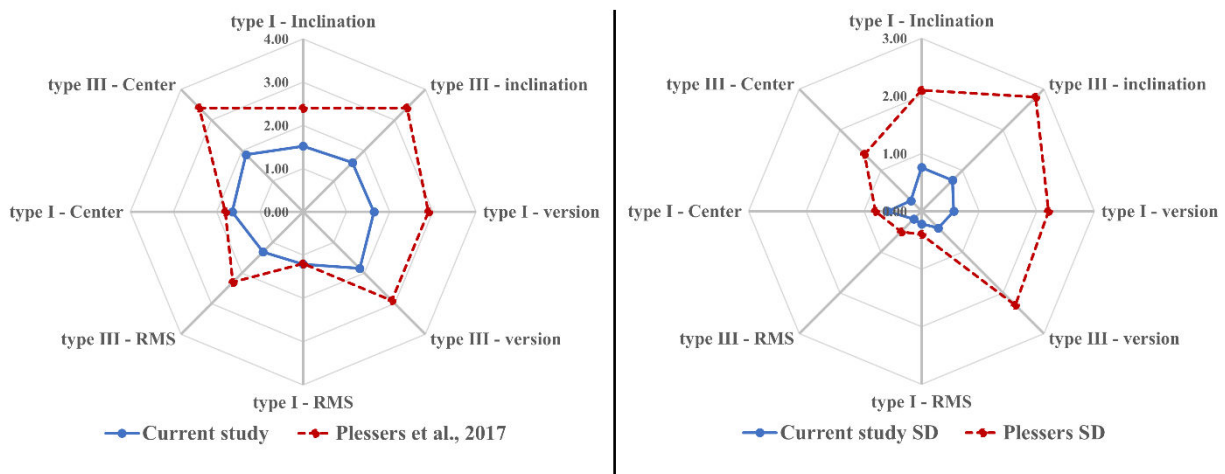


Figure 6. 6: Comparison of prediction errors of the current study with those reported by Plessers et al. [21]. Left web chart compares the errors between two studies whereas right web chart compares the standard deviation associated with respective errors.

Accurately identifying anatomical parameters such as glenoid version is vital during shoulder reconstruction surgery [54, 55] as surgical strategies can change significantly in the presence of higher retro- and ante-version of the glenoid [56]. The glenoid version directly affects the humeral head displacement and the biomechanics of the glenoid component after total shoulder arthroplasty [56, 57]. Literature reports that pre-morbid glenoid version and inclination does not change in individuals with shoulder arthritis [58]. Thus, previously proposed glenoid vault model can be primarily used to predict these measures [18]. However, glenoid vault method can only be applicable to Walch Type B2 glenoid [59] and may not be extrapolated for other glenoid types [60]. To overcome this limitation, Abler and colleagues [20] used SSM of healthy glenoid-only region to reconstruct the premorbid glenoid cavity in 30 scapulae with glenoid osteoarthritis (OA). Using this glenoid-only SSM, Abler et al., reported that the predicted glenoid version was changed towards the healthy anatomical mean [20]. Since no pre-morbid anatomical characteristics were known a priori, there was no way to find whether such change towards healthy mean was desirable in every case. Further, the glenoid-only SSM relied on the assumption that OA affected only a smaller area near glenoid cavity and in cases where OA affects larger region including acromion and coracoid processes, this approach had limited utility. In contrast, our approach used the entire healthy scapular bone shape to build the SSM which incorporated the covariance information for the entire shape. Using our approach, surgeons can identify the OA affected area in the pre-surgery planning tool and not include it in the reconstruction process. This method would effectively provide more control to surgeons and will help predict the pre-morbid shape with better accuracy.

The example shapes used in this study to evaluate the performance of our reconstruction algorithm were categorically selected to map all types of scapular anatomical classification. This method allowed us to identify which scapular shapes are harder to reconstruct. In general, for anatomical measures, scapular shapes with higher and lower CSA were harder to predict as higher prediction errors existed for these scapulae for all anatomical measures including glenoid version, glenoid inclination, and CSA. We also observed that scapular shapes with type III defect (Group 2) were harder to predict (higher prediction errors) over type I defect (Group 1). When the superior part was missing (Group 3), prediction of CSA and glenoid center was difficult indicating that superior region has a higher correlation with these measures. When the inferior part was missing (Group 4), glenoid inclination prediction error was highest indicating that inferior region has a stronger correlation with this anatomical measure.

While we reported absolute prediction errors in the results, we also analyzed the under- or over-prediction of errors in each defect group. In general, retroversion was always underpredicted except in case of higher and lower CSA types in each defect group. Glenoid inclination was evenly predicted in Group 1 and Group 2 but always overpredicted in Group 3 and Group 4 (except scapula with high CSA). The overprediction indicated that either the floor of supraspinatus fossa was reconstructed with a more medial tilt in the frontal plane or the glenoid rim was tilted more laterally in the frontal plane. Further evaluations based on the distance errors between the original and reconstructed shapes indicated that overprediction was due to more laterally tilted glenoid rim in the frontal plane. CSA prediction errors had interesting results with evenly distributed predictions in Group 1, underpredictions in Group 2, and mostly overpredictions in Group 3 and Group 4. This indicated the reliance of CSA on available partial information and suggested that CSA predictions should be dealt with more caution with such reconstruction algorithms.

This study has certain limitations. The gaussian process regression algorithm used for fitting was generic and was not customized for any defect group unlike the ones reported by two other studies [20, 21]. Furthermore, the regression algorithm used first 15 principal components and was limited to 20 iterations of non-rigid registration. We believe that removing these constraints may increase the prediction accuracy further but may not be significant enough. Upon evaluating the reconstruction algorithm results for Group 1 and Group 2 defects on the same scapular shape, we found that same combination of principal components was not used. This is due to the fact that the SSM considered the prior knowledge as a different set between the two defects and thus resulted in different PC combinations. Another limitation of the study was that we inherently introduced a possibility of error while manually selecting landmarks in the rigid alignment process. This may contribute error in prediction but since we allotted a standard error of 0.5mm to the landmark selection while creating the posterior model, we assumed that such error propagation would be minimal.

The results of this study have greater implications for building musculoskeletal models for biomechanical analysis. Building bone geometries through the manual segmentation of medical images is the current gold standard to build patient-specific models. However, such approach is always time consuming and in many cases is limited by the incomplete imaging data. Recent studies have demonstrated the use of SSM to segment pelvis bones and scaling the lower limb musculoskeletal model [61, 62]. Apart from building accurate bone geometries, the current framework can also be effectively employed in deriving patient-specific muscle insertion regions as reported by Salhi and associates [63]. The similarity coefficients reported in this study support the use of predicted geometries in biomechanics models using finite element domains. Future work is targeted in improving prediction accuracy and focusing on the regions with higher Hausdorff distances and also validating the model predictions with deformed scapular shapes.

6.5 Conclusion

For shoulder disorders, pre-morbid glenoid joint, as well as complete anatomy of the scapula and humerus, remains an important reference for both surgical planning for shoulder joint-replacement procedures, and biomechanics research to understand shoulder joint functionality. While there exists a literature on entire humerus and glenoid region of the scapula, no work is previously reported on the entire scapular bone. We have addressed the estimation of entire pre-morbid scapular geometry from patient's remaining scapular bone shape. A data-driven-based IMCP-GPMM process provided an SSM able to fit the remaining part, predict the missing part and reconstruct the entire scapular bone. The SSM was evaluated in terms of compacity, generality, and specificity with excellent results compared to the literature. A Gaussian regression-based reconstruction algorithm was developed specifically for this SSM. Two types of validation confirmed that our SSM is a moderate to excellent predictor of the missing part in the glenoid, inferior, or superior region. Mesh distances and anatomical features deduced from the reconstructed shape outperformed the results of the state-of-art. Such framework can be effectively implemented in pre-surgery planning or shoulder biomechanics modeling pipelines.

4.6 Chapter 6 References

- [1] C. A. Rockwood, Jr. and F. A. Matsen, III, Eds., *The Shoulder, 2 Volume Set*. Philadelphia, PA: Saunders, 2009, p.^pp. Pages.
- [2] P. Boileau, D. J. Watkinson, A. M. Hatzidakis, and F. Balg, "Grammont reverse prosthesis: design, rationale, and biomechanics," *J Shoulder Elbow Surg*, vol. 14, pp. 147S-161S, Jan-Feb 2005.
- [3] C. S. Neer, 2nd, "The classic: Articular replacement for the humeral head. 1955," *Clin Orthop Relat Res*, vol. 469, pp. 2409-21, Sep 2011.
- [4] F. Sirveaux, L. Favard, D. Oudet, D. Huquet, G. Walch, and D. Mole, "Grammont inverted total shoulder arthroplasty in the treatment of glenohumeral osteoarthritis with massive rupture of the cuff. Results of a multicentre study of 80 shoulders," *J Bone Joint Surg Br*, vol. 86, pp. 388-95, Apr 2004.
- [5] B. Wall, L. Nove-Josserand, D. P. O'Connor, T. B. Edwards, and G. Walch, "Reverse total shoulder arthroplasty: a review of results according to etiology," *J Bone Joint Surg Am*, vol. 89, pp. 1476-85, Jul 2007.
- [6] C. S. Neer, 2nd, E. V. Craig, and H. Fukuda, "Cuff-tear arthropathy," *J Bone Joint Surg Am*, vol. 65, pp. 1232-44, Dec 1983.
- [7] M. Frankle, S. Siegal, D. Pupello, A. Saleem, M. Mighell, and M. Vasey, "The Reverse Shoulder Prosthesis for glenohumeral arthritis associated with severe rotator cuff deficiency. A minimum two-year follow-up study of sixty patients," *J Bone Joint Surg Am*, vol. 87, pp. 1697-705, Aug 2005.
- [8] H. Sugaya, J. Moriishi, M. Dohi, Y. Kon, and A. Tsuchiya, "Glenoid rim morphology in recurrent anterior glenohumeral instability," *J Bone Joint Surg Am*, vol. 85-A, pp. 878-84, May 2003.
- [9] D. Mori, J. A. Abboud, S. Namdari, and G. R. Williams, "Glenoid bone loss in anatomic shoulder arthroplasty: literature review and surgical technique," *Orthop Clin North Am*, vol. 46, pp. 389-97, x, Jul 2015.
- [10] A. J. Seidl, G. R. Williams, and P. Boileau, "Challenges in Reverse Shoulder Arthroplasty: Addressing Glenoid Bone Loss," *Orthopedics*, vol. 39, pp. 14-23, Jan-Feb 2016.
- [11] A. Kontaxis and G. R. Johnson, "The biomechanics of reverse anatomy shoulder replacement--a modelling study," *Clin Biomech (Bristol, Avon)*, vol. 24, pp. 254-60, Mar 2009.
- [12] M. Masjedi and G. R. Johnson, "Reverse anatomy shoulder replacement: comparison of two designs," *Proc Inst Mech Eng H*, vol. 224, pp. 1039-49, 2010.
- [13] M. M. Morrow, K. R. Kaufman, and K. N. An, "Shoulder model validation and joint contact forces during wheelchair activities," *J Biomech*, vol. 43, pp. 2487-92, Sep 17 2010.
- [14] M. Zheng, Z. Zou, P. J. Bartolo, C. Peach, and L. Ren, "Finite element models of the human shoulder complex: a review of their clinical implications and modelling techniques," *Int J Numer Method Biomed Eng*, vol. 33, Feb 2017.
- [15] K. Eraly, P. Debeer, F. Gelaude, T. Clijmans, I. Jonkers, and J. Vander Sloten, "CT-based virtual shape reconstruction for severe glenoid bone defects.," presented at the Symposium of the ISB Technical Group on Computer Simulation 13th edition, Leuven, Belgium, 2011.

- [16] K. Eraly, P. Debeer, I. Jonkers, and J. Vander Sloten, "CT-based computerized planning method for shape reconstruction of severe glenoid defects," presented at the EFORT, Berlin, Germany, 2012.
- [17] F. Gelaude, T. Clijmans, P. L. Broos, B. Lauwers, and J. Vander Sloten, "Computer-aided planning of reconstructive surgery of the innominate bone: automated correction proposals," *Comput Aided Surg*, vol. 12, pp. 286-94, Sep 2007.
- [18] J. J. Scalise, M. J. Codsì, J. Bryan, and J. P. Iannotti, "The three-dimensional glenoid vault model can estimate normal glenoid version in osteoarthritis," *J Shoulder Elbow Surg*, vol. 17, pp. 487-91, May-Jun 2008.
- [19] A. Ganapathi, J. A. McCarron, X. Chen, and J. P. Iannotti, "Predicting normal glenoid version from the pathologic scapula: a comparison of 4 methods in 2- and 3-dimensional models," *J Shoulder Elbow Surg*, vol. 20, pp. 234-44, Mar 2011.
- [20] D. Abler, S. Berger, A. Terrier, F. Becce, A. Farron, and P. Buchler, "A statistical shape model to predict the pre-morbid glenoid cavity," *J Shoulder Elbow Surg*, vol. 27, pp. 1800-1808, Oct 2018.
- [21] K. Plessers, P. Vanden Berghe, C. Van Dijck, R. Wirix-Speetjens, P. Debeer, I. Jonkers, *et al.*, "Virtual reconstruction of glenoid bone defects using a statistical shape model," *J Shoulder Elbow Surg*, vol. 27, pp. 160-166, Jan 2018.
- [22] S. Poltaretskyi, J. Chaoui, M. Mayya, C. Hamitouche, M. J. Bercik, P. Boileau, *et al.*, "Prediction of the pre-morbid 3D anatomy of the proximal humerus based on statistical shape modelling," *Bone Joint J*, vol. 99-B, pp. 927-933, Jul 2017.
- [23] L. Vlachopoulos, M. Luthi, F. Carrillo, C. Gerber, G. Szekely, and P. Furnstahl, "Restoration of the Patient-Specific Anatomy of the Proximal and Distal Parts of the Humerus: Statistical Shape Modeling Versus Contralateral Registration Method," *J Bone Joint Surg Am*, vol. 100, p. e50, Apr 18 2018.
- [24] S. Brownlee, K. Chalkidou, J. Doust, A. G. Elshaug, P. Glasziou, I. Heath, *et al.*, "Evidence for overuse of medical services around the world," *Lancet*, vol. 390, pp. 156-168, Jul 8 2017.
- [25] M. Luthi, T. Gerig, C. Jud, and T. Vetter, "Gaussian Process Morphable Models," *IEEE Trans Pattern Anal Mach Intell*, vol. 40, pp. 1860-1873, Aug 2018.
- [26] J. J. Jacq, C. Schwartz, V. Burdin, R. Gerard, C. Lefevre, C. Roux, *et al.*, "Building and tracking root shapes," *IEEE Trans Biomed Eng*, vol. 57, pp. 696-707, Mar 2010.
- [27] B. Borotikar, T. Mutsvangwa, V. Burdin, E. Ghorbel, M. Lempereur, S. Brochard, *et al.*, "Augmented Statistical Shape Modeling for Orthopaedic Surgery and Rehabilitation," in *Medical Image Analysis and Informatics: Computer-Aided Diagnosis and Therapy*, P. M. d. Azevedo-Marques, A. Mencattini, M. Salmeri, and R. M. Rangayyan, Eds., ed Florida, USA: CRC Press, Taylor and Francis Group, 2017, pp. 369-426.
- [28] T. Mutsvangwa, V. Burdin, C. Schwartz, and C. Roux, "An automated statistical shape model developmental pipeline: application to the human scapula and humerus," *IEEE Trans Biomed Eng*, vol. 62, pp. 1098-107, Apr 2015.
- [29] J. J. Jacq, T. Cresson, V. Burdin, and C. Roux, "Performing accurate joint kinematics from 3-D in vivo image sequences through consensus-driven simultaneous registration," *IEEE Trans Biomed Eng*, vol. 55, pp. 1620-33, May 2008.
- [30] A. Myronenko and X. Song, "Point set registration: coherent point drift," *IEEE Trans Pattern Anal Mach Intell*, vol. 32, pp. 2262-75, Dec 2010.

- [31] M. Lüthi. (2014). *SCALable Image analysis and Shape MOdelling*. Available: <https://github.com/unibas-gravis/scalismo>
- [32] I. Jolliffe, "Principal Component Analysis," *Wiley StatsRef: Statistics Reference Online*, 2014/09/29 2014.
- [33] A. Merrill, K. Guzman, and S. L. Miller, "Gender differences in glenoid anatomy: an anatomic study," *Surg Radiol Anat*, vol. 31, pp. 183-9, Mar 2009.
- [34] R. W. Nyffeler and D. C. Meyer, "Acromion and glenoid shape: Why are they important predictive factors for the future of our shoulders?," *EFORT Open Rev*, vol. 2, pp. 141-150, May 2017.
- [35] L. Cherchi, J. F. Ciornochac, J. Godet, P. Clavert, and J. F. Kempf, "Critical shoulder angle: Measurement reproducibility and correlation with rotator cuff tendon tears," *Orthop Traumatol Surg Res*, vol. 102, pp. 559-62, Sep 2016.
- [36] D. M. Rouleau, J. F. Kidder, J. Pons-Villanueva, S. Dynamidis, M. Defranco, and G. Walch, "Glenoid version: how to measure it? Validity of different methods in two-dimensional computed tomography scans," *J Shoulder Elbow Surg*, vol. 19, pp. 1230-7, Dec 2010.
- [37] P. Cignoni, M. Callieri, M. Corsini, M. Dellepiane, F. Ganovelli, and G. Ranzuglia, "MeshLab: an Open-Source Mesh Processing Tool," in *Eurographics Italian Chapter Conference*, Italy, 2008.
- [38] G. Kocsis, D. S. Thyagarajan, K. J. Fairbairn, and W. A. Wallace, "A new classification of glenoid bone loss to help plan the implantation of a glenoid component before revision arthroplasty of the shoulder," *Bone Joint J*, vol. 98-B, pp. 374-80, Mar 2016.
- [39] Z. Zhang, "Iterative point matching for registration of free-form curves and surfaces," *International Journal of Computer Vision*, vol. 13, pp. 119-152, 1994/10/01 1994.
- [40] P. J. Besl and N. D. McKay, "A method for registration of 3-D shapes," *IEEE Transactions on Pattern Analysis and Machine Intelligence*, vol. 14, pp. 239-256, 1992.
- [41] J. C. Gower, "Generalized procrustes analysis," *Psychometrika*, vol. 40, pp. 33-51, 1975/03/01 1975.
- [42] T. Albrecht, M. Luthi, T. Gerig, and T. Vetter, "Posterior shape models," *Med Image Anal*, vol. 17, pp. 959-73, Dec 2013.
- [43] M. Lüthi, C. Jud, and T. Vetter, "Using Landmarks as a Deformation Prior for Hybrid Image Registration," in *Pattern Recognition*, Berlin, Heidelberg, 2011, pp. 196-205.
- [44] C. Letta, A. Schweizer, and P. Furnstahl, "Quantification of contralateral differences of the scaphoid: a comparison of bone geometry in three dimensions," *Anat Res Int*, vol. 2014, p. 904275, 2014.
- [45] M. Dubuisson and A. K. Jain, "A modified Hausdorff distance for object matching," in *Proceedings of 12th International Conference on Pattern Recognition*, 1994, pp. 566-568 vol.1.
- [46] D. P. Huttenlocher, G. A. Klanderman, and W. A. Rucklidge, "Comparing Images Using the Hausdorff Distance," *IEEE Trans. Pattern Anal. Mach. Intell.*, vol. 15, pp. 850-863, 1993.
- [47] R. J. Friedman, K. B. Hawthorne, and B. M. Genez, "The use of computerized tomography in the measurement of glenoid version," *JBJS*, vol. 74, pp. 1032-1037, 1992.

- [48] U. Kandemir, R. B. Allaire, J. T. Jolly, R. E. Debski, and P. J. McMahon, "The relationship between the orientation of the glenoid and tears of the rotator cuff," *J Bone Joint Surg Br*, vol. 88, pp. 1105-9, Aug 2006.
- [49] B. K. Moor, S. Bouaicha, D. A. Rothenfluh, A. Sukthankar, and C. Gerber, "Is there an association between the individual anatomy of the scapula and the development of rotator cuff tears or osteoarthritis of the glenohumeral joint?: A radiological study of the critical shoulder angle," *Bone Joint J*, vol. 95-B, pp. 935-41, Jul 2013.
- [50] T. Suter, A. Gerber Popp, Y. Zhang, C. Zhang, R. Z. Tashjian, and H. B. Henninger, "The influence of radiographic viewing perspective and demographics on the critical shoulder angle," *J Shoulder Elbow Surg*, vol. 24, pp. e149-58, Jun 2015.
- [51] L. R. Dice, "Measures of the Amount of Ecologic Association Between Species," *Ecology*, vol. 26, pp. 297-302, 1945/07/01 1945.
- [52] G. H. Garcia, J. N. Liu, D. M. Dines, and J. S. Dines, "Effect of bone loss in anterior shoulder instability," *World J Orthop*, vol. 6, pp. 421-33, Jun 18 2015.
- [53] L. Hovelius, A. Olofsson, B. Sandstrom, B. G. Augustini, L. Krantz, H. Fredin, *et al.*, "Nonoperative treatment of primary anterior shoulder dislocation in patients forty years of age and younger. a prospective twenty-five-year follow-up," *J Bone Joint Surg Am*, vol. 90, pp. 945-52, May 2008.
- [54] D. Weishaupt, M. Zanetti, R. W. Nyffeler, C. Gerber, and J. Hodler, "Posterior glenoid rim deficiency in recurrent (atraumatic) posterior shoulder instability," *Skeletal Radiol*, vol. 29, pp. 204-10, Apr 2000.
- [55] M. A. Wirth, D. G. Seltzer, and C. A. Rockwood, Jr., "Recurrent posterior glenohumeral dislocation associated with increased retroversion of the glenoid. A case report," *Clin Orthop Relat Res*, pp. 98-101, Nov 1994.
- [56] R. W. Nyffeler, R. Sheikh, T. S. Atkinson, H. A. Jacob, P. Favre, and C. Gerber, "Effects of glenoid component version on humeral head displacement and joint reaction forces: an experimental study," *J Shoulder Elbow Surg*, vol. 15, pp. 625-9, Sep-Oct 2006.
- [57] M. Al Najjar, S. S. Mehta, and P. Monga, "Three dimensional scapular prints for evaluating glenoid morphology: An exploratory study," *J Clin Orthop Trauma*, vol. 9, pp. 230-235, Jul-Sep 2018.
- [58] E. T. Ricchetti, M. D. Hendel, D. N. Collins, and J. P. Iannotti, "Is premorbid glenoid anatomy altered in patients with glenohumeral osteoarthritis?," *Clin Orthop Relat Res*, vol. 471, pp. 2932-9, Sep 2013.
- [59] G. Walch, T. B. Edwards, A. Boulahia, P. Boileau, D. Mole, and P. Adeleine, "The influence of glenohumeral prosthetic mismatch on glenoid radiolucent lines: results of a multicenter study," *J Bone Joint Surg Am*, vol. 84-A, pp. 2186-91, Dec 2002.
- [60] T. B. Edwards, "CORR Insights (R): Is premorbid glenoid anatomy altered in patients with glenohumeral osteoarthritis?," *Clin Orthop Relat Res*, vol. 471, pp. 2940-1, Sep 2013.
- [61] J. S. Bahl, J. Zhang, B. A. Killen, M. Taylor, L. B. Solomon, J. B. Arnold, *et al.*, "Statistical shape modelling versus linear scaling: Effects on predictions of hip joint centre location and muscle moment arms in people with hip osteoarthritis," *J Biomech*, Jan 24 2019.

- [62] E. K. Suwarganda, L. E. Diamond, D. G. Lloyd, T. F. Besier, J. Zhang, B. A. Killen, *et al.*, "Minimal medical imaging can accurately reconstruct geometric bone models for musculoskeletal models," *PLoS One*, vol. 14, p. e0205628, 2019.
- [63] A. Salhi, V. Burdin, T. Mutsvangwa, S. Sivarasu, S. Brochard, and B. Borotikar, "Subject-specific shoulder muscle attachment region prediction using statistical shape models: A validity study," *Conf Proc IEEE Eng Med Biol Soc*, vol. 2017, pp. 1640-1643, Jul 2017.

Part III: Musculoskeletal modeling of pediatric shoulder joint model

Chapter 7

Obstetrical Brachial Plexus Palsy and its evaluation using musculoskeletal modeling: state of the art and challenges

7.1 Introduction

While adult shoulder complex is a fully functional and strong joint, it is not the case with the pediatric shoulder joint. All the bones and muscles are developing through the early phases of childhood and up until adolescent phase or even beyond that in certain cases. Since the global aim of my research is to target pediatric shoulder disorder such as Obstetrical Brachial Plexus Palsy (OBPP), it is important to understand the pediatric shoulder complex structure in the backdrop of our understanding of adult structure as the modeling needs are very different in the pediatric structure. Barring any setbacks, the shoulder complex grows into a stronger and robust structure capable of handling multiple synergistic activities of muscles to provide a fine arm motion (as explained in Chapter 3). However, a perturbation during the development of these structures adversely impacts the healthy growth, normal function, and functional requirements. The maturation of shoulder complex happens sequentially. A newborn has humerus, scapula, and clavicle bones ossified but not fully grown [1]. Each of these bones has multiple ossification centers and skeletal maturation happens as these ossification centers expand themselves and ultimately fuse with each other at the final maturation stage.

A perturbation during child's development leads to impaired shoulder function. This perturbation can be due to a disease or injury. OBPP is one such injury that perturbs the growth and function of the pediatric shoulder. OBPP, also known as birth brachial plexus injury, is an injury of one or several brachial plexus nerve roots that happens during a difficult delivery. OBPP is relatively uncommon, with a rate of incidence between 0.4 and 4 per 1000 newborn in the United States [2]. However, this injury has a debilitating impact on children as their shoulder function is impaired throughout their growth and may even continue after they attain skeletal maturity. In section 2 of this chapter, we will have a brief description of OBPP pathology, its causes and biomechanical impact studied previously in the literature. In the third section, we will review pediatric MSK shoulder models, their use to simulate or evaluate pathologies and the way the modeling parameters used in these models. OBPP pathology being the research scope of this thesis, we will then explain in detail the musculoskeletal (MSK) modeling techniques used for OBPP evaluation in section four. At the end of this chapter, the limitations and the challenges faced by the pediatric MSK modeling studies are discussed in section five.

7.2 Obstetrical Brachial Plexus Palsy OBPP

7.2.1 Description of the pathology

The brachial plexus is a group of nerves originating from the four cervical spine bones viz. C5, C6, C7 and C8 and the first thoracic spine bone T1. This network of nerves controls the function and movement of shoulder, arm and hand. Injury to one or more bundles of these nerves happens during childbirth and leads to impaired shoulder function. Although discovered and named in the 18th century by an English obstetrician, French obstetricians and surgeons have a significant contribution to OBPP research in terms of understanding pathophysiology, devising surgical procedures, and developing clinical sciences [3].

This injury is typically classified into four groups [4]:

- 1) Group 1: Upper Erb's palsy in which the nerves originating from C5 and the C6 are injured and this is the most frequent paralysis with the highest rate of spontaneous recovery.
- 2) Group 2: Extended Erb's palsy in which the nerves from C5 to C7 are injured.
- 3) Group 3: Total palsy, nerves originating from C5 to T1 are injured leading to total paralysis of the upper limb.
- 4) Group 4: total palsy with Horner syndrome, same nerves as group 3 are injured, This injury has the worst functional outcome.

The risk factors (causes) of OBPP vary from one population to another, but the most common could be fetal weight (high birth weight, aka fetal macrosomia), maternal complications (obesity, diabetes, advanced age) and difficulties at the time of delivery (shoulder dystocia, vacuum delivery, vaginal breech deliveries) [5]–[7]. But the occurrence of this injury stays unpredictable and unpreventable because it can happen even after a normal labor and delivery [6], [7]. Although the rate of spontaneous recovery is reported in most of the cases, there are certain cases where the injury persists and leads to serious functional disability [8].

Depending on the stage and the phase of the injury, different treatment strategies could be employed. These treatments include daily physical therapy exercises, botulinum toxin injections, nerve surgical interventions and an advanced stage of the injury may require secondary surgeries, such as tendon/muscle transfer surgery or osteotomies of the humerus or the glenoid [2].

7.2.2 Musculoskeletal impact of OBPP

In more than 75% of the cases, when the injury happens, the child recovers without any further consequences to the musculoskeletal structure of the shoulder complex. However, when the OBPP persists, it adversely affects the musculoskeletal structure and function of the shoulder joint. Such consequences lead to a perturbation of the shoulder complex affecting all the four joints AC, ST, SC, and GH [2]. Further, such pathology may prolong throughout the life. The functional limitations are mainly observed as the contracture in internal rotation or passive external rotation, and other motions with less limitations. The musculoskeletal structural deformation happens as a chain of events. First, the nerve

injury affects the GH musculature, which limits the GH joint ROM. This leads to a mechanical constraint or alteration in terms of joint forces and moments and thus in turn affects the normal development growth of shoulder bones. With the age advancement, this osseous deformation contributes in disturbing the muscular function and the shoulder movement in general and this cycle continues. Many studies have focused on understanding this causative relationship of OBPP pathology from different perspectives. Here, we will describe what has been reported in the literature so far in terms of shoulder osseous deformation and muscular deficiency in children with OBPP.

7.2.2.1 Osseous deformation

OBPP impacts all the bones of the shoulder complex in three ways 1) rate of bone growth, 2) bone morphology, and 3) bone strength. These three ways perturb the shoulder resting pose as well as function in a combined or isolated manner. In general, bone deformities start appearing from first months of age, as observed in an MRI study of the humerus [9], and progress rapidly. Let's consider the nature and impact of each bone and its regions:

Clavicle: In the presence of shoulder dystocia for children with OBPP, there is high risk of fractures of the clavicle. However, this is not solely regarded as an indicator of the risk level of OBPP [10].

Scapula: For scapula, the bone deformities are more pronounced in OBPP than other bones and are also frequently studied. Scapula shows a decreased rate of bone growth which can be explained as the result of the decreased level of applied forces by the scapula stabilizer muscles [11]. Nath RK and Paizi M showed that the ratio of the height to the width of scapular body, excluding acromion has no significant change as compared with the unaffected side, whereas the acromion region was elongated by an average of 19% [11]. In the same study [11], they also proposed a SHEAR (Scapular Hypoplasia, Elevation and Rotation) classification of the scapular deformities, which can give an objective evaluation of the scapular deformity in OBPP.

Coracoid process: Coracoid process also may undergo a hooking effect due to OBPP [12]. Glenoid region of the scapula is the most studied part when the question of the scapular bony deformity is addressed as it forms the articulating surface with the humerus and small deviation from the normal morphology may considerably affect the GH mobility.

Glenoid: In OBPP, glenoid is the most deformed region of the scapula [12]–[14]. The morphological abnormality of the glenoid is mostly quantified through retroversion, orientation and concavity. A study comparing 3D measures of the impaired and the non-impaired side in children with OBPP reported that the glenoid is highly retroverted (12.1° against a normal side of 4.2°), and inferiorly oriented (16° against a normal side of 8.7°) in the impaired side [13]. Such high retroversion of the glenoid is believed to lead to a progressive subluxation of the humeral head [2]. Further, the concavity of glenoid cavity is also pronounced with most of the glenoid cavity being concave [13]. These morphological changes in scapula lead to mal-positioning of the humerus with respect to scapula in all three directions [11].

Humerus: Due to OBPP, the humeral head is reported to have smaller size due to osseous atrophy as compared to non-impaired side [15]. Further, it also gets more flattened shape [12]. Other deformities are mostly mal-positioning due to the changes in the glenoid region of the scapula. Compared to the non-impaired side, the humeral head is reported to be migrated more posteriorly (5.54 mm, $p = 0.007$),

inferiorly (-3.96 mm, $p = 0.013$), and medially (-3.63 mm, $p = 0.002$) [13]. It is also reported to be less retroverted, externally rotated, and in declination on the OBPP side. This humeral head migration then progresses towards a total subluxation [2].

7.2.2.2 Muscular pathology

When we address the question of muscular deficiency, the use of MR imaging modality is a standard clinical practice [16]. In fact, this non-invasive technique allows the quantitative evaluation of each muscle and it has been proved that the muscular morphological abnormality (atrophy) is significantly correlated with limited functionality and the osseous deformity of the GH joint. This correlation was quantified in many studies [16]–[20]. The neurological damage, following OBPP, causes muscle denervation which in turn induces a change in the neuromuscular activity affecting the contractile property of the muscle [21]. The decrease of the mechanical need as a result of the palsy of the shoulder also has consequences on muscles, such as atrophy or a change in the muscular composition with alteration of their functional properties [22].

Subscapularis: In children with OBPP, the studies evaluating the muscle damage most of time focus on understanding the correlation of this muscular abnormality, the osseous deformation and the biomechanics of its functional limitation. These studies specifically highlighted the important damage of the subscapularis muscle with a severe atrophy [16], [18], [20], [23], increased stiffness and reduction in the sarcomere length [24]. The severity of subscapularis muscle atrophy was found to be correlated to the subluxation of the humeral head [16].

Infraspinatus: A notable atrophy of the infraspinatus muscle has been found and reported [16], [18], [20], [23].

Deltoid: The deltoid muscle being innervated by brachial plexus nerve, was also reported to be atrophic in OBPP [17].

Rotator cuff muscles: In general, all the muscles crossing the GH joint in children with OBPP, and more especially the rotator cuff muscle, are considered atrophic [16], [25], with different level of atrophy which induces a muscle imbalance. The rotator cuff muscle atrophy was found to be increased with the glenoid retroversion [16]. In many studies, the muscle atrophy is quantified using muscle volume or cross-sectional area [19], [23], [26], [27]. In a study by Van Gelein Vitringa et al, the subscapularis muscle volume was quantified to be 64% smaller in size as compared with its volume in the unaffected side [23].

The shoulder muscles imbalance between the agonists and antagonists may also explain the shoulder functional limitations in terms of retraction and joint stiffness [2]. In the next part, the impact of muscular efficiency on functional limitation in children with OBPP will be explained.

7.2.3 Biomechanical description of OBPP (the impact on kinematics)

In children with OBPP, shoulder 3D kinematic analysis is a valuable way to quantify the kinematic limitations and complete clinical examination [28]. And as mentioned above, the osseous deformation, muscular damage and function are highly correlated:

- (bone-motion) **The external rotation** contracture is correlated with the retroversion and posterior subluxation of the humeral head [14].

- The **internal rotation** contracture is correlated with the increase of the glenoid retroversion and severity of the rotator cuff muscle atrophy [16].
- (nerve-motion) The injury of C5C6 (Known as Erb’s palsy) leads to a deficiency of shoulder **abduction and external rotation**, whereas, the injury of C5-T1 results in a deficit in shoulder **abduction and internal rotation** [2].
- The range of motion is higher in passive motion as compared with active motion [8]

In conclusion, the three motions affected by OBPP injury are abduction, and external/internal rotation [29]. These motions are presented in the table 7.1 with comparison of range of motion between unaffected shoulder and affected by OBPP and its association with muscular deficiency.

Table 7. 1: RoM of shoulder affected by OBPP and its association with muscular deficiency

Motion	RoM: Healthy side	RoM: Affected side	Reference	Association
GH Abduction contractures		[10° to 65°] mean of 33°	Eismann et al., [17]	Abductor atrophy
Passive External Rotation	90°	[3° to 56°] median of 30°	Eismann et al., [17]	
		[-20° to 85°] mean of 34°	Pöyhiä et al., [16]	Subscapularis atrophy
Internal rotation			Pöyhiä et al., [16]	GH subluxation Brachialis atrophy

In children with OBPP, the kinematic limitation is typically described in terms of limitations in the ROM for each motion (considering all the joints together) but also in terms of each joint separately. GH and ST joints are the main joints that are functionally affected in children with OBPP. The joint stiffness is mainly present in the GH joint [2]. It is also acknowledged that clinical scales such as Mallet classification [30] and Active Movement Scale [31] provide information on general strength but cannot isolate specific joint contributions [32]. Many studies have addressed the compensatory mechanism of the ST joint in shoulder motion in children with OBPP [12],[2],[17], but only few have quantified the GH and The ST joint contributions for a given task [32],[33]. These studies demonstrated that during arm elevation, the scapulothoracic joint had a larger contribution than normal on the affected side [32],[33]. In the study by Russo et al. [33], for ST and GH, three rotational motions were measured for the modified Mallet positions. In table 7.2 bellow we reported these measures for global abduction in the affected side and the increase or decrease ROM (for the same motion) in the group of Erb’s palsy and the extended Erb’s palsy.

Table 7. 2: ST and GH ROM for the Abduction motion in the three groups (Unaffected, Erb’s palsy and Extended Erb’s palsy) (as reported by Russo et al. [33])

Modified Mallet Positions Motion	Joint	Variable	Unaffected (Mean± SD) (degree)	Erb’s palsy (degree)	Extended Erb’s palsy(degree)
Global abduction	ST	upward/downward rotation	35.1±13.0	31.5±13.4	41.4±7.2
		internal/external rotation	-3.9±9.7	-11.6±9.6	-14.0±8.1
		posterior/anterior tilt	1.3 ±5.5	5.1 ±4.8	-0.3 ±2.6
	GH	Abduction/adduction	38.8±18.5	15.2 ±17.4	1.4 ±22.9
		internal/external rotation	-51.2± 14.8	-23.0 ±16.9	-15.4 ±10.3
		flexion/extension	8.0±12.8	4.1 ± 8.7	0.8 ±14.1

7.3 Pediatric MSK modeling for clinical applications

In many pediatric MSK disorders, detecting and understanding the pathology in an early stage and adopting the customized therapy may accelerate the recovery process. In multiple MSK disorders, altered muscle force imbalance, altered muscle strength/dynamics, altered joint moments and altered joint contact mechanics are hypothesized to be the determining factors for pain and functionality. As discussed in the previous chapter, the multi-body dynamics models of the MSK system are an efficient tool to evaluate the causality relationship between the joint functionality and the biomechanics parameters involved (muscle characteristics, structural architecture, internal and external forces, moment arms, joint moments etc.). Thus, pediatric MSK models can provide valuable insights into the diagnosis, treatment, and analysis of multiple MSK disorders by providing quantitative biomechanical assessment of joint and muscle parameters in terms of kinematics and kinetics. This can ultimately enhance the understanding of the pathophysiology, the therapeutic planning, and rehabilitation programs.

However, to our surprise, we found just a handful of studies that developed and used pediatric MSK models to obtain insights into the pathophysiology of a given MSK disorder. This is due to the number of parameters these models use and the sensitivity of these parameters to the inter-individual variation [34]. This level of subject-specific detail in pediatric MSK models is challenging due to the scarcity of the literature documenting these parameters. This would explain the relatively small number of MSK models as compared to number of adult MSK models. Most of the studies that involve pediatric MSK models, scaled a generic model developed from a cadaveric’ measurements in healthy adult. This practice

inherently limits the efficient outcomes of these studies as the scaling affects multiple modeling parameters that are specific to pediatric population.

In this section, we provide an overview of two such pediatric MSK models that have been developed (both developed by the same research group) and used to study a musculoskeletal disorder in upper extremity.

7.3.1 Crutch-assisted gait model [35]

Slaven and colleagues from the department of Biomedical Engineering at the Marquette University, (Milwaukee, Wisconsin, USA) developed an inverse dynamics model of the upper extremity to quantify crutch-assisted gait in children. The model consisted of thorax, upper arms, forearms, hands, and Lofstrand crutches. The model was evaluated and applied to a single pediatric subject to demonstrate its effectiveness in the characterization of crutch-assisted gait during multiple walking patterns. Vicon Body Builder V3.6 (Vicon Motion Systems, Ltd., Oxford, England) was used for the development of the inverse dynamics model. For this model, GH joint was defined with joint center located at the Acromion as per ISB recommendations. The model provided upper extremity joint reaction kinetics to provide better understanding on joint dynamics leading to injury due to long-term use of crutches.

7.3.2 Wheelchair mobility model [36]

The same group as above from Marquette University developed an upper extremity biomechanical model for pediatric wheelchair users. This wheelchair mobility model [36] described the upper extremity joint kinematics and kinetics during wheelchair mobility for pediatric population. This model was a continuation of the model developed by Slavens et al. [37] by adding more segments and refining the joint center and using more accurate kinetic data. It was a bilateral model including total 6 segments on each side: Thorax, scapula, clavicle, upper arm (Humerus), forearm and hand. It had 13 DoF, including three for the wrist, three for the GH joint, three for the AC joint, two for the SC joint and two for the elbow joint. A same Z-X-Y Euler sequence was used for all the joints to describe the joint rotations. To determine anthropometric parameters for their model, authors used equations developed by Jensen et al. [38] to calculate the segment mass and the location of the segment center of mass and for the segment inertia values, authors used equations developed by Yeadon and Morlock [39]. After building the model, Kinetic data was recorded during wheelchair propulsion and used in an inverse dynamics method to quantify joint angles, range of motions, joint forces and moments. This model was then further used by Schnorenberg et al. [40] to characterize joint dynamics of the upper extremity during wheelchair mobility.

Other pediatric MSK models (other than shoulder joint) were also developed and include a Pediatric MSK model of the foot and ankle [41], a pediatric MSK model of the tibiotalar and subtalar joints to investigate the functional response of joint impairment in children with juvenile idiopathic arthritis (JIA) [42] (later extended to estimate the ankle joint forces [43]).

7.4 Pediatric MSK modeling for OBPP

In the context of OBPP injury, an MSK model would be a very helpful tool to understand the correlation between muscle deficiency, osseous deformity and shoulder function limitations and give insights into the way this pathology should be treated. **However, to date, there is no attempt made in the literature to**

develop a subject-specific or generic MSK model for pediatric shoulder joint for healthy or clinical application. Developing a shoulder MSK model specific to pediatric population is an important step toward understanding the complex shoulder dynamics of this population. Pediatric shoulder dynamics is different than the adult shoulder dynamics [44] and hence a customized modeling framework is necessary. The kinetic analysis of upper extremity motion is very difficult as compared with the kinetic analysis of the lower extremity. This is due to mainly two major factors. The first one is that the gait walk is cyclic, modeled by closed kinematic chain topology and easier to reconstruct as compared with the upper extremity which must be modeled by open kinematic chain topology, has more DOF and much complicated to reconstruct. The second factor is that in gait analysis, the kinetics measures (ground reaction forces and moments) are detectable using the force plates installed in the gait lab, whereas, for upper extremity, we do not have access to such reaction forces a priori. One proposed approach, is to use sensors installed in a robot to measure external forces [45], but is not feasible in pediatric research and has a high experimental cost associated with it.

With the increasing clinical and research interest in shoulder muscle and joint function in children with OBPP, a number of studies used MSK models to understand OBPP pathology. However, all these models use generic adult models and scale them down to represent pediatric anthropometry and parameters. The main models include **Kleiber model** [46] (2013), **Crouch model** [47] (2014) and **Cheng model** [48] (2015).

7.4.1 Kleiber model

Kleiber and colleagues proposed a biomechanical inverse kinematic model build using information on subject's anthropometric data, motion analysis system, and a robotic arm used to get external forces at the hand. The objective of this study was to propose an inverse dynamic modeling method to calculate net joint forces in anatomical axes of movement. The modeling structure consisted of five segments on each side: thorax, clavicle, upper arm, forearm and hand. These segments were linked with each other via four joints: SC, Humerothoracic, elbow, and wrist. The feasibility of this model was realized by simulation and later in four children with OBPP. Constrained flexion-extension movements of the shoulder were performed (straightened forearm and hand) using a robotic arm manipulator which also measured the forces exerted by hand. These forces were then used to calculate net joint moments.

This study found that there was increase in net joint forces in the humerothoracic joint due to increase in internal shoulder rotation position in children with OBPP as compared to healthy children. This study did not elaborate on the modeling structure other than the calculation of forces. It scaled down the body inertial parameters from the literature and used in the calculation of joint moments. There were no muscle dynamics involved in the model. It did not specify the joint coordinate system used for the four joints and thus hard to compare or analyze results in clinical setting. Further, humerothoracic joint was modeled that combined the motions of GH and ST joints.

7.4.2 Crouch model

Crouch and colleagues used a musculoskeletal model to simulate two important mechanisms, strength imbalance and impaired longitudinal muscle growth that can mechanically contribute to shoulder deformity following brachial plexus birth palsy. The musculoskeletal model used was a scaled down upper extremity adult model developed by Holzbaur et al [49] using OpenSim Software. The original model from which this study was derived is described in the Chapter 7 (Holzbaur Model) as it was developed for adult population. To simulate the strength imbalance mechanism in OBPP, each muscle was allowed to produce

only 30% of its maximum force. The impaired longitudinal muscle growth, the muscle length was reduced by 30%. The simulated mechanisms, each at a time, had contribution to osseous deformity and postural shoulder deformity in children with OBPP.

Through the simulated strength imbalance mechanism, they found seven muscles (infraspinatus, subscapularis, long head of biceps, latissimus dorsi, teres major, teres minor, and posterior deltoid) to be the contributors of the GH joint force in the axial plane, and that can explain their contribution in the osseous deformity. Among this group of muscles, infraspinatus, subscapularis and latissimus dorsi were found to be the main contributor to the increase in the posteriorly directed GH joint force. Through the same simulated mechanism, the subscapularis muscle reduced the external shoulder rotation (with elbow flexed) ROM and that is thought to be the potential contributor of postural deformity along with the anterior deltoid and the anterior heads of pectoralis major., whereas, no muscle had more than 2° reduction of the ROM of the abduction. Through the simulated impaired growth mechanism, most of the increase in the GH joint force was attributed to the infraspinatus muscle in both posterior and anterior direction (with respect to the glenoid centerline). Looking for ROM for the same simulated mechanism, anterior deltoid and subscapularis muscles reduced the ROM of the external shoulder rotation by 52° and 40° respectively, whereas the abduction ROM was reduced by the long head of triceps by 56°.

7.4.3 Cheng model

Cheng and colleagues extended the Crouch study [48], the effect of these two mechanisms (strength imbalance and impaired longitudinal muscle growth that can mechanically contribute to shoulder deformity following brachial plexus birth palsy) were evaluated when they are isolated and when they are combined focusing only on C5-6 brachial plexus injury. To do so, in those simulated mechanisms, only the muscles that are denervated by C5-6 nerves were considered as affected. In this case, to simulate the muscle imbalance, only the muscles considered as affected were given no resting tone and to simulate the impaired growth, the length of the affected muscles was reduced by 30%. It has been concluded from this study that both the simulated mechanism isolated or combined contribute significantly to restricted ROM and force imbalance, therefore to osseous and postural deformity in children with OBPP. This study also highlighted the effect of subscapularis muscle impairment on the entire shoulder deformity.

7.5 Challenges and limitation of the current MSK model simulations for OBPP

Better management strategies of OBPP need better understanding of the musculoskeletal deformations and abnormal functionality. To adequately represent the OBPP pathology, pediatric modeling structure is a necessary step. However, lack of such modeling in the current literature leads to multiple challenges and limitations.

7.5.1 Limitations

The use of an adult musculoskeletal model to study the biomechanical behavior of pediatric population is the first and foremost limitation for this population. As multiple assumptions and adjustments are

needed to tweak the model to represent pediatric parameters, it is clearly a limitation. Such adult-derived models can be seen in the OBPP study by Crush et al [47] or as it is used in other study to focus on crouch gait kinematics in children with cerebral palsy [50].

The OBPP modeling studies (Cheng and Crouch) made an assumption that scapulothoracic joint kinematics in OBPP population is normal, which is a wrong assumption and it can considerably affect the outcomes. **In fact, the clinical observations highlighted the ST kinematic abnormality in children with OBPP** [33]. Further, no morphological changes in the bone geometry between affected and unaffected sides of the shoulder was considered in both the studies. Although this will also be true in our case, we propose to use subject-specific muscle insertion regions which would help reduce the error due to non-consideration of bony morphology. Another critical assumption made by both OBPP studies was that the GH translation was not taken into consideration (Crouch and Cheng) which was reported to be pathological in terms of OBPP. Muscle architectural parameters are in all the cases taken from adult data and scaled down to the subject anthropometry, whereas muscular and neuromotor function differ a lot between adults and children [51].

7.5.2 Challenges

Multiple challenges exist in this research domain. First is how to include experimental results and clinical observation into computational simulation to investigate the shoulder deformity in children with OBPP. A recent study addressed the issue of bone deformity of the GH joint using a finite element analysis of the bone growth under abnormal loading [52] which could be one of the solutions. Second challenge is to know the muscle and bone parameters to be included in the models. Third challenge is to accurately model muscle spasticity or weakness in case of OBPP and further make it subject specific. Fourth challenge is to validate model simulations. Fifth challenge is to model ST joint and differentiate GH kinematics from ST kinematics. Sixth challenge is to identify the muscles groups that are weak and that lead to force imbalance in OBPP shoulder. Seventh challenge is to differentiate bony deformity from soft tissue deformity. Eight challenge is to use animal models experiments to simulate the biological mechanisms of the injury neurologically in order to understand the impact of muscle growth in shoulder development after OBPP.

While not all these challenges are addressed in this thesis, I have made an attempt to overcome challenges number two and five above in order to get better insights into the pathophysiology of OBPP.

7.6 Chapter 7 References

- [1] J. S. Zember, Z. S. Rosenberg, S. Kwong, S. P. Kothary, and M. A. Bedoya, "Normal Skeletal Maturation and Imaging Pitfalls in the Pediatric Shoulder," *Radiogr. Rev. Publ. Radiol. Soc. N. Am. Inc.*, vol. 35, no. 4, pp. 1108–1122, Aug. 2015.
- [2] A. Abid, "Brachial plexus birth palsy: Management during the first year of life," *Orthop. Traumatol. Surg. Res.*, vol. 102, no. 1, Supplement, pp. S125–S132, Feb. 2016.
- [3] A. Gilbert and G. Pivato, "Obstetrical Palsy: The French Contribution," *Semin. Plast. Surg.*, vol. 19, no. 1, pp. 5–16, Feb. 2005.
- [4] M. M. Al-Qattan *et al.*, "Narakas classification of obstetric brachial plexus palsy revisited," *J. Hand Surg. Eur. Vol.*, vol. 34, no. 6, pp. 788–791, Dec. 2009.
- [5] R. Okby and E. Sheiner, "Risk factors for neonatal brachial plexus paralysis," *Arch. Gynecol. Obstet.*, vol. 286, no. 2, pp. 333–336, Aug. 2012.
- [6] K. Weizsaecker, J. E. Deaver, and W. R. Cohen, "Labour characteristics and neonatal Erb's palsy," *BJOG Int. J. Obstet. Gynaecol.*, vol. 114, no. 8, pp. 1003–1009, Aug. 2007.
- [7] J. G. Ouzounian, "Risk factors for neonatal brachial plexus palsy," *Semin. Perinatol.*, vol. 38, no. 4, pp. 219–221, Jun. 2014.
- [8] S. P. Chauhan, S. B. Blackwell, and C. V. Ananth, "Neonatal brachial plexus palsy: incidence, prevalence, and temporal trends," *Semin. Perinatol.*, vol. 38, no. 4, pp. 210–218, Jun. 2014.
- [9] S. Kwong, S. Kothary, and L. L. Poncinelli, "Skeletal development of the proximal humerus in the pediatric population: MRI features," *AJR Am. J. Roentgenol.*, vol. 202, no. 2, pp. 418–425, Feb. 2014.
- [10] R. A. Gandhi, C. J. DeFrancesco, and A. S. Shah, "The Association of Clavicle Fracture With Brachial Plexus Birth Palsy," *J. Hand Surg.*, Jan. 2019.
- [11] R. K. Nath and M. Paizi, "Scapular deformity in obstetric brachial plexus palsy: a new finding," *Surg. Radiol. Anat. SRA*, vol. 29, no. 2, pp. 133–140, Mar. 2007.
- [12] P. M. Waters, G. R. Smith, and D. Jaramillo, "Glenohumeral deformity secondary to brachial plexus birth palsy," *J. Bone Joint Surg. Am.*, vol. 80, no. 5, pp. 668–677, May 1998.
- [13] S. Brochard, J. D. Mazingo, K. E. Alter, and F. T. Sheehan, "Three dimensionality of gleno-humeral deformities in obstetrical brachial plexus palsy," *J. Orthop. Res. Off. Publ. Orthop. Res. Soc.*, vol. 34, no. 4, pp. 675–682, Apr. 2016.
- [14] S. H. Kozin, "Correlation between external rotation of the glenohumeral joint and deformity after brachial plexus birth palsy," *J. Pediatr. Orthop.*, vol. 24, no. 2, pp. 189–193, Apr. 2004.
- [15] F. T. Sheehan, S. Brochard, A. J. Behnam, and K. E. Alter, "Three-dimensional humeral morphologic alterations and atrophy associated with obstetrical brachial plexus palsy," *J. Shoulder Elbow Surg.*, vol. 23, no. 5, pp. 708–719, May 2014.
- [16] T. H. Pöyhiä, Y. A. Nietosvaara, V. M. Remes, M. O. Kirjavainen, J. I. Peltonen, and A. E. Lamminen, "MRI of rotator cuff muscle atrophy in relation to glenohumeral joint incongruence in brachial plexus birth injury," *Pediatr. Radiol.*, vol. 35, no. 4, pp. 402–409, Apr. 2005.

- [17] E. A. Eismann, K. J. Little, T. Laor, and R. Cornwall, "Glenohumeral abduction contracture in children with unresolved neonatal brachial plexus palsy," *J. Bone Joint Surg. Am.*, vol. 97, no. 2, pp. 112–118, Jan. 2015.
- [18] P. Bhardwaj, T. Burgess, S. R. Sabapathy, H. Venkataramani, and V. Ilayaraja, "Correlation between clinical findings and CT scan parameters for shoulder deformities in birth brachial plexus palsy," *J. Hand Surg.*, vol. 38, no. 8, pp. 1557–1566, Aug. 2013.
- [19] V. M. van Gelein Vitringa, E. O. van Kooten, M. G. Mullender, M. H. van Doorn-Loogman, and J. A. van der Sluijs, "An MRI study on the relations between muscle atrophy, shoulder function and glenohumeral deformity in shoulders of children with obstetric brachial plexus injury," *J. Brachial Plex. Peripher. Nerve Inj.*, vol. 4, p. 5, May 2009.
- [20] S. Hogendoorn, K. L. J. van Overvest, I. Watt, A. H. B. Duijsens, and R. G. H. H. Nelissen, "Structural changes in muscle and glenohumeral joint deformity in neonatal brachial plexus palsy," *J. Bone Joint Surg. Am.*, vol. 92, no. 4, pp. 935–942, Apr. 2010.
- [21] M. Midrio, "The denervated muscle: facts and hypotheses. A historical review," *Eur. J. Appl. Physiol.*, vol. 98, no. 1, pp. 1–21, Sep. 2006.
- [22] M.-A. Giroux-Metges *et al.*, "Effects of immobilizing a single muscle on the morphology and the activation of its muscle fibers," *Exp. Neurol.*, vol. 194, no. 2, pp. 495–505, Aug. 2005.
- [23] V. M. Van Gelein Vitringa, R. Jaspers, M. Mullender, W. J. Ouwkerk, and J. A. Van Der Sluijs, "Early effects of muscle atrophy on shoulder joint development in infants with unilateral birth brachial plexus injury," *Dev. Med. Child Neurol.*, vol. 53, no. 2, pp. 173–178, Feb. 2011.
- [24] F. Einarsson, T. Hultgren, B.-O. Ljung, E. Runesson, and J. Fridén, "Subscapularis muscle mechanics in children with obstetric brachial plexus palsy," *J. Hand Surg. Eur. Vol.*, vol. 33, no. 4, pp. 507–512, Aug. 2008.
- [25] C. Pons, F. T. Sheehan, H. S. Im, S. Brochard, and K. E. Alter, "Shoulder muscle atrophy and its relation to strength loss in obstetrical brachial plexus palsy," *Clin. Biomech. Bristol Avon*, vol. 48, pp. 80–87, Oct. 2017.
- [26] C. Pons, O. Rémy-Néris, B. Médée, and S. Brochard, "Validity and reliability of radiological methods to assess proximal hip geometry in children with cerebral palsy: a systematic review," *Dev. Med. Child Neurol.*, vol. 55, no. 12, pp. 1089–1102, Dec. 2013.
- [27] P. M. Waters, J. T. Monica, B. E. Earp, D. Zurakowski, and D. S. Bae, "Correlation of radiographic muscle cross-sectional area with glenohumeral deformity in children with brachial plexus birth palsy," *J. Bone Joint Surg. Am.*, vol. 91, no. 10, pp. 2367–2375, Oct. 2009.
- [28] F. Fitoussi *et al.*, "Upper extremity kinematics analysis in obstetrical brachial plexus palsy," *Orthop. Traumatol. Surg. Res.*, vol. 95, no. 5, pp. 336–342, Sep. 2009.
- [29] S. Brochard, K. Alter, and D. Damiano, "Shoulder strength profiles in children with and without brachial PLEXUS PALSY.," *Muscle Nerve*, vol. 50, no. 1, pp. 60–66, Jul. 2014.
- [30] J. Mallet, "[Obstetrical paralysis of the brachial plexus. II. Therapeutics. Treatment of sequelae. Priority for the treatment of the shoulder. Method for the expression of results].," *Rev. Chir. Orthop. Reparatrice Appar. Mot.*, vol. 58, p. Suppl 1:166-168, 1972.

- [31] C. Curtis, D. Stephens, H. M. Clarke, and D. Andrews, "The active movement scale: an evaluative tool for infants with obstetrical brachial plexus palsy," *J. Hand Surg.*, vol. 27, no. 3, pp. 470–478, May 2002.
- [32] S. V. Duff, S. Dayanidhi, and S. H. Kozin, "Asymmetrical shoulder kinematics in children with brachial plexus birth palsy," *Clin. Biomech. Bristol Avon*, vol. 22, no. 6, pp. 630–638, Jul. 2007.
- [33] S. A. Russo *et al.*, "Scapulothoracic and glenohumeral contributions to motion in children with brachial plexus birth palsy," *J. Shoulder Elbow Surg.*, vol. 23, no. 3, pp. 327–338, Mar. 2014.
- [34] L. Scheys, K. Desloovere, P. Suetens, and I. Jonkers, "Level of subject-specific detail in musculoskeletal models affects hip moment arm length calculation during gait in pediatric subjects with increased femoral anteversion," *J. Biomech.*, vol. 44, no. 7, pp. 1346–1353, Apr. 2011.
- [35] B. A. Slavens, P. F. Sturm, and G. F. Harris, "Upper extremity inverse dynamics model for crutch-assisted gait assessment," *J. Biomech.*, vol. 43, no. 10, pp. 2026–2031, Jul. 2010.
- [36] A. J. Paul, B. A. Slavens, A. Graf, J. Krzak, L. Vogel, and G. F. Harris, "Upper extremity biomechanical model for evaluation of pediatric joint demands during wheelchair mobility," *Conf. Proc. Annu. Int. Conf. IEEE Eng. Med. Biol. Soc. IEEE Eng. Med. Biol. Soc. Annu. Conf.*, vol. 2012, pp. 4788–4791, 2012.
- [37] B. A. Slavens, N. Bhagchandani, M. Wang, P. A. Smith, and G. F. Harris, "An upper extremity inverse dynamics model for pediatric Lofstrand crutch-assisted gait," *J. Biomech.*, vol. 44, no. 11, pp. 2162–2167, Jul. 2011.
- [38] R. K. Jensen, "Changes in segment inertia proportions between 4 and 20 years," *J. Biomech.*, vol. 22, no. 6–7, pp. 529–536, 1989.
- [39] M. R. Yeadon and M. Morlock, "The appropriate use of regression equations for the estimation of segmental inertia parameters," *J. Biomech.*, vol. 22, no. 6–7, pp. 683–689, 1989.
- [40] A. J. Schnorenberg, B. A. Slavens, M. Wang, L. Vogel, P. Smith, and G. F. Harris, "Biomechanical Model for Evaluation of Pediatric Upper Extremity Joint Dynamics during Wheelchair Mobility," *J. Biomech.*, vol. 47, no. 1, pp. 269–276, Jan. 2014.
- [41] S. Stabelfeldt, M. B. Silver-Thorn, G. Harris, P. Smith, and M. Timins, "Development of a pediatric musculoskeletal model of the foot and ankle," in *Pediatric Gait: A New Millennium in Clinical Care and Motion Analysis Technology*, 2000, pp. 151–158.
- [42] E. Montefiori *et al.*, "An image-based kinematic model of the tibiotalar and subtalar joints and its application to gait analysis in children with Juvenile Idiopathic Arthritis," *J. Biomech.*, vol. 85, pp. 27–36, Mar. 2019.
- [43] J. A. I. Prinold *et al.*, "A Patient-Specific Foot Model for the Estimate of Ankle Joint Forces in Patients with Juvenile Idiopathic Arthritis," *Ann. Biomed. Eng.*, vol. 44, no. 1, pp. 247–257, Jan. 2016.
- [44] B. Beaudette and V. L. Chester, "Upper Extremity Kinematics in Pediatric and Young Adult Populations during Activities of Daily Living," *J Med Biol Eng*, vol. 34, no. 5, p. 7, 2014.
- [45] N. Popovic, S. Williams, T. Schmitz-Rode, G. Rau, and C. Disselhorst-Klug, "Robot-based methodology for a kinematic and kinetic analysis of unconstrained, but reproducible upper extremity movement," *J. Biomech.*, vol. 42, no. 10, pp. 1570–1573, Jul. 2009.
- [46] T. Kleiber, N. Popovic, J. Bahm, and C. Disselhorst-Klug, "A modeling approach to compute modification of net joint forces caused by coping movements in obstetric brachial plexus palsy," *J. Brachial Plex. Peripher. Nerve Inj.*, vol. 8, no. 1, p. 10, Oct. 2013.

- [47] D. L. Crouch, J. F. Plate, Z. Li, and K. R. Saul, "Computational sensitivity analysis to identify muscles that can mechanically contribute to shoulder deformity following brachial plexus birth palsy," *J. Hand Surg.*, vol. 39, no. 2, pp. 303–311, Feb. 2014.
- [48] W. Cheng, R. Cornwall, D. L. Crouch, Z. Li, and K. R. Saul, "Contributions of muscle imbalance and impaired growth to postural and osseous shoulder deformity following brachial plexus birth palsy: a computational simulation analysis," *J. Hand Surg.*, vol. 40, no. 6, pp. 1170–1176, Jun. 2015.
- [49] K. R. S. Holzbaaur, W. M. Murray, and S. L. Delp, "A model of the upper extremity for simulating musculoskeletal surgery and analyzing neuromuscular control," *Ann. Biomed. Eng.*, vol. 33, no. 6, pp. 829–840, Jun. 2005.
- [50] K. M. Steele, A. Seth, J. L. Hicks, M. S. Schwartz, and S. L. Delp, "Muscle contributions to support and progression during single-limb stance in crouch gait," *J. Biomech.*, vol. 43, no. 11, pp. 2099–2105, Aug. 2010.
- [51] R. Dotan, "Children's Neuromotor and Muscle-Functional Attributes - Outstanding Issues," *Pediatr. Exerc. Sci.*, vol. 28, no. 2, pp. 202–209, 2016.
- [52] N. N. Dixit, D. C. McFarland, and K. R. Saul, "Computational analysis of glenohumeral joint growth and morphology following a brachial plexus birth injury," *J. Biomech.*, vol. 86, pp. 48–54, Mar. 2019.

Chapter 8

Multibody system dynamics: theory and Applications in Shoulder

8.1 Introduction

A computational model is a mathematical representation of a simple or complex system to study its behavior by computer simulation. Such models are typically built to study the systems where simple (linear) and intuitive analytical solutions are not available or experimental techniques cannot be effectively employed. Certainly, computational models play an important role in understanding human body, its structure and its function in normal and perturbed situations. In shoulder joint research, computational modeling has led to an important advance in our understanding of shoulder function, surgical planning, shoulder implant behavior, ergonomic practice, and rehabilitation [1]. With the advances in mathematics and informatics and with the increase of the biomechanical interest in shoulder function, complex shoulder mechanics models are built and used in various applications. For example, Li and colleagues [2], built an upper limb model using electromyographic (EMG) data to study an astronaut's upper limb dynamic joint torque in order to study the extravehicular activity of the astronauts and understand the needed training exercises on earth.

Human movement is a complex interaction between its nervous system and the musculoskeletal system. For performing human movement analysis at a joint and tissue level, multiple techniques that are used to build computational models can be broadly categorized into 1) Finite element models, 2) multibody musculoskeletal system dynamics models, and 3) hybrid models that combine finite element and musculoskeletal modeling techniques. In the scope of this thesis, I have chosen multibody musculoskeletal system dynamic modeling because of its merits in identifying and analyzing the underlying shoulder joint mechanics in terms of muscle force distribution and joint movement quantification. In section 8.2, I will provide a brief overview of the multibody dynamics. In section 8.3, I will briefly explain the muscle theory and its activation and contraction dynamics. In section 8.4, I will explain currently available software tools for musculoskeletal modeling. In section 8.5, I will provide a brief overview of the musculoskeletal models of the shoulder complex reported in the literature.

8.2 Multibody dynamics

A multibody system is typically composed of rigid bodies, joints, bearings, particles, springs, dampers, force and position actuators, etc. The rigid bodies and particles are connected by joints resulting in a system of topology which can be classified as a chain, tree or loop topology [3]. A chain topology is easy to formulate and interact with and have further classification of a closed or open chain topology. A loop topology is characterized by the occurrence of kinematic loops and requires special treatment. Multibody systems with loop topology are useful for modeling double stance phase of the gait whereas open chain topology is useful in modeling arm motions. The modeling of multibody systems, as well as the derivation of the corresponding equations of motion, are explained in detail by Schiehlen and in Schiehlen and Eberhard [3]–[5]. They are briefly explained in the following sections.

8.2.1 Joint Kinetics and kinematics

Measurement of spatial positions and orientations of bones with respect to a coordinate system embedded within them is termed as bone kinematics. Quantification of spatial position and orientation of one bone with respect to another in terms of a joint coordinate system formulated between the two bones is then termed as joint kinematics. Such kinematic constraints between the two bodies allow us to understand the mechanical behavior of the ligaments joining the two bones. Management (measurement and quantification) of applied and reaction forces and moments coming onto the joint is termed as joint kinetics. Applied forces and moments are due to the weight, actuator forces and moments, and elements such as springs and dampers. These applied forces and moments are governed by laws relating them to the motion of the joint (or multibody system) and need to be managed while building the musculoskeletal model. Reaction forces and moments, in contrast, are due to kinematic constraints imposed by elements such as joints, bearings, and supports. Here is a brief overview of the joint kinematics and kinetics (all the vectors are represented with bold font):

The kinematics of a multibody system, consisting of p rigid bodies subject to q holonomic constraints, is fully characterized by a set of $f = 6p - q$ generalized coordinates

$$\mathbf{y} = [y_1 \ y_2 \ \dots \ y_f]^T \quad \dots(1)$$

Whose number corresponds to the number of degrees of freedom of the multibody system. The position and orientation of the i^{th} rigid body in an inertial coordinate system I is described by a position vector \mathbf{r}_i of its center of mass and by a rotation matrix \mathbf{S}_i of a body embedded coordinate system as

$$\mathbf{r}_i = \mathbf{r}_i(\mathbf{y}, t) \quad \dots(2)$$

$$\mathbf{S}_i = \mathbf{S}_i(\mathbf{y}, t) \quad \dots(3)$$

The translational velocity of the center of mass is obtained by differentiating the position vector r_i as

$$\mathbf{v}_i = \dot{\mathbf{r}}_i = \mathbf{J}_{T_i}(\mathbf{y}, t)\dot{\mathbf{y}} + \bar{\mathbf{v}}_i(\mathbf{y}, t) \quad \text{.....(4)}$$

Where \mathbf{J}_{T_i} is the Jacobian matrix of translation, and $\bar{\mathbf{v}}_i$ is the local velocity. Similarly, angular velocity vector \mathbf{w}_i , time derivative of infinitesimal rotation vector \mathbf{s}_i , is given as

$$\mathbf{w}_i = \dot{\mathbf{s}}_i = \mathbf{J}_{R_i}(\mathbf{y}, t)\dot{\mathbf{y}} + \bar{\mathbf{w}}_i(\mathbf{y}, t) \quad \text{.....(5)}$$

Where \mathbf{J}_{R_i} is the 3 X f -Jacobian matrix of rotation, and $\bar{\mathbf{w}}_i$ is the local angular velocity.

The angular velocity vector $\mathbf{w}_i = [w_1 \ w_2 \ w_3]^T$ can be obtained from the corresponding skew-symmetric rotation tensor $\tilde{\mathbf{w}}_i$ computed as

$$\tilde{\mathbf{w}}_i = \begin{bmatrix} 0 & -w_3 & w_2 \\ w_3 & 0 & -w_1 \\ -w_2 & w_1 & 0 \end{bmatrix} \quad \text{.....(6)}$$

The motion of the rigid bodies in the multibody system is determined by the acting forces and moments. To derive joint kinematics, as stated earlier, applied forces and moments are due to the weight, actuator (muscle) forces and moments, and elements such as springs and dampers, and are determined by the laws relating them to the motion of the multi-body system. Reaction forces, in contrast, are due to kinematic constraints imposed by elements such as joints, bearings, and supports.

The Newton's and Euler's equations of motion describe the relation between the motion of rigid body i and the forces and moments acting on it as

$$m_i \dot{\mathbf{v}}_i = \mathbf{f}_i^e + \mathbf{f}_i^r \quad \text{.....(7)}$$

$$\mathbf{I}_i \dot{\mathbf{w}}_i + \tilde{\mathbf{w}}_i \mathbf{I}_i \mathbf{w}_i = \mathbf{l}_i^e + \mathbf{l}_i^r \quad \text{.....(8)}$$

Where m_i is the mass of body I

I_i is the inertia tensor with respect to the center of mass,

f_i^e and l_i^e are, respectively, the vectors of the resultant applied force and moment with respect to the center of mass,

f_i^r and l_i^r are, respectively, the vector of resultant constraint (or reaction) forces and moments with respect to the center of mass.

Newton's and Euler's equations for f degrees of freedom are given by

$$M(\mathbf{y}, t)\ddot{\mathbf{y}} + \mathbf{k}(\mathbf{y}, \dot{\mathbf{y}}, t) = \mathbf{q}(\mathbf{y}, \dot{\mathbf{y}}, t) \quad \text{.....(9)}$$

Where M is the symmetric mass matrix, \mathbf{k} is the vector of generalized Coriolis forces, and \mathbf{q} is the vector of generalized applied forces. The motion of multibody system can be further constrained by additional kinematic constraints as

$$\mathbf{c}(\mathbf{y}, t) = 0 \quad \text{.....(10)}$$

And thus, the equations of motion are re-written as,

$$M(\mathbf{y}, t)\ddot{\mathbf{y}} + \mathbf{k}(\mathbf{y}, \dot{\mathbf{y}}, t) = \mathbf{q}(\mathbf{y}, \dot{\mathbf{y}}, t) + \mathbf{C}^T \boldsymbol{\lambda} \quad \text{.....(11)}$$

Where $\boldsymbol{\lambda}$ is a vector of Lagrangian multipliers containing generalized reaction forces arising from the addition of the new constraints and \mathbf{C} is the Jacobian matrix of the constraints.

8.2.2 Multibody musculoskeletal dynamics

A musculoskeletal model (MSM) is a computational model that consists of two or more rigid bone segments modeled as joints and actuated by muscles. MSMs use computational methods to study the kinetic and kinematic behavior of the muscles or ligaments or bones of the joints during movement. MSMs can be used multiple times by using different loading conditions, segmental-motion, material parameters, and other parameters. In this way, musculoskeletal system behavior is examined under different loading/unloading conditions in order to simulate real life situations.

8.2.3 Inverse Dynamics

For musculoskeletal systems, inverse dynamics approach is the most commonly used approach for estimating internal loads. The method is the same for all the human joints and thus is regarded as a standard protocol in many clinical applications such as clinical gait analysis. All forces acting between two body segments are represented by a resultant force and resultant joint moment. The term “inverse dynamics” refers to the fact that the forces are inferred from the movements caused by them. Thus, the equations of motions (11) above can be re-written as

$$\mathbf{q}(\mathbf{y}, \dot{\mathbf{y}}, t, \boldsymbol{\tau}) = \mathbf{M}(\mathbf{y}, t)\dot{\mathbf{y}} + \mathbf{k}(\mathbf{y}, \dot{\mathbf{y}}, t) - \mathbf{C}^T \boldsymbol{\lambda}$$

Here, $\boldsymbol{\tau}$ is the vector of actuator forces and moments. The variable on the right side are known from the measurements and the unknown forces and moments on the left side are solved. When N body segments are included in the analysis, inverse dynamics produces $2N$ vector equations meaning at most $2N$ unknown vectors can be solved. Because of two unknown vector variables at each joint (a force and a moment), the number of joints with unknown loads should not be larger than N . This is because each joint force or moment vector appears twice - once in the equation of first segment and once in the equation of opposite segment. If there are more joints in the body than segments, then there are more unknowns than equations and inverse dynamics cannot produce a unique solution.

8.2.4 Forward Dynamics

While very few measurements are needed to create an inverse dynamic problem and solve it, not all research questions can be answered with this approach. Problems pertaining to reproducibility of the measurements, understanding the mechanical relationship, controllability of variations, experimental costs, and accuracy in force estimates can lead to wrong or misleading inverse dynamics analysis and extreme caution is required. In such situations, direct dynamics or forward dynamics approach is applied. In forward dynamics, the experiment is performed on a computer model instead of on a human subject. A forward dynamics analysis is a simulation of movement using the forces as input. Thus, for forward dynamics simulations, the equations of motions are re-written as

$$\ddot{\mathbf{y}} = \mathbf{M}(\mathbf{y}, t)^{-1} (\mathbf{q}(\mathbf{y}, \dot{\mathbf{y}}, t, \boldsymbol{\tau}) + \mathbf{C}^T \boldsymbol{\lambda} - \mathbf{k}(\mathbf{y}, \dot{\mathbf{y}}, t))$$

Forward dynamic simulations are used in biomechanics to investigate the effects of muscle recruitment strategies, musculoskeletal pathologies and design of assistive devices on motion. The use of forward dynamic simulations is still limited, due to the difficulty (the impossibility in certain cases) of accurate

quantification of musculotendon parameters. In orthopedics and sport injury medicine, forward dynamics were mostly used to investigate the neuromuscular control effect on injuries.

8.2.5 Combined inverse-forward dynamics

A third approach that has emerged near the end of the millennium 2000 is a combined inverse and forward dynamics approach. Computed muscle control implemented in OpenSim multi-body modeling framework is one such research area that adopts this approach using inverse dynamics in conjunction with feed forward and feedback control to optimize a model's kinematics with a measured set of data [6], [7]. The use of forward muscle model that can prescribe allowable muscle activations based on previous time-steps is also widespread [7], [8]. This approach has an advantage that each time step is further coupled to previous time-steps and is also referred to as inverse/forward dynamics model [9].

8.2.6 Open source and commercial software

The modeling and simulation of movement in musculoskeletal systems involve processes that can be performed by any knowledgeable person, but the process is complex, prone to errors, and time-consuming. Fortunately, the most difficult processes such as the derivation of the equations of motion for the skeletal system and modeling of muscle force and muscle path can be either automated or greatly facilitated by the use of software tools. In the past, musculoskeletal modelers have turned to multibody simulation software such as SD-Fast (<https://support.ptc.com/support/sdfast/index.html>) to automate the derivation of the equations of motion for the skeletal system. The modeler must describe the properties of the skeletal system in a text file that can then be used by the software to automatically generate the equations of motion for the skeletal system. Other multibody simulation software with interactive model building tools such as Working Model (www.design-simulation.com) and Adams (www.mscsoftware.com) have the advantage that the user can build the model of the skeletal system graphically. The main disadvantage of these primarily mechanical simulation packages is the lack of tools for modeling specialized biological components such as bones, muscles, and proprioceptors that require specially designed software tools.

The first specialized musculoskeletal modeling software, SIMM (<https://motionanalysis.com/products/simm/>) was developed in the 1990s followed by the development of newer software including those that are freely available to the public. AnyBody (<http://www.anybodytech.com/>) and LifeModeler (<http://www.lifemodeler.com/>) are commercial softwares that focus mainly on inverse dynamics as opposed to forward dynamics. SIMM is a commercial musculoskeletal modeling software that originated from the bioengineering department of Stanford University. It provided a kinematic modeling tool that could be coupled to the Dynamics Pipeline and SD-Fast engines to perform both forward and inverse simulations and animations, but its interactive graphical tools for editing models or building new models are limited.

OpenSim [10] is another musculoskeletal modeling software that is available to the research community. OpenSim [10] is an open source software platform for biomechanical modeling and simulation of the

human musculoskeletal system. OpenSim was developed in Stanford University in C++ and the first working version was realized in 2007. It has the capability of interphase with different engineering software packages like MATLAB and it has an extensible Application Programming Interface (API), providing access to the algorithms and enabling to built on it specific programs or OpenSim plugins adapted to specific applications.

The OpenSim graphical user interface (GUI) is an efficient tool for analyzing and simulating models and motions. In the OpenSim GUI, it is possible to import, visualize and edit models and experimental data and it has a set of important tools to scale the models, perform an inverse kinematics, inverse dynamics, forward dynamics, static optimization, Muscle-driven simulations and probe the models. One Further advantage using this platform is its extensive online support material for beginners as well as advanced users (tutorials, webinars, user's and developer's guide, user forum), its regular training courses events, online model library providing a set of upper and lower limb musculoskeletal models and its community of experts around the world.

OpenSim developed models have been widely adapted for various applications, including musculoskeletal biomechanics research, neuroscience research, medical and biomedical engineering education, orthopedics, design of medical device, rehabilitation, ergonomics studies, sport injuries, robotics, animal movement. Most users of OpenSim take advantage of extensive libraries of musculoskeletal models developed previously in and editable using SIMM (e.g. Arnold et al., 2010 [11]). In this thesis work, I used OpenSim software to build musculoskeletal model of the pediatric shoulder joint (see Chapter 9).

8.3 Muscle modeling

Skeletal muscles are the main actuators for human musculoskeletal system movement. The muscle dynamics has been always considered as a starting point to study and understand the dynamics of the musculoskeletal system. Given the complexity of the anatomical structure of the muscle and the intricate physiological processes involved in muscle force generation, mathematical muscle models have the big challenge to provide equations that are computationally usable in different applications and representative of the muscle dynamic process. The multibody musculoskeletal models described in section 7.2 above are typically driven by mathematical muscle dynamics models. Muscle dynamic models are comprised of two dynamics systems: activation dynamics and contraction dynamics. While the activation dynamics starts with neural excitation and ends with muscle activation, the contraction dynamics takes muscle activation as an input and provides actuator forces acting on the bone. The multibody dynamics model then uses these forces to control the segmental kinematics. In the following sessions, I will briefly describe the muscle contraction theory as understood by the researchers to date and how muscle computational models are built to incorporate activation and contraction dynamics.

8.3.1 Muscle contraction theory

The dynamics of the processes that lead to force generation in the muscle are of fundamental importance to the dynamics of the entire musculoskeletal system [12]. Skeletal muscles are composed of structural units of decreasing size (Figure 8.1).

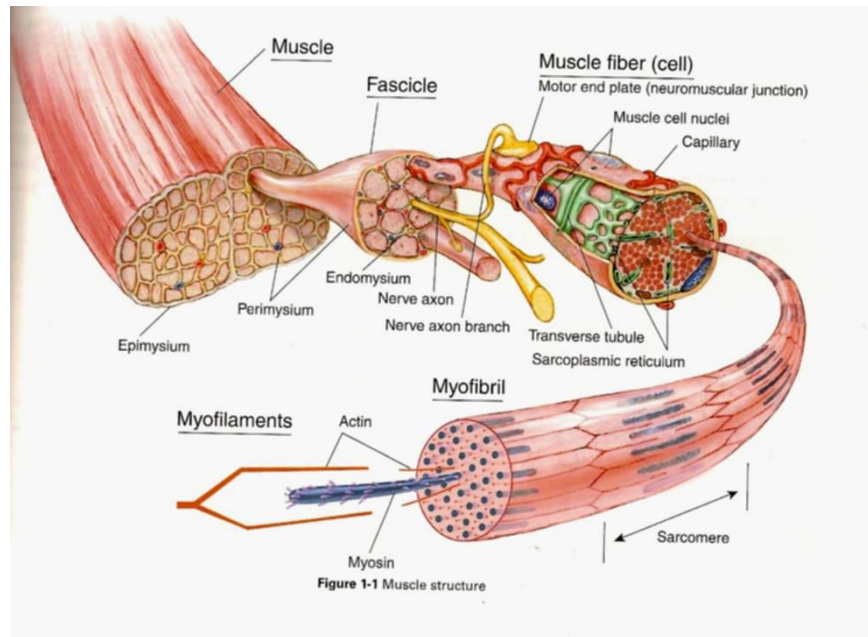


Figure 8. 1: Skeletal Muscle structure (adapted from <https://www.forcefulaction.wordpress.com>)

A muscle fiber contains myofibrils lying parallel to each other. The myofibrils contain sarcomeres - the basic contractile structure of a muscle - in series. The arrangement of the filaments or protein molecules encountered in the sarcomeres gives the skeletal muscle its typical striated pattern, visible with a microscope. Concerning the arrangement of the fibers in the muscle with respect to its line of action or the direction of applied force, muscles can be classified as parallel-fibered or fusiform muscles (figure 8.2), for which the fibers are aligned with the line of action of the muscle, and pennate muscles, for which the fibers make an angle with the line of action of the entire muscle.

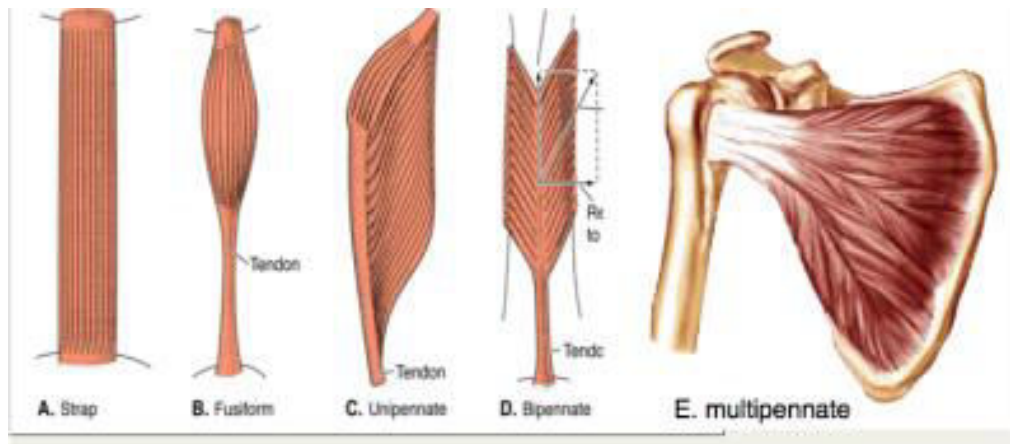


Figure 8. 2: Skeletal muscle shapes and fiber orientations. A: Strap, B: Fusiform, C: Unipennate, D: Bipennate, E: Multipennate. (Adapted from <https://www.studyblue.com>)

Motor units are the smallest controllable units in a muscle. A motor unit is a set of fibers innervated by the same motoneuron and can contain from a few fibers to as many as 2000 fibers. When a motoneuron is simulated, all fibers of the corresponding motor unit generate force. The force applied by the entire muscle is increased either by increasing the firing frequency of already recruited motor units, or by recruiting a further motor unit. According to the accepted size principle, smaller motor units containing less fibers are recruited first to allow for a final force control, followed by larger motor units. This process of recruiting increasingly larger motor units and increasing firing frequency proceeds until all motor units at their respective maximal firing frequencies are recruited, for which state the muscle develops its maximal voluntary force. This force is an important parameter in muscle modeling. According to the sliding filament theory, first suggested by Huxley [13], [14], the changes in muscle length are due to a relative sliding of two sets of filaments, the actin (thin) filaments, and the myosin (thick) filaments, without a significance change in the length of the filaments themselves. The total force applied by an entire muscle is a pulling force that tends to shorten the tissue.

The entire muscle contraction process is regulated by an activation process with a neural action potential generated in a motoneuron. The arrival of this neural action potential at the neuromuscular junction initiates a sequence of biochemical processes that leads to contraction. During the activation and contraction processes described above, chemical energy is consumed. There are multiple factors that influence the muscle force production capabilities, and which are of fundamental importance for the proper modeling of the muscle force generation process. The force applied by a muscle depends on the number of fibers simulated and controlled by recruited motor units. The force at the simulated fibers depends on their activation state, which in turn is influenced by the concentration of calcium ions in the sarcoplasm, which is regulated by the firing frequency. At the molecular level, the force capabilities of a sarcomere are strongly influenced by its current length and shortening velocity. These two effects are described by **force-length** and **force-velocity relations**.

8.3.2 Muscle computational model

Muscle-driven dynamic simulation of the human movement is an important tool to understand and explore the human motions non-invasively. This simulation is based on mathematical models of muscle activation dynamics, force development, and muscle-tendon contraction dynamics. In the literature, there are two main computational models of musculotendon dynamics: cross-bridge model [15] and Hill-type model [16]. Although the cross-bridge models' structure is closer to the physiological description of muscle, the parameters it involves are difficult to measure and scarcely used in a muscle-driven simulation for its complexity and computational tractability.

The Hill-type model, on the other hand, has less detailed description of some specific phenomena such as the reactions of contractile proteins and electro-mechanical delay. However, it is widely used to simulate the behavior of skeletal muscles because of its solid structure, reasonable accuracy, computational efficiency and reduced number of input parameters. There exist many different levels of complexity, but in movement simulation studies, the three-component Hill-type muscle model is almost exclusively used (figure 8.3). The three-element Hill-Type muscle model is composed of a contractile element (CE) and two spring elements, one in series (SE) and one in parallel (PE). The CE represents muscle fibers and the other two elements are nonlinear elements representing the soft tissues mechanical behavior (figure 8.3). The CE is a direct generator of the muscle's force-length curve. the PE represents the passive behavior of the muscle and SE represents the tendon and the myofilaments intrinsic elasticity.

Muscle force generation is determined using a Hill-type muscle model and mainly requires four parameters: maximal isometric force, optimal fiber length, tendon slack length and pennation angle. Different experimental methods have been proposed to estimate these parameters, but the repeatability is always questionable. For adult models, data derived from cadaveric studies are almost always used. One major limitation of cadaveric studies is the age range. The morphology, muscle masses, muscle strength may change with age. For children, these parameters are scarce. The sensitivity of the musculoskeletal models to these musculotendon parameters is widely discussed in the literature [17]–[19]

The Hill-type muscle model incorporated activation and contraction dynamics. The muscle force generated in this type of muscle model is the sum of the forces generated by each element.

$$f^m = f_{CE} + f_{SE} + f_{PE} \quad \dots\dots(12)$$

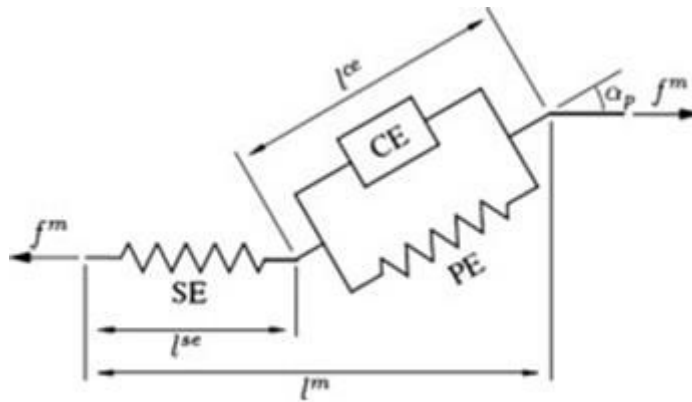


Figure 8. 3: Hill-type muscle model [20]

Activation dynamics

Since the force generated by the fibers of all active motor units sum up resulting in the total active muscle force applied by the muscle tissue, we assume that a normalized neural excitation $u(t)$ that represents 1) the number of fibers excited, and 2) the corresponding firing frequencies. For isometric muscle contraction (no change in length), when the steady state is achieved leading to muscle contraction, the total force f^m is proportional to neural excitation u . A neural excitation $u = 1$ represents the excitation of all motor units at their maximal firing frequencies and causes, under isometric conditions at the optimal length of fibers, and after steady state is reached, the maximal isometric force f_{max}^m .

This process leading to an activation of state $a(t)$ of the muscle is modeled by a first order differential equation and is called activation dynamics. This has a following form:

$$\dot{a}(t) = (u(t) - a(t))(t_1 u(t) + t_2) \quad \dots\dots(13)$$

Where,

$t_2 = 1/t_d$ and $t_1 = 1/(t_a - t_2)$ are time constants,

$u(t)$ is the neural excitation such that $0 \leq u \leq 1$,

$a(t)$ is the muscle activation such that $0 \leq a \leq 1$,

t_d is the time constant for deactivation,

t_a is the time constant for activation.

The time constant for activation t_a is smaller than the time constant of deactivation.

Contraction dynamic

The force generated by the contractile element (f_{ce}) is a function of muscle CE length l^{CE} and shortening velocity v^{CE} according to the force-length and force-velocity relations of the muscle fibers and is further modulated by the activation $a(t)$ resulting in

$$f^{CE} = f^{CE}(a, v^{CE}, l^{CE}) \quad \dots(14)$$

The force-length relation (Figure 8.4) describing the CE force of a muscle contracting isometrically and fully activated ($a = 1$) presents a maximum at the optimal CE length l_{opt}^{CE} . For lengths greater or lesser than optimal length, the force capability of CE decreases. The force-velocity relation (Figure 8.4) describes the muscle CE force as a function of its shortening velocity v^{CE} for a fully activated muscle ($a = 1$) and at the fibers optimal length l_{opt}^{CE} . The combination of these two relations results in the force-length-velocity relation (Figure 8.5). The scaling of the muscle CE force with the activation can be performed by simply scaling the force-length-velocity relation with a . However, in order to better account for the dependence of the maximal shortening velocity v_{max}^{CE} , indicating the velocity for $f_{CE} = 0$, on the activation level, modifications of the general force-length-velocity relation form at submaximal activations are also used [21], [22].

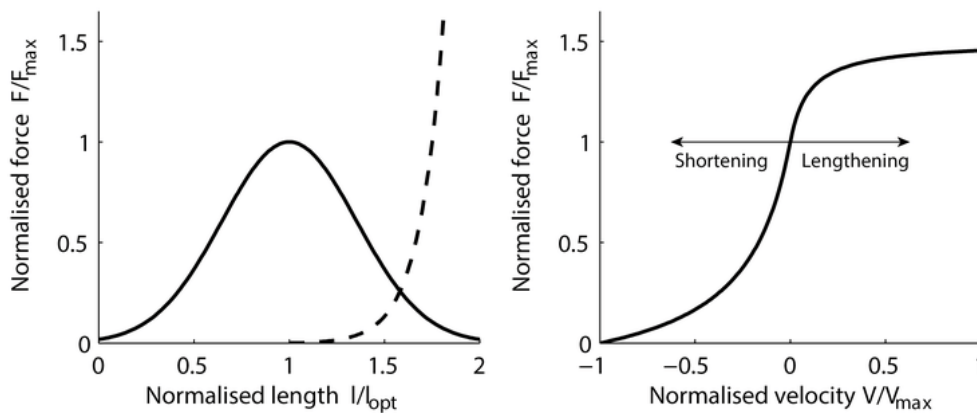


Figure 8. 4: Muscle Force-Length and force-velocity curve [7].

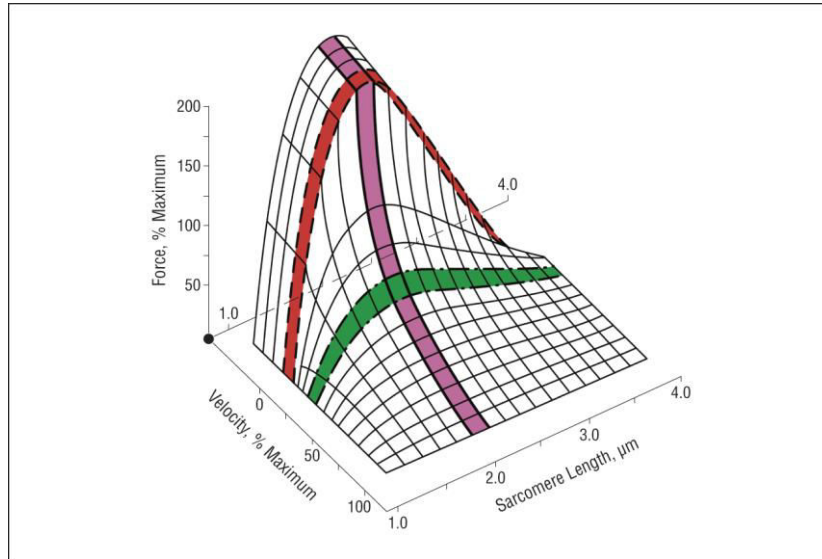


Figure 8. 5: Relationship among sarcomere length, contractile force, and contraction velocity under isotonic conditions [23].

The properties of the tendon are complex, but for the purpose of studying muscle coordination, they are modeled as an elastic element (SE), with a generic force-strain relation [20]. The tendon can be modeled by a simple quadratic force-strain curve characterized by a strain ε_0^T of 3% to 5% occurring at the maximal isometric muscle force f_{max}^m [24], yielding the force-length curve

$$f^{SE}(l^{SE}) = \begin{cases} k^T (l^{SE} - l_{slack})^2 & \text{if } l^{SE} \geq l_{slack} \\ 0 & \text{if } l^{SE} < l_{slack} \end{cases} \quad \dots(15)$$

Where,

$$k^T = f_{max}^{CE} / (\varepsilon_0^T l_{slack})^2,$$

l_{slack} = tendon slack length for which the tendon or SE, respectively, just begun to resist lengthening.

For tendon lengths less than the slack length, no force is transmitted to the skeletal system (typically $\varepsilon_0^T = 4\%$ is used).

Since the force-length curve of the SE is known, its length can be computed from the muscle force f^m , and then the time derivative of the muscle force \dot{f}^m can be found as a function of shortening velocity of the series elastic element v^{SE} as:

$$l^{SE} = l^{SE}(f^m) \quad \text{.....(16)}$$

$$\dot{f}^m = \dot{f}^m(v^{SE}) \quad \text{.....(17)}$$

Thus, from the considered muscle model, with constant pennation angle ($\alpha_p \approx \text{constant}$), it follows that

$$v^{CE} = v^m - \frac{v^{CE}}{\cos \alpha_p} \quad \text{.....(18)}$$

$$f^{CE} = \frac{f^m}{\cos \alpha_p} - f^{PE}(l^{CE}) \quad \text{.....(19)}$$

$$l^{CE} = \frac{l^m - l^{SE}}{\cos \alpha_p} \quad \text{.....(20)}$$

Where the force-length relation for the muscle parallel elastic element $f^{PE}(l^{CE})$ can be obtained, as adapted by Delp S., in his PhD thesis (1990) [25]. From equations (14) to (20), the contraction dynamics for the muscle model results in a relation shown as

$$\dot{f}^m = \dot{f}^m(a, v^m, l^m, f^m) \quad \text{.....(21)}$$

Which describes the muscle contraction dynamics and arises due to the elastic element in series to the CE. Thus, the dynamics depends on the muscle activation $a(t)$, and on the total muscle length $l^m(t)$ and shortening velocity $v^m(t)$. These velocities are directly computed from the skeletal system generalized coordinates $y(t)$ and their derivatives $\dot{y}(t)$. The skeletal system dynamics in equation (11) and the muscle dynamics in equation (21) are thus coupled.

The models of the activation dynamics, of the force-length-velocity relationship, and of the force-length curve for the tendon can be scaled by a few muscle-specific parameters such as

f_{max}^m = maximal isometric muscle force,

l_{opt}^{CE} = optimal muscle fiber length,

α_p = pennation angle of the fibers,

v_{max}^{CE} = maximal shortening velocity,

a parameter to adjust the force-length relation *width/scale*,

f_t = percentage of fast fibers,

t_a = activation constant,

t_d = deactivation constant,

l_{slack} = tendon slack length,

ε_0^T = tendon strain for $f^{CE} = f_{max}^{CE}$

One or all of these parameters can be experimentally measured or selected from the literature which facilitates the application of these models in simulations of the musculoskeletal dynamics involving many muscles. At the same time, determining these parameters in case of a disease or disorder is always a challenge to the modelling community.

8.3.3 Muscle Paths

A realistic representation of muscle paths in a computational model is important as it has central impact on underlying biomechanics parameters such as muscle lengths and muscle moment arms which in turn governs muscle force generation. In musculoskeletal modeling, muscle paths are one of the central input parameters and can be personalized based on the underlying boney geometries as constraints. Muscle paths are typically modeled as line elements in musculoskeletal models. These line elements are modeled to best represent a single muscle by either grouping multiple elements to originate from single point of insertion or by dividing the muscle elements into sub- regions for those muscles with broader attachment sites (E.g. Pectoralis). Muscle paths also influence the moment arm created around the joint. Wrapping surfaces are typically used to guide the muscle paths over the joints and along the bones. Such wrapping surfaces form an intrinsic part of any musculoskeletal model.

8.4 Musculoskeletal models of the Shoulder

Multibody models have long been used to solve inverse dynamics problems for human movement [26], and models of musculoskeletal anatomy were added to allow estimation of forces in joints and orthopedic implants [27]. These inverse dynamics approaches, however, require data collection on human subjects performing the movements of interest. Muscle-driven forward dynamic approaches were developed simultaneously, and these allow simulation of novel and hypothetical movements. Pioneering work on models of musculoskeletal dynamics, and methods for simulation and optimal control, was done by Hatze [28]. Subsequent applications include rehabilitation [29] and basic research in motor control [30], where simulation allows the testing of general hypotheses. Forward dynamics has also been applied in orthopedics and sports medicine to study the effect of neuromuscular control on injuries [31] and to design neuromuscular strategies for reducing joint loads in osteoarthritis [32].

Historically, simulation based orthopedic and biomechanics research of the shoulder has been overwhelmed with the ones focusing on the knee and the hip. One orthopedic reason could be the larger number of joint replacements at the knee and the hip joint as compared with the shoulder joint. From a modelling point of view, the complexity of the shoulder joint and the difficulties to get enough accurate data to build and validate the models makes it a challenging task. However, with the increase of clinical and research interest of the community to understand the internal forces that cannot be measured in vivo, musculoskeletal models of the shoulder showed their potential capability to give clinical insights and predicts different outcomes. And this explains the exponential increase of the number of publications focusing on numerical models of the shoulder [33]. Multiple clinical issues are currently addressed using shoulder models. These include models to study GH instability, rotator cuff tears, shoulder arthroplasty, tendon transfer surgeries etc.

In the absence of non-invasive methods to understand deeply the shoulder muscle and joint function, mathematical and computational models have been used since 1899 (Shoulder organ by Mollier in 1899 [34]) to go deeper in details of the shoulder complex. It was attractive for people that was very curious to know more the real behavior of muscles and joints of the shoulder, giving them a tool to test their hypothesis and feel free to ask what/if questions. The earliest computational shoulder models were two-dimensional models, representing muscle and joint forces in one plane [35]. Driven by the increasing interest on understanding the musculoskeletal function of the human body, many shoulder models were developed from specific data for specific a clinical research-based aim. After that, these models were extensively used by other researchers, making change on them to adapt it the research question they are trying to answer. These musculoskeletal models were used to investigate physiological and clinical problems of shoulder biomechanics to give insights into clinical problem and develop adequate clinical strategies.

In this section we will only describe and discuss the models that are frequently used and re-used to give a comprehensive understanding of shoulder joint mechanics. A common point between these models is that they all assume the bones to be rigid elements. We identified following seven models used for shoulder research.

1. Swedish shoulder Model (SwSM) [36] [37]
2. Delft shoulder model (DSM) [38] [8]
3. Garner and Pandy's model (GPM)(2001) [39]
4. Holzbaur's upper extremity model (HM) (2005) [40]
5. Newcastle shoulder Model (NSM)(2006)[41]
6. Dickerson's (Waterloo) model (DM) (2007) [42]
7. Wu Model (WM) (2016) [43]

Model parameters

Tables 8.1 and 8.2 provide an overview of the type of model and its parameters used for the seven models above. It can be noted that there is no forward dynamic model present and the musculotendon model parameters used in the models (Maximum isometric force (F_0^M), fiber length (L_0^M), pennation angle (α) and tendon slack length (L_s^T)) are either derived from the literature or from the anatomical measurements.

Table 8. 1: Model type, degrees of freedom, first use and validation method used.

Model Name	Degrees of Freedom	Inverse/Forward dynamics	First use (Application)	Validation
SwSM	12	Inverse	Shoulder rhythm	EMG
DSM	11	inverse	Shoulder joint motion evaluation	EMG; implanted GH joint measurement
GPM	13	inverse	Shoulder, elbow, and wrist motion	Muscle moment arms
HM	15	inverse	Muscle moment arms, max moment generating capacity of muscles, coupling between joints, force generating properties of muscles	Muscle moment arms
NSM	11	inverse	Glenohumeral joint forces in daily living activities	Previously reported muscle forces
DM	10	inverse	Ergonomic analysis	Previously reported muscle forces
WM	10	inverse	Shoulder function	

Table 8. 2: Definitions of joint rotation centers used, number of muscles used, methods used to determine segment inertias and musculotendon parameters

Model Name	Joint rotation centers	Skeletal geometry	Number of muscles	Segment inertia	Bony landmarks	Musculotendon parameters
SwSM	Ball joints with fixed center of rotation	No	21	cadavers	Cadavers	Anatomical measurements
DSM	Instantaneous helical axis	yes	31	cadavers	Cadavers	Anatomical measurements
GPM	Fixed center of rotation	Visible Human Male	26	literature	Cadaver	Optimization and VHM
HM	Ball and socket, regression equations	Yes, manually segmented	50	literature	Cadavers	Anatomical measurements
NSM	Sphere fitting	Visible Human Male	31	literature	Literature	Anatomical measurements
DM	Motion data	Visible Human Male	23	literature	literature	Anatomical measurements
WM	Ball and socket	Visible Human Male	26	literature	literature	Scaled down from literature

Body segment parameters:

Body segment's parameters have an important influence on the musculoskeletal output [44]. In multiple studies, scapula and clavicle masses were considered as zero or negligible (Table 8.3).

Table 8. 3: Body segment parameters used in the models.

Models	Clavicle	Scapula	Humerus	Center of mass & inertia
SwSM	0 kg	0 kg	1.81 (2.7%)	Veeger et al 1991 [45]
DSM	0.16	0.7	2.05	Högfors et al, 1987 [36]
HM	0.15600	0.70396	1.99757	Anthropometric survey of US Army personnel: methods and summary [46]
NSM	0	0	1.09 (1.62%)	de Leva, 1996 [47]

Swedish model

The Swedish model [36], [37] was developed to calculate muscle forces. The model employed 21 muscles as straight lines between origin and insertions. To validate the results, the predicted muscle forces were compared with EMG measurements, although inconsistency was found in some muscles which may be attributed to the oversimplification of the muscle paths, no model of muscle force-length properties, and no mechanism to mathematically predict muscle co-contraction. It was also used to investigate strength profiles of the shoulder joint in the scapular plane. However, the Swedish model provided new perspectives in shoulder modelling by employing three-dimensional musculoskeletal geometry in estimating shoulder muscle forces.

Delft model

The Delft shoulder model was first developed in 1994 by van der Helm [38] and was further modified in a series of development and validation studies [8]. The current Delft model has 11 degrees of freedom and employs 139 individual muscle-tendon actuators representing 23 shoulder muscles and 8 elbow muscles [8]. To date, the Delft model has been used in a variety of studies including wheelchair propulsion and tendon transfers surgery.

Garner & Pandy

Garner and Pandy developed an adult shoulder model in 2001 [39] to investigate glenohumeral joint stability during abduction. Its ST, AC, GH joints were each modelled with 3 DoFs, and the elbow and wrist joints each with 2 DoFs. The model employed 42 muscle-tendon actuators to simulate the action of 26 upper limb muscles. Muscle paths and geometries were estimated using anatomy defined from the VHM project. This model first introduced an 'obstacle-set method' to define muscle paths, with standard shaped rigid bodies such as cylinders and spheres used to simulate anatomical structures around which the muscle segments wrapped, and the use of via points.

Holzbaur model

This was the first musculoskeletal model the entire upper limb [40] in the OpenSim software [10] and was used to investigate clavicle dysfunction and rotator cuff repair[48], [49]. The model employed 50 muscle-tendon actuators for the upper limb muscles from the shoulder complex down to the index finger. Muscle paths were developed from a set of cadaveric measurements on muscle moment arms. A limitation of this study is that the shoulder girdle muscles were incomplete as they lacked all axioscapular muscles. This model has not been used for muscle-force prediction as it was designed primarily as an anatomical model.

Newcastle model

Charlton and Johnson in 2006 developed the Newcastle shoulder model [41] to primarily investigate the biomechanics of reverse shoulder replacement surgeries. This model had 11 degrees of freedom and employed 99 musculo-tendon actuators to represent 31 muscles that wrapped around a series of standard-shaped objects (ellipsoids, spheres, and cylinders) to define the muscle paths. The motion of the clavicle and scapula was prescribed using regression equations that were a function of humeral position. The muscle-tendon had no force-length relationship and no force-velocity relationships, which limited the ability of this model to represent muscle activity over a range of joint positions. Static optimization was employed to predict muscle force during activities of daily living by minimizing the sum of squared muscle stresses. Model validation was performed by comparing the predicted joint reaction forces with those from the Delft Shoulder model.

Dickerson Model

This musculoskeletal shoulder model was developed in 2007 [42] to predict shoulder and elbow joint moments [50]. Thirty-eight muscle-tendon actuators were used to represent the function of 23 muscles of shoulder and elbow. The origin and insertion sites were derived from the VHM dataset. A scapulohumeral rhythm algorithm was used to predict the scapular motion based on the position of the humerus. Muscle forces were predicted using static optimization by minimizing the sum of cubed muscle stresses with constraints on the orientation of GH joint force. The predicted outcomes were validated against the outputs of the previous models.

Wu model

The Wu model was developed in OpenSim to perform inverse kinematics and inverse dynamics to obtain joint angles and joint moments. Model employed 10 DoFs and 26 musculo-tendon actuators that represented major axioscapular, axiohumeral, and scapulohumeral muscle groups. The model was made generic and then scaled down to six subject-specific datasets to calculate muscle and glenohumeral joint loading. The study concluded that generic and scaled generic musculotendon parameters do not provide the necessary accuracy for subject specific evaluations.

8.5 Chapter 8 References

- [1] B. M. Nigg and W. Herzog, Eds., *Biomechanics of the Musculo-skeletal System*, 3 edition. New Jersey: Wiley, 2007.
- [2] J. Li, Q. Ye, L. Ding, and Q. Liao, "Modeling and dynamic simulation of astronaut's upper limb motions considering counter torques generated by the space suit," *Comput. Methods Biomech. Biomed. Engin.*, vol. 20, no. 9, pp. 929–940, Jul. 2017.
- [3] W. Schiehlen, "Computational dynamics: theory and applications of multibody systems," *6th EUROMECH Solid Mech. Conf.*, vol. 25, no. 4, pp. 566–594, Jul. 2006.
- [4] W. Schiehlen, "Multibody System Dynamics: Roots and Perspectives," *Multibody Syst. Dyn.*, vol. 1, no. 2, pp. 149–188, Jun. 1997.
- [5] W. Schiehlen and P. Eberhard, "Multibody Systems and Applied Dynamics," in *Simulation Techniques for Applied Dynamics*, M. Arnold and W. Schiehlen, Eds. Vienna: Springer Vienna, 2009, pp. 1–20.
- [6] A. Seth and M. G. Pandy, "A neuromusculoskeletal tracking method for estimating individual muscle forces in human movement.," *J. Biomech.*, vol. 40, no. 2, pp. 356–366, 2007.
- [7] D. G. Thelen, F. C. Anderson, and S. L. Delp, "Generating dynamic simulations of movement using computed muscle control.," *J. Biomech.*, vol. 36, no. 3, pp. 321–328, Mar. 2003.
- [8] A. A. Nikooyan, H. E. J. Veeger, E. K. J. Chadwick, M. Praagman, and F. C. T. van der Helm, "Development of a comprehensive musculoskeletal model of the shoulder and elbow," *Med. Biol. Eng. Comput.*, vol. 49, no. 12, pp. 1425–1435, Dec. 2011.
- [9] V. J. Caiozzo and K. M. Baldwin, "Determinants of work produced by skeletal muscle: potential limitations of activation and relaxation.," *Am. J. Physiol.*, vol. 273, no. 3 Pt 1, pp. C1049-1056, Sep. 1997.
- [10] S. L. Delp *et al.*, "OpenSim: open-source software to create and analyze dynamic simulations of movement," *IEEE Trans. Biomed. Eng.*, vol. 54, no. 11, pp. 1940–1950, Nov. 2007.
- [11] E. M. Arnold, S. R. Ward, R. L. Lieber, and S. L. Delp, "A model of the lower limb for analysis of human movement.," *Ann. Biomed. Eng.*, vol. 38, no. 2, pp. 269–279, Feb. 2010.
- [12] W. Herzog, *Skeletal Muscle Mechanics: From Mechanisms to Function*. John Wiley & Sons, 2000.
- [13] J. HANSON and H. E. HUXLEY, "Structural Basis of the Cross-Striations in Muscle," *Nature*, vol. 172, no. 4377, pp. 530–532, Sep. 1953.
- [14] H. HUXLEY and J. HANSON, "Changes in the Cross-Striations of Muscle during Contraction and Stretch and their Structural Interpretation," *Nature*, vol. 173, no. 4412, pp. 973–976, May 1954.
- [15] E. Eisenberg, T. L. Hill, and Y. Chen, "Cross-bridge model of muscle contraction. Quantitative analysis," *Biophys. J.*, vol. 29, no. 2, pp. 195–227, Feb. 1980.
- [16] A. V. Hill, "The Heat of Shortening and the Dynamic Constants of Muscle," *Proc. R. Soc. Lond. B Biol. Sci.*, vol. 126, no. 843, pp. 136–195, 1938.
- [17] D. C. Ackland, Y.-C. Lin, and M. G. Pandy, "Sensitivity of model predictions of muscle function to changes in moment arms and muscle-tendon properties: a Monte-Carlo analysis," *J. Biomech.*, vol. 45, no. 8, pp. 1463–1471, May 2012.

- [18] Y. Nam and H. W. Uhm, "Tendon slack length and its effect on muscle force-generation characteristics," *J. Mech. Med. Biol.*, vol. 11, no. 02, pp. 445–456, Apr. 2011.
- [19] C. Redl, M. Gfoehler, and M. G. Pandy, "Sensitivity of muscle force estimates to variations in muscle-tendon properties," *Hum. Mov. Sci.*, vol. 26, no. 2, pp. 306–319, Apr. 2007.
- [20] F. E. Zajac, "Muscle and tendon: properties, models, scaling, and application to biomechanics and motor control.," *Crit. Rev. Biomed. Eng.*, vol. 17, no. 4, pp. 359–411, 1989.
- [21] A. J. van Soest and M. F. Bobbert, "The contribution of muscle properties in the control of explosive movements.," *Biol. Cybern.*, vol. 69, no. 3, pp. 195–204, 1993.
- [22] B. R. Umberger, K. G. M. Gerritsen, and P. E. Martin, "A model of human muscle energy expenditure.," *Comput. Methods Biomech. Biomed. Engin.*, vol. 6, no. 2, pp. 99–111, Apr. 2003.
- [23] B. J. Kushner, "Incomitant Strabismus: Does Extraocular Muscle Form Denote Function?Muscle," *Arch. Ophthalmol.*, vol. 128, no. 12, pp. 1604–1609, Dec. 2010.
- [24] J. M. Winters, "Hill-Based Muscle Models: A Systems Engineering Perspective," in *Multiple Muscle Systems: Biomechanics and Movement Organization*, J. M. Winters and S. L.-Y. Woo, Eds. New York, NY: Springer New York, 1990, pp. 69–93.
- [25] S. L. DELP, "Surgery simulation:A computer graphics system to analyze and design musculoskeletal reconstructions of the lower limb," PhD Dissertation, Stanford University, 1990.
- [26] D. A. Winter, *The biomechanics and motor control of human gait : normal, elderly and pathological*, 2nd ed. Waterloo, Ont. : University of Waterloo Press, 1991.
- [27] R. D. Crowninshield and R. A. Brand, "The prediction of forces in joint structures; distribution of intersegmental resultants.," *Exerc. Sport Sci. Rev.*, vol. 9, pp. 159–181, 1981.
- [28] H. Hatze, "The complete optimization of a human motion," *Math. Biosci.*, vol. 28, no. 1, pp. 99–135, Jan. 1976.
- [29] F. E. Zajac, R. R. Neptune, and S. A. Kautz, "Biomechanics and muscle coordination of human walking: part II: lessons from dynamical simulations and clinical implications.," *Gait Posture*, vol. 17, no. 1, pp. 1–17, Feb. 2003.
- [30] C. L. Vaughan, "Theories of bipedal walking: an odyssey.," *J. Biomech.*, vol. 36, no. 4, pp. 513–523, Apr. 2003.
- [31] A. J. van den Bogert, "Analysis and simulation of mechanical loads on the human musculoskeletal system: a methodological overview.," *Exerc. Sport Sci. Rev.*, vol. 22, pp. 23–51, 1994.
- [32] B. J. Fregly, J. A. Reinbolt, K. L. Rooney, K. H. Mitchell, and T. L. Chmielewski, "Design of patient-specific gait modifications for knee osteoarthritis rehabilitation.," *IEEE Trans. Biomed. Eng.*, vol. 54, no. 9, pp. 1687–1695, Sep. 2007.
- [33] P. Favre, J. G. Snedeker, and C. Gerber, "Numerical modelling of the shoulder for clinical applications," *Philos. Transact. A Math. Phys. Eng. Sci.*, vol. 367, no. 1895, pp. 2095–2118, May 2009.
- [34] S. Mollier, *Ueber die Statik und Mechanik des menschlichen Schultergürtels unter normalen und pathologischen Verhältnissen: mit 7 Tabellen*. Fischer, 1899.
- [35] C. J. De Luca and W. J. Forrest, "Force analysis of individual muscles acting simultaneously on the shoulder joint during isometric abduction," *J. Biomech.*, vol. 6, no. 4, pp. 385–393, Jul. 1973.
- [36] C. Högfors, G. Sigholm, and P. Herberts, "Biomechanical model of the human shoulder--I. Elements," *J. Biomech.*, vol. 20, no. 2, pp. 157–166, 1987.

- [37] C. Högfors, B. Peterson, G. Sigholm, and P. Herberts, "Biomechanical model of the human shoulder joint--II. The shoulder rhythm," *J. Biomech.*, vol. 24, no. 8, pp. 699–709, 1991.
- [38] F. C. van der Helm, "Analysis of the kinematic and dynamic behavior of the shoulder mechanism," *J. Biomech.*, vol. 27, no. 5, pp. 527–550, May 1994.
- [39] B. A. Garner and M. G. Pandy, "Musculoskeletal model of the upper limb based on the visible human male dataset," *Comput. Methods Biomech. Biomed. Engin.*, vol. 4, no. 2, pp. 93–126, Feb. 2001.
- [40] K. R. S. Holzbaur, W. M. Murray, and S. L. Delp, "A model of the upper extremity for simulating musculoskeletal surgery and analyzing neuromuscular control," *Ann. Biomed. Eng.*, vol. 33, no. 6, pp. 829–840, Jun. 2005.
- [41] I. W. Charlton and G. R. Johnson, "A model for the prediction of the forces at the glenohumeral joint," *Proc. Inst. Mech. Eng. [H]*, vol. 220, no. 8, pp. 801–812, Nov. 2006.
- [42] C. R. Dickerson, D. B. Chaffin, and R. E. Hughes, "A mathematical musculoskeletal shoulder model for proactive ergonomic analysis," *Comput. Methods Biomech. Biomed. Engin.*, vol. 10, no. 6, pp. 389–400, Dec. 2007.
- [43] W. Wu, P. V. S. Lee, A. L. Bryant, M. Galea, and D. C. Ackland, "Subject-specific musculoskeletal modeling in the evaluation of shoulder muscle and joint function," *J. Biomech.*, vol. 49, no. 15, pp. 3626–3634, 07 2016.
- [44] G. Rao, D. Amarantini, E. Berton, and D. Favier, "Influence of body segments' parameters estimation models on inverse dynamics solutions during gait," *J. Biomech.*, vol. 39, no. 8, pp. 1531–1536, 2006.
- [45] H. E. Veeger, F. C. Van der Helm, L. H. Van der Woude, G. M. Pronk, and R. H. Rozendal, "Inertia and muscle contraction parameters for musculoskeletal modelling of the shoulder mechanism," *J. Biomech.*, vol. 24, no. 7, pp. 615–629, 1991.
- [46] "For good measure -- Natick releases raw data from Army-wide anthropometric survey," *www.army.mil*. [Online]. Available: https://www.army.mil/article/188601/for_good_measure_natick_releases_raw_data_from_army_wide_anthropometric_survey. [Accessed: 17-Apr-2019].
- [47] P. de Leva, "Adjustments to Zatsiorsky-Seluyanov's segment inertia parameters," *J. Biomech.*, vol. 29, no. 9, pp. 1223–1230, Sep. 1996.
- [48] B. Patel, P. A. Gustafson, and J. Jastifer, "The effect of clavicle malunion on shoulder biomechanics; a computational study," *Clin. Biomech. Bristol Avon*, vol. 27, no. 5, pp. 436–442, Jun. 2012.
- [49] K. R. Saul, S. Hayon, T. L. Smith, C. J. Tuohy, and S. Mannava, "Postural dependence of passive tension in the supraspinatus following rotator cuff repair: a simulation analysis," *Clin. Biomech. Bristol Avon*, vol. 26, no. 8, pp. 804–810, Oct. 2011.
- [50] S. L. Fischer, E. C. Brenneeman, R. P. Wells, and C. R. Dickerson, "Relationships between psychophysically acceptable and maximum voluntary hand force capacity in the context of underlying biomechanical limitations," *Appl. Ergon.*, vol. 43, no. 5, pp. 813–820, Sep. 2012.

Chapter 9

Development of a pediatric shoulder joint model

9.1 Introduction

Obstetric Brachial Plexus Palsy (OBPP) is a nerve injury during child birth, associated with muscle imbalances and contractures resulting in bone deformities and function loss in the shoulder complex. Surgical treatment and rehabilitation are typical remedies, however, the lack of understanding in abnormal muscular behavior drastically reduces the success of treatment. Computational modeling can be effectively used to elucidate OBPP patho-mechanics to expand on the clinical assessment, rehabilitation or treatment strategies. Computational modeling domains typically include (but not limited to) finite element modeling, discrete element physics-based modeling, and multi-body musculoskeletal modeling. Multi-body modeling has a unique advantage in evaluating the function of the musculoskeletal system using dynamics principles and deriving muscle and joint related parameters such as joint moments, muscle forces and moment arms, predictive kinematics, etc. All these parameters can positively guide the treatment and rehabilitation process for OBPP. However, to date, no pediatric multibody shoulder models of pediatric shoulder joint exist. **This study is focused on the development of a multi-body musculoskeletal modeling framework for a healthy pediatric shoulder joint.** This model will be used in the future (not in the scope of the thesis) for evaluating OBPP by making subject-specific simulations for daily living activities.

As reviewed in the previous chapter (Chapter 7), lack of shoulder musculoskeletal model for the pediatric population is the first limitation in this research domain leading to many more associated limitations. **To overcome this major limitation, a musculoskeletal model of the pediatric shoulder joint was developed and simulated using and customizing the opensource multi-body modeling framework OpenSim [1].** The pediatric musculoskeletal model was constructed based on a pediatric MRI scan of a 13-year-old healthy girl with no previous shoulder or upper limb injury. This chapter provides a detailed description of the model development process and the methodology followed. Section 2 explains Kinematics of the model which includes bone geometry and coordinate systems, joint geometry (how each of the ST, SC, AC, and GH joints are modeled), and muscle geometry (muscle structure is modeled in terms of its origin and insertion on bones, its prescribed path, and definitions of wrapping surfaces used in the model).

Section 3 describes Dynamics of the model detailing body segment parameters used in the model and the parameters used for musculotendon actuator dynamics (activation and contraction).

9.2 Kinematics

9.2.1 Bone: Geometry and embedded coordinate system

To build the model structure, MRI dataset of a healthy girl child was extracted and used. Data was retrospectively acquired on a 3T Philips scanner (Philips Achieva, Best, Netherlands) from CHRU's radiology department for a 13-year-old girl who had an upper body MRI for reasons not related to shoulder pathology.

A custom-made e-THRIVE sequence was used for static MRI acquisition of the shoulder joint in the sagittal and axial plane(s). Following imaging parameters were used:

Table 9. 1: *MRI acquisition parameters*

Imaging Parameter	Value
MR acquisition type	3D
Field of View	450 X 450 mm
Voxel size	0.28 X 0.28 X 0.1 mm
Number of slices	600
TR	9.46 ms
TE	5.75 ms
Slice Thickness	1.5 mm
Slice gap	0.75 mm
Flip Angle	10°
Fold over suppression	Yes
Fold over direction	ML
NSA	1

The demographical information about the healthy volunteer is shown in Table 9.2:

Table 9. 2: *Demographic patient information*

Sex	Age (years)	Weight (Kg)	Height (cm)	Handedness
Female	13	46	160	Right handed

Right shoulder and right limb were targeted for model building. Skeletal geometry of thorax (including sternum, spine and the important part of the ribs), clavicle, scapula, and humerus (Figure 9.1) was acquired from MRI data. For this, manual segmentation of each bone was first performed in a 3D modeling software called Amira (Amira, FEI, Hillsboro, V5.4) and 3D surface mesh of each bone (rigid body) was created (Figure 9.1). For each bony segment, a local coordinate system was defined from a set of bony landmarks as per the recommendation from the International Society of Biomechanics (ISB) [2]. The landmarks, used to define the axes of the coordinate system for each segment, were selected in Amira (Amira, FEI, Hillsboro, V5.4). Then, 3D position of each landmark was saved and used to determine the local (body fixed) coordinate frame. Coordinates of these landmarks were expressed in the global frame (MRI frame) and described in Table 9.3. The embedded coordinate system is a set of axes, which defines the orientation of the segment in the global frame, and location of the origin, which defines the position of the segment in the global frame.

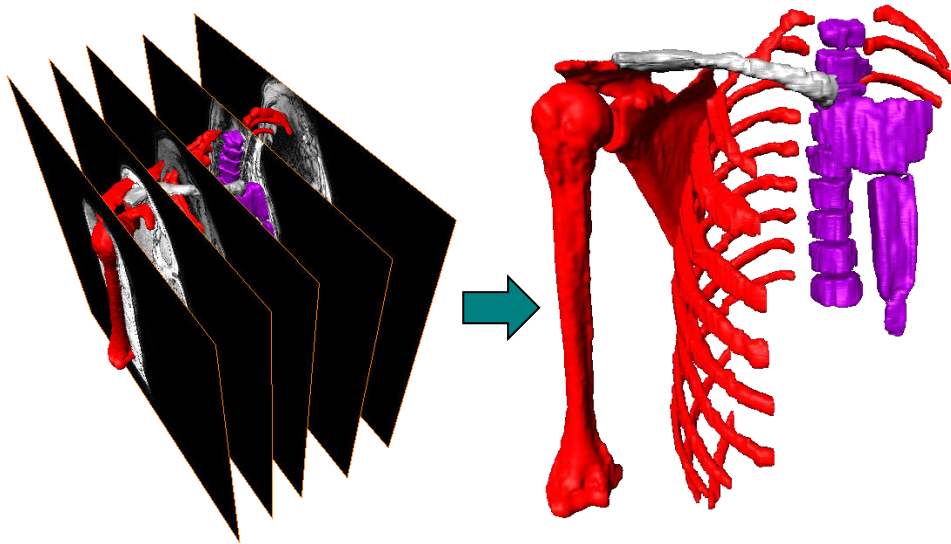


Figure 9. 1: *Model building: From MRI data to 3D reconstruction*

The orientation is described in 3x3 rotation matrix ${}^G R^S$ containing the three direction vectors (\bar{X} , \bar{Y} and \bar{Z}). Each direction vector is a unit vector defining the angle of that axis with the axes of the global coordinate system. The axes of segment coordinate frame are expressed in the global frame.

Rotation of the segment S in the global frame G is expressed as:

$${}^G R^S = [{}^G[\bar{X}] \quad {}^G[\bar{Y}] \quad {}^G[\bar{Z}]]$$

With, ${}^G[\bar{X}]$ the x-axis of the frame S expressed in the frame G.

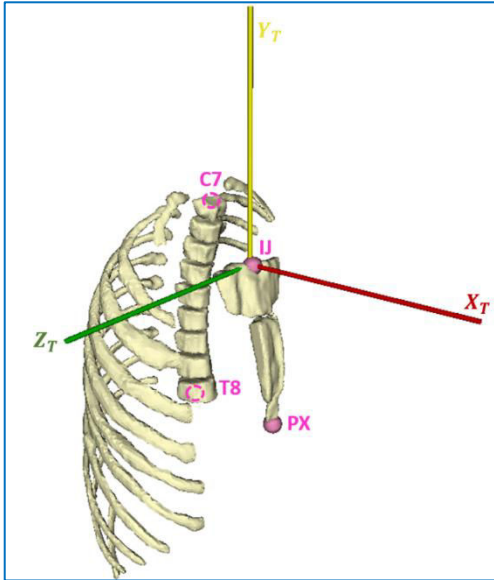
The embedded coordinate system, which represents the configuration of the segment frame S, is represented in a 4x4 transformation matrix combining rotation matrix and position (translation) of origin point in the global coordinate frame ${}^G P^S = \begin{bmatrix} x \\ y \\ z \end{bmatrix}$. The transformation matrix of the segment frame S expressed in the global frame G is written as follows:

$${}^G T^S = \begin{bmatrix} {}^G R^S & {}^G P^S \\ 0 & 1 \end{bmatrix}$$

Bellow, an explanation of how the coordinate system was created for each of the bones, used in the model for 1) thorax (including sternum, spine and the important part of the ribs), 2) clavicle, 3) scapula and 4) humerus, is provided. A set of bony landmarks were used to define the segments' locale frames (Table 9.3). Then, the transformation matrices for each segment embedded coordinate system, which were computed using Matlab (Mathworks, Natick, MA, USA), are reported in Table 9.4.

9.2.1.1 Thorax

The bony landmarks used to define thorax embedded coordinate system are: The spinous process of the seventh cervical vertebra (C7), the spinal process of the eighth thoracic vertebra (T8) and the suprasternal notch (IJ) and the processus xiphoideus (PX) (figure 9.2).



$$\bar{Y}_{Thorax} = \frac{\frac{(IJ+\bar{C7})}{2} - \frac{(PX+\bar{T8})}{2}}{\left| \frac{(IJ+\bar{C7})}{2} - \frac{(PX+\bar{T8})}{2} \right|}$$

$$\bar{Z}_{Thorax} = \frac{(IJ - \frac{(\bar{C7} + IJ)}{2}) \times \bar{Y}_{Thorax}}{\left| (IJ - \frac{(\bar{C7} + IJ)}{2}) \times \bar{Y}_{Thorax} \right|}$$

$$\bar{X}_{Thorax} = \bar{Y}_{Thorax} \times \bar{Z}_{Thorax}$$

$$Origin_{Thorax} = IJ$$

Figure 9. 2: Thorax coordinate system according to ISB. \bar{Y}_T : the axis connecting point 1 p_1 defined as the midpoint between PX and T8 and point 2 p_2 defined as the midpoint between IJ and C7, pointing to p_2 .

\bar{Z}_T : the axis perpendicular to the plane formed by C7, IJ and p_1 , pointing to the right.

\bar{X}_T : the axis perpendicular to \bar{Z}_{Thorax} and \bar{Y}_{Thorax} , pointing forward.

9.2.1.2 Clavicle

The body coordinate system for clavicle is defined by the two bony landmarks located on each side of the clavicle on the joints formed between clavicle and thorax ventrally (SC joint) on the medial side and clavicle and scapula dorsally (AC joint) on the lateral side of the clavicle. Considering the flat and long shape of the clavicle the Y axis of the thorax is used in the coordinate system definition (figure 9.3).

$$\bar{Z}_{Clavicle} = \frac{\overline{AC} - \overline{SC}}{|\overline{AC} - \overline{SC}|}$$

$$\bar{X}_{Clavicle} = \frac{\bar{Y}_{Thorax} \times \bar{Z}_{Clavicle}}{|\bar{Y}_{Thorax} \times \bar{Z}_{Clavicle}|}$$

$$\bar{Y}_{Clavicle} = \bar{Z}_{Clavicle} \times \bar{X}_{Clavicle}$$

$$Origin_{Clavicle} = SC$$

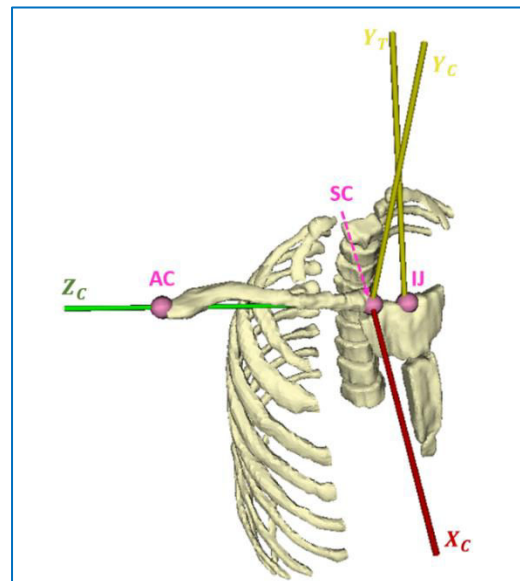
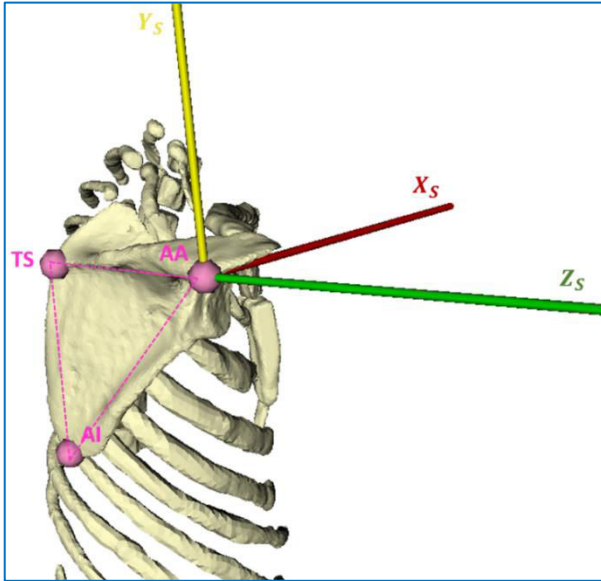


Figure 9. 3: Clavicle coordinate system according to ISB. \bar{Z}_C : the axis connecting Ac and SC, pointing to AC. \bar{X}_C : the common axis perpendicular to \bar{Z}_C and \bar{Y}_T . \bar{Y}_C : the common axis perpendicular to \bar{X}_C and \bar{Z}_C , pointing upward.

9.2.1.3 Scapula

The scapula embedded coordinate system definition uses the three most discerned bony landmarks of the scapula: the Angulus Acromialis (AA), the Trigonum Spinae (TS) and the Angulus Inferior (AI) (figure 9.4).



$$\bar{Z}_{Scapula} = \frac{\overline{AA} - \overline{TS}}{|\overline{AA} - \overline{TS}|}$$

$$\bar{X}_{Scapula} = \frac{(\overline{AA} - \overline{AI}) \times \bar{Z}_{Scapula}}{|(\overline{AA} - \overline{AI}) \times \bar{Z}_{Scapula}|}$$

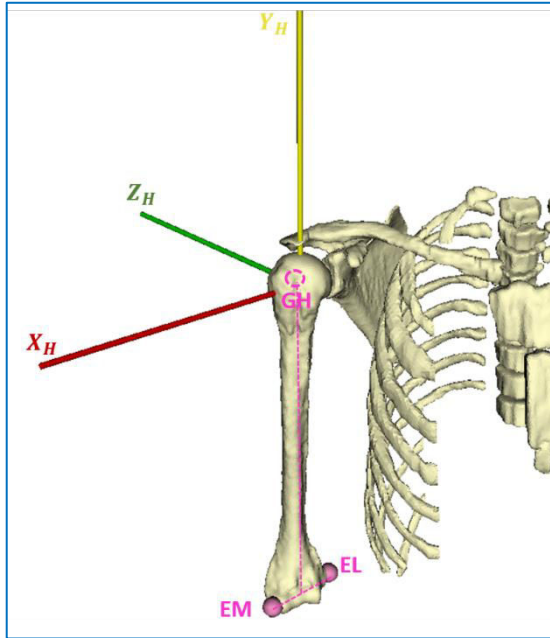
$$\bar{Y}_{Scapula} = \bar{Z}_{Scapula} \times \bar{X}_{Scapula}$$

$$Origin_{Scapula} = AA$$

Figure 9. 4: Scapula coordinate system according to ISB. \bar{Z}_S : the axis from the TS to AA. \bar{X}_S : The axis perpendicular to the plane formed by AA, AI and TS, pointing forward. \bar{Y}_S : the common axis perpendicular to \bar{X}_S and \bar{Z}_S , pointing upward.

9.2.1.4 Humerus

For the humerus, in addition to the two most distinguished bony landmarks of the lateral epicondyle (EL) and the medial epicondyle (EM), the center of rotation of the glenohumeral joint (GH) is used to define the embedded coordinate system. The GH joint center is determined as the center of the sphere fitted to the humeral head.



$$\bar{Y}_{Humerus} = \frac{\overline{GH} - \frac{(\overline{EL} + \overline{EM})}{2}}{\left| \overline{GH} - \frac{(\overline{EL} + \overline{EM})}{2} \right|}$$

$$\bar{Z}_{Humerus} = \frac{(\overline{EL} - \overline{EM}) \times \bar{Y}_{Humerus}}{|(\overline{EL} - \overline{EM}) \times \bar{Y}_{Humerus}|}$$

$$\bar{X}_{Humerus} = \bar{Y}_{Humerus} \times \bar{Z}_{Humerus}$$

$$Origin_{Humerus} = GH$$

Figure 9. 5: *Humerus coordinate system according to ISB.* \bar{Y}_H : the axis from the midpoint of EM and EL to GH. \bar{Z}_H : the axis perpendicular to the plane formed by EM, EL and GH, pointing backward. \bar{X}_H : the common axis perpendicular to \bar{Y}_H and \bar{Z}_H , pointing to the right.

Table 9. 3: *Position of bony landmarks (in cm) used to define the segments' locale frames determined using a Matlab algorithm (Mathworks, Natick, MA, USA).*

Bony Landmarks	Abbreviation	X	Y	Z
Seventh Cervical vertebra	C7	0.41	3.93	26.42
Eighth Thoracic vertebra	T8	0.96	6.87	9.87
Incisura Jugularis	IJ	1.19	0.15	21.54
Processus Xiphoideus	PX	1.57	-2.67	8.4
Acromioclavicular fissura	AC	-14.42	4.19	24.5
Sternoclavicular fissura	SC	-1.39	-0.07	22.36
Angulus Acromialis	AA	-16.06	6.29	23.48
Trigonum Spinae	TS	-6.57	10.19	21.42
Angulus Inferior	AI	-8.10	11.15	11.49
Lateral Epicondyle	EL	-19.32	5.87	-4.72
Medial Epicondyle	EM	-14.38	8.5	-3.97
Glenohumeral joint center	GH	-15.88	3.25	20.91

Table 9. 4: Transformation matrices of the segment's local frames, computed using a Matlab algorithm (Mathworks, Natick, MA, USA). (frame origin coordinates are in meters)

Segment	Transformation Matrix			
Thorax	0.1487	-0.0315	-0.9884	0.0119
	-0.9888	-0.01387	-0.1483	-0.0015
	-0.0090	0.9994	-0.0332	0.2154
	0	0	0	1
Clavicle	-0.3144	0.1396	-0.9390	-0.0139
	-0.9490	-0.0703	0.3073	-0.0007
	-0.0231	0.9877	0.1546	0.2236
	0	0	0	1
Scapula	0.3498	0.2361	-0.9066	-0.1606
	-0.9259	-0.0602	-0.3729	0.0629
	-0.1426	0.9699	0.1976	0.2348
	0	0	0	1
Humerus	-0.8756	0.0380	-0.4815	-0.1588
	-0.4812	-0.1540	0.8630	0.0325
	-0.0413	0.9873	0.1531	0.2091
	0	0	0	1

It is important here to note that, in OpenSim, the segmented mesh file for each segment is used only for visualization and no geometric information, more than the ones indicated by the modeler (landmarks, wrapping surfaces, muscle origins, and insertions), are used during simulation.

9.2.2 Muscles geometry: insertions, paths and wrapping surfaces

An anatomical description of the shoulder muscles origins and insertions with their main functions are presented in Chapter 2. Shoulder muscles are divided into three shoulder muscle groups: **axioscapular**, **axiohumeral** and **scapulohumeral** as described in Chapter 2. **The model contains 52 musculo-tendon actuators to represent 14 shoulder muscles. Three axioscapular muscles are included: the superior trapezius, the middle trapezius, and the inferior trapezius. The axiohumeral muscle group is represented by the latissimus dorsi and pectoralis major(thoracic) and pectoralis major(clavicular) muscles. Finally, eight scapulohumeral muscles are included viz, anterior deltoid, middle deltoid, posterior deltoid, infraspinatus, supraspinatus, subscapularis, teres minor, and teres major.**

In table 9.5, the coordinates of muscle origin and insertion are defined in their respective segment frame. The number of fascicles is selected to proportionally represent the muscle volume, meaning larger

muscles have a greater number of fascicles and so on. The locations of muscle attachment sites were determined by distributing the fascicles isometrically over the insertion regions on the bone (as described in chapter 2).

Table 9. 5: Muscle presented in the models, number of fascicules presenting each muscle and coordinates of origins and insertions.

Muscle	Short Name	No. of fascicles	Origin Bone and frame	Muscle origin coordinates				Insertions bone	Muscle insertion coordinates		
					X	Y	Z		X	Y	Z
Trapezius Superior	TrapSup	3	Thorax	L1	-0.06	0.061	-0.005	Clavicle	-0.002	0	0.131
				L2	-0.046	0.092	-0.004		-0.012	0.005	0.106
				L3	-0.034	0.124	-0.003		-0.012	0.01	0.09
Trapezius Middle	TrapMid	2	Thorax	L1	-0.073	-0.002	-0.005	Scapula	0.021	0.027	-0.09
				L2	-0.064	0.037	0.001		0.009	0.01	-0.008
Trapezius Inferior	TrapInf	3	Thorax	L1	-0.077	-0.047	-0.006	Scapula	0.016	0.023	-0.094
									0.004	0.009	-0.022
				L2	-0.082	-0.1	-0.004		0.009	0.019	-0.097
									-0.001	0.01	-0.038
Supraspinatus	SupS	3	Scapula	L1	0.004	0.007	-0.089	Humerus	0.019	0.013	0.003
				L2	0.01	0.014	-0.087		0.019	0.015	-0.003
				L3	0.016	0.02	-0.081		0.019	0.014	-0.001
Subscapularis	SubS	6	Scapula	L1	0.015	0.01	-0.091	Humerus	0.005	0	-0.021
					0.038	-0.013	-0.031				
				L2	0.008	-0.002	-0.099		0.006	-0.006	-0.022
					0.034	-0.024	-0.032				
				L3	0.005	-0.023	-0.104		0.003	-0.012	-0.02
					0.028	-0.034	-0.036				
				L4	0.005	-0.038	-0.105		0.003	-0.019	-0.019
					0.026	-0.044	-0.043				
				L5	0.003	-0.054	-0.105		0.002	-0.026	-0.016
					0.023	-0.056	-0.051				
Anterior Deltoid	DeltAnt	3	Clavicle	L1	0.0	0.004	0.094	Humerus	-0.005	-0.012	-0.024
									0.012	-0.106	-0.003
				L2	0.002	0.001	0.108		0.007	-0.001	-0.026

									0.009	-0.103	-0.004
				L3	0.01	-0.002	0.125		0.02	0.006	-0.018
									0.01	-0.092	-0.002
Middle Deltoid	DeltMid	3	Scapula	L1	0.01	0.001	0.01	Humerus	0.014	-0.003	0.02
									0.013	-0.105	0.002
				L2	0.023	0.005	0.013		0.027	0.007	0.008
									0.014	-0.1	-0.001
				L3	0.035	0.005	0.012		0.027	0.012	-0.009
							0.013	-0.093	-0.002		
Posterior Deltoid	DeltPost	4	Scapula	L1	0	0	0	Humerus	0.013	-0.085	0
				L2	-0.001	0.004	-0.017		0.012	-0.092	0.001
				L3	0.001	0.008	-0.039		0.012	-0.099	0.001
				L4	-0.001	0.006	-0.058		0.012	-0.105	0.001
Infraspinatus	InfS	6	Scapula	L1	-0.004	-0.048	-0.1	Humerus	0.016	0.009	0.013
				L2	-0.002	-0.072	-0.099		0.021	0.011	0.006
				L3	-0.002	-0.015	-0.093		0.02	0.012	0.007
				L4	-0.002	-0.027	-0.097		0.018	0.013	0.011
				L5	-0.004	-0.039	-0.1		0.017	0.013	0.011
				L6	-0.004	-0.06	-0.1		0.02	0.01	0.01
Teres Minor	Tmin	2	Scapula	L1	0.002	-0.069	-0.073	Humerus	0.018	0.001	0.014
				L2	0.004	-0.06	-0.069		0.018	0.009	0.013
Teres Major	Tmaj	3	Scapula	L1	0.001	-0.077	-0.081	Humerus	-0.006	-0.04	-0.007
				L2	0.001	-0.083	-0.089		-0.007	-0.049	-0.005
				L3	-0.001	-0.092	-0.095		-0.006	-0.056	-0.004
Pectoralis Major (Thoracic)	PecMajThor	5	Thorax	L1	0.005	-0.013	0.019	Humerus	0.013	-0.024	-0.01
				L2	0.014	-0.031	0.018		0.011	-0.033	-0.01
				L3	0.028	-0.054	0.012		0.009	-0.042	-0.009
				L4	0.032	-0.071	0.013		0.008	-0.048	-0.009
				L5	0.033	-0.093	0.013		0.008	-0.048	-0.009
Pectoralis Major (Clavicular)	PecMajClav	3	Clavicle	L1	0.006	0.003	0.013	Humerus	0.01	-0.036	-0.009
				L2	0.006	0.006	0.036		0.011	-0.028	-0.009
				L3	0.008	0.006	0.054		0.014	-0.02	-0.01
Latissimus Dorssi	LatD	6	Thorax	L1	-0.085	-0.112	-0.01	Humerus	0.007	-0.036	-0.01
				L2	-0.084	-0.131	-0.009		0.007	-0.036	-0.01
				L3	-0.074	-0.161	-0.01		0.007	-0.036	-0.01
				L4	-0.074	-0.178	-0.008		0.007	-0.036	-0.01
				L5	-0.074	-0.194	-0.006		0.007	-0.036	-0.01
				L6	-0.074	-0.206	-0.006		0.007	-0.036	-0.01

One of the major challenges of musculoskeletal modeling is to define muscle paths and design wrapping surfaces for muscles to accurately mimic the way in which muscles glide over the bones and other musculoskeletal constraints. The challenge is posed in defining the muscle paths during all the RoM tasks. Many previous musculoskeletal models were affected by the lack of muscle wrapping surfaces or absence of muscle path definitions that lead to exerting wrong forces on the connecting bones or muscles penetrating the adjacent bones without restrictions for certain movements. To avoid this in the current model, muscle path is defined by either a **fixed point and/or moving points** and/or a **wrap points** as defined in OpenSim software. **Fixed points** are the attachment points which are fixed in the segment coordinate frame. Each pair of adjacent points is connected by a straight line and the set of these straight lines defines the muscle path. To assist the muscle stay afloat the bone, **wrapping surfaces** can be defined in OpenSim which then are associated with relevant bone geometries. For these wrapping surfaces, bony contours are represented by analytical geometric shapes (sphere, ellipsoid, cylinder) to wrap the muscle around and avoid penetrating through the bone.

9.2.2.1 Thorax

In our model, two ellipsoids are used to represent the thorax: one to cover the posterior rib surface and second to cover the anterior rib surface (figure 9.6). The one covering the posterior ribs provides a wrapping surface for latissimus dorsi and trapezius with insertions on the scapula (middle trapezius and inferior trapezius) and the one covering the anterior ribs serves as wrapping surface for the pectoralis major with insertion in the sternum. The dimensions of these ellipsoids are justified by the bony structure that they are representing.

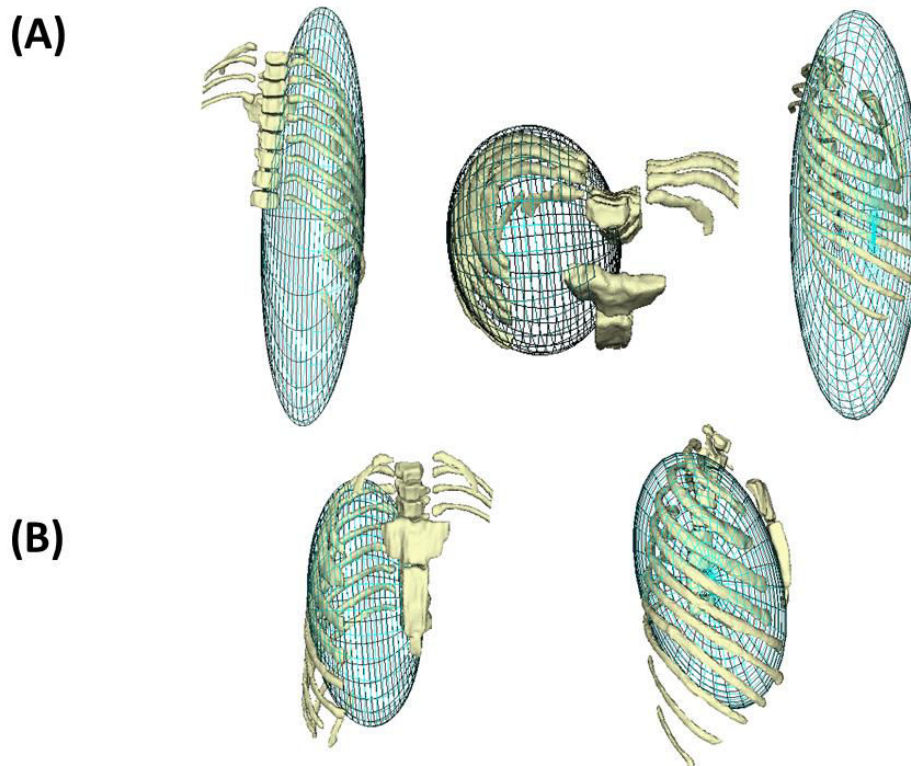


Figure 9. 6: (A) Back, top and side views of ellipsoid covering posterior ribs (B) front and side views of the ellipsoid covering the anterior ribs.

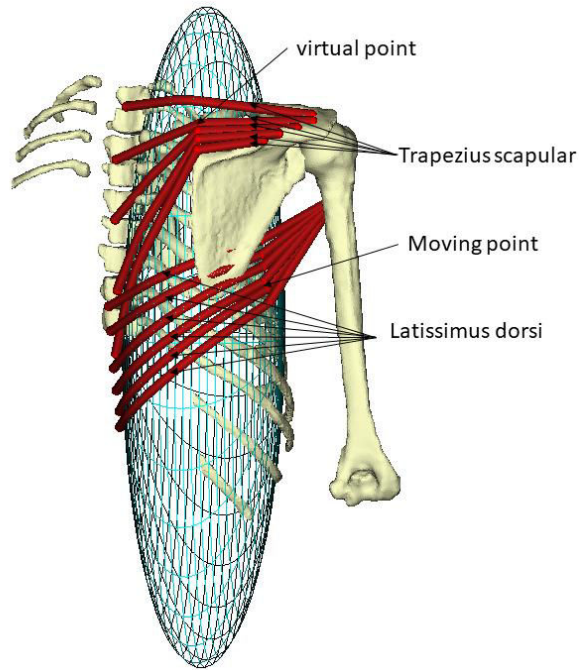


Figure 9. 7: latissimus dorsi and trapezius with scapular insertion wrapping around the posterior ribs.

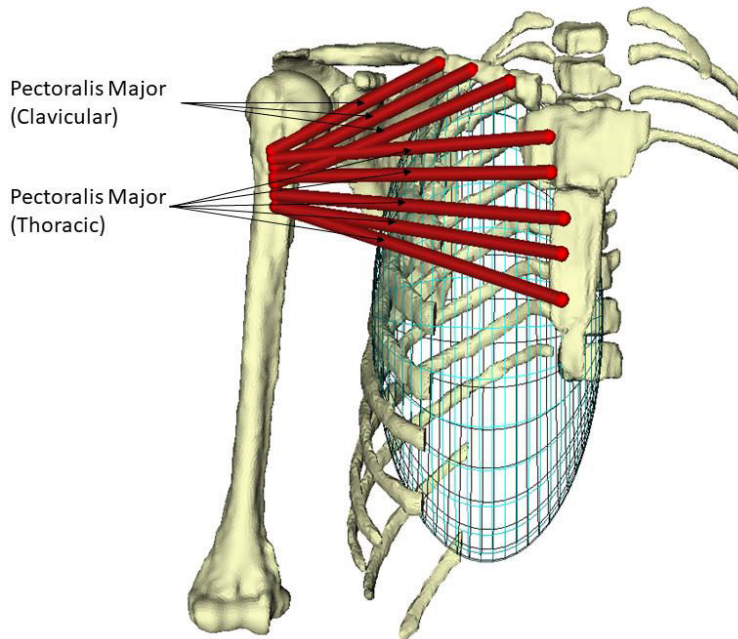


Figure 9. 8: Pectoralis Major with clavicular insertion and Pectoralis major with sternum insertion wrapping around the anterior ribs.

9.2.2.2 Humerus

Humeral column is represented by a cylinder wrapping surface, providing a wrapping to the posterior deltoid muscle (figure 9.9). A sphere was used as a wrapping surface around the humeral head to prevent muscles crossing the humeral head. A set of six muscles wrap around this surface, including supraspinatus, subscapularis, deltoid anterior, middle deltoid, infraspinatus and teres Minor (Figure 9.10).

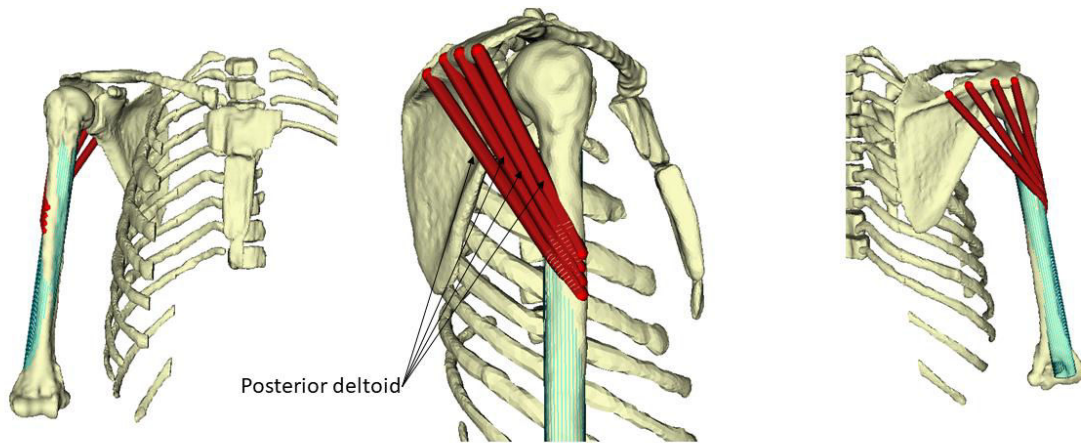


Figure 9. 9: Humeral column wrapping surface (cylinder) with posterior deltoid wrapping.

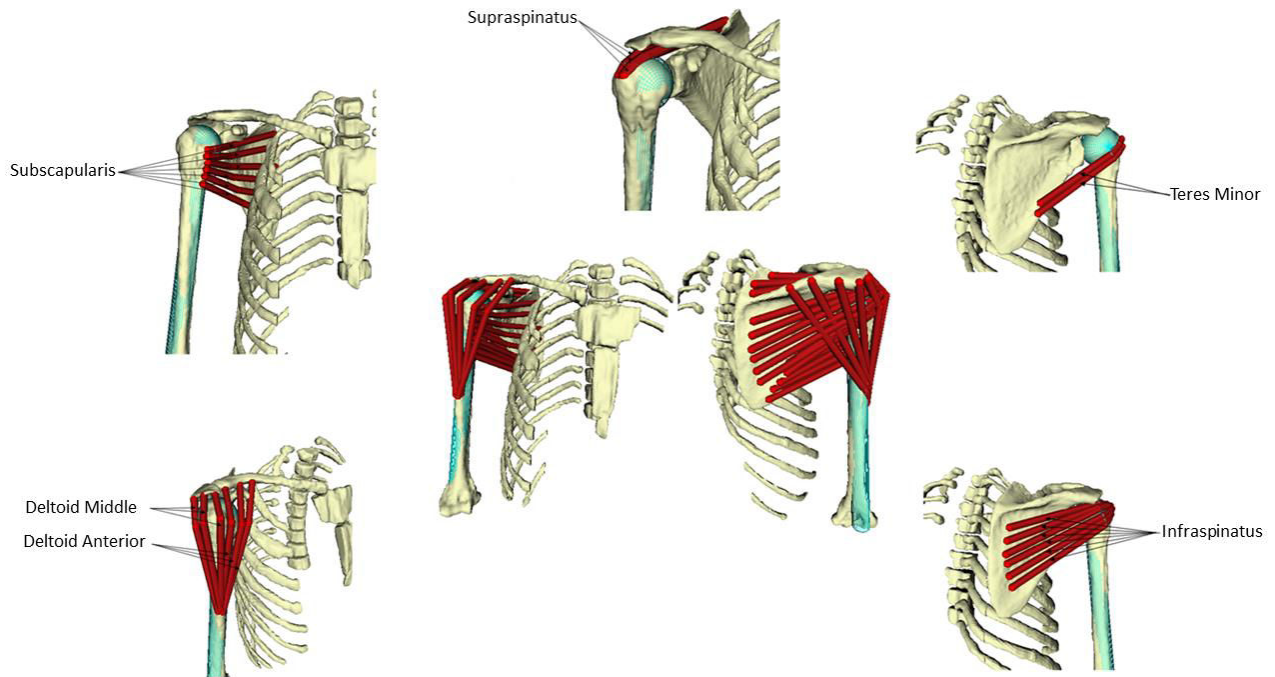


Figure 9. 10: Muscles wrapping around the humeral head wrapping surface, including supraspinatus, subscapularis, deltoid anterior, middle deltoid, infraspinatus and teres Minor.

For some muscles (for e.g., deltoid), I added more points along the muscle-fiber path to represent the curved aspect of the line of action and avoid that the muscles penetrate the adjacent bones in different RoM. In this case, the muscle-fiber path is represented by more than the two points of origin and insertion. These points are defined either as **virtual points** or **moving points** (figure 9.7). The virtual points have a fixed coordinate in their associated segments, whereas, moving points coordinates are function of joint coordinates. For example, for trapezius muscle with scapular insertion, the muscle line of action wrap around the posterior ribs represented as an ellipsoid but also has some virtual points to represent as close as possible the anatomical path of the muscle (figure 9.7). To avoid the sudden unphysiological changes in muscle path wrapping for the latissimus dorsi muscle, for which the muscle path moves as the shoulder abduct, the best muscle path representation is using moving muscle points (figure 9.7).

In OpenSim, three algorithms are available to calculate the muscle paths over ellipsoid wrapping surface including: **midpoint wrapping** surface, **axial wrapping** method and **hybrid wrapping** method. The hybrid wrapping method will be used for all the muscles subjected to wrapping in the model. Midpoint wrapping algorithm, as its name implies, calculates the midpoint of the imaginary muscle straight line passing through the ellipsoid and then finds the closest point on the ellipsoid surface to that midpoint. This algorithm determines a wrapping plane based on this closest point to the midpoint and the intersections of the imaginary muscle straight path with the ellipsoid surface. This method showed numerically instable results when the muscle line passes close to the ellipsoid center. The axial wrapping algorithm takes the intersection of the of the imaginary muscle straight line passing through the ellipsoid and one of planes perpendicular to one chosen principal axis (most parallel to the muscle line) to determine the wrapping path. This method is mostly chosen when the muscle line stays always parallel to one of the ellipsoid principal axes during the entire RoM. The hybrid algorithm combines the midpoint and axial algorithms, computing a weighted average of the results from both.

Table 9. 6: Muscle wrapping surfaces used in the model. All the coordinates are in meters

Structure	Bone	Shape	Center			Axes for ellipsoid, Radius for sphere and Radius and length of the cylinder			Rotation around (deg)		
			X	Y	Z	Radius			X	Y	Z
Humeral head	Humerus	sphere	-0.0018	0.002	0.001	0.022			0	0	0
Humeral column	Humerus	cylinder	0.002	-0.128	0.006	Radius	Length				
						0.01	0.25		85	0	0
Anterior ribs	Thorax	Ellipsoid	-0.52	-0.1	0.049	A_x	A_y	A_z	0	0	15
Posterior ribs	Thorax	Ellipsoid	-0.052	-0.14	0.055	0.07	0.13	0.06	0	0	-6.30

Table 9. 7: The muscles affected by the wrapping and the associated wrapping surfaces

Muscle	Wrapping Object
Trapezius middle	Posterior ribs
Trapezius inferior	Posterior ribs
Supraspinatus	Humeral head
Subscapularis	Humeral head
Deltoid Anterior	Humeral head
Middle Deltoid	Humeral head
Posterior Deltoid	Humeral column
Infraspinatus	Humeral head
Teres Minor	Humeral Head
Pectoralis Major (thoracic)	Anterior ribs
Latissimus dorsi	Posterior ribs

9.2.3 Joint geometry

9.2.3.1 Joint modeling in OpenSim and Pediatric shoulder model topology

Joint kinematics describes the connection (relationship) between each segment and its proximal segment in terms of rotations and translations. The model is based on an internal-coordinate joint formulation [3] called “**Mobilizer**” (Figure 9.11). The mobilizer formulation allows the representation of joint kinematics with less differential equations and no algebraic constraint equations. This complexity reduction is a considerable advantage in multibody dynamic simulations. The idea of mobilizer is representing the motion only by the coordinates that have degrees of freedom (DoF) associated with the physical joint. The concept of internal coordinate is built on top of the “hinge matrix” concept. In the multi-body dynamics books, this is referred as “hinge map matrix” or “joint motion map matrix” theory. The hinge matrix consists of mapping the mobilities with the associated spatial kinematics that are used to formulate the equations of motion. Thus, the mobilizer represents the kinematic relationship between two segments parameterized by one to six mobilities (associated with DoFs) in the Euclidian space. A mobilizer connects each “**child**” **body** local frame to its unique “**parent**” **body** local frame (Figure 9.11). More details on the mobilizer concept are presented in these references in details [3]–[5].

A joint in the model is defined by rotation and translation of a distal segment bone relative to the proximal segment bone, as a mobilizer, and using the associated DoFs. At the time of defining a new segment, we define its connection to its proximal segment. For example, clavicle with respect to thorax, scapula with respect to thorax and humerus with respect to scapula etc. The international society of biomechanics (ISB) [2] proposed a definition of joint coordinate system (JCS) for each articulating joint in the musculoskeletal structure. The main aim of these recommendations is to standardize the procedure of model development and the protocol of data collection, in order, to facilitate communication among researchers and clinicians. The SC joint JCS was constructed using the ISB recommendations. For GH and ST joints, we used more clinically relevant definition of the JCS. Joint motions in the OpenSim model are defined with Euler sequences. Joints in OpenSim can have different constructs depending on the use of DoF associated with the joint to be modeled. These include 1) Pin joint (no DoFs, only two bodies are constrained to move together), 2) Hinge joint (one rotational DoF), 3) Ball and socket joint (3 rotational DoF), 4) Free joint (all translational and rotational DoFs), 5) Custom joint (Up to 6 DoFs that can be customized for any combination). These predefined joints come with their predefined type of Euler sequence, except the custom joint for which you can customize the rotation sequence. **In our model, all the joints are defined as custom joints with the appropriate Euler sequences.**

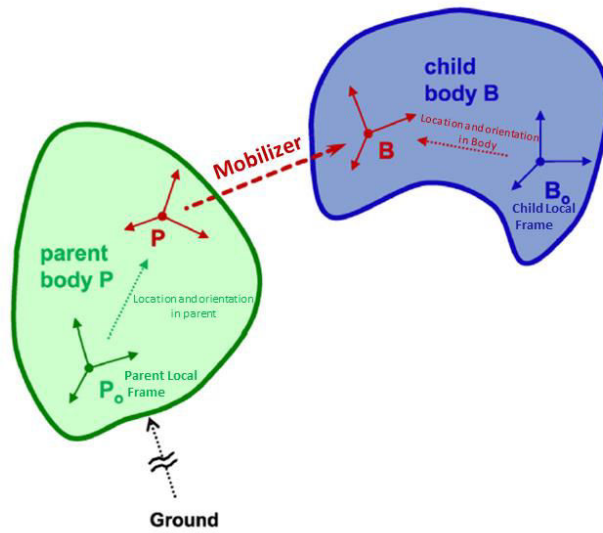


Figure 9. 11: Concept of a mobilizer to define a joint between two bodies (adapted from [3]).

The pediatric model developed in this thesis work has the following joints: 1) Ground to Thorax, 2) SC joint, 3) AC joint, 4) ST joint, and 5) GH joint. The model structure topology following (Figure 9.12):

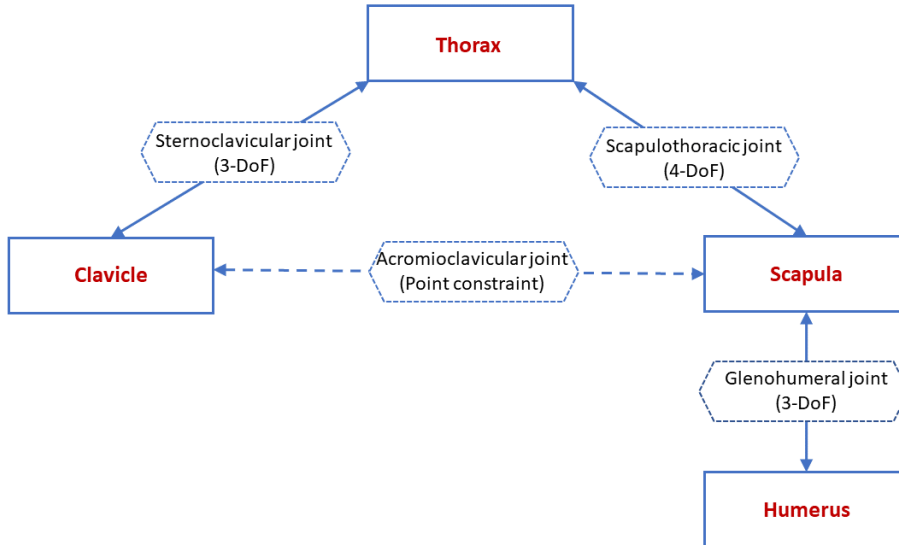


Figure 9. 12: Model structure topology.

The joint between the ground and the thorax is defined as a free joint since the individual can move his/her torso in any direction in the space. In the following sections, I describe the construct of each of the four joint definitions. While SC and AC joints need minimum description, I have provided a broader

attention and explanation on ST and GH joints as these joint are home to most of the shoulder pathologies and conditions in both adult and pediatric shoulder joints and most of the shoulder treatments and rehabilitation strategies are focused on these joints. For each joint, α is the rotation angle around the first axis, β is the rotation angle around the second axis and γ is the rotation angle around the third axis with respect to the order of the Euler sequence used.

9.2.3.2 Sternoclavicular Joint

The SC joint is modeled by 3DoFs. For the motion of the SC joint (clavicle relative to the thorax), Y-X-Z Euler rotation sequence was used as per ISB standardization committee recommendations [2].

α_{SC} : The rotation around the \bar{Y}_T axis of the thorax coordinate system.

β_{SC} : The rotation around the \bar{X}_C axis of the clavicle coordinate system.

γ_{SC} : The rotation around the \bar{Z}_C axis of the clavicle coordinate system.

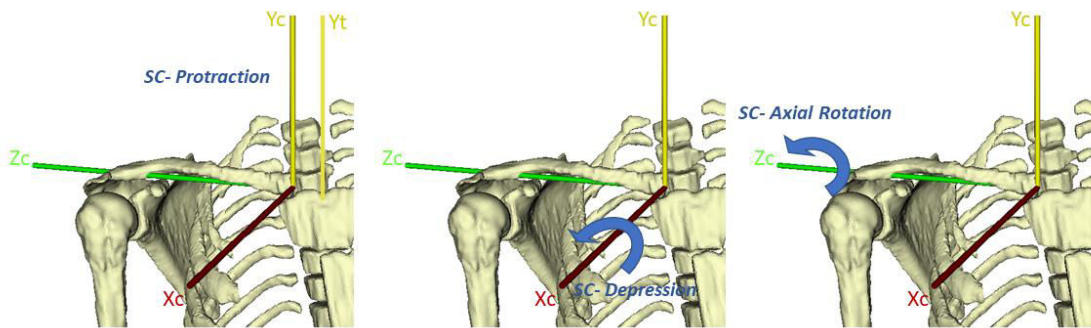


Figure 9. 13: Sternoclavicular joint coordinate system. Rotation (α_{SC}): retraction (negative) /protraction (positive). Rotation (β_{SC}): elevation (negative)/depression (positive). Rotation (γ_{SC}): Axial rotation of the clavicle.

9.2.3.3 Acromioclavicular joint

The AC joint is represented as a point constraint in the model. A point constraint in OpenSim consists of fixing a point with respect to the two adjacent segments. Here, we used the AC point as a fixed point. To achieve that the AC point coordinates were calculated in both the local coordinate frame of clavicle and scapula and through the motion the AC point is fixed in both the frame. That means there will be rotation between clavicle and scapula, but no translation is allowed. This choice is mainly conducted for two reasons: first in our model topology we do not want to create a closed loop chain and second, we want to conserve the AC joint congruency especially while achieving high RoM of the arm motion. If the shoulder joint is defined as a closed loop kinematic chain, the model scaling becomes problematic as small errors/changes in segment length can lead a big changes in model kinematics [6]. Thus, it is recommended to avoid the fixed closed chain mechanism in order to obtain more accurate kinematic measurement with minimal optimization [7].

9.2.3.4 Scapulothoracic Joint

The scapulothoracic rhythm is the kinematic description of the scapula movement with respect to thorax. Biomechanical knowledge of the exact scapulothoracic rhythm in modeling is very limited. It is vital to pay more attention to this particular joint because it plays an important role determining the dysfunction of the shoulder generally [8] and the more precisely, the posterior shoulder instability [9] which is a common problem in children with OBPP. In the current model, we made sure that we are precisely modeling the scapular kinematics with respect to thorax, as the model will be used in future to evaluate OBPP pathology. It is reported in the literature that for OBPP pathology, the scapular kinematics are different than the typically developed shoulder and these may provide insights into the adequate rehabilitation strategy. It is also important for understanding the compensatory mechanism of the ST joint in shoulder motion in children with OBPP. However, many unknown parameters of this joint make ST joint modeling one of the most challenging joints in the musculoskeletal modeling framework. First, the space between the supraspinatus fossa of the scapula and the posterosuperior part of the thoracic cage during movement is not easily quantifiable. So, if we are modeling the thoracic cage as an ellipsoid, we don't know the thickness to be added to the fitted ellipsoid to represent the muscles present in that region. Second, the quantification of scapular motion with respect to the thorax is complicated which makes it less described in the literature as compared to the GH motion. Third, clinicians rest their analysis on an intuitive humerothoracic motion that involves addition of GH and ST joint motion. Providing a non-intuitive scapulothoracic motion to clinicians without a ground truth or formal education in its behavior is a challenging task.

The scapulothoracic joint kinematics are commonly modelled as the motion of the three bony landmarks (AA, AI and TS) approximating the shape of the scapula and an ellipsoid surface approximating the rib cage [10]–[12]. As explained in Chapter 3, the scapula motion on the thoracic surface involves coupled rotations and translations [13] as scapular elevation, abduction, upward rotation and internal rotation (winging). In the current model, we defined the motion of the scapula with respect to the thorax using four DoFs [14]: elevation, abduction of the scapula on the ellipsoid fitted to the thorax, upward rotation of the scapula normal to the ellipsoid and internal rotation of the scapula to represent medial border lift-off from the surface of the thorax. This joint formulation created is based on the internal minimal coordinate joint formulation as explained in detail by Seth and colleagues [3].

Ellipsoid parameters:

The classical practice reported in the literature consists of fitting an ellipsoid to points of the ribs and AI and TS point. This technic seems questionable especially in the case where the model is used to simulate high RoM. During high RoM, these points (covered by the ellipsoid) don't represent a good constraint for the entire RoM of the scapula in medial/lateral and superior/inferior direction as the resulting ellipsoid is taller and wider than the rib cage size. To overcome this, we selected 30 landmarks covering the first nine ribs anteriorly, posteriorly and laterally in Amira. An ellipsoid is fitted to pass through these points (Figure 9.14)

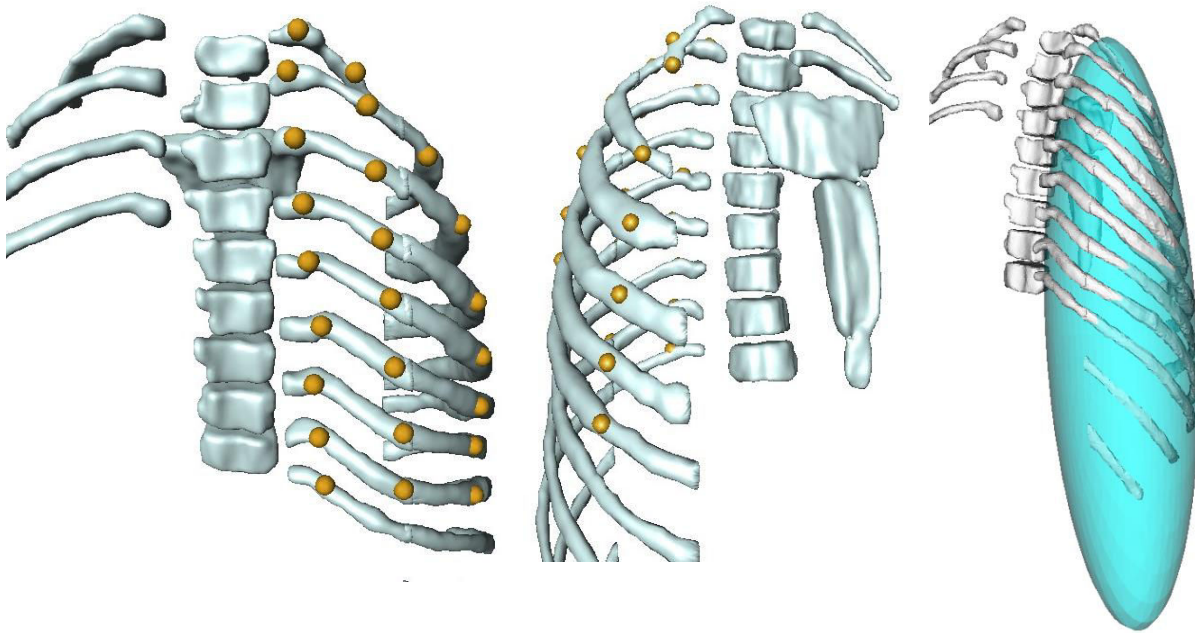


Figure 9. 14: Landmark selected to fit an ellipsoid (front and back views) and fitted ellipsoid.

Following this method, and even after increasing the radii of the ellipsoid to represent the space (the muscles) between the supraspinatus fossa of the scapula and the posterosuperior part of the thoracic cage, we got an unrealistic position of the scapula during motion. This is due to the definition of the joint coordinates, dimensions and the curvature of the ellipsoid. In fact, according to the definition of the coordinates, centroid of the scapula is almost always in the surface of the ellipsoid. An if we keep this ellipsoid, the scapula will slide (or glide) on or near the apex region of the ellipsoid, making the scapular motion abrupt and non-physiological as scapula tend to enter in the ribs during simulations at certain positions. To overcome this problem, two things were taken into consideration:

- mean equatorial plane (It is also called equator) of the ellipsoid should be passing through the first posterior ribs, where the scapular motion occurs more. (around the centroid for the initial pose)
- No big difference between ellipsoid radii to avoid abrupt change of scapular position.

Thus, in the model, thorax is fitted with an ellipsoid covering mostly the posterior first 9 ribs (figure 9.14). The ellipsoid center is taken around the fourth thoracic vertebra T4 such that the ellipsoid equatorial plane passes through the scapular centroid (figure 9.15). For this construct:

Ellipsoid radii: [width, height, depth] = [0.0751, 0.15, 0.0751]

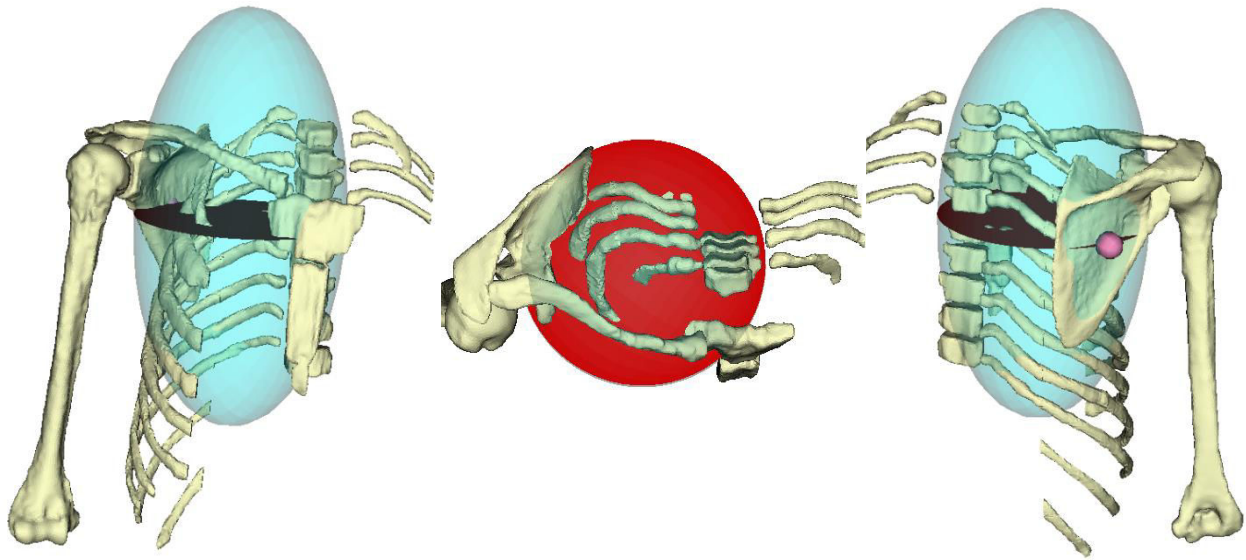


Figure 9. 15: Ellipsoid passing through the posterior rib surface and equatorial plane (shown in red) passing through the centroid of the scapula. This construct is used to define ST joint motion in the model.

Joint origin and axes:

The origin of the joint frame on the scapula is defined as the centroid of the three anatomical landmarks AA, TS and AI. We will refer to this centroid as the centroid of the scapula in the rest of the thesis. The axes of the joint reference frame on the scapula are defined as the axes of the scapula local frame rotated by -90 degrees about Y axis. This is done in order to have the upward rotation angles positive which is more coherent with the expected angles (measured by clinicians). The origin of the joint frame on the thorax is the center of the ellipsoid representing the scapulothoracic surface.

ST motion description (Figure 9.16):

- The coordinates of Abduction/adduction followed by elevation/depression, allow determination of the centroid of the scapula (the joint origin on the scapula) on the thoracic surface (ellipsoid). This is similar to how we define the location of a point on geographic coordinate system by longitude and latitude.
- Upward rotation defines the rotation of the scapula at its centroid at the normal to the ellipsoid.
- Internal rotation or winging defines the rotation of the scapula about the tangent axis of the ellipsoid in the scapular plane. This allows the Angulus Inferior (AI) and the medial border of the scapula to raise off the ellipsoid representing the thoracic surface.

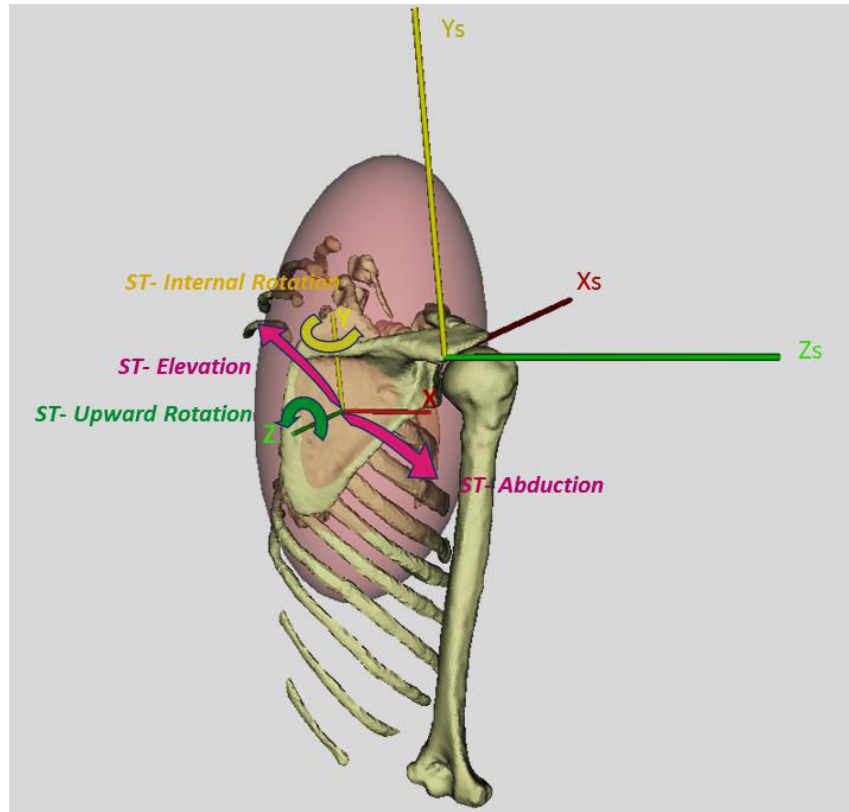


Figure 9. 16: Scapulothoracic joint coordinate system. Four degrees of freedom: Abduction/adduction followed by elevation/depression on the ellipsoid, upward rotation about the normal to the surface (Z-axis) and internal rotation (winging) about scapula Y-axis, which remains tangent to the ellipsoid.

9.2.3.5 Glenohumeral Joint

For GH joint, the most prominent question to address is which rotation sequence to use. As GH joint represents a very large range of motion (see Chapter 2), the rotation sequence of the GH joint should be selected such that the gimbal lock incidence (singularity) is avoided. The proposed rotation sequence, for the GH joint, according to ISB recommendation is $Y_S-X'_H-Y''_H$ (YXY). However, this sequence was discussed in other studies [15], [16] in terms of clinical interpretation and compared with other rotation sequence in terms of the gimbal lock avoidance and amplitude coherence. The amplitude coherence, as defined by Senk et al. [15], is the relation between the computed angle amplitude around the defined axis for given motion and the expected maximum angular range. They showed that for a given motion at their full range of motion, the gimbal lock is achieved when applying the ISB standardized sequence. Among the different proposed sequences, the XZY rotation sequence showed less vulnerability to gimbal lock incidence with highest amplitude coherence [15]. The findings of the study by Phadke et al. [16] were in agreement with study by Senk et al. [15] and they recommended this sequence for GH motion description. Thus, in the current model, we used the XZY rotation sequence as follows:

α_{GH} : The rotation around the $\bar{X}_{scapula}$ axis of the scapula coordinate system.

β_{GH} : The rotation around the axis parallel to the Y-Z plane.

γ_{GH} : The rotation around the $\bar{Y}_{Humerus}$ axis of the humerus coordinate system.

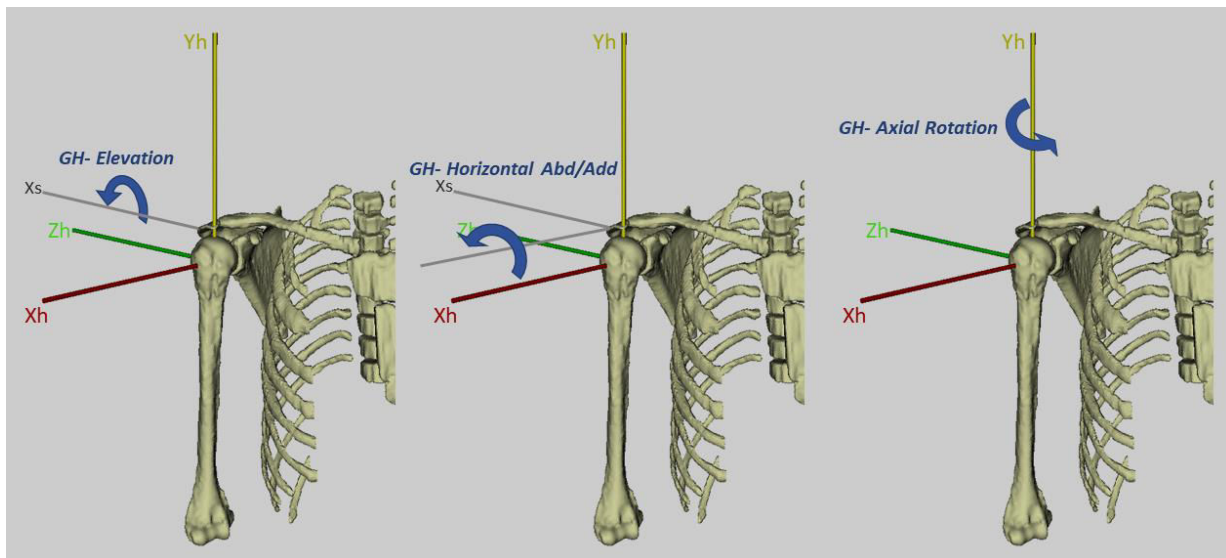


Figure 9. 17: Glenohumeral joint coordinate system. Rotation (α_{GH}): GH elevation. Rotation (β_{GH}): GH horizontal abduction/adduction (or flexion/extension). Rotation (γ_{GH}): GH axial rotation.

9.2.3.6 Joint geometry summary

A summary of the joint definitions with the associated Euler rotation sequences and rotation terminology are provided in table 9.8 below.

Table 9. 8: Summary of Joint definitions

Joint	Parent segment	Child segment	DoF	Rotation Sequence	Rotation Terminology			
SC	Thorax	Clavicle	3	Y-X-Z	Retraction/ protraction	Axial rotation	Elevation/ depression	
ST	Thorax (ellipsoid)	Scapula	4		Abduction/ Adduction	Elevation/ depression	Upward rotation	Internal rotation or winging
AC	Clavicle	Scapula	0	-	-	-	-	-
GH	Scapula	Humerus	3	X-Z-Y	GH Abduction/ Adduction	GH Flexion/ Extension	GH Axial rotation	

9.3 Dynamics

9.3.1 Body segment parameters

Since in musculoskeletal modeling, the upper arm is divided into segments considered as rigid bodies, determining the inertial characteristics of these segments is a key model building step. For quantitative dynamic simulations of the shoulder motion, accurate determination of inertial characteristics of the rigid body segments will lead to realistic analysis of dynamic motion to be studied. These characteristics are known as the body segment parameters. The body segment parameters include segment masses, centers of each segment mass and segment inertia properties and have an important influence on the musculoskeletal kinetics and kinematics output [17].

Typically, body segment parameters are derived from the literature which hosts data on healthy adult population. Not surprisingly, for pediatric population, these parameters are scarce. Most of the available anthropometric pediatric data in the literature are available from product safety design studies [18]. Further, such data is reported in terms of a ratio of limb segments over body segments (humerus over upper limb, tibia over lower leg etc.). For lower limb, it is still possible to use this ratio as the bone segments (foot, leg, thigh, etc.) are directly measurable. But for upper limb, we lack these measures for bones that are not directly measurable (scapula) or not reported in these studies (clavicle). Table 9.9 summarizes the studies that provided these parameters, generally related to upper limb for pediatric population for different age ranges [18].

Table 9. 9: *studies on pediatric mass distribution CG: center of gravity*

Study	Age range	segments	Calculated measures
Schneider and Zernicke [19]	0-1.5 years	Upper and lower limb segments	Mass, center of mass, moment of inertia
Sun and Jensen [20]	2-9 months	Upper and lower limb segments	Mass and principal moment of inertia
Snyder et al. [21]	2-10 years	Whole body	CG
Jensen [22]	4-20 years	Upper and lower limb segments	Mass, inertia
Li Dangerfield [23]	8-16 years	Upper and lower limb segments	CG, radius of gyration, volume and inertia

The body segment parameters for each segment are mostly expressed as ratio of the body properties (weight, height, size). There are different ratios for child and adult, and this is obviously due to the growth pattern in human body [18]. Even among pediatric population, there are different ratios for different age range (table 9.9). The difference in size with gender start having a significant difference from the age of 10 years old [18]. In my modeling framework, I will refer to the body segment parameters reported in Li Dangerfield [23] as the age of the volunteer used in my study falls within the age range used in this study. Whenever not available, I have used the appropriate ratios proposed by David Winter [24].

9.3.1.1 Segment mass

The segment mass is mostly expressed as a ratio of the total body mass. For the thorax segment mass ratio, we adopted the ratio proposed in David Winter Book [24].

$$M_{Thorax} = 0.216 * M = 0.216 * 46 = 9.936 \text{ kg}$$

Where, M is the total body mass.

For the humerus, we took the ratio of the upper arm weight over body weight from Li Dangerfield [23].

$$M_{Humerus} = 0.0284 * M = 0.0284 * 46 = 1.3064 \text{ kg}$$

In most of the shoulder Musculoskeletal models developed for shoulder joint (see chapter 7), the scapula and clavicle are considered as massless bodies with negligible inertia, given their small sizes and reduced movement as compared with other segments forming the shoulder joint. However, scapula plays important role in shoulder function in pediatric population. Furthermore, in our study, since we are paying a particular attention to scapular kinematics, we want to provide due consideration to the clavicle and the scapula mass. This is also important for the future perspective of this modeling framework which will be used to evaluate dynamics of motion during daily living activities in children with OBPP. So, analyzing the table provided in chapter 7 which summarize the body segment parameters of the existing shoulder models, there are two models which don't consider scapula and clavicle as massless (Holzbaur's upper extremity model (HM) [25] and Delft shoulder model (DSM) [26]). We calculated the fraction ($M_{scapula}/M_{Humerus}$) and it was equal to 0.3524 for HM and 0.3414 for DSM. Then, we took an average of these two ratios = 0.345.

$$M_{scapula} = 0.345 * M_{Humerus} = 0.345 * 1.3064 \approx 0.4507 \text{ kg}$$

Similarly, for clavicle, we calculated the $(M_{clavicle}/M_{Humerus})$ for both the model and both the ratios were averaged to 0.078. Thus,

$$M_{Clavicle} = 0.078 * M_{Humerus} = 0.078 * 1.3064 \approx 0.1018 \text{ kg}$$

9.3.1.2 Segment Center of mass

The segment center of mass is typically expressed as a ratio of the segment lengths. For clavicle and scapula, we proposed the center of mass from the definition of center of mass (The point around which the distribution of mass is balanced). For clavicle, we took the midpoint of SC and AC (all the coordinates are in the segment local frame). The coordinates of center of mass (Rx, Ry, Rz) for each segment are presented in their respective segment local frame (Table 9.6). For scapula, we took the centroid of the triangle formed by the three anatomical landmarks AI, AA and TS as a center of mass.

$$\bar{C}_{Clavicle} = (\overline{SC} - \overline{AC})/2$$

$$\bar{C}_{Scapula} = (\overline{AA} + \overline{AI} + \overline{TS})/3$$

The location of center of mass for humerus and thorax were calculated as a percentage [24] of the segment length from the proximal end [24].

$$\bar{C}_{Humerus} = (\overline{GH} - (\overline{EL} + \overline{EM})/2) * 0.436$$

$$\bar{C}_{Thorax} = (\overline{PX} + s\overline{T8})/2$$

9.3.1.3 Segment inertia

Radius of gyration of a body about an axis of rotation is defined as “the radial distance of a point from the axis of rotation at which, if whole mass of the body is assumed to be concentrated, its moment of inertia about the given axis would be the same as with its actual distribution of mass.” On Wikipedia. Further, “Mathematically the radius of gyration is the root mean square distance of the object's parts from either its center of mass or a given axis, depending on the relevant application. It is actually the perpendicular distance from point mass to the axis of rotation.” In biomechanics, the radius of gyration is typically expressed as a ratio of the length of each segment about the center of mass, the proximal end and the distal end. Inertia is the physical property of any matter/object to resist any change in its state of rest or state of motion. Thus, the amount of force needed to change the state of the object is termed as inertia. Using these two definitions, we get:

$$\text{Body Inertia} = (\text{Radius of Gyration})^2 * \text{body mass}$$

For humerus, the radius of gyration of the humerus($RG_{Humerus}$) is defined as 0.3031% of its length ($l_{Humerus}$).

$$\therefore l_{Humerus} = |(\overline{GH} - (\overline{EL} + \overline{EM})/2)| = 0.1279$$

$$\therefore RG_{Humerus} = 0.3031 * l_{Humerus} = 0.38766$$

The inertial parameters of the remaining segment were either calculated from the ratios provided by Winter [24] or approximated from the existing models of Wu [27] and Holzbaur [25] (see table 9.10 below).

Table 9. 10: *Inertial parameters for the model segments*

Segment	Mass (kg)	Center of mass (m)			Inertia (kg.m ²)		
		Rx	Ry	Rz	Ixx	Iyy	Izz
Thorax	9.936	-0.02095	-0.1245	0	1	0.5	1
Clavicle	0.1018	0	0	0.06941	0	0	0
Scapula	0.4507	0	-0.03346	-0.07287	0.001	0.001	0.001
Humerus	1.3064	0	-0.11153	0	0.0101	0.00059	0.0101

9.3.2 Muscle (actuator) dynamics

Number of studies have shown the sensitivity of the musculoskeletal model capability of muscle force estimations to the variations of the parameters used to describe the muscle-tendon actuation (optimal muscle-fiber length, muscle physiological cross-sectional area (PCSA), tendon slack length) [28],[29].

Many studies have evaluated the significance of these parameters between adult and children and they have concluded that these parameters should not be scaled across these two populations [30], [31]. Hence, it is important to select these parameters carefully, especially for pediatric population.

Muscle dynamics is modeled in OpenSim using a modified Hill-type equation by Millard et al. [32] and available as a plugin. This model is a generic muscle-tendon actuator model as described first by Zajac [33] and later modified by Thelen [34]. This model required four input parameters viz. Maximum isometric force, optimal muscle fiber length, tendon slack length, and pennation angle. These parameters define the force-length and force-velocity relationship of the muscle contraction and thus control the muscle

contraction dynamics in the modified Hill-type muscle model. Thus, these parameters can be tweaked to represent fatigued, pathological, weak, spastic, or atrophied muscles.

The ultimate aim of muscle modeling is typically to identify muscle structure and muscle dynamics parameters from the experimental data. With lack of such a data and experiments in the scope of this thesis, I have extracted as many parameters possible from the available MR imaging dataset. These include muscle and tendon lengths of most of the muscles and their insertion/origin locations. Rest of the structural and model parametric data was derived using the muscle and tendon length data and data adopted from the literature wherever available. In the following sections, I will describe how I derived muscle structural and functional parameters.

9.3.2.1 Muscle Volumes

The muscle volume is known to be a good predictor of force generation capacity of the muscle and forms an important parameter in the muscle modeling as well. The physiological cross-sectional area (PCSA) of each muscle is the functional parameter used in the muscle model (as described above) which is ultimately derived from muscle volumes. For our model, the muscle volumes are adopted from a pediatric dataset [35] representing shoulder muscle volume averaged from 14 typically developing children/adolescents with no history of pathology/injury. This dataset includes muscle volumes of the deltoid represented as two compartments (anterior deltoid and posterior deltoid), supraspinatus, subscapularis, pectoralis major, teres minor/infraspinatus (combined) and teres major.

Based on the deltoid division (two segments - anterior and posterior deltoid) made in the volumes reported in this study [35] and based on the definitions proposed by Brown et al. that the deltoid can be split into seven functionally independent segments [36], we extracted and categorized muscle volumes for three compartments of the deltoid (anterior, posterior and middle deltoid). For this, one-third of the anterior deltoid muscle volume and one-fourth of the posterior deltoid volume were extracted to represent the volume of the middle deltoid.

In the same study [35] the muscle volume of infraspinatus and teres minor muscle is reported as a combined volume as the boundaries between these two muscles are indistinct, which makes their segmentation in MRI difficult. In order to quantify these volumes as separate muscles, we calculated a **volume fraction**, determined as a percentage of the summed volumes of deltoid, subscapularis, supraspinatus, Teres major and pectoralis major in the pediatric dataset [35] and in the dataset of shoulder muscle volume for young adult [37]. Since the fractions of other muscles are almost the same in both the dataset (except for teres Major), we calculated the muscle volume of Infraspinatus and teres minor using their corresponding fractions from young adult volumes. The infraspinatus muscle volume was quantified as 81.1% of the combined volume and the teres minor as 18.9%.

Then, for each muscle a ratio (V_{DS1}/V_{DS2}) of the volume presents in the dataset of young adult [37](DS1) to the volumes of the same muscle from the dataset of children (DS2) [35] was determined. The average of all the ratios was used to approximate the volume of the Latissimus Dorsi muscle and confirmed with a master-level unpublished report by Bowed ETW [38]. The trapezius muscle volume is not reported in both the studies and thus is adopted from another study [39]. Using the average of ratios from all the known muscle ratios between adult and pediatric data, we determined the trapezius muscle volume.

Volumes of these muscles are reported in table 9.11.

9.3.2.2 Muscle and tendon lengths

The musculotendon lengths were quantified from axial and/or sagittal plane MRI as the distance from the muscle origin to insertion on the respective bones (mostly scapula and humerus) [40]. Table x.x reports the origin and insertion coordinates of these muscles.

Table 9. 11: origin and insertion coordinates

Muscle	Humerus Insertion			Scapula insertion			3D Length
	X	Y	Z	X	Y	Z	mm
subscap inferior	-161.30	5.50	204.60	-84.60	105.40	157.30	134.54
subscap inferior	-160.70	4.90	206.10	-86.60	102.80	164.80	129.54
subscap inferior	-161.60	4.40	210.60	-87.40	101.30	171.60	128.13
subscap middle	-161.00	3.50	212.10	-88.30	99.60	180.60	124.55
subscap middle	-161.00	3.50	213.60	-84.20	94.00	193.30	120.42
subscap superior	-161.60	4.70	215.10	-79.80	94.00	203.80	121.63
subscap superior	-159.80	5.50	216.60	-80.10	90.20	211.30	116.42
Teres Minor 1	-180.30	35.10	197.10	-115.60	91.40	150.60	97.56
Teres Minor 2	-180.00	32.80	198.60	-116.70	89.90	152.10	97.11
Teres Minor 3	-180.30	33.10	200.10	-113.80	90.80	153.60	99.57
Teres Minor 4	-179.40	35.10	201.60	-114.10	89.90	155.10	97.10
Teres Major 1	-154.80	34.80	172.30	-91.30	109.00	124.30	108.82
Teres Major 2	-155.70	37.50	170.80	-89.80	110.40	122.80	109.37
Teres Major 3	-155.10	33.10	169.30	-91.00	110.40	121.30	111.30
Teres Major 4	-155.40	35.10	166.30	-92.10	109.50	119.10	108.49
Infraspinatus 1	-180.90	24.60	221.80	-86.90	109.80	134.10	154.23
Infraspinatus 2	-181.50	21.90	219.60	-86.00	110.40	139.30	152.97
Infraspinatus 3	-181.80	21.10	217.30	-86.60	105.40	152.80	142.58
Supraspinatus 1	-158.90	20.20	234.60	-78.70	73.50	242.10	96.59
Supraspinatus 2	-158.60	19.00	233.80	-81.30	77.90	238.30	97.29
Supraspinatus 3	-158.60	19.00	233.10	-76.30	84.90	233.80	105.44

Supraspinatus 4	-159.80	18.70	232.30	-83.60	83.80	227.80	100.32
Pectoralis major	-160.10	10.20	191.80	9.20	-12.90	194.80	170.89
Anterior Deltoid	-71.50	31.90	120.60	-105.30	26.90	245.10	129.10
Middle Deltoid	-175.00	36.90	104.80	-163.00	29.60	240.60	136.52
Posterior deltoid	-178.30	42.20	98.80	-132.90	71.20	232.30	143.96
	Spinal Process Insertion			Scapula/Humerus Insertion			3D length
	X	Y	Z	X	Y	Z	mm
Trapezius sup 1	3.20	63.20	308.50	136.20	35.10	269.50	141.42
Trapezius sup 2	4.30	72.60	289.70	138.50	43.90	267.20	139.07
Trapezius sup 3	4.90	72.60	275.50	130.90	46.20	264.20	129.23
Trapezius mid 1	5.70	88.90	73.60	152.60	46.20	76.20	153.00
Trapezius mid 2	4.80	91.80	37.60	151.00	51.10	73.60	155.97
Trapezius inf 1	6.00	101.20	-7.40	144.80	58.10	72.10	165.66
Trapezius inf 2	9.50	102.30	-68.20	138.40	62.50	70.60	193.56
Trapezius inf 3	13.10	105.30	-89.90	130.50	69.80	66.80	198.99
Latissimus D 1	9.20	110.50	-70.40	170.00	25.30	5.30	197.09
Latissimus D 2	13.00	114.10	-93.70	171.80	24.70	3.80	206.68
Latissimus D 3	12.40	114.90	-117.60	171.80	24.70	3.10	219.35
Latissimus D 4	12.70	110.50	-146.70	172.10	25.60	0.80	233.18
Latissimus D 5	13.30	106.40	-167.90	172.40	23.80	-0.70	245.14
Latissimus D 6	16.50	100.00	-201.60	173.90	25.00	-2.20	264.88

Based on these, the averaged musculotendon lengths are as below in table 9.12.

Then to separate Muscle lengths and tendon lengths, we used the adult muscle and tendon lengths measured and reported separately in a cadaveric study by Langenderfer et al. [41]. Using the reported values, we determined the ratio of muscle to tendon length distribution and applied the same ratio to the musculo-tendon length measures (table 9.12) of our study to separate the muscle and tendon lengths.

Table 9. 12: Muscle volumes, muscle lengths, and tendon lengths derived from MRI data and by adapting length and volume ratios from the literature.

Muscles		Muscle Volume (cm ³)	Musculotendon length (cm)	Muscle Length (cm)	Tendon Length (cm)
Trapezius	Superior	71.11	13.60	10.55	3.04
	Middle	88.35	15.50	12.02	3.47
	Inferior	120.68	18.60	14.42	4.17
Supraspinatus		28.60	10.00	7.42	2.60
Subscapularis	Superior	92.70	11.90	8.12	3.78
	Middle		12.20	8.85	3.35
	Inferior		13.10	10.21	2.89
Deltoid	Anterior	54.54	12.90	10.70	2.20
	Middle	53.16	13.65	12.25	1.40
	Posterior	77.70	14.40	11.41	2.99
Infraspinatus		64.40	15.00	10.46	4.54
Teres Minor		15.00	9.80	8.15	1.65
Teres Major		79.40	10.95	9.26	1.69
Pectoralis Major	Thorax	143.50	17.10	13.40	3.70
	Clavicle			14.90	2.20
Latissimus Dorsi		139.00	25.05	19.05	5.99

9.3.2.3 Optimal muscle fiber length (OML)

OML is defined as the length of the muscle at which the sarcomeres are at their optimal length. The optimal sarcomere length in humans is reported to be equal to $2.8 \mu m$ [42]. When the muscle is at its muscle optimal fiber length it generates its maximum force. To derive OML in pediatric population L_{mp}^0 , we first calculated a ratio of adult optimal fiber length L_m^0 to muscle length L_m from Langenderfer et al. [41] and then the OML of the pediatric population L_{mp}^0 is calculated based this ratio and the measured muscle length from MRI L_m^{meas} (Table 9.13).

$$r_{fl} = L_m^0 / L_m$$

$$L_{mp}^0 = r_{fl} * L_m^{meas}$$

9.3.2.4 Physiological Cross-sectional Area (Table 9.13)

The physiologic cross-sectional area is calculated by dividing the muscle volume V_M by the optimal muscle fiber length L_{mp}^0 .

$$PCSA = V_M / L_{mp}^0$$

9.3.2.5 Maximum isometric muscle force (Table 9.13)

The maximum isometric muscle force F_{max} is obtained by the multiplication of the PCSA of each Muscle with the specific tension σ , which was set to 33 N/cm² [43]

$$F_{max} = PCSA * \sigma$$

9.3.2.6 Tendon slack length (Table 9.13)

Tendon slack length is defined as the length of tendon on elongation at which the tendon just begins to develop force [33]. To determine the tendon slack lengths, we assumed that the slack length is equivalent to the tendon lengths that are derived from MRI in table 9.12 above. We base our assumption on the fact that the MRI was acquired while the volunteer was in a relaxed and resting position. This position will require to keep the shoulder joint in equilibrium position by minimally holding the forces in the musculotendon units. Thus, the musculotendon lengths will represent tendon slack lengths directly.

9.3.2.7 Pennation angles (Table 9.13)

Pennation angle is defined as the angle between the muscle fibers and the axis of the muscle force generation. The pennation angle does not differ between children and adults [31]. For the current study, the pennation angles were adopted from Langenderfer et al. [41].

Table 9. 13: Muscle dynamics model input parameters.

Muscle		Optimal fiber length(cm)	PCSA (cm ²)	Maximum isometric muscle Force (N)	Tendon slack length (cm)	Pennation angle (deg)
Trapezius	Superior	9.76	7.28	240.34	3.04	20
	Middle	7.78	11.34	374.48	3.47	10
	Inferior	17.24	6.99	230.98	4.17	5
Supraspinatus		6.17	4.63	152.85	2.60	7
Subscapularis		8.56	10.82	357.19	3.78	20
Deltoid	Anterior	8.59	6.35	209.56	3.35	22
	Middle	10.10	5.26	173.58	2.89	15
	Posterior	10.58	7.35	242.35	2.20	18
Infraspinatus		7.39	8.72	287.61	1.40	19
Teres Minor		5.44	2.76	90.96	2.99	24
Teres Major		11.14	7.13	235.17	4.54	16
Pectoralis Major	(Thorax)	11.27	12.73	420.02	1.65	25
	(Clavicle)	14.46	9.25	327.50	1.69	17
Latissimus Dorsi		18.29	4.19	138.47	5.99	22

9.4 Summary and conclusion

This chapter thoroughly described the modeling framework with details on how the model parameters are obtained or determined using available data. The model was built in OpenSim framework from scratch as there is no such model available in the OpenSim repository. Overall, there is a paucity of anthropometric and body segment parameter data in pediatric population. Furthermore, the available data does not always match with the age range for which model is built. As these parameters are relatively constant in adults but largely vary in pediatric population based on the age, I had difficulties finding the correct set of parameters for the age range (13 to 15 years) for which the pediatric model is built. Furthermore, multiple musculo-tendon actuator parameters are not readily available and thus have to be approximated from the literature data. For certain parameters like optimal fiber lengths, other researchers have used sarcomere lengths from adult studies. Since no sarcomere lengths in the pediatric population are known, we derived the optimal fiber lengths based on the average ratios obtained from other muscles. This could be regarded as a major limitation of the study, but we believe this to be the best approach at this point. Future experimental studies will focus on 1) Improving the model with a greater

number of muscle representations to provide more robust and complete analysis, 2) Improving the muscle representation using wrapping surfaces.

The outcome of this model is a .osim file which retains all the parameters in the model and can be used by other researchers for their own research. The developed model is named as French Pediatric Shoulder Model (FPSM) and is now uploaded as OpenSim project (<https://simtk.org/projects/fpsm>). User will soon be able to download the .osim file. The model was also presented last year at the International Shoulder Group meeting at Mayo Clinic, Rochester, MN, USA. The critics were well received, and certain suggestions are implemented in the model.

9.5 Chapter 9 References

- [1] S. L. Delp *et al.*, “OpenSim: open-source software to create and analyze dynamic simulations of movement,” *IEEE Trans. Biomed. Eng.*, vol. 54, no. 11, pp. 1940–1950, Nov. 2007.
- [2] G. Wu *et al.*, “ISB recommendation on definitions of joint coordinate systems of various joints for the reporting of human joint motion--Part II: shoulder, elbow, wrist and hand,” *J. Biomech.*, vol. 38, no. 5, pp. 981–992, May 2005.
- [3] A. Seth, M. Sherman, P. Eastman, and S. Delp, “Minimal formulation of joint motion for biomechanisms,” *Nonlinear Dyn.*, vol. 62, no. 1, pp. 291–303, Oct. 2010.
- [4] G. Rodriguez and A. Jain, “Spatial operator algebra for multibody system dynamics,” *J. Astronaut. Sci.*, 1992.
- [5] H. G. Kwatny and G. L. Blankenship, “Symbolic construction of models for multibody dynamics,” *IEEE Trans. Robot. Autom.*, vol. 11, no. 2, pp. 271–281, Apr. 1995.
- [6] I. W. Charlton and G. R. Johnson, “A model for the prediction of the forces at the glenohumeral joint,” *Proc. Inst. Mech. Eng. [H]*, vol. 220, no. 8, pp. 801–812, Nov. 2006.
- [7] J. Prinold, “The Scapula in Musculoskeletal Modelling of Extreme Activities,” Oct. 2012.
- [8] F. Struyf, J. Nijs, J.-P. Baeyens, S. Mottram, and R. Meeusen, “Scapular positioning and movement in unimpaired shoulders, shoulder impingement syndrome, and glenohumeral instability,” *Scand. J. Med. Sci. Sports*, vol. 21, no. 3, pp. 352–358, Jun. 2011.
- [9] H. C. Bäcker, S. E. Galle, M. Maniglio, and M. P. Rosenwasser, “Biomechanics of posterior shoulder instability - current knowledge and literature review,” *World J. Orthop.*, vol. 9, no. 11, pp. 245–254, Nov. 2018.
- [10] F. C. van der Helm, “Analysis of the kinematic and dynamic behavior of the shoulder mechanism,” *J. Biomech.*, vol. 27, no. 5, pp. 527–550, May 1994.
- [11] B. A. Garner and M. G. Pandy, “A Kinematic Model of the Upper Limb Based on the Visible Human Project (VHP) Image Dataset,” *Comput. Methods Biomech. Biomed. Engin.*, vol. 2, no. 2, pp. 107–124, 1999.
- [12] W. Maurel and D. Thalmann, “A Case Study on Human Upper Limb Modelling for Dynamic Simulation,” *Comput. Methods Biomech. Biomed. Engin.*, vol. 2, no. 1, pp. 65–82, 1999.
- [13] A. Roren, M.-M. Lefevre-Colau, S. Poiraudau, F. Fayad, V. Pasqui, and A. Roby-Brami, “A new description of scapulothoracic motion during arm movements in healthy subjects,” *Man. Ther.*, vol. 20, no. 1, pp. 46–55, Feb. 2015.
- [14] A. Seth, R. Matias, A. P. Veloso, and S. L. Delp, “A Biomechanical Model of the Scapulothoracic Joint to Accurately Capture Scapular Kinematics during Shoulder Movements,” *PLOS ONE*, vol. 11, no. 1, p. e0141028, Jan. 2016.
- [15] M. Senk and L. Chèze, “Rotation sequence as an important factor in shoulder kinematics,” *Clin. Biomech. Bristol Avon*, vol. 21 Suppl 1, pp. S3-8, 2006.
- [16] V. Phadke, J. P. Braman, R. F. LaPrade, and P. M. Ludewig, “Comparison of glenohumeral motion using different rotation sequences,” *J. Biomech.*, vol. 44, no. 4, pp. 700–705, Feb. 2011.

- [17] G. Rao, D. Amarantini, E. Berton, and D. Favier, "Influence of body segments' parameters estimation models on inverse dynamics solutions during gait," *J. Biomech.*, vol. 39, no. 8, pp. 1531–1536, 2006.
- [18] J. R. Crandall, B. S. Myers, D. F. Meaney, and S. Z. Schmidtke, Eds., *Pediatric Injury Biomechanics: Archive & Textbook*. New York: Springer-Verlag, 2013.
- [19] K. Schneider and R. F. Zernicke, "Mass, center of mass, and moment of inertia estimates for infant limb segments," *J. Biomech.*, vol. 25, no. 2, pp. 145–148, Feb. 1992.
- [20] H. Sun and R. Jensen, "Body segment growth during infancy," *J. Biomech.*, vol. 27, no. 3, pp. 265–275, Mar. 1994.
- [21] R. G. Snyder and And Others, *Anthropometry of Infants, Children, and Youths to Age 18 for Product Safety Design. Final Report*. 1977.
- [22] R. K. Jensen, "Changes in segment inertia proportions between 4 and 20 years," *J. Biomech.*, vol. 22, no. 6–7, pp. 529–536, 1989.
- [23] Y. Li and P. H. Dangerfield, "Inertial characteristics of children and their application to growth study," *Ann. Hum. Biol.*, vol. 20, no. 5, pp. 433–454, Oct. 1993.
- [24] D. A. Winter, *Biomechanics and Motor Control of Human Movement*. John Wiley & Sons, 2009.
- [25] K. R. Saul *et al.*, "Benchmarking of dynamic simulation predictions in two software platforms using an upper limb musculoskeletal model," *Comput. Methods Biomech. Biomed. Engin.*, vol. 18, no. 13, pp. 1445–1458, 2015.
- [26] A. A. Nikooyan, H. E. J. Veeger, E. K. J. Chadwick, M. Praagman, and F. C. T. van der Helm, "Development of a comprehensive musculoskeletal model of the shoulder and elbow," *Med. Biol. Eng. Comput.*, vol. 49, no. 12, pp. 1425–1435, Dec. 2011.
- [27] W. Wu, P. V. S. Lee, A. L. Bryant, M. Galea, and D. C. Ackland, "Subject-specific musculoskeletal modeling in the evaluation of shoulder muscle and joint function," *J. Biomech.*, vol. 49, no. 15, pp. 3626–3634, 07 2016.
- [28] C. Redl, M. Gfoehler, and M. G. Pandy, "Sensitivity of muscle force estimates to variations in muscle-tendon properties," *Hum. Mov. Sci.*, vol. 26, no. 2, pp. 306–319, Apr. 2007.
- [29] D. C. Ackland, Y.-C. Lin, and M. G. Pandy, "Sensitivity of model predictions of muscle function to changes in moment arms and muscle-tendon properties: a Monte-Carlo analysis," *J. Biomech.*, vol. 45, no. 8, pp. 1463–1471, May 2012.
- [30] M. E. Vidt, M. Daly, M. E. Miller, C. C. Davis, A. P. Marsh, and K. R. Saul, "Characterizing upper limb muscle volume and strength in older adults: A comparison with young adults," *J. Biomech.*, vol. 45, no. 2, pp. 334–341, Jan. 2012.
- [31] T. D. O'Brien, N. D. Reeves, V. Baltzopoulos, D. A. Jones, and C. N. Maganaris, "Muscle-tendon structure and dimensions in adults and children," *J. Anat.*, vol. 216, no. 5, pp. 631–642, May 2010.
- [32] M. Millard, T. Uchida, A. Seth, and S. L. Delp, "Flexing computational muscle: modeling and simulation of musculotendon dynamics," *J. Biomech. Engin.*, vol. 135, no. 2, p. 021005, Feb. 2013.
- [33] F. E. Zajac, "Muscle and tendon: properties, models, scaling, and application to biomechanics and motor control," *Crit. Rev. Biomed. Engin.*, vol. 17, no. 4, pp. 359–411, 1989.
- [34] D. G. Thelen, "Adjustment of muscle mechanics model parameters to simulate dynamic contractions in older adults," *J. Biomech. Engin.*, vol. 125, no. 1, pp. 70–77, Feb. 2003.

- [35] H. S. Im, K. E. Alter, S. Brochard, C. Pons, and F. T. Sheehan, "In vivo pediatric shoulder muscle volumes and their relationship to 3D strength," *J. Biomech.*, vol. 47, no. 11, pp. 2730–2737, Aug. 2014.
- [36] J. M. M. Brown, J. B. Wickham, D. J. McAndrew, and X.-F. Huang, "Muscles within muscles: Coordination of 19 muscle segments within three shoulder muscles during isometric motor tasks," *J. Electromyogr. Kinesiol. Off. J. Int. Soc. Electrophysiol. Kinesiol.*, vol. 17, no. 1, pp. 57–73, Feb. 2007.
- [37] K. R. S. Holzbaur, W. M. Murray, G. E. Gold, and S. L. Delp, "Upper limb muscle volumes in adult subjects," *J. Biomech.*, vol. 40, no. 4, pp. 742–749, 2007.
- [38] "Latissimus Dorsi to Biceps Transfer in Children with Arthrogryposis: Influence of Preoperative Volume on Outcome and Comparison to Reference Values." [Online]. Available: <http://scripties.umcg.eldoc.ub.rug.nl/root/geneeskunde/2017/BovenETW/>. [Accessed: 09-Apr-2019].
- [39] B. A. Garner and M. G. Pandy, "Musculoskeletal model of the upper limb based on the visible human male dataset," *Comput. Methods Biomech. Biomed. Engin.*, vol. 4, no. 2, pp. 93–126, Feb. 2001.
- [40] R. L. Lieber, M. D. Jacobson, B. M. Fazeli, R. A. Abrams, and M. J. Botte, "Architecture of selected muscles of the arm and forearm: anatomy and implications for tendon transfer," *J. Hand Surg.*, vol. 17, no. 5, pp. 787–798, Sep. 1992.
- [41] J. Langenderfer, S. A. Jerabek, V. B. Thangamani, J. E. Kuhn, and R. E. Hughes, "Musculoskeletal parameters of muscles crossing the shoulder and elbow and the effect of sarcomere length sample size on estimation of optimal muscle length," *Clin. Biomech. Bristol Avon*, vol. 19, no. 7, pp. 664–670, Aug. 2004.
- [42] R. L. Lieber, "Skeletal muscle architecture: implications for muscle function and surgical tendon transfer," *J. Hand Ther. Off. J. Am. Soc. Hand Ther.*, vol. 6, no. 2, pp. 105–113, Jun. 1993.
- [43] W. A. Weijs and B. Hillen, "Cross-sectional areas and estimated intrinsic strength of the human jaw muscles," *Acta Morphol. Neerl. Scand.*, vol. 23, no. 3, pp. 267–274, 1985.

Chapter 10

Simulating OBPP pathology using the pediatric shoulder model: A Feasibility Study

10.1 Introduction

This chapter illustrates the simulation capability of the pediatric shoulder musculoskeletal model built in chapter 9 to evaluate OBPP pathology using inverse dynamics model simulations in OpenSim. To be able to perform the simulations, an experimental motion analysis data on children with OBPP is required. This data was obtained from the regional university hospital (CHRU de Brest) which was collected as a part of the clinical evaluations of OBPP population that visits the hospital. Throughout my PhD, total five children were enrolled in the regional hospital of CHRU to get treatment for OBPP. Out of these five, only one child underwent motion analysis data capture with the set of markers that can be effectively used for deriving model kinematics. Other children did not have the required marker-set and thus we could not use that data for model simulations. More details will be explained in this chapter. For the one child data used to drive the simulations, we could perform evaluation of flexion movement on both healthy and impaired side. The enrollment and data collection are described briefly in section 10.2. Within this evaluation, we first scaled our pediatric shoulder model to the subject-specific anthropometry using scaling techniques in OpenSim. Details of these are explained in section 10.2. Next, we employed inverse kinematics to transform marker-trajectories to the scaled pediatric model to generate model-based kinematics with respect to standardized joint coordinate systems. This is described in section 10.2. The outcome of inverse kinematics was then used to determine generalized forces (joint reaction moments and joint reaction forces) experienced by the model joints. Description and related results are explained in section 10.3. At each level, we have compared the outcomes between healthy and impaired side and a brief discussion and analysis of results are discussed in section 10.4.

10.2 Kinematics Simulations

10.2.1 Experimental data collection

Experiments were formed as a part of an ongoing clinical protocol in place to treat children with OBPP at the CHRU. Under this protocol, every individual with OBPP undergoes clinical evaluations followed by a

motion analysis laboratory visit. During this visit, each child typically undergoes marker placements on his/her impaired arm. Placement of markers is then followed by at least 10 movements of daily activities. A state-of-the-art motion analysis system (Vicon Inc., USA) with ten high frequency infrared cameras then captures these movements with each movement performed three times. Similar set-up is then performed on the healthy contralateral side and similar trials are collected. The marker dataset then can be used to track the motion of each bone in the pediatric model by first registering the experimental marker set to the model marker set and then applying an experimental marker set trajectory to model markers. This means, model needs trajectories for each of the modeled bones if we want to derive marker based inverse kinematics from the model. While this may not pose as a limitation of the model, we found that scapular motion was not typically tracked in the experiments using Angulus Acromialis (AA), Angulus inferior (AI), and Superior Angle (SA) markers. Instead, a marker triad was used that was placed on the Angulus Acromialis. Since I did not define scapulothoracic joint motions at the Angulus Acromion, I could not use these markers to derive the scapulothoracic joint kinematics in the absence of the three markers mentioned above. Scapular and scapulothoracic joint motion is an important aspect of the OBPP pathology and that is why we modeled it in the first place. Without any information on the scapular motion, the model we built would not be able to evaluate this motion. Thus, we searched for those children for whom the three scapular markers were used to specifically track the scapular bone motion.

10.2.1.1 Patient and motion(s)

Total five children underwent clinical visits at CHRU. Thirty-four reflective markers were placed on left and right arms and shoulder joint (figure 10.1). Arm markers included three on each hand, two on each wrist joint, one each on mid forearm, two each on elbow joint, four marker cluster on each mid humeral thorax, and three marker cluster on acromion. Four markers were placed on C7, T8, Incisura Jugularis, and Processus Xiphoides. In cases where scapular bone was tracked, the AA, AI and SA markers were in place in addition to the above mentioned 34 markers. Each child performed static and dynamic trials and marker trajectories were recorded. After going through each child's motion analysis data collection folders, we found only one adolescent with only one motion (forward flexion) for which AI, AA, and SA markers on scapula were placed – for both impaired and non-impaired shoulders (Figure 10.1). Thus, we used this data to perform the model simulations. For the OBPP child selected, right side was impaired. The flexion range of motion was restricted to around 110°-120° where as left shoulder had complete healthy range of motion. The age of the adolescent was 16 years, height 160cm, and weight 56kg



Figure 10. 1: An adolescent with OBPP was enrolled at CHRU and motion analysis data was collected on both impaired and non-impaired shoulders. Marker set-up on the impaired arm is shown here.

10.2.2 Scaling

To register the movement tracking data to the model, we first need to scale the model to match the size of the subject. This is typically done using a static motion file and a scaling tool in OpenSim [1], [2]. Scaling tool scales the body segments of the model along with body segment parameters (center of mass and mass). A recent study conducted by Nolte and colleagues [3] reported that linear scaling of subject-specific models with the closest ratio of body height to shoulder width and from the same gender yield best modeling results for glenohumeral joint loading, with significant improvements in model estimations when compared to a linearly scaled generic model. Our model was developed using a 13 year old girl MRI data and scaling this model using marker specific segment ratios corroborated well with the proposed method by Nolte and colleagues [3]. Three inputs are required for performing the scaling:

1. Experimental data from static trial - measured with the motion capture system in the gait lab and contains the marker positions over time. In this static trial, the subject was seated on the chair with arms resting on the side in a comfortable position and elbow comfortably extended (figure 10.1). OpenSim uses .trc file (Track Row Column) format for scaling (and for kinematics as well). Thus, the C3D (Coordinate 3D) file format provided by the motion capture system was converted to .trc using available algorithms provided by OpenSim community. The .trc file was then modified and markers that are used only for scaling the segments of the model are included in these files (Table 10.1).
2. The musculoskeletal model - The OpenSim pediatric shoulder musculoskeletal model (described in chapter 9) was used in .osim format. Virtual markers were placed in this model at the same anatomical

locations as the experimental markers (figure 10.2) with due consideration given to the existence of skin and fat while placing these markers. Same marker names were attributed to the corresponding markers in both the virtual markers and the experimental markers in the .trc file.

3. Settings used for the scaling algorithm - The **scale factor** can be either manually computed (from some anthropometric analyses) and attributed to any body segment or computed from measurements. The measurement-based scaling consists of comparing the distances between virtual marker pairs and experimental marker pairs. One or more marker pairs can be used to scale one body segment along one direction. **Marker weights** can also be attributed to the markers, to prioritize the matching between the virtual and experimental markers by attributing more weight to it. In our case, a uniform weight is attributed to all the markers since they are all assumed to have the same uncertainty.

The process of scaling a kinematic model is described in the schematic diagram below (figure 10.2) and consisted of scaling the dimensions of the body segments, the body segment properties (mass, center of mass and inertia) and the joint parameters (joint frame locations, wrapping objects, etc.). Each segment in the model was scaled such that the virtual markers (the markers placed in the model) matched the experimental markers (table 10.2). This matching was based on the scale factor attributed to the segment along each of its directions (X,Y and Z). The experimental marker positions over time interval of the static trial were averaged and the average positions were used to compute the distances between the marker pairs for determining the scale factors. Finally, an inverse Kinematic task was also performed to move the virtual markers to match the experimental markers.

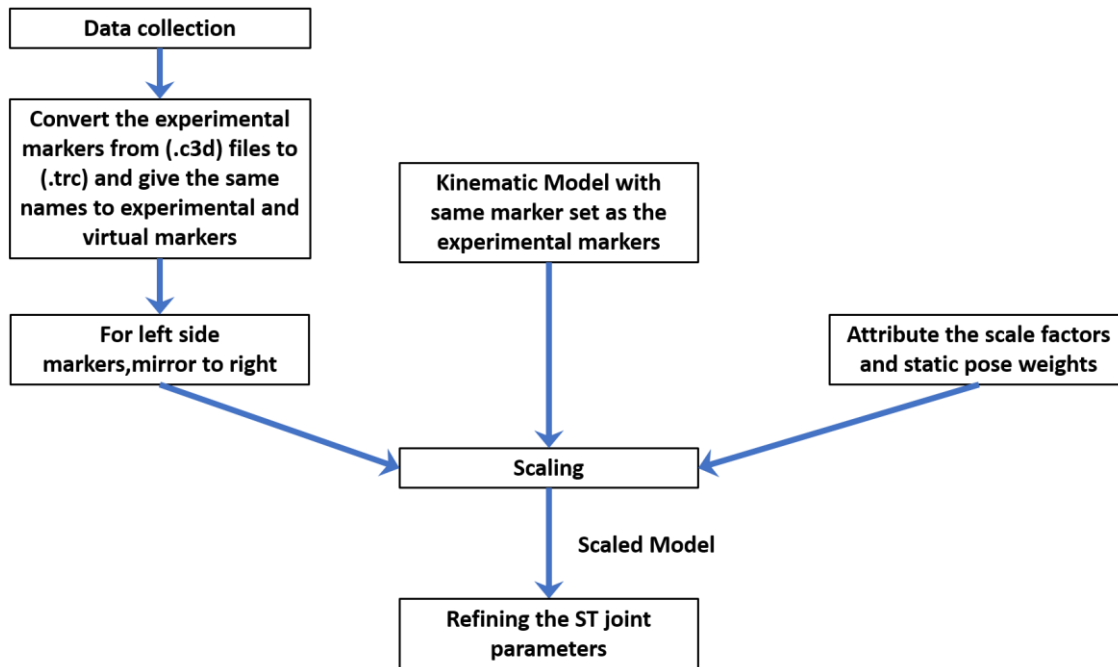


Figure 10. 2: Schematic diagram explaining the scaling process adapted.

Table 10. 1: List of bony palpable markers used for scaling

Bone	Bony markers	Abbreviation
Thorax	Seventh Cervical vertebra	C7
	Incisura Jugularis	IJ
	Eighth Thoracic vertebra	T8
	Processus Xiphoideus	PX
Scapula	Angulus Acromialis	AA
	Angulus Inferior	AI
	Superior angle	SA
Humerus	Lateral Epicondyle	EL
	Medial Epicondyle	EM

Since the pediatric shoulder model was developed for right side, the .trc file was mirrored to match the location of experimental markers with the model markers. The mirroring was done by multiplying -1 to all the Z coordinates. Then the mirrored .trc file was translated to make experimental markers come as close to model markers as possible before starting the scaling process.

Table 10. 2: Scaling pairs used to compute scale factors: the same markers pairs were used to scale the right shoulder markers and left mirrored to right

Body segment	X	Y	Z
Thorax	(IJ, PX), (C7, T8)	(IJ, PX), (C7, T8)	(IJ, AA)
Clavicle	(IJ, AA)	(IJ, AA)	(IJ, AA)
Scapula	(AA, AS)	(AS, AI)	(AA, AS)
Humerus	(EM, EL)	(AA, EM)	(EM, EL)

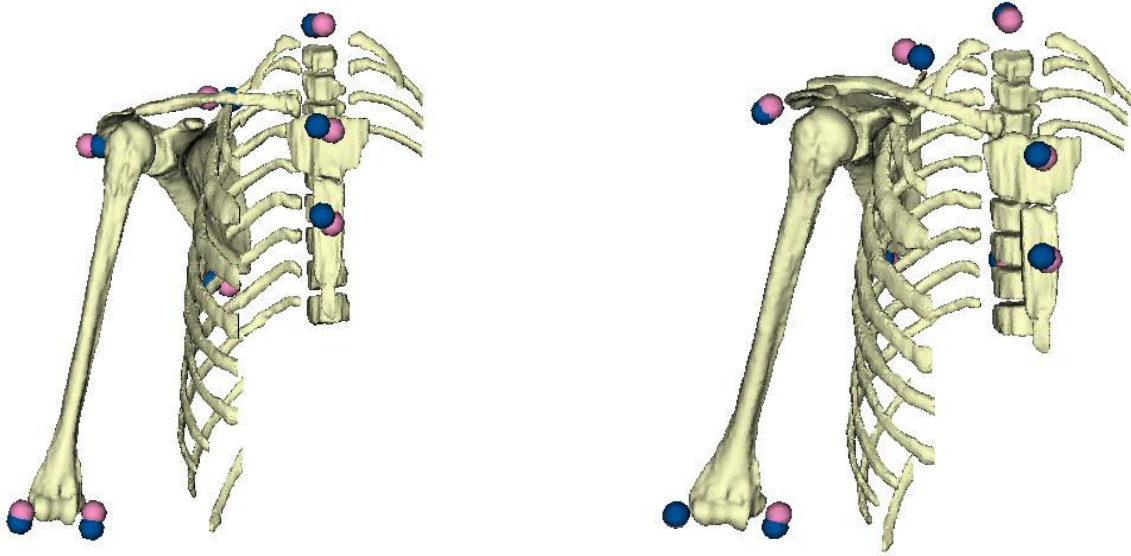


Figure 10. 3: Model after scaling (static pose). Left: impaired right: healthy. The experimental markers are in blue. Note that the posterior and anterior displacement of the humerus with respect to scapula in the impaired GH joint is clearly visible in the right shoulder (left image).

After performing the scaling (figure 10.3), parameters of the scapulothoracic joint were adjusted to respect the description of the joint coordinate system as described in chapter 9. After scaling, marker error for right shoulder scaling was RMS= 1.4cm (Max = 1.9cm (TS)) and marker error for left shoulder scaling was RMS= 1.2cm (Max = 1.9cm (TS)). Also, after scaling, ST joint parameters (ellipsoid definitions) were adjusted to match with the scaled model as the scaled model did not retain the optimal parameters put in place in the original model.

10.2.3 Inverse kinematics

The inverse kinematics tool provided in OpenSim converts the experiment-based marker trajectory file into a model based kinematic motion file of joints in the model with the defined joint coordinate systems. The algorithm sweeps the position of the experimental markers in all the time frame. In each time step, the IK algorithm aims to find the pose of the model (generalized coordinates) that has “best match” with the experimental markers at the same time step. The “best match” is mathematically formulated as a minimization problem, which searches for the generalized coordinates whose marker and coordinate errors are minimum. It is also possible to include experimental generalized coordinate values obtained from another motion capture system for the same trial. In our case, we don’t have these values, thus we used only experimental marker positions through each time step of the motion.

The weighted least squares equation can be written as follow:

$$\min_q \left[\sum_{i=1}^n w_i \|x_i^{exp} - x_i(q)\|^2 \right]$$

Where n is the number of markers used, q is the vector of the generalized coordinates, x_i^{exp} is the position vector of the experimental marker i and $x_i(q)$ is the position vector of the corresponding model marker i . Thus, at each time frame, the algorithm tries to find the generalized coordinates that minimize the marker errors, which is the distance between the model marker and the associated experimental marker. w_i is the weight that we can attribute to a given associated experimental and model marker depending on the accuracy of marker placement.

In our case, we applied a uniform weight for all the marker positions since they were all assumed to have the same certainty (accuracy) of placement. The inverse kinematic algorithm was solved for flexion motion trajectory in both right and left shoulder (impaired and non-impaired) using marker matching through time. When the joint kinematics were compared, the difference between healthy and impaired side was clearly highlighted as expected.

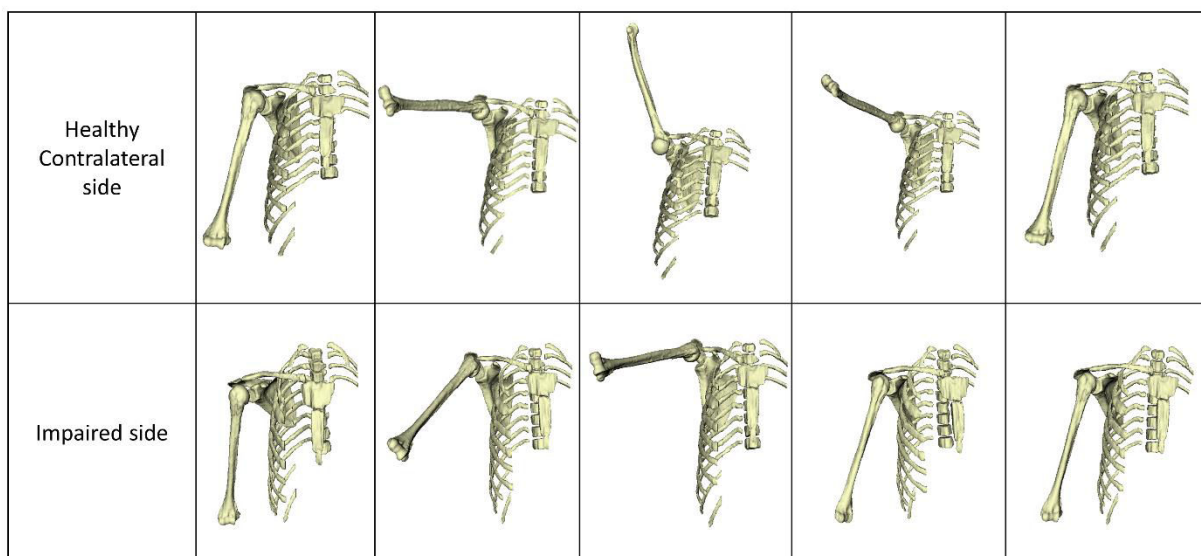


Figure 10. 4: Healthy and impaired kinematic model movement in one forward flexion cycle movement.

The impaired side (right side) of the child was restricted to the qualitative thoracohumeral flexion of approximately 90° from its resting position (figure 10.4). Thorax kinematics with respect to ground revealed compensatory role of thorax motion during the motion of impaired hand (10.5). While the rotations on healthy side were stable, for unhealthy side, the thorax rotated forward during initial flexion and then rotated backward. Thorax also rotated towards the healthy side at the end of the flexion motion. So, the backward and medial tilt to the thorax provided the means to have more flexion.

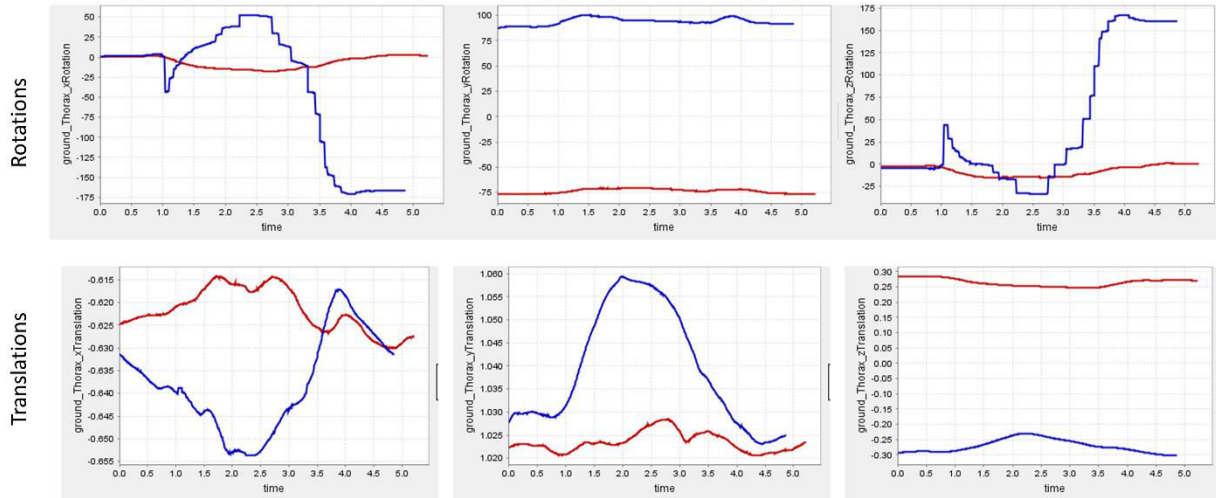


Figure 10. 5: Thorax-ground kinematics for all six degrees of freedom. Healthy kinematics is represented by red curve and impaired kinematics is represented by blue curve.

The sternoclavicular kinematics also revealed differences in its axial rotation and elevation/depression kinematics (figure 10.6). While it is expected to have these differences, we do not know the exact effect of these on the shoulder function. It may be that these differences are a side effect of the thorax compensatory motion.

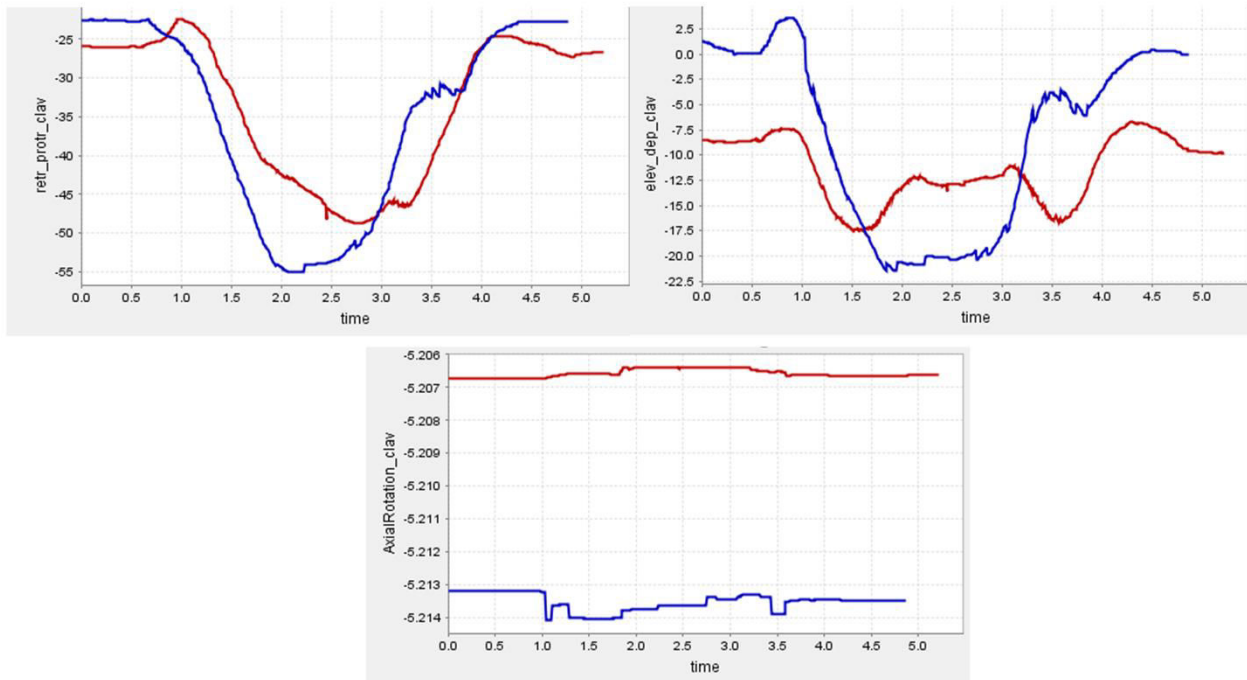


Figure 10. 6: Sternoclavicular kinematics for three rotational degrees of freedom. Healthy kinematics is represented by red curve and impaired kinematics is represented by blue curve.

The two most important and interesting kinematics were GH joint and ST joint kinematics. For GH joint kinematics, the impaired side could not elevate to the entire range of motion (figure 10.7) and was also constrained by the increased internal rotation of the humerus instead of normal external rotation on the healthy side. This internal rotation could be due to the stiffness in the subscapularis muscle that makes excessive internal-medial rotation of the arm as it flexes. The reduced range of motion could also be due to the bone deformities in the GH joint, however, we could not identify those as no imaging data was available.

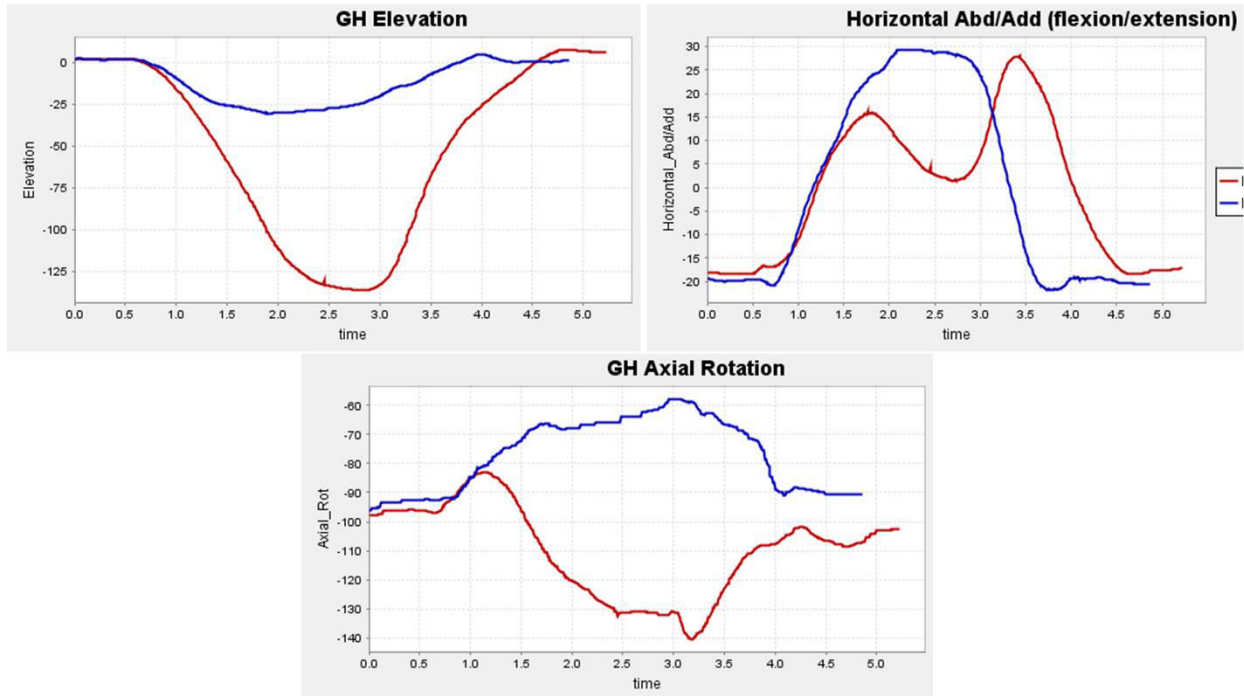


Figure 10. 7: Glenohumeral kinematics for three rotational degrees of freedom. Healthy kinematics is represented by red curve and impaired kinematics is represented by blue curve.

For the scapulothoracic joint, the impaired side showed increased scapular abduction with increased scapular elevation as well as upward rotation (figure 10.8). As proposed previously by Seth and associates [4], scapular abduction, upward rotation and elevation are coupled ST motions. In our case, for the impaired side they were more pronounced. Scapular internal rotation or winging showed interesting kinematics for the impaired side. While the healthy side provided a much needed internal rotation with a range of around 17° to 18°, the impaired side was externally rotated since the beginning and did not rotate much (range of 5°). The ST kinematics on the healthy side corroborated well with the one reported in Seth study [4] indicating an indirect validation of the model simulations. However, we could not comment on the impaired side as no previous studies have reported an impaired ST kinematics in pediatric population with OBPP. To our knowledge, this is the first study to report computational derivation of ST kinematics for an OBPP case study.

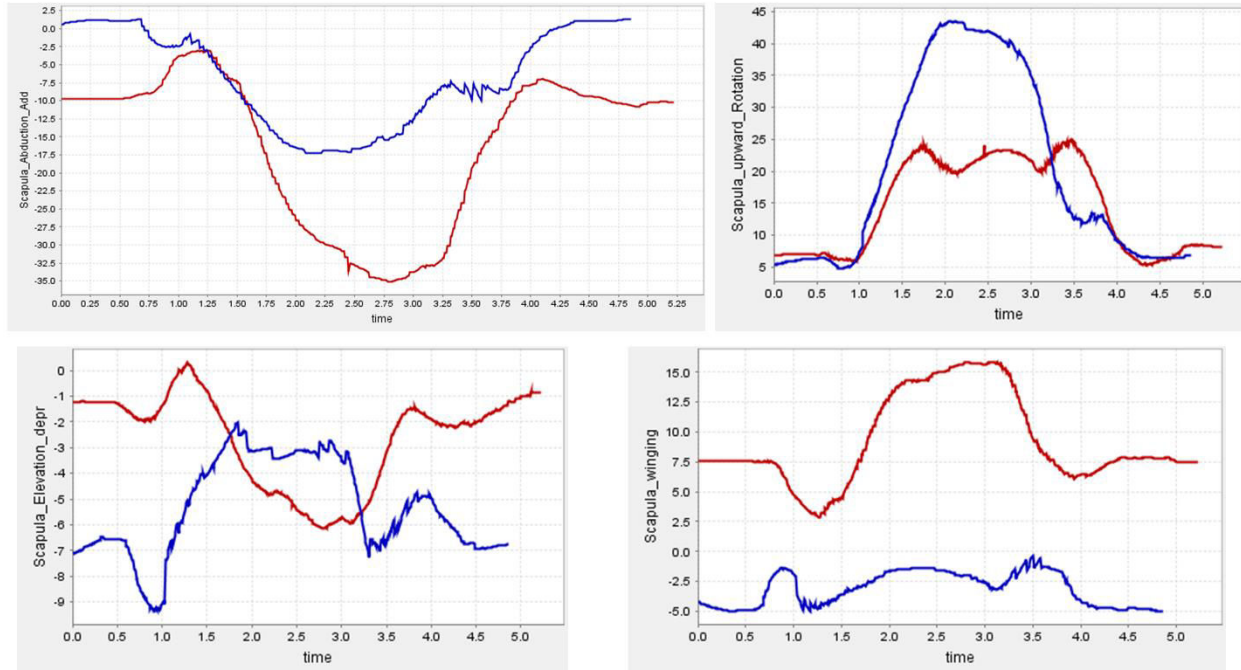


Figure 10. 8: Scapulothoracic kinematics for scapular upward rotation, scapular abduction, scapular elevation and scapula winging. Healthy kinematics is represented by red curve and impaired kinematics is represented by blue curve.

10.3 Inverse Dynamics

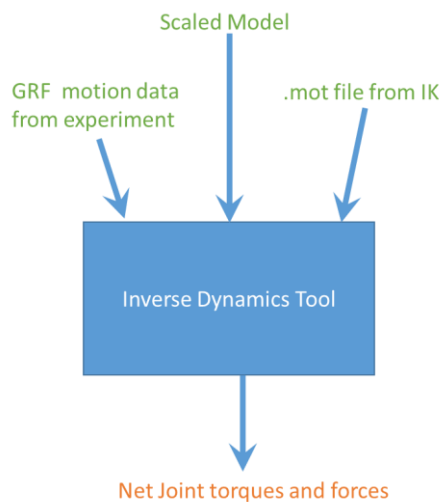


Figure 10. 9: Schematic diagram of inverse dynamics tool input and output parameters

Inverse dynamics analysis provides generalized forces of the multibody system as we have seen in chapter 8. OpenSim inverse dynamics tool takes into consideration the external forces if available from the experiments, the scaled model, and the motion file (.mot) that is the output of IK tool (figure 10.9). We did not have any experimental data on external forces, hence we skipped that input. Other two inputs were provided to the ID tool to understand the net joint forces and moments for a given motion (forward flexion).

The results of the ID tool were analyzed for GH and ST joints only. For GH joint, three joint torques were predicted that corresponded with rotational degrees of freedom of the GH joint (figure 10.10, and 10.11, and 10.12). For healthy side, all the joint torques ranged from -Nm to +2Nm whereas the impaired model showed a considerable amount of fluctuations. While the fluctuations may be regarded as a result of fluctuations in marker dataset, they also might be due to the realistic behavior of the impaired GH joint itself. The muscle imbalance is a well-known phenomenon in children with OBPP. To

create the desired movement, a child with OBPP has to go through an imbalanced trajectory that fluctuates kinematically. This could lead to the fluctuations in the joint torques that we are seeing here.

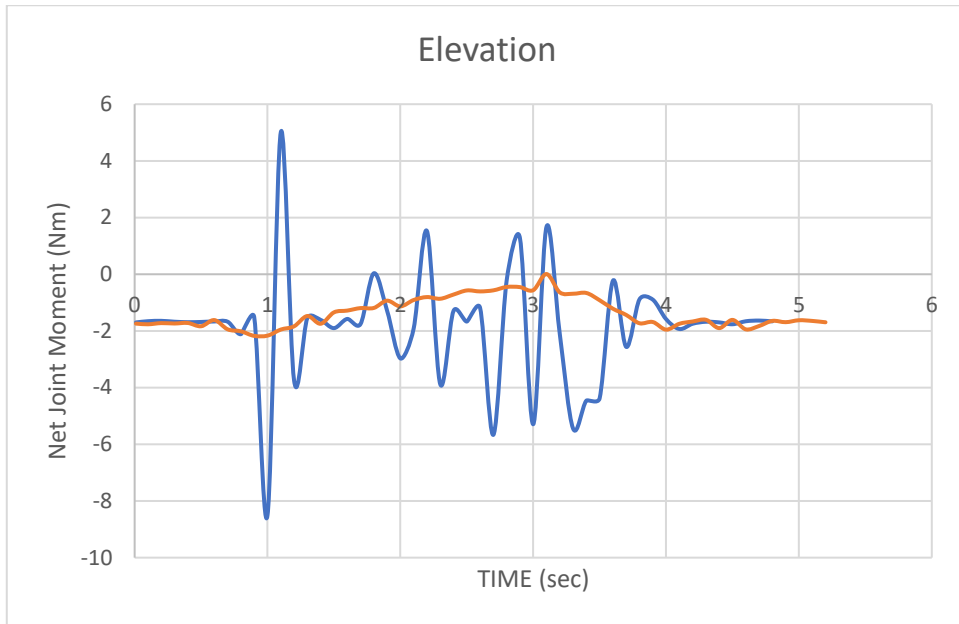


Figure 10. 10: Net joint torque for forward flexion movement between healthy and impaired side in the glenohumeral plane of elevation. Blue line indicates impaired side and orange line indicates healthy side.

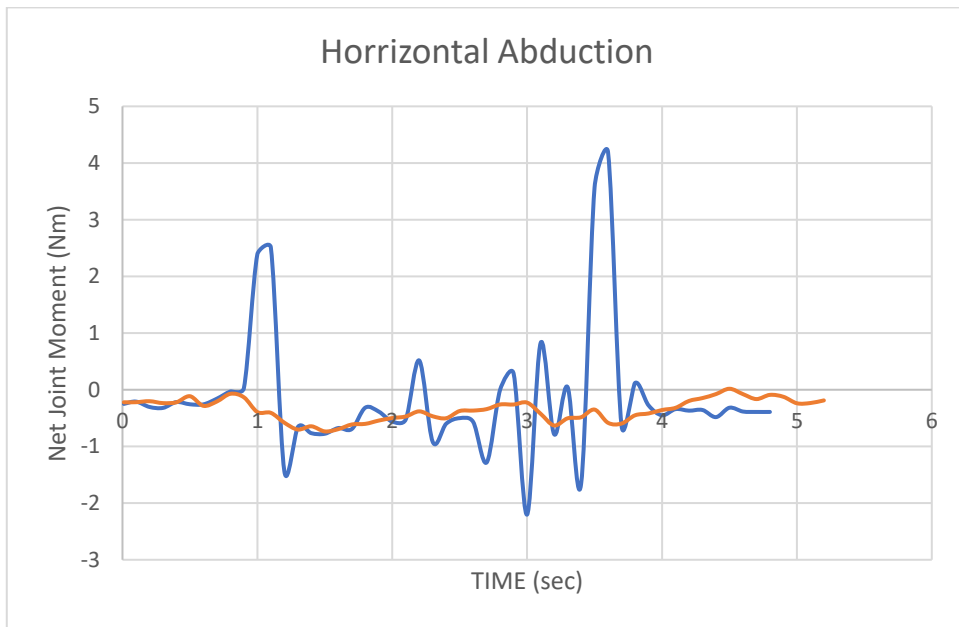


Figure 10. 11: Net joint torque for forward flexion movement between healthy and impaired side in the glenohumeral plane of horizontal abduction. Blue line indicates impaired side and orange line indicates healthy side.

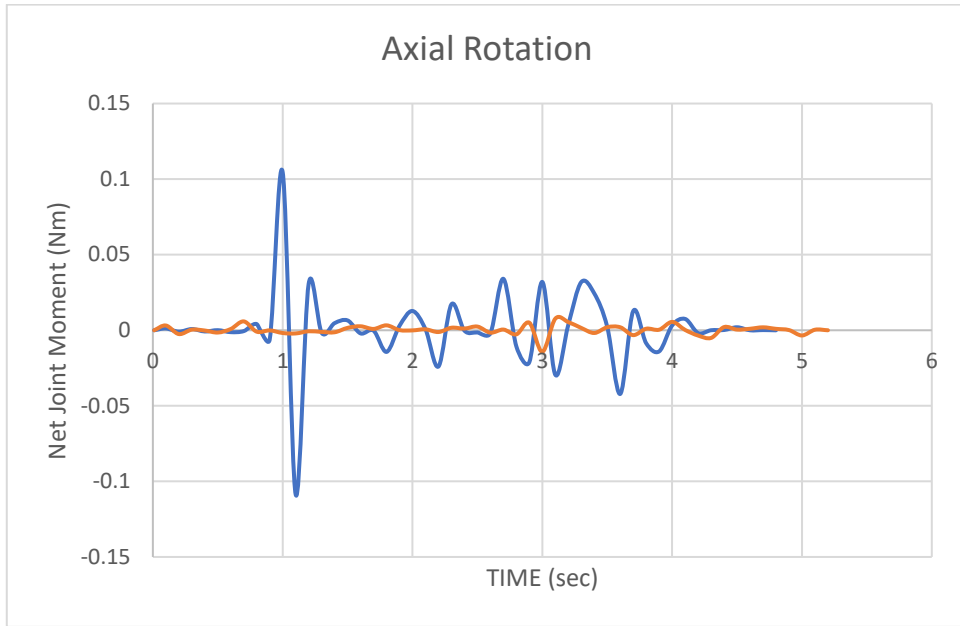


Figure 10. 12: Net joint torque for forward flexion movement between healthy and impaired side in the axial rotation. Blue line indicates impaired side and orange line indicates healthy side.

For the scapulothoracic joint, similar pattern of smooth and fluctuating joint torques between healthy and impaired side was found (figure 10.13, 10.14, 10.15 and 10.16). The pattern of the joint torques for ST motion corroborated well with previous study [4]. Another study by Wu and colleagues [5] have reported fluctuations in joint torques for movement velocities in children with Cerebral Palsy. While we may not extend the similar conclusion to OBPP pathology, it might provide an important insight into the treatment and rehabilitation of children with OBPP.

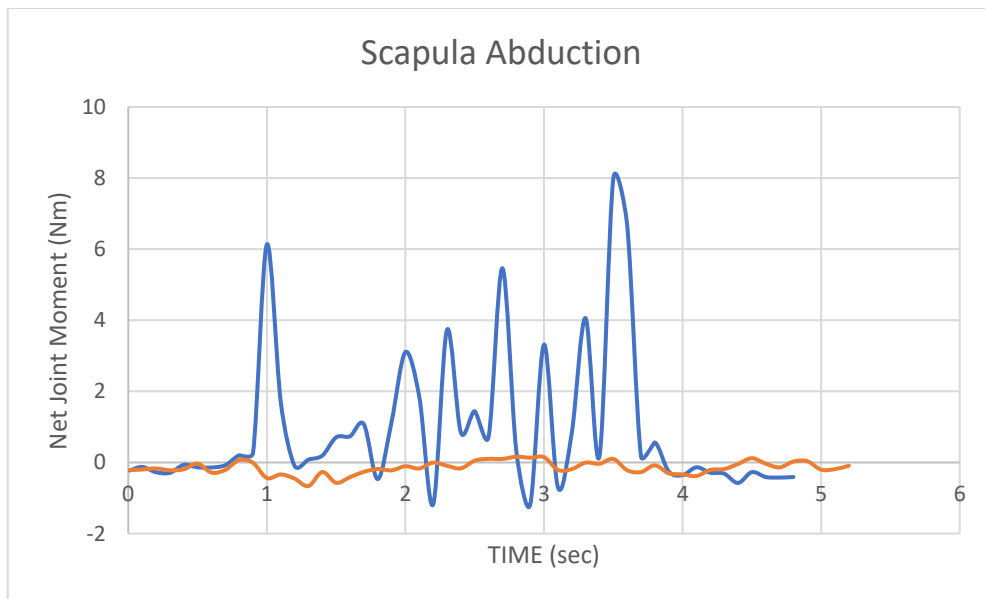


Figure 10. 13: Net joint torque for forward flexion movement between healthy and impaired side for scapula abduction. Blue line indicates impaired side and orange line indicates healthy side.

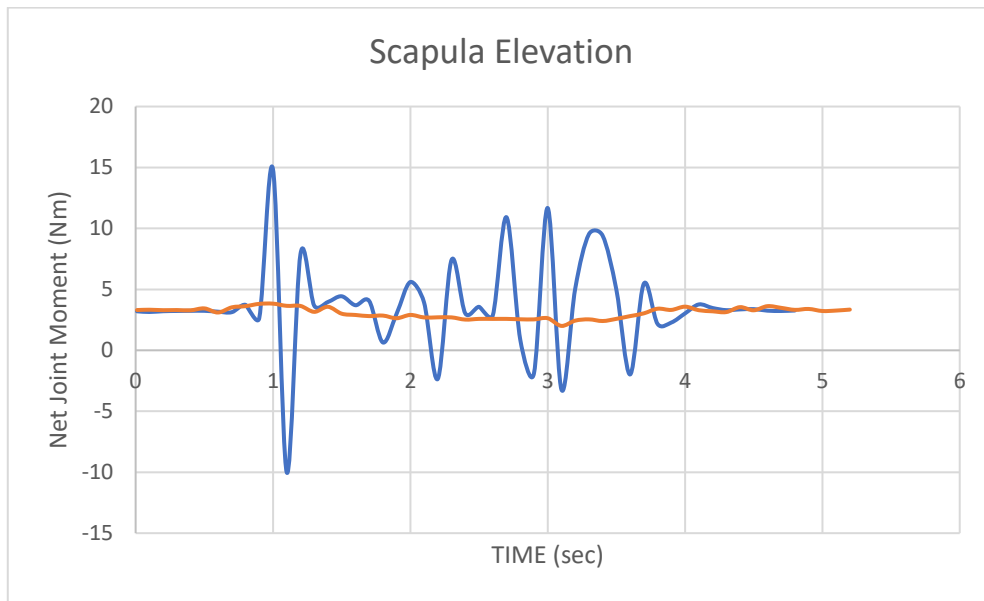


Figure 10. 14: Net joint torque for forward flexion movement between healthy and impaired side for scapula elevation. Blue line indicates impaired side and orange line indicates healthy side.

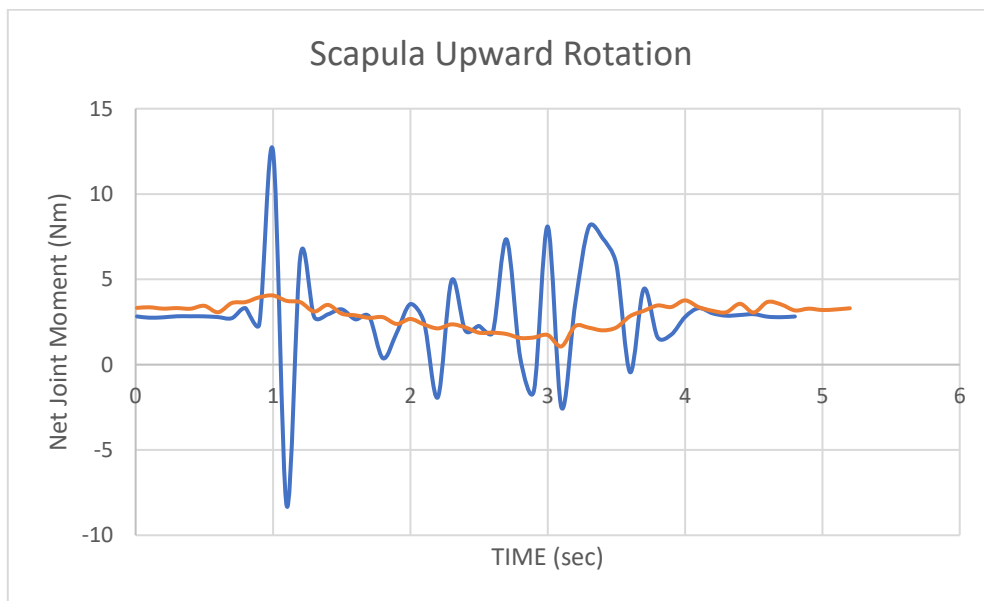


Figure 10. 15: Net joint torque for forward flexion movement between healthy and impaired side for scapula upward rotation. Blue line indicates impaired side and orange line indicates healthy side.

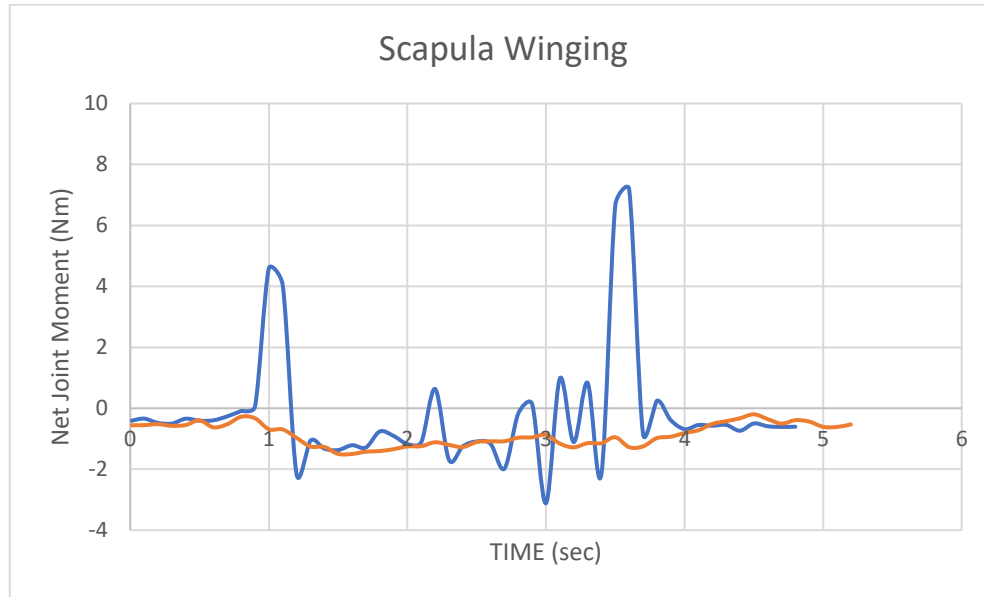


Figure 10. 16: Net joint torque for forward flexion movement between healthy and impaired side for scapula winging. Blue line indicates impaired side and orange line indicates healthy side.

10.4 Discussion

This chapter provides an inverse kinematics and inverse dynamics analysis of a child with OBPP using our pediatric shoulder musculoskeletal model developed based on a healthy child data. The subject-specific scaling was performed using linear ratios of body segments as proposed in a previous study [3]. The scaling RMS errors were reported to be less than 2cm on each side. Although the scaling process was performed, we do not expect to achieve accurate scaling on the impaired side. The marker based linear scaling may not perform well especially with respect to the resting position of the scapula and humerus bones on the impaired side. Such an information is quintessential for the clinical evaluations. We did achieve the maximum marker offset error of 1.9cm which was less than a recommended threshold of 2cm in the OpenSim community. However, such error is associated with adult models and we do not know if we can simply take the same threshold for pediatric population as well.

Scapulothoracic kinematics is a complex phenomenon with challenging mathematical construct. Most researchers either ignore evaluating the ST joint or simplify the joint so much that it loses its evaluation potential. In OBPP, restricted GH joint motion forces ST joint to share greater load during any daily living motion. Thus it is very important for us to have a evaluation capability of the ST joint. The pediatric shoulder musculoskeletal model successfully identified the pathological kinematics and in doing so provided greater insights into the ST kinematics. One worry about the modeling of the ST joint is the way the sliding surface of ellipsoid is constructed. After performing a scaling operation, this ellipsoid must be readjusted to have optimal fit. This poses a potential limitation to the modeling and future work will be directed to eliminate this problem. Another limitation arises from the fact that there is a lot of skin motion artifact on scapula markers and this might negatively impact the ST kinematics. A method proposed by Brochard and colleagues might prove to be a valid alternative where scapula underwent double

calibration method [6]. In comparison with adult kinematics, the quantified GH kinematics for healthy side showed similar pattern and provided an indirect validation of the model.

Inverse dynamics provided an insight in joint torques and moreover highlighted the joint stability in terms of fine muscle balance on healthy side and muscle imbalance leading to unsmooth handling of joint torque requirements on the impaired side. While literature does not report any events of joint toques on upper limb in children with OBPP, it must be studied in a clinically oriented research study and also to see if such an information can be regarded as a baseline and a performance measure for identifying improvements in rehabilitation training.

In summary, the pediatric shoulder musculoskeletal model illustrated its capability in predicting inverse kinematics and deriving inverse dynamics measures. Such a model will be used for a greater study involving higher number of healthy and impaired cohort and analyzing their shoulder joint mechanics.

10.5 Chapter 10 References

- [1] S. L. Delp *et al.*, “OpenSim: open-source software to create and analyze dynamic simulations of movement.,” *IEEE Trans. Biomed. Eng.*, vol. 54, no. 11, pp. 1940–1950, Nov. 2007.
- [2] A. Seth, M. Sherman, J. A. Reinbolt, and S. L. Delp, “OpenSim: a musculoskeletal modeling and simulation framework for in silico investigations and exchange.,” *Procedia IUTAM*, vol. 2, pp. 212–232, 2011.
- [3] C. Klemm *et al.*, “Anthropometric Scaling of Anatomical Datasets for Subject-Specific Musculoskeletal Modelling of the Shoulder.,” *Ann. Biomed. Eng.*, vol. 47, no. 4, pp. 924–936, Apr. 2019.
- [4] A. Seth, R. Matias, A. P. Veloso, and S. L. Delp, “A Biomechanical Model of the Scapulothoracic Joint to Accurately Capture Scapular Kinematics during Shoulder Movements.,” *PLoS One*, vol. 11, no. 1, p. e0141028, 2016.
- [5] Y.-N. Wu, Y. Ren, A. Goldsmith, D. Gaebler, S. Q. Liu, and L.-Q. Zhang, “Characterization of spasticity in cerebral palsy: dependence of catch angle on velocity.,” *Dev. Med. Child Neurol.*, vol. 52, no. 6, pp. 563–569, Jun. 2010.
- [6] S. Brochard, M. Lempereur, and O. Remy-Neris, “Double calibration: an accurate, reliable and easy-to-use method for 3D scapular motion analysis.,” *J. Biomech.*, vol. 44, no. 4, pp. 751–754, Feb. 2011.

Chapter 11

Summary and Future Perspectives

11.1 Summary

Shoulder joint is a complex structure to manage both clinically and computationally. Clinical and surgical understanding of shoulder function before and after intervention leads to successful outcomes and pain free shoulders. Efficacy in shoulder surgery planning in adults and understanding shoulder biomechanics in pediatric population for musculoskeletal disorders such as OBPP are crucial components of treatment. State-of-the-art techniques used in medical imaging, machine learning, and musculoskeletal modeling can provide such an understanding or efficacy to certain extent. However, these techniques do not individually excel in complete understanding of the patho-physiology of the shoulder joint. Thus, new pathways must be established either by adapting an interdisciplinary approach or by devising completely new techniques.

In this thesis, I had set my research aims towards the global goal of building a combined framework of two research domains – Statistical Shape Modeling (SSM) and musculoskeletal modeling to evaluate musculoskeletal disorders in pediatric shoulder joint. The first part provided thorough details about shoulder joint anatomy and biomechanics. Second part was focused on SSM domain and related research. As proposed in the first specific aim, I successfully built SSMs of adult shoulder bones and reported on the clinical utility of such SSMs in predicting new bone shapes (Chapter 4). We learned that when an SSM is augmented with a set of anatomical landmarks, the clinical utility of such augmented SSM is higher than when using the SSM alone. We also evaluated three landmark sets and selected the one that provided best clinical utility. As per the second specific aim, we illustrated and validated the methodology to accurately predict muscle insertion regions for scapula and humerus bones. In the process, we learned that such techniques can be applicable to all the bones and respective muscle insertions. In the third specific aim, I successfully developed an algorithm to automatically predict missing scapular bone shape and validated the algorithm for a group of scapulae that mapped the anatomical variations in the scapula. We learned that this algorithm can be effectively employed in presurgical planning to predict a pre-morbid scapula shape which forms an important information for surgery planning. Similar algorithm can also be used to predict complete scapular shape from incomplete imaging data and thus subject-specific scapular geometry (and muscle insertions) could be incorporated in the modeling domains. The fourth aim focused on building a framework to integrate SSM and musculoskeletal domains to achieve subject-specific model parameters. We used a previously developed shoulder musculoskeletal model (NSM) and the muscle insertion prediction algorithm developed in third specific aim to generate subject-specific muscle insertions. The comparison between generic and subject-specific models showed altered muscle moment arms, joint contact forces, and joint torques. While we could not validate that subject-specificity was achieved, the results corroborated well with the literature. Thus, it was illustrated at the end of part II that a combined framework can be established for adult shoulder biomechanics evaluations.

Part III of the thesis was focused on the musculoskeletal modeling development for pediatric shoulder joint. After providing a brief summary on the theory of multibody system dynamics, a pediatric healthy shoulder musculoskeletal model was built. This model has 13 degrees of freedom, 52 musculotendon actuators to represent 14 shoulder muscles, representation of GH, ST, SC, and AC joints and wrapping surfaces for muscles to follow the realistic contraction path. The muscles were modeled as Hill-type muscle models and no ligaments were present in the model. The model was developed in the open source framework OpenSim specially designed for musculoskeletal modeling. The geometrical information and landmarks used to define the embedded coordinate frames were extracted from an imaging dataset of a 13-year-old girl. The body segment and musculotendon parameters were derived from either the imaging data or literature. In chapter 10, this generic model was used to analyze a forward flexion movement on one adolescent data with OBPP and to generate a comparison between subject's healthy side and impaired side. The generic kinematic model was scaled to subject's anthropometric data using static marker set derived linear scale ratios. The motion analysis marker tracking was applied to the scaled model and model predicted inverse kinematics was determined. Using this inverse kinematics, generalized forces (joint torques and joint forces) were derived through inverse dynamics analysis. Throughout this study, a healthy parameter was compared against its impaired counterpart. All the results show intuitive and qualitative difference between the two sides and can be explained with known knowledge about the subject and OBPP.

Thus, a combined framework for adult shoulder analysis was established and a pediatric shoulder musculoskeletal model was successfully generated. Despite achieving multiple novel solutions in the course of this thesis, there were limitations as well. Limitations exist in the SSM as well as musculoskeletal modeling areas. For SSM domain, the first limitation is the number of sample size used to build SSM of shoulder adult bones and second limitation was unavailability of pediatric data to build SSM of shoulder pediatric bones. However, this thesis was able to create a generic framework for deriving subject-specific bone shapes and muscle insertions for shoulder bone shape. In the musculoskeletal modeling domain, the first and foremost limitation is the validation of the developed model and simulations. To validate the musculoskeletal model, we would need an experimental protocol to acquire data on children with OBPP. To set-up such a protocol in the pediatric population needs an approval from the ethical research committee which is hard and is thus a long process since it involves parents as well. Since this was not possible within the span of my thesis, I could not build such data. Thus, the validation of the developed model is not performed. However, the model predictions can be qualitatively compared with other studies to confirm that the model behavior is in agreement. For same reasons, a complete framework for pediatric population could not be established due to non-availability of data needed to build pediatric bone SSMs. However, the developed methods can be easily transferred in future when such a dataset is available.

11.2 Perspectives

This thesis proposed a combined framework and illustrated in adult population. Based on the current state of the results obtained, following perspectives are planned.

- 1) Objective: Validate the SSM-based muscle insertion prediction algorithm using MRI data from real adult volunteers.

Methods: This is one of the immediate perspectives from this thesis. Current muscle insertions algorithm is not validated on real MRI data and thus needs such validation for its use as a clinical utility tool. Shoulder muscle insertions cannot be made visible in a single MRI scan and multiple MRI scans that are oriented in the direction (or transverse to) of the muscle are needed. In this objective, I propose to acquire MRI data on at least five healthy adult individuals with the best possible sequence and orientations to image the six muscles that were predicted by the algorithm (Infraspinatus, supraspinatus, Teres Major, Teres Minor, Subscapularis, and Deltoid). The MRI will be segmented manually to create bone shapes of scapula and humerus. Muscle insertions will be identified and segmented by expert radiologist and will be used as a gold standard. Model predictions will then be validated against this gold standard.

2) Objective: Building SSMs of pediatric shoulder bones

Methods: This is the second immediate perspective given the current state of this thesis. To develop the proposed combined framework of SSM and musculoskeletal modeling in the pediatric population, we first need a database to generate the SSMs of pediatric bones. Only then we will be able to employ the missing part and muscle insertion prediction algorithms in the framework. Thus, in this objective, I propose to acquire MRI data on pediatric population with OBPP pathology, and in the age range of 7 to 14 year-old ($n = 30$ ideally), including the contralateral healthy side. This process will start with seeking an approval from the ethical committee. Once the approval is obtained, 30 children with OBPP will be enrolled in the study. An MRI protocol to acquire images of entire scapula and humerus bones will be used and high-resolution images of these bones will be acquired. The images will be manually segmented to create a database of pediatric healthy and OBPP shoulder bone surface meshes. This database will then be run through SSM pipeline explained in Chapter 4 of this thesis to build pediatric bone models. These pediatric SSMs will be tested for their robustness criteria. Further, using the methods explained in chapter 5, muscle insertions will be segmented on the bone shapes and an augmented SSM with muscle insertion regions will be developed. This augmented SSM will then be used to predict muscle insertions in the new data to create subject-specific muscle insertions that can be imported in the musculoskeletal pipeline.

3) Objective: To validate pediatric shoulder musculoskeletal model using EMG-based experimental data

Methods: Validation of the developed pediatric shoulder model will be the first future research direction of the musculoskeletal modeling part. MRI data will be ideally used for scaling the generic pediatric musculoskeletal model to each subject anthropometry. For this, a cohort of children with no prior shoulder injury will be targeted ($n = 15$ ideally). Each child will visit the radiology department at the CHRU Cavale Blanche and motion analysis laboratory at the CHRU Morvan and motion experiments will be performed. The imaging protocol will include high resolution MRI scans of the entire scapula and humerus bones. In the experimental protocol, first step would be to obtain all the anthropometric and demographic data. In the second step, maximal voluntary isometric contractions for shoulder musculature will be collected using hand-held dynamometer data. In the third step, standard reflective markers will be on anatomical palpable locations of the shoulder. Additional markers would also be used to determine the rotation center and define the entire forearm. Muscle surface EMG electrodes will be placed on muscles of interest and whenever feasible (deltoid, trapezius – clavicle segment, latissimus dorsi upper segment, pectoralis all regions). Using this set-up, subject will perform standard static trials

and dynamic trials (3 each) of daily living activities. Subjects will also perform a standard protocol to determine GH rotation center.

Pediatric shoulder model will then be scaled using the parameters extracted from the imaging dataset. The scaled model will then undergo inverse kinematics and inverse dynamics analysis to derive joint kinematics and generalized joint forces (joint torques and joint reaction forces). Then, a computerized muscle control evaluation to optimally distribute the joint toques and forces into the muscles will be performed. The model will be validated with leave one out strategy where muscle activation of one muscle at a time will be predicted and compared with the experimental data. Next, the muscle control algorithm will be supplied the muscle activations collected during the movements. Muscle forces in the remaining muscles will then be predicted using optimization algorithms. These muscle forces will provide a baseline for understanding muscle forces in pediatric shoulder and its comparison with OBPP.

Once the generic pediatric model is verified and validated the next objectives could be targeted.

- 4) Objective: To evaluate muscle force imbalances in children with OBPP using the EMG driven subject-specific pediatric shoulder model.

Methods: In this for this objective, a pediatric cohort with OBPP will be enrolled ($n = 15$). Inclusion criteria will be – no botulinum toxin injection or surgical procedure in last 6 months and the presence of OBPP is clinically evaluated with restrictions in the range of motions for shoulder movement. This cohort will undergo similar data collection sequence as for the healthy cohort. This will include MRI acquisition as well as motion analysis. The movement analysis protocol will include data collection from both healthy and unhealthy sides using the proposed marker sets needed for the model tracking. Data from each child will be used to build subject-specific musculoskeletal models. The collected EMGs will then be processed to extract muscle activations which will work as an input to the computerized muscle control algorithm in OpenSim. This will lead to EMG-based muscle force predictions for healthy and unhealthy sides. The results of predictions of inverse kinematics, inverse dynamics, and muscle forces will then be compared between the cohorts. This will provide us insights with 1) muscle imbalance in the children with OBPP in comparison with healthy controls and using a validated pediatric musculoskeletal model, 2) effect of OBPP on contralateral shoulder, 3) muscle contraction strategies employed by OBPP cohort for various movements.

- 5) Objective: Simulating rehabilitation strategies for children with OBPP

Methods: In this study, the previously developed subject-specific models of children with OBPP will be used to derive multiple rehabilitation strategies which are again subject-specific. Within the study, following rehabilitation strategies will be modeled and analyzed: 1) What muscles need to be strengthened/targeted to have isolated improvements in range of motions in each direction, 2) what muscles need to be focused to have combined improvements in all the range of motions. 3) What will be the effect of botulinum toxin injections in one of the muscles. 4) How a change in muscle model property (optimal fiber length, maximal force production) can affect the outcome motion. These simulations will provide valuable insights in the way clinicians can treat OBPP on subject specific levels.

11.3 Future directions

Generating subject-specific musculoskeletal models to eliminate errors associated with generic model parameters is one of the long-term aims of this project. To incorporate higher level of subject-specificity in the musculoskeletal geometry, we have already developed an algorithm to predict muscle insertions. Future studies will focus on determination of subject-specific joint axes and joint center from the experiments and/or imaging data. Considering the availability of the dataset in shoulder bones, we plan to work on building age specific bone SSMs and then build a statistical tool to predict bone growth pattern. Such an analysis will provide valuable insights in case of pathological deformity in bone morphology.

Deep learning methodology has been involved in many important tools in medical imaging (image segmentation, tumor detection, image classification). We are planning to use this advanced technology in the future work. The choice of deep learning as future focus is motivated mainly by 1) **the scarcity of imaging data in the pediatric population:** This can be achieved by combining SSM and deep learning to provide data augmentation. In fact, we can use an SSM built from a relatively small training set to generate anatomically valid shapes of the same bone to be used in training the deep neural network. 2) **The segmentation of the pediatric shoulder bones:** the segmentation of different medical image modalities (MRI, CT, etc.) using deep learning has shown promising results in adult population. The segmentation of pediatric bones remains a challenging task as the bone is in a growth phase and differentiating the growth cartilage tissue from the bone is not a straightforward task. 3) **Classification of healthy and pathological shoulder** using the anatomical measures extracted automatically from medical images along with the bone shape.

In conclusion, this thesis has a direct contribution to the activities, dedicated to the children, of IMAGINE team, of our lab “LaTIM INSERM U1101”. This is the first engineering thesis, in our lab, combining state-of-the-art SSM and musculoskeletal modeling methods to evaluate pediatric shoulder disorder. Thus, the framework and algorithms proposed in this thesis lay the foundation for many more studies and improvements to come. Such a foundation will provide a stepping stone for students and researchers to join the LaTIM in future.

Titre : Vers un framework combinant la modélisation statistique de forme et la modélisation musculosquelettique pour l'articulation de l'épaule pédiatrique

Mots clés : Processus gaussiens, Prédiction de l'insertion des muscles, Forme scapulaire pré-morbide, Analyse morphométrique, Biomécanique de l'épaule, Paralysie du plexus brachial obstétrique

Résumé : La paralysie obstétricale du plexus brachial (POPB) est une paralysie du membre supérieur qui survient à la naissance et peut entraîner une déformation de l'articulation et un fonctionnement anormal de l'épaule. Bien que le traitement de la POPB tente de restaurer la fonction de l'épaule, la pathomécanique sous-jacente n'est pas encore clairement comprise. Les modèles computationnels sont efficaces pour fournir de telles informations, mais il n'existe aucun modèle d'articulation de l'épaule pédiatrique pour comprendre la POPB. Ainsi, ce travail de recherche a pour but de construire un framework combinant les avancées dans les domaines de la modélisation statistique de forme (MSF) et de la modélisation musculo-squelettique multi-corps (MCM). Due à l'insuffisance des données dans la cohorte pédiatrique, ce cadre a été mis en place pour l'articulation de l'épaule adulte.

Pour cela, la précision de la MSF a été illustrée en prédisant 1) la forme de l'omoplate pré-morbide, et 2) les régions d'insertion musculaire sur l'omoplate et l'humérus. Cette méthode a ensuite été intégrée aux modèles MCM pour l'épaule adulte pour souligner l'importance des modèles spécifique-patient pour l'usage clinique. Pour le second objectif de cette thèse, j'ai développé un modèle MCM pédiatrique du complexe articulaire de l'épaule en utilisant le logiciel OpenSim. Grâce aux approches de cinématique et dynamique inverse, le modèle a permis de déterminer les différences de dynamique articulaires entre le côté sain et le côté pathologique. Les travaux futurs seront axés sur l'extension du travail réalisé pour la population pédiatrique afin de comprendre la pathomécanique de POPB.

Title : Towards a Combined Statistical Shape and Musculoskeletal Modeling Framework for Pediatric Shoulder Joint

Keywords : Gaussian processes, Muscles insertion prediction, Premorbid scapular shape, Morphometric analysis, Shoulder biomechanics, Obstetrical Brachial Plexus Palsy

Abstract : Obstetrical Brachial Plexus Palsy (OBPP) is a common birth injury in children leading to shoulder joint deformity and abnormal function. While the management of OBPP disorder focuses on restoring the shoulder joint function, the underlying pathomechanics is not clearly understood yet. Computational models are effective to provide such insights, however, there is no pediatric shoulder joint model to understand the OBPP disorder. Thus, the global aim of this research work was to build a computational framework combining the advances in statistical shape modeling (SSM) and multi-body musculoskeletal modeling (MSKM) domains. Due to a lack of sufficient data in the pediatric cohort, I first developed the framework for adult shoulder joint. For this, I illustrated the accuracy of SSM in predicting 1) missing part of the scapula, and 2) muscle insertion regions on scapula and humerus bones.

This method was then integrated with adult shoulder MSKMs to show the differences between generic and subject specific constructs. For the second aim of this thesis, I developed a pediatric MSKM of the shoulder joint complex using OpenSim software. Pediatric MSKM represented scapulothoracic, sternoclavicular, acromioclavicular, and glenohumeral joints with 13 degrees of freedom, and actuated by 52 musculotendon actuators representing 14 shoulder muscles. Using inverse kinematics and inverse dynamics approaches, the model was used to determine the differences in joint kinematics, and joint dynamics between healthy and unhealthy side of a single OBPP subject. Future work is focused on completing the framework on pediatric population and understanding the pathomechanics of OBPP.